Wegener Center for Climate and Global Change
University of Graz

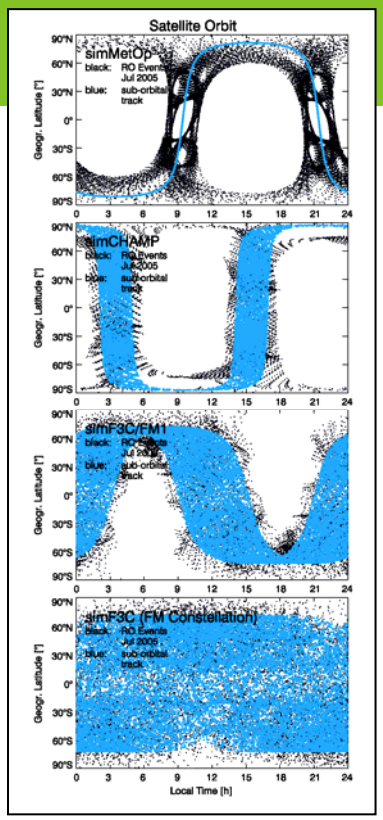

Scientific Report No. 33-2010

Multi-Satellite Climatologies of Fundamental Atmospheric Variables From Radio Occultation and Their Validation

Barbara Pirscher

May 2010

Wegener Center
www.wegcenter.at

UNI GRAZ

FWF
Der Wissenschaftsfonds.

The **Wegener Center for Climate and Global Change** combines as an interdisciplinary, internationally oriented research center the competences of the University of Graz in the research area „Climate, Environmental and Global Change“. It brings together, in a dedicated building close to the University central campus, research teams and scientists from fields such as geo- and climate physics, meteorology, economics, geography, and regional sciences. At the same time close links exist and are further developed with many cooperation partners, both nationally and internationally. The research interests extend from monitoring, analysis, modeling and prediction of climate and environmental change via climate impact research to the analysis of the human dimensions of these changes, i.e., the role of humans in causing and being effected by climate and environmental change as well as in adaptation and mitigation. (more information at www.wegcenter.at)

The present report is the result of a PhD thesis work completed in March 2010. The work was funded by the Austrian Science Fund (FWF) under research grands P18837-N10 (CLIMROCC), P21642-N21 (TRENDEVAL), and P22293-N21 (BENCHCLIM).

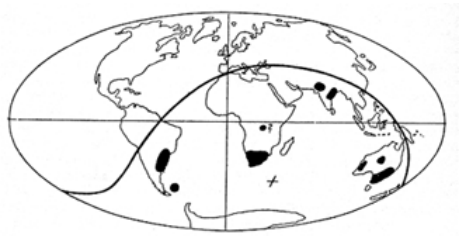

Alfred Wegener (1880-1930), after whom the Wegener Center is named, was founding holder of the University of Graz Geophysics Chair (1924-1930) and was in his work in the fields of geophysics, meteorology, and climatology a brilliant, interdisciplinary thinking and acting scientist and scholar, far ahead of his time with this style. The way of his ground-breaking research on continental drift is a shining role model — his sketch on the relationship of the continents based on traces of an ice age about 300 million years ago (left) as basis for the Wegener Center Logo is thus a continuous encouragement to explore equally innovative scientific ways: *ways emerge in that we go them* (Motto of the Wegener Center).

Wegener Center Verlag • Graz, Austria

ISBN 978-3-9502940-3-3

May 2010

Contact: Barbara Pirscher
barbara.pirscher@uni-graz.at

Wegener Center for Climate and Global Change
University of Graz
Leechgasse 25
A-8010 Graz, Austria
www.wegcenter.at

Mag. Mag. Mag. Barbara Pirscher

Multi-Satellite Climatologies of Fundamental Atmospheric Variables From Radio Occultation and Their Validation

Dissertation

zur Erlangung des akademischen Grades einer
Doktorin der Naturwissenschaften
an der naturwissenschaftlichen Fakultät der
Karl-Franzens-Universität Graz

Betreuer:

Univ.-Prof. Mag. Dr. Gottfried Kirchengast

Assist. Prof. Mag. Dr. Ulrich Foelsche

Graz, März 2010

Wegener Zentrum für Klima und Globalen Wandel
und
Institutsbereich Geophysik, Astrophysik und Meteorologie,
Institut für Physik
Karl-Franzens-Universität Graz

Acknowledgments

I have had the fortune to work on my Ph.D. thesis under the supervision of my advisers Univ.-Prof. Mag. Dr. Gottfried Kirchengast and Assist. Prof. Mag. Dr. Ulrich Foelsche who supported me and my work wherever possible. The sharing of their knowledge during the course of research for this thesis has been invaluable.

I have also been exceptionally lucky to work with my colleague Dr. Michael Borsche in the CLIMROCC team. I would like to thank him for his every day teamwork, help, and fruitful discussions. Even though he is at the Max-Planck Institute in Hamburg, Germany, since July 2009, he tireless supported me throughout my thesis. Very special thanks also to Dr. Andrea Steiner for actively supporting my scientific work and encouraging me whenever necessary.

I am very grateful to all members of the ARSCliSys Research group for their assistance and support, especially to Mag. Florian Ladstädter who was incredibly generous with his time and expertise concerning computer issues. I received invaluable feedback and support on EGOPS development from Dr. Johannes Fritzer and Dr. Andreas Gobiet but my appreciation also goes to Mag. Michael Pock for providing this LaTeX template.

The WEGC provided me an excellent surrounding and infrastructure for my work. Thanks to all colleagues of the DiplomandInnen-/DissertantInnenzimmer for contributing to the excellent working atmosphere in our workplace. In this regard, very special thanks to Mag. Matthias Themeßl and Mag. Georg Heinrich.

During my Ph.D. studies I had the unique opportunity to make a research visit in Boulder, CO, USA. Many thanks to Dr. Ying-Hwa Kuo, Dr. Christian Rocken, and the CDAAC team who cordially hosted me for this period. Heartfelt thanks also to Judy and Louis Etschmaier for their open invitation and for showing me the wonderful landscape close to Boulder during the weekends.

I benefit from extensive and very helpful comments received during seven scientific conferences in Boulder, CO, USA (2006, 2007, 2009), Vienna, Austria (2006, 2009), Graz, Austria (2008), and Taipei, Taiwan (2008) where I got to know a number of scientists from various countries. In this regard, I especially thank Dr. Jens Wickert and Dr. Christian Marquardt.

I am grateful to DMI (Copenhagen, Denmark), GFZ (Potsdam, Germany), JPL (Pasadena, CA, USA), and UCAR (Boulder, CO, USA) for providing RO data, ECMWF (Reading, UK) and NCEP (Asheville, NC, USA) for providing forecast, analysis, and reanalysis data, and Celestrack (Colorado Springs, CO, USA) for making available TLE files. Furthermore, I gratefully acknowledge financial support from the FWF research projects CLIMROCC, TREND-EVAL, and BENCHCLIM.

Most of all, I would also like to thank my family for the emotional support they provided me throughout my entire life. Thanks also to my friends for their encouragement.

I dedicate this thesis to Marko.

Abstract

Monitoring of global climate change requires high quality observations not only on the Earth's surface but also in the free atmosphere. Global Positioning System (GPS) Radio Occultation (RO) observations are known to have the potential to deliver very accurate, precise, and long-term stable measurements between about 8 km and 30 km altitude.

This thesis investigates the suitability of RO observations to serve as climate benchmark record by validating the consistency of RO data provided by different satellites. The main focus lies on systematic differences of RO climatologies, originating from different data processing, data quality, spatio-temporal sampling, and particular orbit characteristics. Data of six RO satellite missions (including one multi-satellite constellation) are analyzed.

Largest disagreements of RO climatologies are observed when comparing data provided by different processing centers. Mean absolute temperature differences between 8 km and 30 km altitude amount to 0.5 K, while climate time series of temperature changes agree much closer.

Utilizing RO data from the same data center and considering spatio-temporal sampling yield remarkable consistency of temperature climatologies with mean differences being smaller than 0.1 K. Disagreements are found to be largest at 35 km, where they exceed 0.2 K. This results from different data quality and its utilization within the processing scheme. Climatologies, which are derived from data with the same quality agree to within 0.02 K also at high altitudes. The measurement's local time, which depends on the satellite's orbit, has a minor but clearly understandable influence on differences in RO climatologies. The results underline the utility of RO data for long-term monitoring of the global climate.

Zusammenfassung

Um den globalen Klimawandel überwachen zu können, sind Daten von hoher Qualität nicht nur auf der Erdoberfläche sondern auch in der freien Atmosphäre unabdingbar. Messungen von Global Positioning System (GPS) Radiookkultation (RO) sind für ihre exakten und langzeit-stabilen Daten zwischen ca. 8 km und 30 km Höhe bekannt.

In dieser Arbeit wird die Konsistenz von RO Messungen verschiedener Satelliten validiert um festzustellen, ob die Daten tatächlich als Referenzklimadatensatz geeignet sind. Das Hauptaugenmerk liegt auf der Untersuchung systematischer Unterschiede zwischen Klimatologien, welche durch verschiedene Prozessierungssysteme, unterschiedliche Datenqualität, Orte und Zeiten der Messungen sowie ausgewählte Orbiteigenschaften zustande kommen. Es werden Daten von sechs Satellitenmissionen (darunter eine Multisatellitenmission) analysiert.

Größte Unterschiede zwischen RO Klimatologien entstehen, wenn man Daten verschiedener Prozessierungszentren vergleicht. Mittlere absolute Temperaturdifferenzen zwischen 8 km und 30 km Höhe betragen 0.5 K, während Klimazeitreihen von Temperaturänderungen viel genauer übereinstimmen.

Verwendet man Daten vom selben Datenzentrum und berücksichtigt unterschiedliche Orte und Zeiten der Messungen, so findet man eine bemerkenswerte Übereinstimmung der Klimatologien (im Mittel $\Delta T < 0.1$ K). Größte Differenzen ($\Delta T > 0.2$ K) lassen sich in großen Höhen (35 km) ausmachen. Die Ursache dafür liegt in der unterschiedlichen Datenqualität, welche in der Prozessierung verwendet wird. Klimatologien, welche von Daten gleicher Qualität berechnet wurden, stimmen auch in großen Höhen bis auf 0.02 K überein. Unterschiedliche Lokalzeiten der Messungen, die von den Satellitenbahnen abhängen, haben nur einen geringen Einfluss auf Unterschiede zwischen Klimatologien verschiedener Satelliten. Die Ergebnisse unterstreichen die Wichtigkeit von RO Daten für die Langzeitklimabeobachtung.

Contents

Acronyms

Symbols

1D-Var 1-Dimensional Variational.

3D-Var 3-Dimensional Variational.

4D-Var 4-Dimensional Variational.

C/A-code Coarse/Acquisition code.

FORMOSAT-3 FORMOsa SATellite mission-3.

P-code Precision code.

TerraSAR-X Terra: the Earth; SAR: Synthetic Aperature Radar; X: X-band radar (wavelength).

A

AIRS Atmospheric Infrared Sounder.

AMSU Advanced MSU.

ARSCliSys Atmospheric Remote Sensing and Climate System [research group].

AS Anti-Spoofing.

B

BENCHCLIM BENCHmark CLIMatologies from radio occultation data.

C

CA California.

CDAAC COSMIC Data Analysis and Archive Center.

CHAMP CHAllenging Mini-Satellite Payload.

CIRA COSPAR International Reference Atmosphere [model of the middle atmosphere].

CLIMROCC CLImate Monitoring with Radio OCCultation Data.

CLIPS Climatology Processing System.

CMAM Canadian Middle Atmosphere Model.

CO Colorado.

CONAE Comisión Nacional de Actividades Espaciales [Argentine Commission on Space Activities].

COSMIC Constellation Observing System for Meteorology, Ionosphere, and Climate.

COSPAR COmmittee on SPAce Research.

CPTP Cold Point Tropopause.

CT Canonical Transform.

D

DE Diurnal wave migrating Eastward.

DJF December–January–February.

DLR Deutsches Zentrum für Luft und Raumfahrt.

DMI Danish Meteorological Institute.

DW Diurnal wave migrating Westward.

E

ECHAM ECMWF–MPI-M Hamburg [general circulation model].

ECI Earth Centered Inertial reference frame.

ECMWF European Centre for Medium-Range Weather Forecasts.

EGOPS End-to-End Generic Occultation Performance Simulation and Processing System.

EQC External Quality Control.

ERA ECMWF Re-Analysis.

EUMETSAT European Organization for the Exploitation of Meteorological Satellites.

F

F3C FORMOSAT-3/COSMIC.

FM FlightModel.

FSI Full-Spectrum Inversion.

FWF Austrian Science Fund (Fonds zur Förderung der wissenschaftlichen Forschung).

G

GENESIS Global Environmental & Earth Science Information System.

GFS Global Forecast System.

GFZ German Research Centre for Geosciences [former GeoForschungsZentrum].

GLONASS Global'naya Navigatsionnaya Sputnikovaya Sistema/Global Navigation Satellite System.

GNSS Global Navigation Satellite System.

GO Geometric Optics.

GOLPE GPS Occultation and Passive reflection Experiment.

GOX GPS Occultation Experiment.

GPS Global Positioning System.

GPS/MET Global Positioning System/Meteorology [experiment].

GRACE Gravity Recovery And Climate Experiment.

GRAS Global Navigation Satellite System Receiver for Atmospheric Sounding.

GRAS-SAF GRAS/Satellite Application Facility.

GSWM Global Scale Wave Model.

I

IASI Improved Atmospheric Sounding Interferometer.

IFS Integrated Forecasting System.

IGS International GNSS Service.

IOX Ionospheric Occultation Experiment.

IQC Internal Quality Control.

J

JJA June–July–August.

JPL Jet Propulsion Laboratory.

L

LEO Low Earth Orbit.

LRTP Lapse Rate Tropopause.

LS Lower Stratosphere.

LT Lower Troposphere.

LTC Local Time Component.

M

MAM March–April–May.

MetOp Meteorological Operational [satellite series].

MLT Mesosphere and Lower Thermosphere.

MSIS Mass Spectrometer and Incoherent Scatter Radar [model of the middle atmosphere].

MSL Mean Sea Level.

MSU Microwave Sounding Unit.

N

NASA National Aeronautics and Space Administration.

NAVSTAR NAVigation System with Timing And Ranging.

NC North Carolina.

NCAR National Center for Atmospheric Research.

NCDC National Climatic Data Center.

NCEP National Centers for Environmental Prediction.

NHP Northern Hemisphere Polar [region].

NHSM Northern Hemisphere Subtropics and Mid-latitudes.

NOAA National Oceanic and Atmospheric Administration.

NOMADS NOAA Operational Model Archive and Distribution System.

NWP Numerical Weather Prediction.

O

OL Open Loop.

OPS Occultation Processing System.

OPSv52 Occultation Processing System Version 5.2 [EGOPS revision number 611].

OPSv53 Occultation Processing System Version 5.3 [EGOPS revision number 811].

OPSv54 Occultation Processing System Version 5.4 [EGOPS revision number 979].

OPSv55 Occultation Processing System Version 5.5.

P

PLL Phase Locked Loop.

POD Precise Orbit Determination.

PRN Pseudo-Random Noise.

Q

QC Quality Control.

QF Quality Flag.

R

RAER Retrieval to Apriori Error Ratio.

realCHAMP real CHAMP.

RMS Root Mean Square [error].

RO Radio Occultation.

ROPP Radio Occultation Processing Package.

ROSA Radio Occultation Sounder for Atmospheric Studies.

S

SABER Sounding of the Atmosphere using Broadband Emission Radiometry.

SAC-C Satélite de Aplicaciones Científicas C.

SE Sampling Error.

SHP Southern Hemisphere Polar [region].

SHSM Southern Hemisphere Subtropics and Mid-latitudes.

simCHAMP simulated CHAMP.

simF3C simulated F3C.

simMetOp simulated MetOp.

SNR Signal to Noise Ratio.

SON September–October–November.

SUNSAT Stellenbosch UNiversity SATellite.

SW Semi-diurnal wave migrating Westward.

T

TLE Two-Line Element.

TRENDEVAL Climate Trends and Model Evaluation by Radio Occultation.

TRO Tropics.

U

UCAR University Corporation for Atmospheric Research.

UK United Kingdom.

US United States.

USA United States of America.

UT Upper Troposphere.

UT Universal Time.

UTC Universal Time Coordinated.

UTLS Upper Troposphere–Lower Stratosphere [region].

UV Ultraviolet.

W

WEGC Wegener Center for Climate and Global Change [University of Graz].

WO Wave Optics.

Z

zRAER50 impact height, where retrieval to apriori error ratio equals 50 %.

Introduction

Anthropogenic climate change is clearly evident in long-term surface records of atmospheric parameters. Over the past hundred years (1906 to 2005), global mean surface temperature has increased by about $0.74\ \mathrm{K} \pm 0.18\ \mathrm{K}$ (Trenberth et al. 2007). Apart from the surface, the knowledge about atmospheric changes is still limited (GCOS 2004). The number of measurements and their spatial density in the Upper Troposphere–Lower Stratosphere (UTLS) region was very sparse in the pre-satellite era (before 1979), since aircraft, radiosonde, lidar, and radar data were the only measurements available in the free atmosphere. Because these data are unevenly distributed over the globe (e.g., poor coverage in the southern hemisphere) their global information is limited.

Since 1979 satellite data provide important information about the climate system from a global perspective. Microwave radiance measurements performed by the Microwave Sounding Unit (MSU)/Advanced MSU (AMSU) satellites constitute the first satellite record, which has been used in climate research (e.g., Christy and Spencer 2005; Mears and Wentz 2005; Vinnikov et al. 2006). Discrepancies in sign and magnitude of temperature trends, which arose from incorrect inter-calibration and correction procedures between different satellites, now seem to be resolved to a large extend but some uncertainties still remain (Karl et al. 2006). Global monitoring of atmospheric change can also be performed by high-resolution infrared sounders like Atmospheric Infrared Sounder (AIRS) and Improved Atmospheric Sounding Interferometer (IASI) but also by Global Positioning System (GPS) Radio Occultation (RO).

The GPS RO method is an active limb sounding technique. Measurements are performed when a GPS antenna mounted in the front or in the aft of a Low Earth Orbit (LEO) satellite tracks a signal of a GPS satellite. Due to the satellites' motions, the atmosphere is scanned from top to bottom (setting event) or from bottom up (rising event). Because the GPS signals are modified by the atmosphere depending on its refractive properties, the modifications are a measure for physical atmospheric parameters, in particular refractivity, from which density, pressure/geopotential height, temperature, and humidity profiles can be derived (see e.g., Kursinski et al. 1997; Steiner et al. 2001; Hajj et al. 2002).

Since the calibration strategy of the method is traceable to the international standard for the second, the RO method has the potential to deliver climate benchmark measurements (Leroy et al. 2006). RO data are known to be of high accuracy (tem-

perature error is less than 1 K between 8 km and 30 km altitude) and feature a very high vertical resolution (0.1 km to 0.5 km in the lower troposphere and approximately 1.5 km in the stratosphere) (Melbourne et al. 1994). Nearly polar orbiting LEO satellites yield global coverage of RO measurements and the frequency domain of GPS signals enables measurements to be performed during virtually all weather conditions.

First RO data are available from the Global Positioning System/Meteorology (GPS/MET) mission, which has been launched in 1995 and provided data intermittently within the years 1995 to 1997 (Rocken et al. 1997). Data of the Satélite de Aplicaciones Científicas C (SAC-C) satellite, currently available at Wegener Center for Climate and Global Change (WEGC) only from 2001 to 2002 overlap with CHAllenging Mini-Satellite Payload (CHAMP) data. CHAMP (May 2001 to October 2008), FORMOSAT-3/COSMIC (F3C) (since August 2006), Gravity Recovery And Climate Experiment (GRACE) (since March 2007), and Meteorological Operational (MetOp) (October 2007) complete the RO record currently available at WEGC and allow to investigate the consistency of RO climate products.

The overlap of different satellite systems does not only allow to maintain the homogeneity and consistency of RO time-series but also to determine potential inter-satellite biases (Hajj et al. 2004; Schreiner et al. 2007; Foelsche et al. 2009*b*), which are important principles for climate monitoring specified by GCOS (2009). In this thesis I validated characteristics of RO data and derived climate products of different satellites and identified time-dependent and random errors inherent in this record.

The structure of the thesis is as follows: A description of the RO technique and the data processing are given in Chapter 1. The RO record available at WEGC is introduced in Chapter 2, where data characteristics of different satellites and the temporal evolution of data quality are also presented. The mathematical calculation of RO climatologies is explained in Chapter 3. In addition, spatio-temporal sampling, which causes a "sampling error" in RO climatologies and the systematic difference of RO climatologies relative to European Centre for Medium-Range Weather Forecasts (ECMWF) operational analyses (and ECMWF Re-Analysis (ERA)-40 data) are discussed. Chapter 4 discusses the consistency of RO climatologies of different satellites and demonstrates causes of inconsistencies. One cause for disagreements in RO climatologies of different satellites results from different orbit characteristics. This influence is studied in Chapter 5. Chapter 6 gives an application of RO data in atmospheric physics. Since the six spacecraft of the F3C satellite constellation are evenly distributed in space, this mission is able to sample at all local times within one month and data can be used to detect atmospheric diurnal and semi-diurnal tides at low and mid-latitudes. The chapter presents atmospheric thermal tides observed in the UTLS region. The thesis closes with a summary and conclusions.

1 From Atmospheric Phase Delay to Profiles of Meteorological Parameters

The Radio Occultation (RO) method is a state-of-the-art remote sensing technique used to probe the Earth's atmosphere. It has originally been developed in planetary sciences where it has been used to study atmospheres, e.g., from Mars, Venus, and Jupiter (Fjeldbo and Eshleman 1968; Eshleman 1973).

In 1995 the first proof-of-concept mission sensing the terrestrial atmosphere has been launched into Earth orbit. Data from the Global Positioning System/Meteorology (GPS/MET) mission (Ware et al. 1996) confirmed that RO data are of importance for operational meteorology, i.e., numerical weather prediction, (Kuo et al. 2000), climate monitoring (Steiner et al. 2001), ionospheric research (Schreiner et al. 1999), and space weather science (Jakowski et al. 2002).

The RO technique is based on measurements of the path of radio waves passing through the atmosphere from one satellite to another. Atmospheric density gradients yield bending of this path. Bending angle profiles can be inverted to refractive index profiles by an Abel inversion and utilization of physical laws (ideal gas law, hydrostatic equation) yield profiles of atmospheric parameters like pressure and temperature.

1.1 Measurement Principle

The RO method belongs to the active limb sounding techniques. In contrast to passive limb sounding techniques, where the transmitted electromagnetic signal stems from a natural source (e.g., Sun, Moon, or bright stars), the RO method utilizes artificial signals transmitted by Global Navigation Satellite System (GNSS) satellites. Global Positioning System (GPS), Global'naya Navigatsionnaya Sputnikovaya Sistema/Global Navigation Satellite System (GLONASS), and GALILEO satellites are contemporary part of the GNSS system. However, in practice only GPS-signals have been used for RO measurements so far.

Radio signals transmitted by GNSS satellites penetrate the atmosphere, where they are affected by the Earth's atmospheric density field. On the way through the ionosphere and neutral atmosphere these signals are refracted and received on a Low Earth Orbit (LEO) satellite (see Figure 1.1). Physical characteristics of the

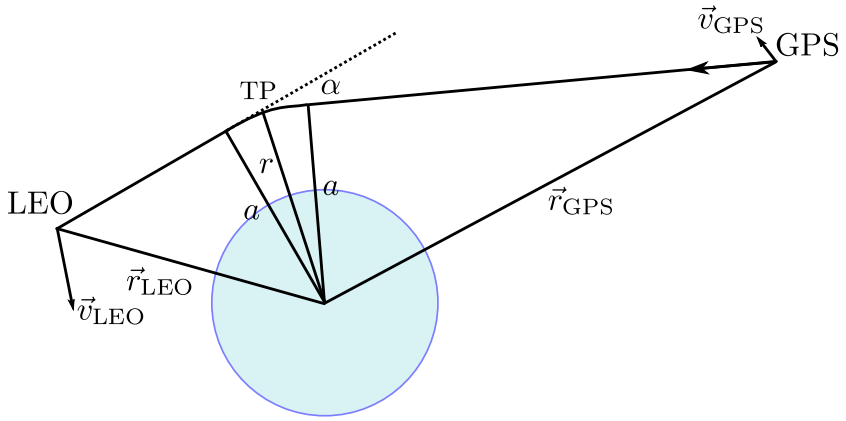

Figure 1.1: Occultation geometry of a setting RO event. The signal, which is transmitted by a GPS satellite, is refracted by the ionosphere and neutral atmosphere before it is received at a LEO satellite. TP is the tangent point, r is the tangent radius, a the impact parameter (the perpendicular distance between either of the ray asymptotes and the center of refraction), α the bending angle, and $\vec{r}_{\mathrm{LEO}}$ and $\vec{r}_{\mathrm{GPS}}$ the position vectors of the LEO and the GPS satellite, respectively.

atmosphere between the transmitter and the receiver satellite and movements of the both satellites yield a frequency shift of the electromagnetic signal.

The measured quantity aboard the LEO satellite is the phase change as a function of time between the intrinsically transmitted signal (replicated in the receiver) and the Doppler-shifted incoming signal.

Figure 1.2 shows a simplified illustration of that phase change measurement. The top panel shows the vacuum path, which can be expected from orbit geometry and the respective GPS and LEO velocities only. The bottom panel shows the ray, which is bent due to ionospheric and neutral atmospheric refraction. The Doppler shift of the phase is different in both cases. The artifice of the RO retrieval is to extract the signal delay, which is caused by the neutral atmosphere (i.e., to correct all other proportions to phase delay), and to derive atmospheric characteristics by applying an inversion technique. These measurements are performed on both GPS frequencies, $f_1 = 1575.42$ MHz and $f_2 = 1227.60$ MHz.

Due to the relative motion of the GPS and LEO satellites, the radio signals (continuously broadcast by the GPS satellite) penetrate the atmosphere at different tangent heights and the atmosphere is scanned from top downwards (setting event) or from bottom up (rising event). This results in a near vertical profile of phase measurements as a function of time. Within the upper troposphere, the lower stratosphere

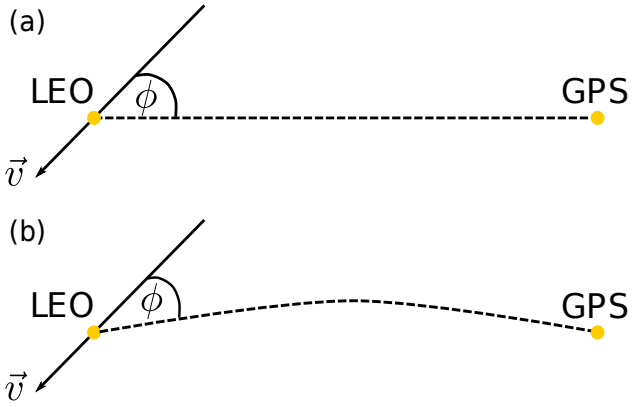

Figure 1.2: Sketch of the measurement of phase delays. Panel (a) shows the vacuum path of an electromagnetic signal. The Doppler shift only depends on the relative velocities of both satellites, including the incident angle ϕ between the direction of the ray and the direction of the LEO satellite. Panel (b) shows the ray, which is bent due to atmospheric refraction (after Syndergaard (1999)).

and beyond, the phase delay[1] relative to vacuum phase can be inverted to profiles of atmospheric parameters using simple principles of Geometric Optics (GO).

The GO approximation is valid if (i) the refractive index is close to one, (ii) the refractive index gradients are moderate, (iii) the scattering structures in the atmosphere are much smaller than the signal's wavelengths, and (iv) there are no hard apertures, except the Earth's surface (Jensen et al. 2004*a*). In the upper troposphere and above, these assumptions typically apply to the Earth's atmosphere because the wavelengths are $\lambda_1 \approx 0.190$ m and $\lambda_2 \approx 0.244$ m for the two GPS frequencies respectively but the molecular size is distinctively smaller. In the ionosphere (where free electrons contribute to the signal's bending) and lower troposphere (presence of water vapor), however, small-scale atmospheric structures affect refraction of radio waves, which cannot be handled by GO. While an ionospheric correction eliminates the ionospheric contribution of refraction in a large part, the performance of the RO retrieval in the lower troposphere is improved by applying Wave Optics (WO). Possibilities to deal with lower tropospheric signals are the application of the Canonical Transform (CT) method (Gorbunov 2002) or the Full-Spectrum Inversion (FSI) technique (Jensen et al. 2003; Jensen et al. 2006).

The Wegener Center for Climate and Global Change (WEGC) retrieval version Occultation Processing System Version 5.4 (OPSv54) (cf. Section 1.3) is a dry air

[1] Phase delay is also called atmospheric phase delay, excess phase delay, excess phase, or excess phase path (Syndergaard 1999).

retrieval, which is based on GO: Knowledge of phase delay profiles as a function of time allows the calculation of Doppler shift. Involvement of precise orbit information (space- and velocity-vectors of the LEO and GPS satellites) yields bending angle profiles as a function of impact parameter. Since bending angles are frequency-dependent, the main ionospheric contribution of the measurement can be removed by a linear combination of two bending angles, derived from both GPS frequencies separately. An Abel transformation of the ionosphere-corrected bending angle profile gives a refractive index profile as a function of height (more accurate, as a function of tangent point radius). Neglecting the moist contribution of refractivity yields atmospheric dry density profiles by involvement of the Lorentz-Lorenz formula. Dry pressure profiles as a function of height, geopotential height profiles as a function of dry pressure height, and dry temperature profiles as a function of height are calculated using the hydrostatic equation and the equation of state.

The restriction of a dry atmosphere is valid in the upper troposphere and above, where water vapor density is low (regions where the volume mixing ratio is less than 10^{-4} (Kursinski et al. 1997)). This holds true to better than 0.1 K accuracy for altitudes above 8 km at polar latitudes and 14 km at tropical latitudes (Foelsche et al. 2008*b*).

In the lower troposphere, however, where the proportion of water vapor becomes significant, dry atmosphere parameters differ significantly from "true" physical atmosphere parameters. The difference between physical and dry atmospheric temperature can reach several tens of kelvins in the lower troposphere (Foelsche et al. 2008*b*). The RO retrieval allows to derive profiles of physical atmospheric parameters and water vapor, using auxiliary temperature data as provided, e.g., by operational analysis centers.

1.2 The Global Positioning System and Excess Phase Delay

The NAVigation System with Timing And Ranging (NAVSTAR) GPS was developed by the United States (US) military. Its main task is the determination of time, position, and velocity of objects with very high precision for navigation purposes. GPS comprises space, user, and control segments (also called ground segments). The space segment consists of a minimum of 24 satellites at orbit altitudes of 20200 km and orbit inclinations of 55°. The satellites are arranged in six orbital planes, separated by 60°. The signals are broadcast by these space segments. The ground segment is responsible for steering the GPS system and the user segments comprise all elements needed to receive the signals. The main source of information used for the description below was provided by Hofmann-Wellenhof et al. (2008); specific further sources are cited in context.

1.2.1 GPS Signals

Each GPS satellite transmits right-handed circular polarized electromagnetic waves at two (carrier) frequencies, $f_1 = 1575.42$ MHz and $f_2 = 1227.60$ MHz, which correspond to wavelengths of $\lambda_1 \approx 0.190$ m and $\lambda_2 \approx 0.244$ m, respectively (Hofmann-Wellenhof et al. 2008). Frequencies from 1 GHz to 2 GHz belong to the microwave (radio) frequency domain[2] and are attributed to the L-band. For that reason, GPS signals are also called L1- and L2-signals. Two Pseudo-Random Noise (PRN) codes are modulated onto the signals: the Coarse/Acquisition code (C/A-code) and the Precision code (P-code). The C/A-code is modulated only on the L1-signal with a chip rate of 1.023 MHz (wavelength of 293 m).

The L1-signal has the following structure:

$$S_{\mathrm{L1}}(t) = A_{\mathrm{C/A}} C_i(t) D_i(t) \cos(\omega_1 t) + A_{\mathrm{P}} P_i(t) D_i(t) \sin(\omega_1 t), \tag{1.1}$$

the structure of the L2-signal looks like:

$$S_{\mathrm{L2}}(t) = B_{\mathrm{P}} P_i(t) D_i(t) \sin(\omega_2 t). \tag{1.2}$$

In Eq. (1.1) $A_{\mathrm{C/A}}$ is the amplitude of the modulated C/A-code and $C_i(t)$ is the C/A-code sequence for the ith satellite. The power of the C/A-code is stronger than the power of the P-code by 3 dB. The P-code is modulated on both, the L1- and the L2-signal with a chip rate of 10.23 MHz (wavelength of 29 m). A_{P} and B_{P} denote the amplitudes of the P-code of the L1 and L2 signals, respectively, $P_i(t)$ is the P-code sequence for the ith satellite. In addition to the PRN-codes, a navigation message is modulated onto the carrier frequencies. It is denoted by $D_i(t)$ and contains information about the satellite status, its orbit, and the transmitter clock bias (Hofmann-Wellenhof et al. 2008).

1.2.2 Signal Propagation

Intrinsically, the GPS concept relies on measurements of ranges (because of differences in system times of the transmitter and the receiver, the ranges are called more exactly pseudoranges). These ranges (i.e., the distance between the transmitter and the receiver) are deduced from measured time or phase differences relative to the transmitted electromagnetic signal. These differences are primarily caused by the relative motion of the transmitter and the receiver (kinematic Doppler shift). Measurements which rely on measured time (code pseudoranges) are less accurate than that of phase differences (phase pseudoranges) so that latter are used for RO measurements.

[2] Radio waves range from less than a centimeter to hundreds of meters, while microwave wavelengths range from approximately one millimeter to thirty centimeters.

A GPS receiver is able to replicate the PRN-code of a satellite signal. This receiver-generated signal is compared to the received signal. Measured phase change $\Delta\varphi$ (in cycles) is proportional to the range difference $\Delta\rho$ (in meter)

$$-\Delta\varphi = -\int_{t_0}^{t} \Delta f \mathrm{d}t = \frac{1}{\lambda}\int_{t_0}^{t} \dot{\rho}\mathrm{d}t = \frac{1}{\lambda}\Delta\rho, \tag{1.3}$$

where $\int_{t_0}^{t} \Delta f \mathrm{d}t$ is the integrated Doppler shift and λ is the signal's wavelength. The signal is broadcast from the GPS satellite at an initial epoch t_0 and received at epoch t onboard a LEO satellite. The phase pseudorange Φ, expressed in cycles, is

$$\Phi = -\Delta\varphi_{\mathrm{LEO}}^{\mathrm{GPS}} = \frac{1}{\lambda}\rho + \frac{c}{\lambda}\delta_{\mathrm{LEO}} + \frac{c}{\lambda}\delta_{\mathrm{GPS}} + N, \tag{1.4}$$

where $\Delta\varphi_{\mathrm{LEO}}^{\mathrm{GPS}}$ is the beat phase (deviation between the generated frequency and the incoming frequency), ρ is the distance between the GPS satellite at time epoch t_0 and the receiver onboard the LEO satellite at time epoch $t_0 + \Delta t$, $c = 299\,792\,458$ m/s is the speed of light in vacuum (Mohr et al. 2008), δ_{LEO} and δ_{GPS} are the differences from the receiver and transmitter clocks to a common time system, and N is the initial integer number of cycles between the transmitter and the receiver. Multiplication of Eq. (1.4) by the wavelength λ yields the range L, expressed in meter:

$$L = \lambda\Phi = \rho + c\delta_{\mathrm{LEO}} + c\delta_{\mathrm{GPS}} + \lambda N. \tag{1.5}$$

At microwave wavelengths, the phase of an electromagnetic wave can be measured with a precision better than 0.01 cycles; the corresponding range is measured with millimeter precision (Hofmann-Wellenhof et al. 2008).

1.2.3 Determination of Atmospheric Phase Delay Used for the Radio Occultation Inversion Process

Equations (1.4) and (1.5) show that the measured phase pseudorange Φ and the range L are dependent on the kinematic Doppler shift and on transmitter and receiver clock errors. However, pseudorange measurements are also affected by an ionosphere induced Doppler shift, a neutral atmosphere induced Doppler shift, and by diverse measuring inaccuracies like orbital errors or delays in electronic hardware. In principle, the actual carrier phase observation can be described by

$$\begin{aligned} L = \lambda\Phi = \rho + \mathrm{d}\rho + c\delta_{\mathrm{LEO}} + c\delta_{\mathrm{LEO,sys}} + c\delta_{\mathrm{GPS}} + c\delta_{\mathrm{GPS,sys}} + \lambda N \\ + \lambda\Phi_{\mathrm{neutral}} + \lambda\Phi_{\mathrm{iono}} + \epsilon_{\mathrm{antenna}} + \epsilon_{\mathrm{multi}} + \epsilon_{\mathrm{rel}} + \epsilon_{\mathrm{cycle\,slips}} + \epsilon. \end{aligned} \tag{1.6}$$

Newly added terms comprise orbital errors, $\mathrm{d}\rho$, systematic errors, which result from delays in the receiver and its antenna (e.g., cables, electronics), $\delta_{\mathrm{LEO,sys}}$, systematic

Table 1.1: Overview of range biases contributing to the measurement. These errors are listed in Eq. (1.6).

Source	Effect	Symbol
GPS satellite	Orbital errors	$\mathrm{d}\rho$
	Clock bias	$c\delta_{\mathrm{GPS}}$
	Systematic GPS hardware delays	$c\delta_{\mathrm{GPS,sys}}$
Signal propagation	Neutral atmosphere refraction	$\lambda\Phi_{\mathrm{neutral}}$
	Ionospheric refraction	$\lambda\Phi_{\mathrm{iono}}$
	Atmospheric multipath	$\epsilon_{\mathrm{multi}}$
	Relativistic effects	ϵ_{rel}
LEO satellite	Orbital errors	$\mathrm{d}\rho$
	Clock bias	$c\delta_{\mathrm{LEO}}$
	Systematic LEO hardware delays	$c\delta_{\mathrm{LEO,sys}}$
	Antenna phase center variation	$\epsilon_{\mathrm{antenna}}$
	Local multipath	$\epsilon_{\mathrm{multi}}$
	Cycle slips	$\epsilon_{\mathrm{cycle\,slips}}$
	Observation noise	ϵ

transmitter errors, $\delta_{\mathrm{GPS,sys}}$, signal delay induced by the neutral atmosphere, Φ_{neutral}, and by the ionosphere, Φ_{iono}, errors due to LEO antenna phase center variations, $\epsilon_{\mathrm{antenna}}$, errors resulting from multipath, $\epsilon_{\mathrm{multi}}$, relativistic effects, ϵ_{rel}, cycle slips (a sudden jump of cycles), $\epsilon_{\mathrm{cycle\,slips}}$, and residual noise, ϵ. Table 1.1 summarizes these range biases and attributes them to the GPS satellite, the medium between transmitter and receiver (signal propagation), or to the LEO satellite.

The "conventional" GPS community, which is interested in time, position, and velocity of an object, favors the knowledge of the range due to kinematic Doppler shift and tries to correct the other parts. The RO community, however, tries to separate the phase change, which results from the neutral atmosphere only, to infer physical atmosphere characteristics.

In the following the range biases contributing to the RO measurement are shortly discussed:

True geometric range and orbital error Ephemerides of the transmitter and the receiver satellites (as well as their velocities) are derived from Precise Orbit Determination (POD) processes. UCAR/CDAAC (University Corporation for Atmospheric Research/COSMIC Data Analysis and Archive Center), e.g., uses the Bernese software to perform POD of LEO satellites (Schreiner et al. 2009). All space- and velocity vectors are given in an Earth Centered Inertial

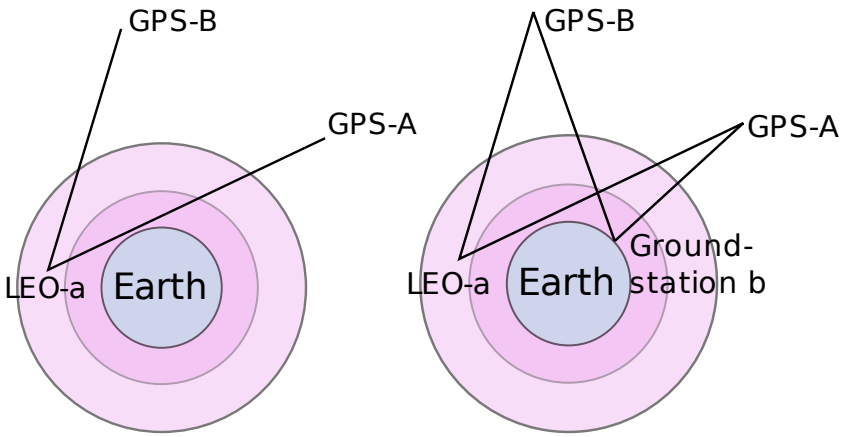

Figure 1.3: Principles of single differencing (left panel) and double differencing (right panel). The concentric circles denote the Earth (blue), neutral atmosphere (dark violet) and the ionosphere (light violet).

reference frame (ECI) coordinate system[3] as a function of time.

GPS broadcast orbits are known with an accuracy of about 100 cm (IGS 2009), LEO orbits are determined to a Root Mean Square (RMS) error smaller than 10 cm (Bertiger et al. 1994). The orbital velocity errors due to LEO POD are better than 0.02 mm/s (Schreiner et al. 2009).

Precise knowledge of space- and velocity vectors of both satellites is necessary to precisely infer the kinematic Doppler shift.

Receiver and transmitter clock errors Each GPS satellite carries a precise atomic clock with an accuracy of between 10^{-12} and 10^{-13} (Seeber 2003). These clocks produce the reference frequency by stimulated radiation of rubidium or cesium. The GPS control segment monitors the synchronization error and drift error of each GPS clock. This information is included in the navigation message, which is modulated onto the signals. The receiver clock error depends on the quality of the clock established on the receiver.

Application of the single difference technique eliminates the LEO clock error by forming the difference between the measurements of two different GPS satellites (the occulted satellite, A, and another, non-occulted satellite, B; see left

[3]The origin of the ECI coordinate system is located at the center of the Earth, the z-axis passes through the North Pole, and the equatorial plane of the Earth lies in the x-y plane (Diamond and Austin 1975).

panel of Figure 1.3). Neglecting the true distance between transmitter and receiver and summarizing systematic LEO and GPS errors, orbital, ambiguity, and multipath errors, as well as antenna phase center variations, relativistic effects, cycle slips, and noise by the error term ϵ_{sum}, the two carrier phase observations can be approximated by

$$L^{\text{A}} = \lambda\Phi^{\text{A}} = c\delta_{\text{LEO}} + c\delta^{\text{A}}_{\text{GPS}} + \lambda\Phi^{\text{A}}_{\text{neutral}} + \lambda\Phi^{\text{A}}_{\text{iono}} + \epsilon^{\text{A}}_{\text{sum}}, \tag{1.7}$$

$$L^{\text{B}} = \lambda\Phi^{\text{B}} = c\delta_{\text{LEO}} + c\delta^{\text{B}}_{\text{GPS}} + \lambda\Phi^{\text{B}}_{\text{iono}} + \epsilon^{\text{B}}_{\text{sum}}. \tag{1.8}$$

The difference

$$\Delta L^{\text{AB}} = L^{\text{A}} - L^{\text{B}} = c\Delta\delta^{\text{AB}}_{\text{GPS}} + \lambda\Phi^{\text{A}}_{\text{neutral}} + \lambda\Delta\Phi^{\text{AB}}_{\text{iono}} + \epsilon^{\text{AB}}_{\text{sum}} \tag{1.9}$$

contains the differenced GPS clock errors, the tropospheric delay of the occulted satellite, a differenced ionospheric delay, and residual noise. Disadvantages of the single difference technique are the extra requirements associated with data management and the computation of the GPS clocks at high rates to capture all transmitter clock fluctuations (Schreiner et al. 2009).

The double difference technique makes use of two different GPS satellites, A and B, and two receivers, one mounted on the LEO satellite, and another one, established on a ground station (see right panel of Figure 1.3). It cancels out all clocks errors, that from both GPS satellites, the LEO satellite, and the ground station.

$$\Delta L^{\text{AB}}_{\text{a}} = c\Delta\delta^{\text{AB}}_{\text{GPS}} + \lambda\Phi^{\text{A}}_{\text{neutral a}} + \lambda\Delta\Phi^{\text{AB}}_{\text{iono a}} + \epsilon^{\text{AB}}_{\text{sum a}}, \tag{1.10}$$

$$\Delta L^{\text{AB}}_{\text{b}} = c\Delta\delta^{\text{AB}}_{\text{GPS}} + \lambda\Phi^{\text{A}}_{\text{neutral b}} + \lambda\Phi^{\text{B}}_{\text{neutral b}} + \lambda\Delta\Phi^{\text{AB}}_{\text{iono b}} + \epsilon^{\text{AB}}_{\text{sum b}}, \tag{1.11}$$

$$\Delta\Delta L^{\text{AB}}_{\text{ab}} = \lambda\Delta\Phi^{\text{AB}}_{\text{neutral ab}} + \lambda\Delta\Phi^{\text{AB}}_{\text{iono ab}} + \epsilon^{\text{AB}}_{\text{sum ab}} \tag{1.12}$$

A significant disadvantage of the double difference technique is its susceptibility to ground data error sources (like multipath, residual atmospheric and ionospheric noise, data interpolation, and thermal noise) (Schreiner et al. 2009). However, the double difference technique was of particular importance when GPS clocks were degraded ("Selective Availability"), which caused GPS clock errors to be distinctively larger. The GPS selective availability mode has been terminated on May 2, 2000.

As noticed within Eqs. (1.9) and (1.12), both difference techniques introduce new errors, which are caused by atmospheric effects induced on the signals used. These additional errors can only be prevented, when using an ultra stable clock aboard the LEO satellite, which spares application of a differencing technique ("zero differencing").

Systematic transmitter/receiver errors and integer ambiguity The retrieval process from phase delay to atmospheric bending angle utilizes the time derivative of phase change (Doppler shift instead of integrated Doppler shift) and the determination of atmospheric phase delay only necessitates the correction of all temporarily non constant factors in Eq. (1.6). For that reason all terms in Eq. (1.6), which are constant during the occultation measurement can be omitted. These comprise systematic transmitter and receiver errors as well as the integer ambiguity of the measurement.

LEO antenna and antenna phase center variations Satellite orbits are referred to the center of mass of the satellite. The GPS satellite oscillator and the receiver antenna are usually not located at the corresponding center of mass and it is necessary to correct that displacement (Wickert 2002). Furthermore, the electrical antenna phase center varies with elevation, azimuth, intensity of the satellite signal, and its frequency (Hofmann-Wellenhof et al. 2008) and each received signal is attributable to a unique electrical antenna phase center. Phase center variations of the receiver and transmitter antenna are a remaining uncertainty in POD of LEO satellites using GPS measurements. Combined ground and in-flight calibration can improve the phase modeling (Montenbruck et al. 2009).

Multipath error Local multipath occurs, when multiple signals, which result from scattering in the vicinity of the receiver antenna, travel along different paths and are detected by the receiver at the same time. Local multipath errors depend on the spacecraft geometry, on the occultation-viewing geometry, and on electrical properties in the vicinity of the receiver antenna. Directional antennas and modeling reduce the local multipath error (Kursinski et al. 1997).

Atmospheric multipath results from sharp vertical variations in atmospheric refractivity structures, which might occur in the lower troposphere, especially in the tropics. It results in a severe degradation of the signal and introduces errors into the retrieved parameters. Application of the CT method (Gorbunov 2002), the FSI method (Jensen et al. 2003; Jensen et al. 2006), or the phase matching method (Jensen et al. 2004*b*) improve the accuracy of the retrieval in the presence of atmospheric multipath effects.

Relativistic effects The transmitter and receiver clocks and the main clock by which the GPS system time is defined, operate at places with different gravitational potential. Furthermore, clocks are moving with different velocities. Both effects yield an apparent frequency shift in the satellite oscillator (general and special theory of relativity) (Seeber 2003) and have to be corrected. Double differencing does not only eliminate GPS and LEO clock errors but also

relativistic contributions to the signal. Using single differencing or zero differencing necessitates the correction of relativistic effects. This can be done by solving for an a priori receiver orbit and clock offset and by modeling the periodic relativistic effect between the GPS satellite clock and proper time due to non-circular orbit and the gravitational delay between the satellite and the receiver (Schreiner et al. 2009).

Cycle slips If the receiver looses the lock of a signal, the carrier phase shows a sudden jump of cycles (cycle slips). This jump amounts to an integer number, the fractional part of the phase remains unchanged (Seeber 2003). Since cycle slips are not constant with time they have to be removed (cycle slip repair), see e.g., Hofmann-Wellenhof et al. (2008).

After correction of receiver and transmitter clock errors, errors due to antenna phase center variations, multipath errors, relativistic effects, and cycle slips, the residual phase delay only contains contributions, which stem from the relative motion of the satellites (kinematic Doppler effect), from the ionosphere, and the neutral atmosphere. The separation of these phase changes follows later in the retrieval process.

The sampling rate of phase delay profiles (given as a function of time) is 50 Hz. Since the time derivative of the phase change is of main interest in the RO retrieval (not the phase itself), the first ray of the measurement profile is allocated to a fixed value. In doing so, the RO data center UCAR/CDAAC allocates the phase delay at the top of the atmosphere of setting RO events to 0 m, whereas German Research Centre for Geosciences (GFZ) (another center providing RO data) allocates it to 1 m. In case of setting events, atmospheric phase accumulates with time and corresponding phase delay values increase. In case of rising events, the first ray measures maximum phase delay so that it decreases with time. However, phase delay profiles of rising events can be rearranged to correspond with setting events.

1.3 Occultation Processing System Version 5.4—Derivation of Atmospheric Parameters from Excess Phase Delay

At the WEGC, University of Graz, an RO retrieval scheme has been established, which uses phase delay profiles and precise orbit information (level 1 data) provided by other data centers. Retrieved products are primarily utilized for climate applications. The RO retrieval has been designed and developed by G. Kirchengast (Kirchengast 1996; Kirchengast 1998), K. Hocke (Hocke 1997; Hocke et al. 1997), A. K. Steiner (Steiner et al. 1999), S. Syndergaard (Syndergaard 1999), and M. E. Gorbunov (Gorbunov 2002) and is an improved version of the ccrv2 retrieval, mainly implemented by A. Gobiet (Gobiet 2005) and M. Borsche (Borsche

2008). Current Occultation Processing System (OPS) development is led by J. Fritzer (Fritzer et al. 2009).

1.3.1 OPSv54 Input Data

The WEGC OPSv54 retrieval is a dry air GO retrieval, which uses profiles of atmospheric phase delay and precise orbit information (position and velocity vectors of LEO and GPS satellites) for generating atmospheric profiles. OPSv54 retrieval input data are provided by UCAR/CDAAC and by EUMETSAT (European Organization for the Exploitation of Meteorological Satellites) (Meteorological Operational satellite data (MetOp) only). Data provided by GFZ have only been used for validation of level 1 processing.

1.3.2 Occultation Geometry

Knowledge of space vectors of the LEO and the GPS satellites allows the determination of the occultation geometry, e.g., the mean tangent point location or the distance of the mean occultation event to the LEO or to the GPS satellite.

Mean Tangent Point Location

Within the OPS retrieval, the location of the mean tangent point of an occultation event is defined as that point, where the straight line between the LEO and the GPS satellite is tangent to the Earth's surface. That straight line corresponds to a bent ray at an altitude of 10 km to 15 km.

The vector from the GPS to the LEO satellite $\vec{r}_{\text{GPS-LEO}} = \vec{r}_{\text{LEO}} - \vec{r}_{\text{GPS}}$ and its norm $r_{\text{GPS-LEO}} = \sqrt{\vec{r}_{\text{GPS-LEO}} \cdot \vec{r}_{\text{GPS-LEO}}}$ as well as the corresponding unity vector $\vec{e}_{\text{GPS-LEO}} = \vec{r}_{\text{GPS-LEO}}/r_{\text{GPS-LEO}}$ are determined by the known space vectors of the GPS and the LEO satellite. The product of the unity vector $\vec{e}_{\text{GPS-LEO}}$ and the space vector of the GPS satellite $\vec{r}_{\text{GPS}}$ yields the projection of $\vec{r}_{\text{GPS}}$ on the direction GPS to LEO, which is negative because the angle $(\vec{e}_{\text{GPS-LEO}}, \vec{r}_{\text{GPS}})$ is larger than 90° (see Figure 1.4). The occultation point $\vec{r}_{\text{occ}}$ is derived from

$$\vec{r}_{\text{occ}} = \vec{r}_{\text{GPS}} - \vec{e}_{\text{GPS-LEO}}(\vec{e}_{\text{GPS-LEO}} \cdot \vec{r}_{\text{GPS}}). \tag{1.13}$$

By definition of the mean occultation point, the magnitude of this vector at mean occultation event location is equal (or at least approximately equal) to the Earth's mean radius: $r_{\text{occ}} = \sqrt{\vec{r}_{\text{occ}} \cdot \vec{r}_{\text{occ}}} \approx r_{\text{e}} = 6371\,\text{km}$. Latitude and longitude (in

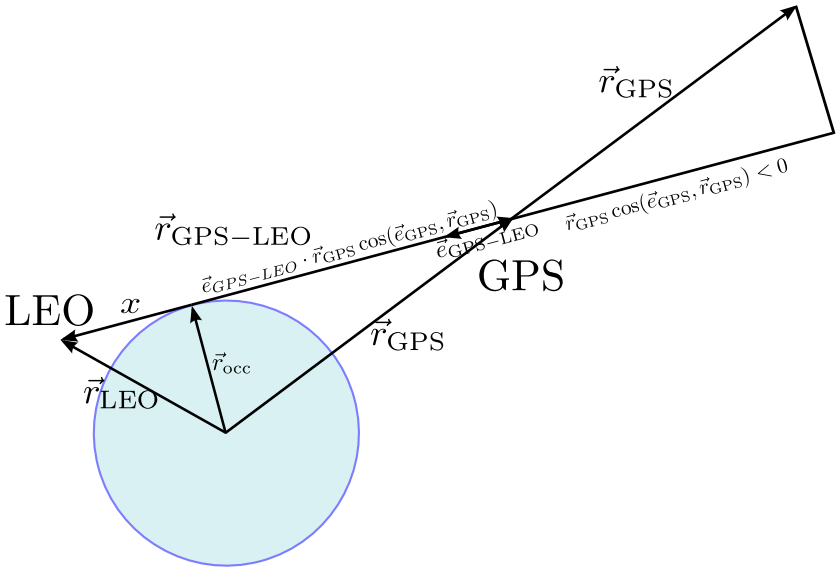

Figure 1.4: Determination of the mean tangent point location applied within the WEGC retrieval. The mean tangent point of an occultation event is defined as that point, where the straight line between LEO and GPS satellites is tangent to the Earth's surface. x denotes the distance from the LEO satellite to the mean occultation event location.

degree) of mean occultation event are calculated from

$$\varphi = 90 - \arccos\left(\frac{r_{\mathrm{occ},z}}{r_{\mathrm{occ}}}\right)\frac{180}{\pi} \tag{1.14}$$

$$\vartheta = \arctan\left(\frac{r_{\mathrm{occ},y}}{r_{\mathrm{occ},x}}\right)\frac{180}{\pi} \tag{1.15}$$

where φ is the latitude and ϑ is the longitude of the occultation event location, $r_{\mathrm{occ},x}$, $r_{\mathrm{occ},y}$, $r_{\mathrm{occ},z}$ are x-, y-, and z-components of vector $\vec{r}_{\mathrm{occ}}$.

At mean occultation event location, co-located profiles of other data sets are extracted to be used as background information within the retrieval and for validation purpose after the retrieval.

Distance from the LEO Satellite to Mean Tangent Point Location

The altitude of the LEO satellite determines the distance of the mean tangent point location to the LEO satellite, x. On the surface, x can be approximated by

$$x = \sqrt{r_{\mathrm{LEO}}^2 - r_{\mathrm{e}}^2}, \tag{1.16}$$

where r_{LEO} is the altitude of the LEO satellite (referred to the Earth's center) and r_{e} is the mean radius of the Earth. The distance of an RO event to a satellite at an orbit altitude of 400 km amounts to approximately 2300 km, an RO event of a satellite at an orbit altitude of 800 km is detected about 3300 km away from the LEO satellite.

1.3.3 Data Preparation

Some plausibility checks and corrections are applied to the input data before entering in the retrieval.

If the event is shorter than the minimal event duration of 15 s or if there are no data available in Phase Locked Loop (PLL) mode, the event is discarded (internal QF = 9). Since the retrieval cannot handle negative velocities of GPS satellites and because the choice of the coordinate system yields very small GPS velocities, all velocities of GPS satellites smaller than 10^{-10} m/s are set to the value of 10^{-10} m/s. All measurement quantities are sorted into phase-ascending order so that the signal always runs from top of the atmosphere to bottom (regardless of setting or rising event). By convention of the OPSv54 retrieval, the value of the phase delay at the top of the atmosphere is zero or (slightly) positive. Negative phase delays often result from technical aspects of the RO receiver. These negative phase delays are replaced by 10^{-12} m. Recent improvements of the retrieval (Occultation Processing System Version 5.5 (OPSv55), Fritzer et al. (2009)) showed that a simple shift of the profile (e.g., by 10 m) can overcome that problem.

Outliers of excess phase delay profiles are removed separately for the L1- and the L2-signal. This is done by calculating the mean and standard deviation of the data recorded within one second (50 data points because sampling rate is 50 Hz). If the point in the middle of the second deviates by more than three standard deviations from the interval's mean, it is replaced by the intervals mean. L1- and L2-phases are smoothed using a regularization method (Feng and Herman 1999). It aims at removing high frequency noise, which is necessary to avoid non-physical data and non-physical oscillations in the retrieved data products.

The smoothed excess phase time series $\vec{y}$ is calculated from

$$\vec{y} = \left(\mathbf{I} + \lambda \mathbf{S}^{\mathrm{T}}\mathbf{S}\right)^{-1} \vec{x} \tag{1.17}$$

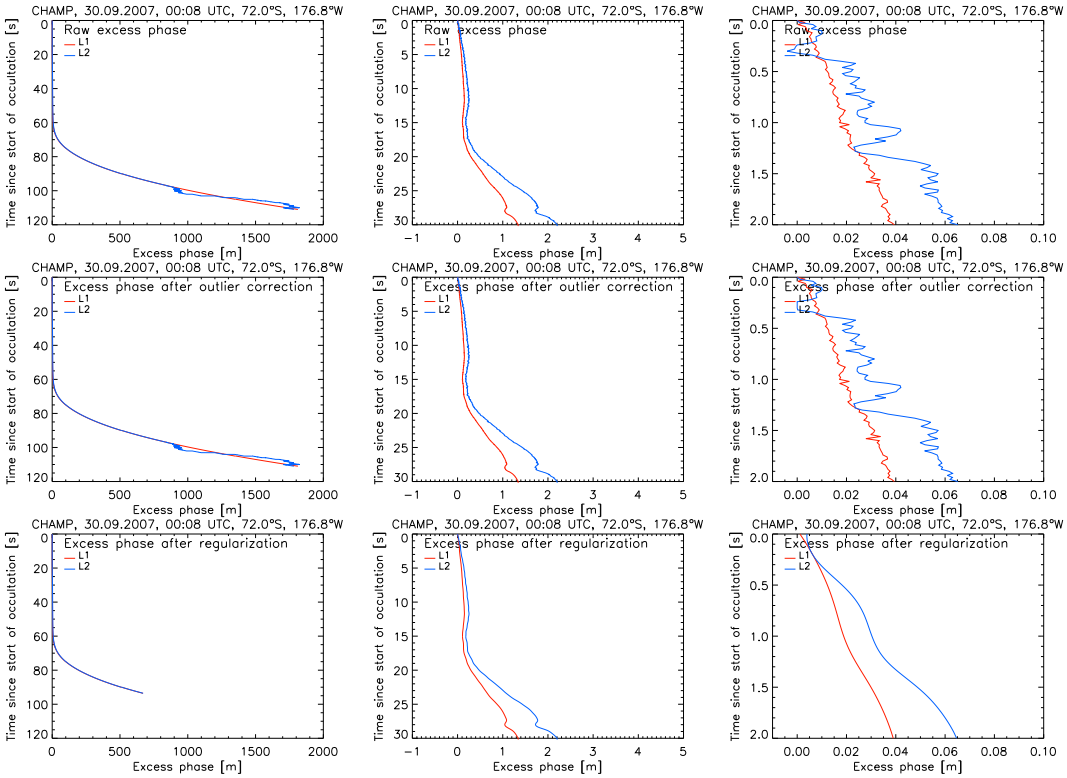

Figure 1.5: Phase delay data as a function of time of a CHAMP setting event at high southern latitudes. Raw phase delays (top row), phase delays after correction of outliers (middle row), and after smoothing with the regularization filter (bottom row). All data are depicted for three different time intervals: 120 s (left), 30 s (middle), and 2 s (right).

where $\mathbf{I}$ is the unit matrix, λ is the regularization parameter, $\lambda = 10^{\text{sample rate}/10} = 10^5$ (Syndergaard 1999), $\mathbf{S}$ is a third difference operator,

$$\mathbf{S} = \begin{pmatrix} -1 & 3 & -3 & 1 & 0 & 0 & \cdots \\ 0 & -1 & 3 & -3 & 1 & 0 & \cdots \\ & \ddots & & & & \ddots & \\ \cdots & & 0 & -1 & 3 & -3 & 1 \end{pmatrix}, \tag{1.18}$$

and $\vec{x}$ the raw excess phase time series. Equation (1.17) is solved by a conjugate gradient method (Hestenes and Stiefel 1952), with the iteration stopping if the relative change in the solution from the last iteration is less than 10^{-10}.

Figure 1.5 shows the atmospheric phase delays of a sample profile for the L1-signal (red) and the L2-signal (blue) as a function of time for different time intervals.

Data of this CHAMP setting event were recorded end of September 2007 at high southern latitudes (72.0°S). The top row shows uncorrected phase delays as obtained by UCAR/CDAAC. The middle row shows outlier corrected data and the bottom row depicts smoothed phase delays, after application of the regularization method.

The RO event lasts about 2 minutes, but after approximately 90 seconds, large ambiguities occur in the L2-signal. However, the CHAMP receiver also has (less distinctive) sampling problems with the L1-signal and for that reason, the phases are cut off after 93.5 s. The middle row of Figure 1.5 shows a zoom of the phase delays at the first 30 s of the occultation event. The dispersive ionospheric influence is clearly seen after approximately 18 s, where the L2 phase delay becomes larger than the L1 phase delay. Differences in the signals' characteristics are best seen in a zoom of only 2 s (right row) in the raw phases. Since the power of the L1-signal is stronger than that of the L2-signal by 3 dB, the L1-signal exhibits distinctively less noise than the L2-signal.

1.3.4 Correction of the Earth's Oblateness

Meteorological parameters are not exactly spherically distributed around the globe. The Earth's gravitational field yields contours of constant values of atmospheric parameters to follow the shape of the geoid. The geoid approximates to an ellipsoid and the oblateness of the ellipsoid has to be accounted for in the retrieval process to first order because spherical symmetry is assumed in the retrieval process and neglecting the Earth's oblateness causes a temperature bias of up to 3 K at an altitude of 10 km and 6 K at the ground (Syndergaard 1998). Spherical symmetry is assumed in the retrieval of bending angle so that all satellite positions have to be referred to the local center of refraction instead of the Earth's center. The center of refraction is defined by the origin of a sphere, which is tangential to the ellipsoid at the mean occultation event location (see Figure 1.6). The OPSv54 retrieval applies the correction procedure proposed by Syndergaard (1998); it delivers a vector $\Delta\vec{r}$, the difference of the Earth's radius vector at mean tangent point location $\vec{r}_{\mathrm{e}}$ and the radius vector from the new center to the tangent point $\vec{r}_{\mathrm{c}}$:

$$\Delta\vec{r} = \vec{r}_{\mathrm{e}} - \vec{r}_{\mathrm{c}} \tag{1.19}$$

All satellite positions have to be corrected according to:

$$\vec{r}_{\mathrm{LEO,Refraction}} = \vec{r}_{\mathrm{LEO,Earth}} + \Delta\vec{r} \tag{1.20}$$

$$\vec{r}_{\mathrm{GPS,Refraction}} = \vec{r}_{\mathrm{GPS,Earth}} + \Delta\vec{r}, \tag{1.21}$$

where $\vec{r}_{\mathrm{LEO,Refraction}}$ denotes the LEO position vector referred to the center of refraction, $\vec{r}_{\mathrm{GPS,Refraction}}$ is the corresponding GPS position vector, and $\vec{r}_{\mathrm{LEO,Earth}}$ and $\vec{r}_{\mathrm{GPS,Earth}}$ are the LEO and the GPS position vectors referred to the center of the

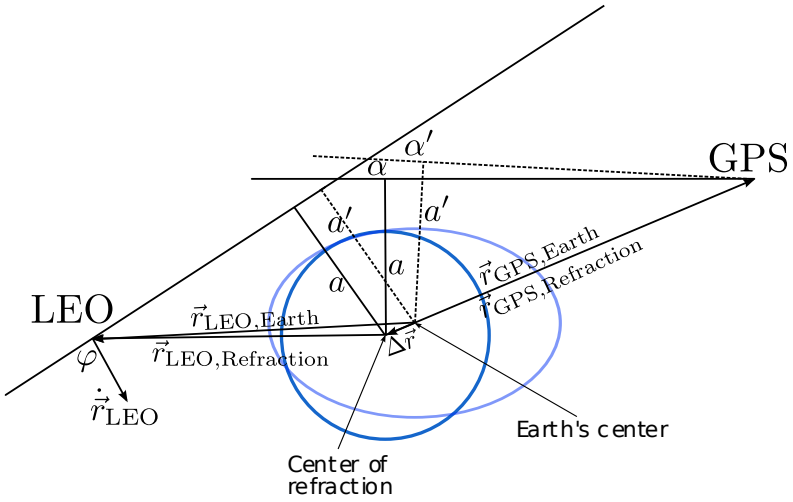

Figure 1.6: Correction of the Earth's oblateness: In the RO retrieval, the Earth's center has to be replaced by the center of refraction yielding the correct bending angle α as a function of impact parameter a instead of α' as a function of a'. After Syndergaard (1998).

Earth, respectively. The radius of curvature, $r_{\mathrm{c}} = |\vec{r}_{\mathrm{c}}|$ is used in the refractivity retrieval.

1.3.5 Bending Angle Retrieval

The bending angle retrieval is one main part in the radio occultation processing chain. Phase delay profiles are used to calculate atmospheric Doppler profiles, from which raw bending angle profiles are derived. Ionosphere-corrected bending angle profiles are statistically optimized using background information.

Excess Doppler and Doppler Shift

The excess Doppler of L1 and L2, $\mathrm{d}L_i/\mathrm{d}t$, is derived by differentiating the excess phase delays. Within the OPSv54 retrieval a 3-point differentiation formula is used:

$$\frac{\mathrm{d}L_i}{\mathrm{d}t} = \frac{L_i(n+1) - L_i(n-1)}{2\Delta t}. \tag{1.22}$$

$i = 1, 2$ denotes the frequency components of the carrier phases, $\Delta t = t(n+1) - t(n)$ the sample time interval, and n the time steps.

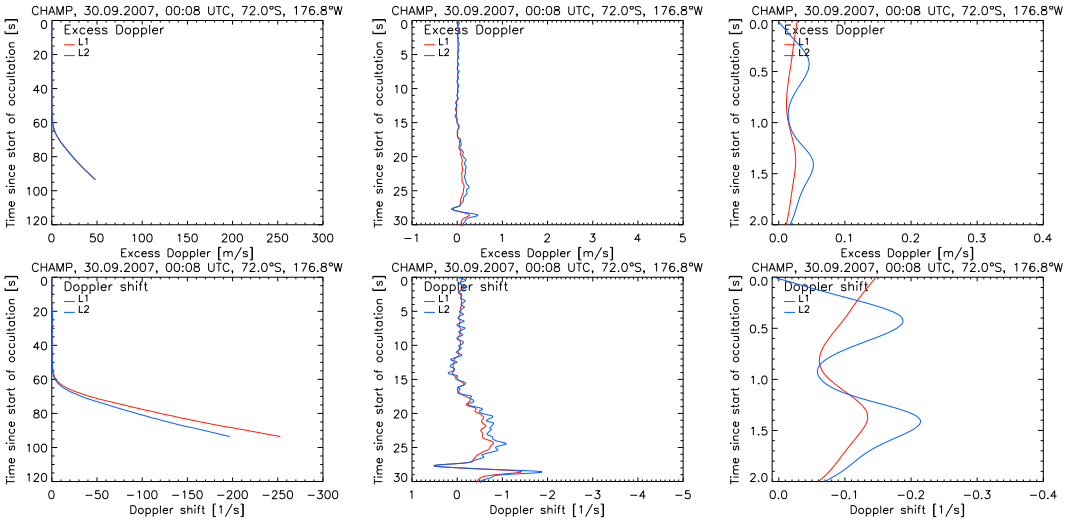

Figure 1.7: Excess Doppler profiles (top) and Doppler shift profiles (bottom) as a function of time. Doppler shift is the negative excess Doppler scaled by the frequency f and the speed of light c. Differences of the L1- and L2-signal are better visible in the Doppler shift profiles.

The atmospheric Doppler shift Δf_i is the negative excess Doppler scaled by the frequency f_i and the speed of light c

$$\Delta f_i = -\frac{f_i}{c}\frac{\mathrm{d}L_i}{\mathrm{d}t}. \tag{1.23}$$

Figure 1.7 shows excess Doppler and Doppler shift as a function of time for different time intervals for the same profile as shown in Figure 1.5.

Bending Angle

Knowledge of excess Doppler and occultation geometry enables the calculation of atmospheric bending angle α as a function of impact parameter a. The only assumption is local spherical symmetry, which is valid after correcting the Earth's oblateness (cf. Subsection 1.3.4). The determination of bending angle is done separately for each frequency.

As shown by Melbourne et al. (1994), the excess Doppler $\mathrm{d}L_i/\mathrm{d}t$ depends only upon local coordinates and velocities of the satellites:

$$\frac{\mathrm{d}L_i}{\mathrm{d}t} = |\dot{\vec{r}}_{\mathrm{LEO}}|\cos(\varphi_i(a_i)) + |\dot{\vec{r}}_{\mathrm{GPS}}|\cos(\chi_i(a_i)) - \dot{\vec{r}}_{\mathrm{LEO\text{-}GPS}}, \tag{1.24}$$

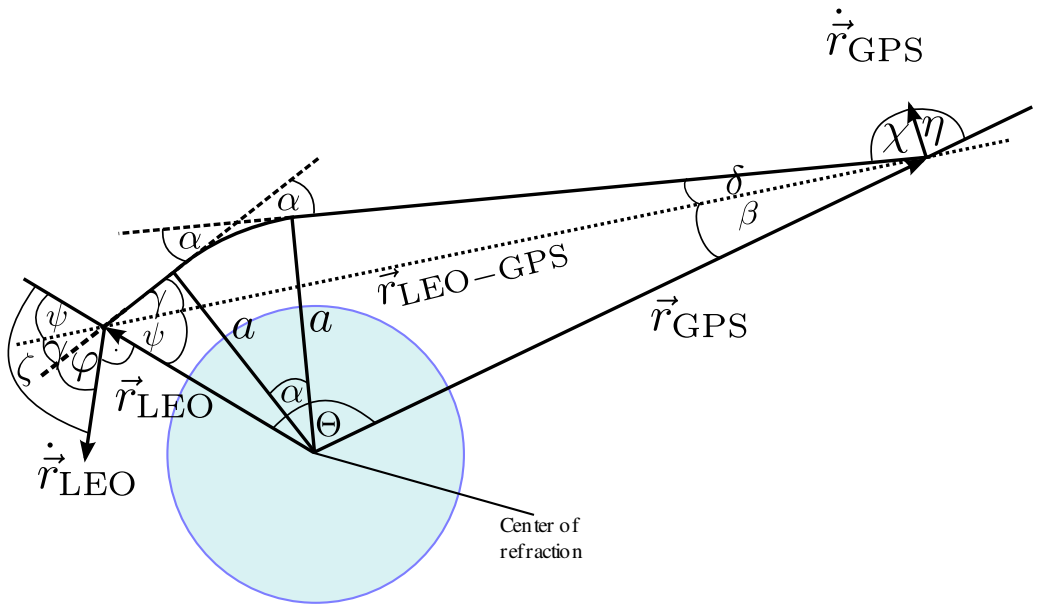

Figure 1.8: Geometry of an occultation event, defining various parameters. $\dot{\vec{r}}_{\mathrm{LEO}}$ and $\dot{\vec{r}}_{\mathrm{GPS}}$ are the projections of the satellite velocities into the occultation plane, which is defined by the position of the satellites and the center of refraction.

where $\dot{\vec{r}}_{\mathrm{LEO}}$ is the projection of the LEO satellite velocity into the occultation plane, φ_i is the angle between $\dot{\vec{r}}_{\mathrm{LEO}}$ and the vector of the ray path from the LEO's perspective, a_i is the impact parameter, $\dot{\vec{r}}_{\mathrm{GPS}}$ is the projection of the GPS satellite velocity into the occultation plane, χ_i is the angle between $\dot{\vec{r}}_{\mathrm{GPS}}$ and the vector of the ray as seen from the GPS satellite, and $\dot{\vec{r}}_{\mathrm{LEO\text{-}GPS}}$ is the temporal deviation of the geometrical distance between the LEO and the GPS satellite, which accounts for the kinematic Doppler shift. All these quantities are shown in Figure 1.8.

From the Bouguer formula[4] one may obtain

$$a_i = |\vec{r}_{\mathrm{LEO}}| \sin(\psi + \gamma_i) = |\vec{r}_{\mathrm{GPS}}| \sin(\beta + \delta_i), \tag{1.25}$$

where the angles ψ, γ, β, and δ are all defined by occultation geometry (see Fig-

[4]The exact form of the Bouguer formula states $nr\sin(\phi) = \text{constant} = a$, where n is the refractive index and ϕ is the angle between the position vector $\vec{r}$ and the ray direction (see Subsection 1.3.6). In Eq. (1.25), the refractive index is set to one. Hajj and Romans (1998) showed that ignoring the deviation of n from unity yields only a small error. The accuracy of Eq. (1.25) mainly depends on the orbit altitude of the LEO satellite and on ionospheric conditions.

ure 1.8). Eq. (1.25) can be used to express the angles φ_i and χ_i by

$$\varphi_i(a_i) = \zeta - \gamma_i - \psi = \zeta - \arcsin\left(\frac{a_i}{|\vec{r}_{\mathrm{LEO}}|}\right) \tag{1.26}$$

$$\chi_i(a_i) = \pi - \eta - \delta_i - \beta = (\pi - \eta) - \arcsin\left(\frac{a_i}{|\vec{r}_{\mathrm{GPS}}|}\right). \tag{1.27}$$

Equations (1.24), (1.26), and (1.27) are solved iteratively for the impact parameter a_i with the iteration stopping when the relative change of the impact parameter is less than 10^{-10}.

The bending angle α_i as a function of impact parameter a_i is derived from

$$\alpha_i = \Theta - \arccos\left(\frac{a_i}{|\vec{r}_{\mathrm{LEO}}|}\right) - \arccos\left(\frac{a_i}{|\vec{r}_{\mathrm{GPS}}|}\right) \tag{1.28}$$

where Θ the angle between $\vec{r}_{\mathrm{LEO}}$ and $\vec{r}_{\mathrm{GPS}}$.

Ionospheric Correction

The input data used for the OPSv54 retrieval, the atmospheric phase delay, does not only include neutral atmospheric phase delay, but also ionospheric phase delay. This ionospheric fraction is different for the L1- and the L2-signal because of the ionospheric dispersive nature. Because the neutral atmosphere characteristics are of our main interest, the ionospheric influence on the atmospheric phase delay has to be removed.

It is possible to apply the ionospheric correction on the phase delay profiles (before calculating excess Doppler) or on bending angle profiles. Both methods take advantage of the two GPS frequencies, which yield two separate measurements performed at the same time.

When ionospheric correction is based on phase delay profiles as a function of time, L1 and L2 phase delays are combined by (Dixon 1991)

$$L_{\mathrm{c}}(t) = \frac{f_1^2 L_1(t) - f_2^2 L_2(t)}{f_1^2 - f_2^2} \tag{1.29}$$

where f_1 is the L1 carrier frequency and f_2 the L2 carrier frequency. The underlying assumption is that the L1- and L2-signals travel along identical ray paths, which is not exact due to the dispersive nature of the ionosphere.

This "dispersion" residual (cf. Syndergaard 2000) is avoided applying the linear combination of L1 and L2 bending angle profiles as a function of a common impact parameter, as proposed by Vorob'ev and Krasil'nikova (1994)

$$\alpha_{\mathrm{c}}(a) = \frac{f_1^2 \alpha_1(a) - f_2^2 \alpha_2(a)}{f_1^2 - f_2^2}. \tag{1.30}$$

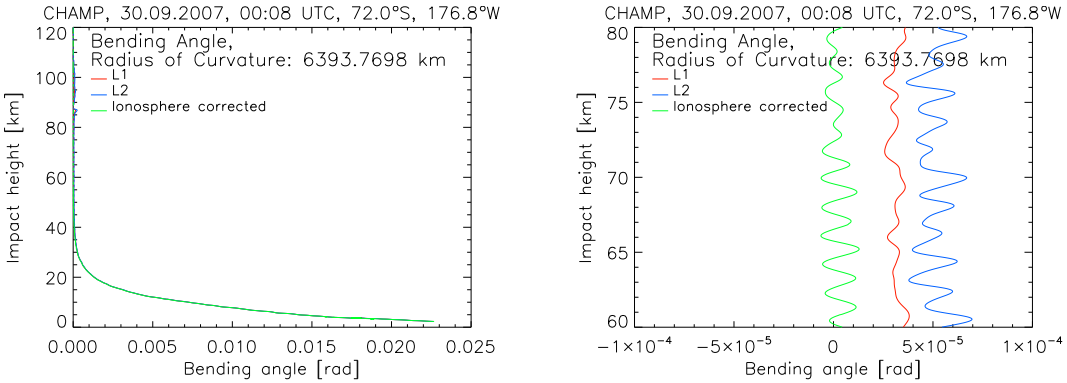

Figure 1.9: Raw L1 and L2 bending angles, as well as ionosphere-corrected bending angle as a function of impact height. To the first order, the ionosphere-corrected bending angle only includes bending of the neutral atmosphere, so that it is smaller than the raw L1 and L2 bending angles.

The disadvantage of this method is that small-scale bending angle fluctuations of the L2-signal, which are often related to corrupted data, result in enhanced artificial noise (Hocke et al. 2003).

For that reason, the OPSv54 retrieval applies a modified ionospheric correction where low-pass filtered bending angle profiles, $\overline{\alpha}_1$ and $\overline{\alpha}_2$, are linearly combined but the high-pass fraction of the L1 bending angle, $\delta\alpha_1(a) = \alpha_1(a) - \overline{\alpha}_1(a)$, which actually accounts for small scale features appearing in the neutral atmosphere, is added again (Hocke et al. 2003):

$$\alpha_c(a) = \frac{f_1^2\overline{\alpha}_1(a) - f_2^2\overline{\alpha}_2(a)}{f_1^2 - f_2^2} + \delta\alpha_1(a). \tag{1.31}$$

Testing CHAMP RO data, Gobiet (2005) showed that smoothing with a boxcar filter with 1 km filter width performed best.

Due to the stronger power of the L1-signal, the GPS signals of both frequencies are not of the same quality. The L2-signal is of worst quality in the lowest atmosphere and very often it does not range towards the surface. To maintain high data quality down to the lower troposphere and to ensure ionospheric correction for the whole profile, the L2-signal is extrapolated below 15 km. For this purpose, the L1 minus L2 phase delay profile is extrapolated downward from higher impact heights towards the end of the L1-signal. The linear gradient is calculated between an impact height of 15 km and 20 km so that the L2 profile is extended downward of 15 km. This extended L2 phase delay profile is used in the bending angle retrieval.

Figure 1.9 depicts L1 and L2 bending angle profiles as well as the ionosphere-corrected bending angle profile as a function of impact height. Impact height is

defined as impact parameter minus radius of curvature. It can be seen in the right panel of Figure 1.9 that the "neutral" bending angle is smaller than both, the L1 and the L2 bending angles. Between 60 km and 80 km, where atmospheric density is small, the atmospheric bending angle oscillates around zero.

Bending Angle Bias, Noise, and Observational Error

The bending angle bias and the bending angle noise are estimated by comparing the ionosphere-corrected bending angle profile to its co-located Mass Spectrometer and Incoherent Scatter Radar (MSIS) (Hedin 1991) profile between 65 km and 80 km. At these height levels, the measurement is dominated by measurement noise and ionospheric residuals because atmospheric density is small.

The bias[5] is found as the difference between the mean RO bending angle and the mean MSIS bending angle within that altitude range:

$$\text{bias} = \frac{1}{k} \sum_{k=65\text{ km}}^{80\text{ km}} (\alpha_{\text{RO}})_k - \frac{1}{k} \sum_{k=65\text{ km}}^{80\text{ km}} (\alpha_{\text{MSIS}})_k \,. \tag{1.32}$$

The bending angle noise is defined as the standard deviation of the RO profile relative to the shifted MSIS profile (shifted by the bias):

$$\text{noise} = \sqrt{\frac{1}{k+1} \sum_{k=65\text{ km}}^{80\text{ km}} \left[(\alpha_{\text{RO}})_k - ((\alpha_{\text{MSIS}})_k + \text{bias})\right]^2} \tag{1.33}$$

The characteristic of the observational data noise (i.e., the observational error) is needed for statistical optimization of bending angle at high altitudes as it determines the weight of the measurement (see Section 1.3.5).

Experience with CHAMP data showed that the bending angle noise often does not reflect the real quality of the measurement (Gobiet 2005) so that, in some cases, the observational error is not equal to bending angle noise but is modified according to some additional quality checks.

These quality checks comprise:

1. More than 25 data points have to be available between 65 km and 75 km. If there are less than 25 data points within that altitude range, the observational error is set to 50 μrad and the Quality Flag (QF) is set to a non-zero value (QF = 2).

2. An estimated bending angle noise, which is smaller than 0.5 μrad seems to be unrealistically small, so that the observational error is set to 50 μrad and the QF is set to a non-zero value (QF = 6).

[5] The term "bias" may be confusing because both, the RO and the MSIS bending angle exhibit a bias relative to the truth.

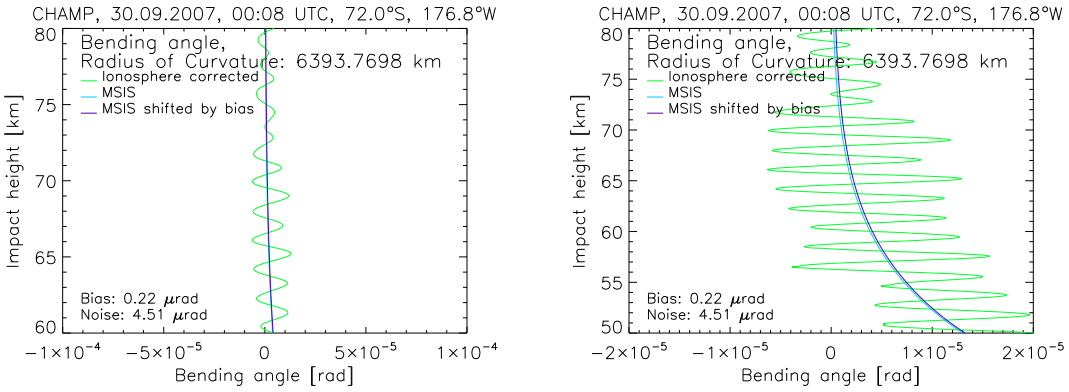

Figure 1.10: CHAMP ionosphere-corrected bending angle, co-located MSIS bending angle, and MSIS bending angle, which is shifted by the bias of the observed bending angle. The bending angle bias is much smaller than the differences of L1, L2, and the ionosphere-corrected bending angle.

3. If the absolute value of the bias is larger than the estimated bending angle noise, the profile is discarded and the QF is set to a non-zero value (QF = 7).

4. An estimated bending angle noise larger than 50 μrad seems to be unrealistically large. The profile is discarded, the QF is set to a non-zero value (QF = 8).

5. After the ionospheric correction, the bending angles at high altitudes are sometimes smaller than zero because of superimposed noise. However, the atmospheric density field yields signals bending and atmospheric bending angle should not be negative below 65 km. If negative bending angles occur below 65 km, the observational error is set to 10 μrad. Negative bending angles are removed and the top of the profile is cut off.

6. If negative bending angles occur below 55 km, the observational error is set to 50 μrad. Negative bending angles are removed and the top of the profile is cut off.

7. If negative bending angles occur below 50 km, the profile is discarded, the QF is set to a non-zero value (QF = 5).

This (conservative) approach, which proved to be useful for comparatively noisy CHAMP data, leads to stronger weighting of the bending angle background when performing statistical optimization.

Figure 1.10 shows the ionosphere-corrected bending angle, the co-located MSIS bending angle, and the MSIS bending angle, which is shifted by the bias of the

observed CHAMP data. All data are shown as a function of impact height[6]. To get a better feeling of the magnitudes of the bending angle bias, the left panel of Figure 1.10 has the same x-range (from -100 μrad to 100 μrad) as the right panel of Figure 1.9. The oscillations of the CHAMP bending angle profile are clearly visible, but the difference between the original MSIS profile and the shifted MSIS profile is too small to be noticeable. The right panel of Figure 1.10, which depicts the zoom of the bending angle to -20 μrad to 20 μrad, allows to see the difference between both MSIS profiles. The bias of the CHAMP profile amounts to 0.22 μrad, the estimated bending angle noise amounts to 4.51 μrad. However, it also can be seen, that negative CHAMP bending angles occur down to an impact height of about 56 km, which means that the observational error used for statistical optimization is artificially set to 10 μrad.

High Altitude Initialization and Statistical Optimization

In the next "main" step of the retrieval, the calculation of microwave refractivity is performed by an Abel transformation, which involves an integral (cf. Subsection 1.3.6). The upper bound of this integral is infinity. Since RO data are usually available only up to 80 km, the Abel integral needs an upper boundary initialization. A bad initialization of the bending angle at highest altitudes (in the lower thermosphere) results in errors in the refractivity profile. As already seen in Figure 1.9 and Figure 1.10, bending angles at high altitudes (upper stratosphere and beyond) are characterized by high noise, which also results in non-negligible errors in the refractivity profile.

To reduce the effect of error propagation downward in the Upper Troposphere–Lower Stratosphere (UTLS) region, the bending angle is initialized with background information. The retrieved bending angle profile is optimized in a statistically optimal way (Rodgers 2000) yielding a "statistically optimized bending angle", which is used for further calculations. Gobiet (2005) emphasizes that "statistical optimization does not improve the quality of observed profiles themselves at high altitudes but rather delivers an improved combined profile thanks to the sensible inclusion of background information".

Background information used for this process can be given by climatological models (e.g., MSIS or CIRA (COSPAR International Reference Atmosphere, Fleming et al. (1990)) climatologies) or by meteorological data as provided e.g., by the European Centre for Medium-Range Weather Forecasts (ECMWF) or National Centers for Environmental Prediction (NCEP). It depends on the users' needs, which background information is desirable. Middle atmospheric climatologies are independent from Numerical Weather Prediction (NWP) models but as shown by Randel et al. (2004), they are biased in some regions of the atmosphere. Such a bias would also induce a

[6] The difference between impact height and height amounts approximately to 2 km near the surface, see Subsection 1.3.6 for more details.

bias into the retrieved profiles. The OPS retrieval uses ECMWF data (at four time layers, 00 Universal Time Coordinated (UTC), 06 UTC, 12 UTC, 18 UTC) for statistical optimization since these data are believed to be the best-possible data set available. However, RO data retrieved at WEGC are not fully independent from ECMWF at high altitudes.

Retrieval versions up to Occultation Processing System Version 5.2 (OPSv52) used ECMWF analysis fields (or MSIS climatologies optionally) as background information. Because RO data have been assimilated at ECMWF since December 2006, Occultation Processing System Version 5.3 (OPSv53) changed background information using ECMWF short-term forecast fields (24 h to 30 h forecasts) because the operational analyses are not independent of RO data any more. The optimization is performed between 30 km and 120 km impact height. In February 2006 ECMWF increased the number of vertical levels from 60 to 91 (L60 to L91) with an increase of the top-most levels from 0.1 hPa (about 65 km) to 0.01 hPa (about 80 km). Above that top-most level, ECMWF data are pieced together with MSIS data, which are used up to 120 km. The horizontal resolution is chosen to match the horizontal resolution of RO data (approximately 250 km), which corresponds to T42 (spectral representation with triangular truncation at wave number 42). The background profile is extracted from that ECMWF field, which time layer is closest to the RO event time. Co-location is derived from spatial interpolation to the mean RO event location.

The statistical optimization within the OPSv54 retrieval is performed by an inverse covariance weighting, where unbiased (Gaussian) errors and a linear problem are assumed (Gobiet and Kirchengast 2004):

$$\alpha_{\mathrm{opt}} = \alpha_{\mathrm{bg}} + \mathbf{B}(\mathbf{B} + \mathbf{O})^{-1}(\alpha_{\mathrm{obs}} - \alpha_{\mathrm{bg}}) \tag{1.34}$$

where α_{opt} is the optimized bending angle profile, α_{bg} and α_{obs} are the background bending angle profile and the observed bending angle profile, respectively, and $\mathbf{B}$ and $\mathbf{O}$ are the corresponding background error and observation error covariance matrices.

The matrices $\mathbf{B}$ and $\mathbf{O}$ are calculated from

$$\mathbf{B}_{ij} = \sigma_{\mathrm{bg}i}\sigma_{\mathrm{bg}j} \exp\left(-\frac{|a_i - a_j|}{L_{\mathrm{bg}}}\right), \tag{1.35}$$

$$\mathbf{O}_{ij} = \sigma_{\mathrm{obs}i}\sigma_{\mathrm{obs}j} \exp\left(-\frac{|a_i - a_j|}{L_{\mathrm{obs}}}\right), \tag{1.36}$$

with $\sigma_{\mathrm{bg}i}$ and $\sigma_{\mathrm{bg}j}$ being the estimated standard deviations of the background model for two height levels i and j, which are assumed to amount to 15 % of the background bending angle profile, $\sigma_{\mathrm{bg}} = 0.15\alpha_{\mathrm{bg}}$. $\sigma_{\mathrm{obs}i}$ and $\sigma_{\mathrm{obs}j}$ equal to the observational error

estimated from the ionosphere-corrected bending angle profile (see above), a_i and a_j denote the impact parameters at height levels i and j, and $L_{\mathrm{bg}} = 10$ km and $L_{\mathrm{obs}} = 2$ km describe the error correlation lengths for the background model and the observational data.

This method strongly depends on the error characteristics of the observational and the background bending angle profile. At high altitudes, where the observational error is larger than the background error, the background profile has more weight in the optimization process than the observed profile. At lower altitudes (in the lower stratosphere), however, where the background error exceeds the observational error, the statistically optimized profile is strongly affected by the observational profile.

The ratio of the retrieval error and the a priori (background) error (Retrieval to Apriori Error Ratio (RAER)) gives a measure of relative importance of the background and observation information as it gives the fraction of the retrieval error stemming from the background. According to Rieder and Kirchengast (2001), it is estimated from

$$\mathrm{RAER} = 100\frac{\sigma_{\mathrm{ret}}}{\sigma_{\mathrm{bg}}} \tag{1.37}$$

where σ_{ret} contains the square root of the diagonal elements of the retrieval error $\mathbf{R}$, which is given by

$$\mathbf{R} = (\mathbf{B}^{-1} + \mathbf{O}^{-1})^{-1}. \tag{1.38}$$

The RAER profile is given in percent. The statistically optimized bending angle is background dominated if RAER is larger than 50 % and observation dominated if RAER is smaller than 50 %. $a_{\mathrm{RAER=50\,\%}}$ denotes the transition impact parameter between these two regimes, $z_{\mathrm{RAER=50\,\%}}$ (impact height, where retrieval to apriori error ratio equals 50 % (zRAER50)) is the corresponding impact height. The measurement error strongly determines the value of zRAER50 because observations are inversely weighted with the measurement error so that small observation errors lead to large zRAER50 values.

Figure 1.11 depicts the ionosphere-corrected bending angle profile, the co-located ECMWF forecast bending angle profile, and the statistically optimized bending angle profile as a function of impact height at different impact height ranges and the corresponding RAER profile (right). The co-located ECMWF bending angle is shown only for the interval of statistical optimization down to 30 km. The effect of statistical optimization is best visible in Figure 1.11 in the bottom left panel: following the yellow line shows that the statistically optimized bending angle profile is almost identical with the co-located ECMWF profile at 50 km but it coincides with the RO profile at impact heights of about 35 km. The transition height between background dominance and observation dominance lies at an impact height of 42.87 km. This is a typical height level for a profile with an observational error set to 10 μrad.

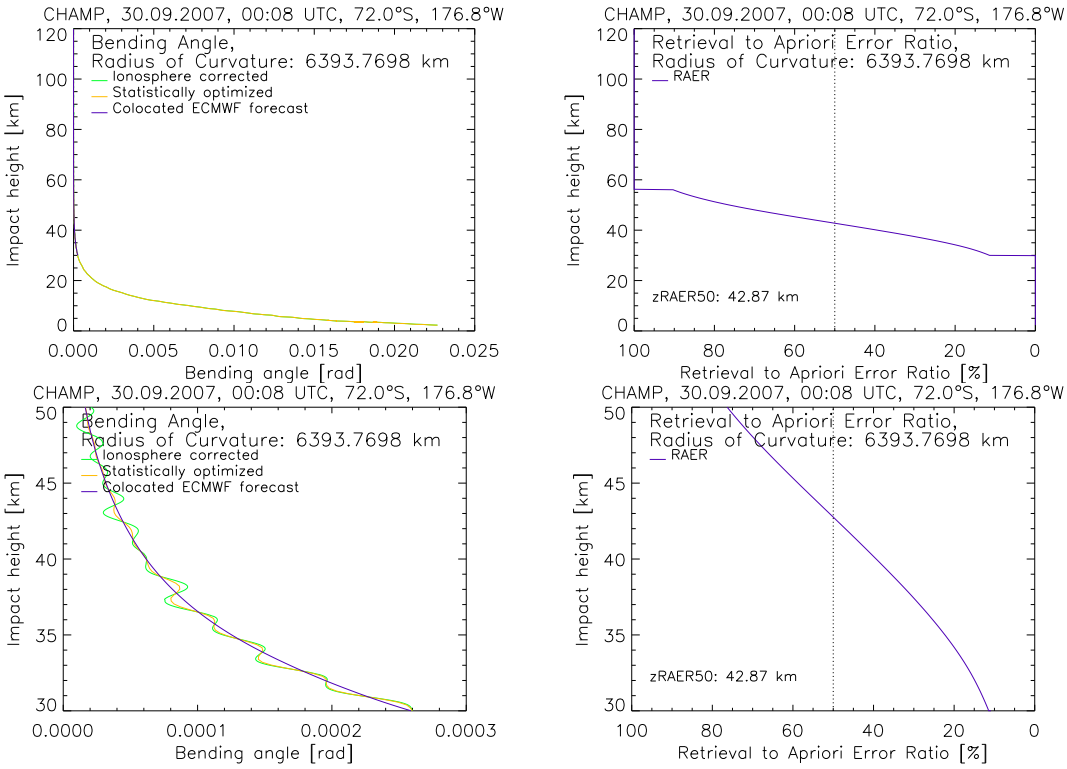

Figure 1.11: Ionosphere-corrected bending angle, statistically optimized bending angle, and ECMWF forecast bending angle as a function of impact height (left) and corresponding retrieval to a priori error ratio profile (right) between the surface and 120 km (top) and between 30 km and 50 km (bottom). Statistical optimization is performed between 30 km and 120 km.

1.3.6 Atmospheric Refraction

The OPSv54 retrieval is a GO retrieval, i.e., the propagation of electromagnetic signals can be described by GO approximations. The RO retrieval makes use of some of these geometric approximations, e.g., Fermat's principle, law of refraction (Snell's law), or Bouguers's rule, all of them are derived and described in detail in Born and Wolf (1999).

The Fermat's principle (or principle of the shortest optical path, also known as principle of least time, (Born and Wolf 1999)) states that the path of a ray passing through a medium, e.g., the atmosphere from a GPS satellite to a LEO satellite, takes

the least time

$$\int_{\text{GPS}}^{\text{LEO}} n\mathrm{d}s = \min, \tag{1.39}$$

with n being the refractive index and s the ray's path.

The law of refraction (Snell's law), which holds true at the interface between two media, says that

$$\frac{\sin\theta_1}{\sin\theta_2} = \frac{v_1}{v_2} = \frac{n_2}{n_1}, \tag{1.40}$$

where θ_1 and θ_2 are the angle of incidence and the angle of refraction, respectively, v_1 and v_2 are velocities in medium 1 and medium 2, and n_1 and n_2 are the corresponding refractive indices.

All rays are curves, situated in a plane. The formula of Bouguer, which represents the law of refraction in a spherical symmetric refractive medium, states that along each ray it applies

$$\vec{r} \times n\vec{s} = \text{constant} \equiv a \qquad \text{(vectorial form)}, \tag{1.41}$$

and

$$nr\sin\phi = \text{constant} \equiv a \qquad \text{(scalar form)}, \tag{1.42}$$

where $\vec{r}$ is the position vector, r is the distance to the ray path, $\vec{s}$ is the unit vector in ray direction, ϕ is the angle between the position vector $\vec{r}$ and $\vec{s}$, and a is the impact parameter. From Eq. (1.42) it follows that

$$n(r)r_{\text{LEO}}\sin\phi_{\text{LEO}} = n(r)r_{\text{GPS}}\sin\phi_{\text{GPS}} = a. \tag{1.43}$$

The impact parameter a is constant along the ray path. At the point of closest approach, where $\phi = 90$ and $\sin\phi = 1$ (ray tangent radius r_{t}, a equals to $a = n(r_{\text{t}})r_{\text{t}}$.

These fundamental physical laws are the basis for the derivation of the relation between bending angle and refractive index. Use of Eq. (1.42) implicates local spherical symmetry, which is therefore assumed in the retrieval process.

Bending of a ray is caused by radial variations of the refractive index n. The total bending angle α is the integral of incremental bending along the entire ray path. Figure 1.12 illustrates the ray path geometry and the polar coordinate system. r and ϕ are the polar coordinates, β is the angle of incidence, and α is the bending angle. Fjeldbo et al. (1971) utilized the physical laws mentioned above and Figure 1.12 to

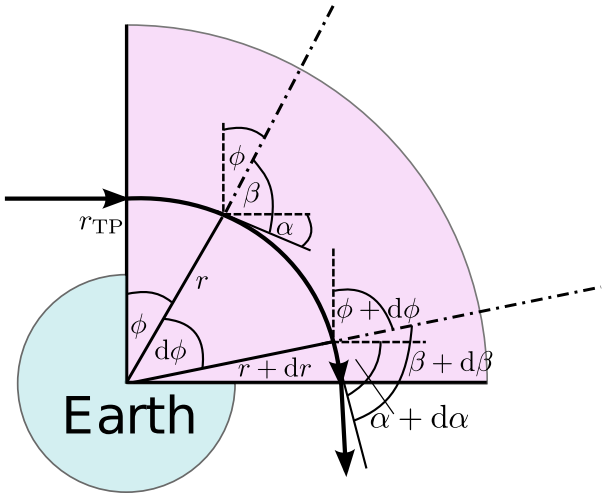

Figure 1.12: Geometry of the ray path in a spherical medium. r and ϕ are polar coordinates describing the bending angle, β is the angle of incidence. The total bending angle α is the integral of incremental bending $\mathrm{d}\alpha$ along the entire ray path. After Foelsche (1999).

derive the ray path equation. Thereby, Fjeldbo et al. (1971) showed that the total bending angle α is calculated from

$$\alpha(a) = \int_0^{\alpha} \mathrm{d}\alpha' = 2a \int_{r=r_{\mathrm{t}}}^{r=\infty} \frac{1}{\sqrt{(nr)^2 - a^2}} \frac{\mathrm{d}\ln(n)}{\mathrm{d}r} \mathrm{d}r. \tag{1.44}$$

Equation (1.44) is an Abel integral equation ("Forward Abel Transform").

The inversion of this Abel integral equation (the corresponding derivation is shown e.g., by Steiner (1998)) yields

$$n(r_1) = \exp\left[-\frac{1}{\pi} \int_{a_1}^{\infty} \frac{\alpha(a)}{\sqrt{a^2 - a_1^2}} \mathrm{d}a \right], \tag{1.45}$$

where a_1 is the impact parameter for a particular ray and $r_1 = r_{\mathrm{t}}$ is the radius of the corresponding tangent point, $a_1 = n(r_1)r_1$.

Equation (1.45) contains a singularity at $a = a_1$, which is inconvenient for numerical solutions. A modified version of Eq. (1.45), as inferred by Steiner (1998), avoids

the pole in the integrand by integrating parts:

$$n(r_1) = \exp\left[\frac{1}{\pi}\int\limits_{\alpha=\alpha(a_1)}^{\alpha=0} \ln\left(\frac{a(\alpha)}{a_1} + \sqrt{\left(\frac{a(\alpha)}{a_1}\right)^2 - 1}\right) \mathrm{d}\alpha\right]. \tag{1.46}$$

Equation (1.46) yields the refractive index n only knowing the bending angle α and the impact parameter a. This equation is used in the OPSv54 retrieval.

Since the refractive index is close to unity in the free atmosphere and refractive index variations are very small, the atmospheric community prefers using atmospheric refractivity N rather than the refractive index n. It is defined by

$$N(h) = (n(h) - 1) \cdot 10^6, \tag{1.47}$$

with

$$h = r - r_\mathrm{c} = \frac{a}{n(a)} - r_\mathrm{c}, \tag{1.48}$$

where h is the height above Earth's ellipsoid and r_c is the radius of curvature of the ellipsoidal Earth at the location of the occultation event.

Figure 1.13 shows the relationship between refractivity and the consequential difference between impact height and height. It follows from Eq. (1.48) that the values of the impact height vector are always larger than the corresponding values of the height vector. Largest differences between impact height and height occur near the surface where atmospheric refractivity takes its largest values. At an altitude of about 0.6 km, where refractivity amounts to 280 N-Units, the difference between impact height and height yields more than 1.8 km.

After calculation of atmospheric refractivity as a function of height, the profile is smoothed by a Blackman window filter. The coefficients $w(n)$ of the Blackman window filter are obtained from

$$w(n) = 0.54 + 0.46\cos\left(\frac{2\pi n}{N}\right) + 0.08\cos\left(\frac{4\pi n}{N}\right), \tag{1.49}$$

where $n = 1, \ldots, N$ is the number of coefficients and N is the filter width. The Blackman filter smooths the measurement's noise variability and eliminates numerical noise.

Figure 1.14 depicts the CHAMP refractivity profile and the corresponding co-located ECMWF refractivity profile (extracted from ECMWF analysis fields) in linear space (left panel) and in logarithmic space (middle panel) as a function of Mean Sea Level (MSL) altitude. Since refractivity decreases exponentially with height, the logarithmic depiction facilitates the understanding of refractivity vertical behavior.

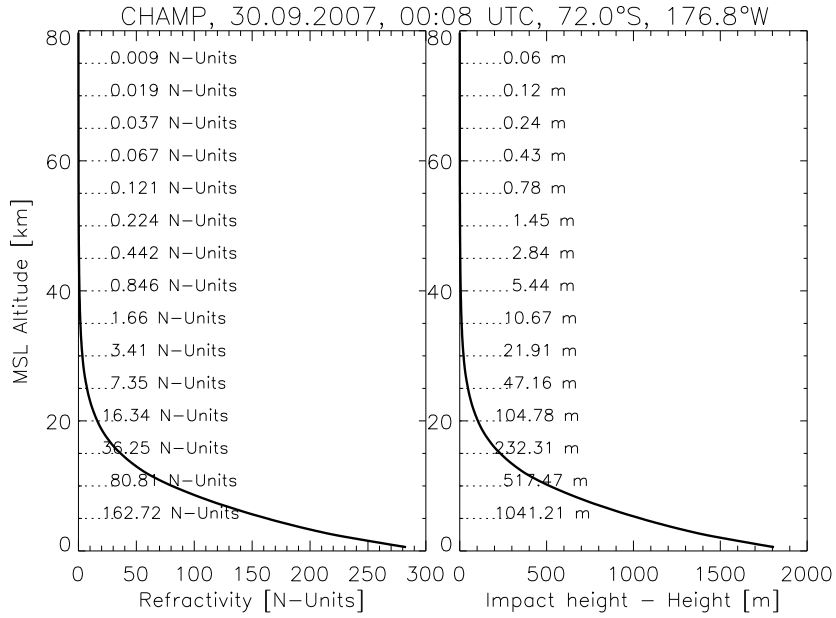

Figure 1.13: Refractivity profile (left) and the consequential difference between impact height and geometric height (right) as a function of MSL altitude. The impact height is defined as the difference between the impact parameter and the radius of curvature. The relationship between impact height and geometric height is given by Eq. (1.48). The values of the impact height vector are always larger than the values of the corresponding height vector because refractivity is always a positive quantity in the neutral atmosphere.

The right panel shows the systematic difference between CHAMP and ECMWF refractivity, given in percent (the systematic difference is calculated from ((ECMWF − RO)/ RO)100 %). Up to an altitude of 20 km the systematic difference is small oscillating around 0 %. At 22.5 km the difference between both profiles is larger than 1 % but it decreases again above 24 km. Above 30 km the systematic difference between the RO profile and the co-located ECMWF profile shows large oscillations (up to ±2 %).

1.3.7 Retrieval of Other Atmospheric Parameters

Atmospheric refractivity at microwave wavelengths as derived from GPS signals depends on conditions of the dry atmosphere, the moist atmosphere, the ionosphere, and on atmospheric scattering from liquid water or ice crystals. To first order this

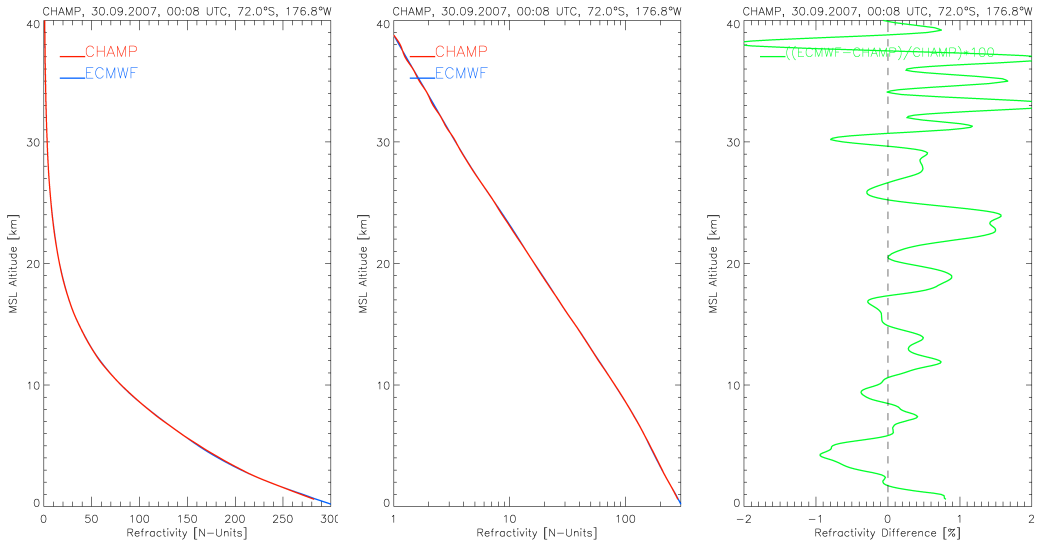

Figure 1.14: RO and ECMWF refractivity profiles (left: in linear scale, middle: in logarithmic scale) as a function of MSL altitude. Their systematic difference, given in percent, is depicted in the right panel.

relationship is given by (Smith and Weintraub 1953; Kursinski et al. 1997)

$$N = 77.6\frac{p}{T} + 3.73 \times 10^5 \frac{e}{T^2} - 4.03 \times 10^7 \frac{n_\mathrm{e}}{f^2} + 1.4W, \tag{1.50}$$

where p is the atmospheric pressure (in hPa), T atmospheric temperature (in K), e partial pressure of water vapor (in hPa), n_e is the electron density (in electrons/m^3), f the transmitter frequency (in Hz), and W is the mass of condensed water in the atmosphere (in g/m^3).

The first term in Eq. (1.50) represents the contribution of the dry atmosphere and the constant $k_1 = 77.6$ K/hPa basically accounts for the contribution of dry air to total refractivity. The first estimation of k_1 stems from Smith and Weintraub (1953) but since that time several publications report on the estimation of k_1 and its uncertainty (see e.g., Foelsche 1999; Rüeger 2002; Healy 2009). The second term in Eq. (1.50) represents the contribution of the moist atmosphere and the constant $k_2 = 3.73 \times 10^5$ (Smith and Weintraub 1953) accounts for the contribution of water vapor to total refractivity. The ionospheric contribution to refractivity (third term) can be neglected because the ionospheric correction has already been done on bending angle level. The last term, which represents the scattering term, is negligible because the content of liquid water is very small compared to the other terms.

The first and the second term of Eq. (1.50) remain important in further considerations. However, the OPSv54 retrieval is a "dry air retrieval", which means that

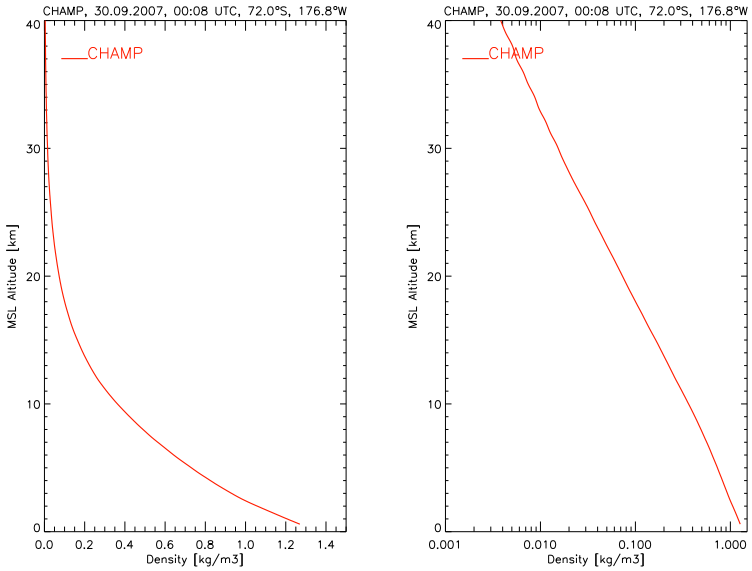

Figure 1.15: RO dry density profile (left: in linear space, right: in logarithmic space) as a function of MSL altitude.

the second term of Eq. (1.50) is neglected. The neglect of moisture yields dry atmospheric parameters, e.g., "dry temperature". Physical atmospheric parameters and humidity profiles can only simultaneously be derived using auxiliary information obtained from independent data sets.

Derivation of Dry Density

In atmospheric regions where moisture is negligible, which holds true for altitudes above 8 km (polar winter) and 14 km (tropics) (Foelsche et al. 2008*b*), refractivity at microwave wavelengths mainly depends on the density of dry air. Dependent on the polarizability, each single atom and molecule contributes to refractivity (Foelsche 1999). Within the homosphere, the chemical constituents are well-mixed and density of particles is proportional to density of mass. For that reason, refractivity is directly proportional to air density:

$$N_{\mathrm{dry}} = 77.6\frac{p_{\mathrm{dry}}}{T_{\mathrm{dry}}} = 77.6\rho_{\mathrm{dry}}\frac{R}{M_{\mathrm{dry}}}, \tag{1.51}$$

where $R = 8.314\ \mathrm{J/(K\,mol)}$ is the gas constant (Mohr et al. 2008) and $M_{\mathrm{dry}} = 28.964\ \mathrm{kg/kmol}$ is the mean molecular mass of dry air (Khélifa et al. 2007). The relationship between density, pressure, and temperature, as used above, is given by the state law of an ideal gas.

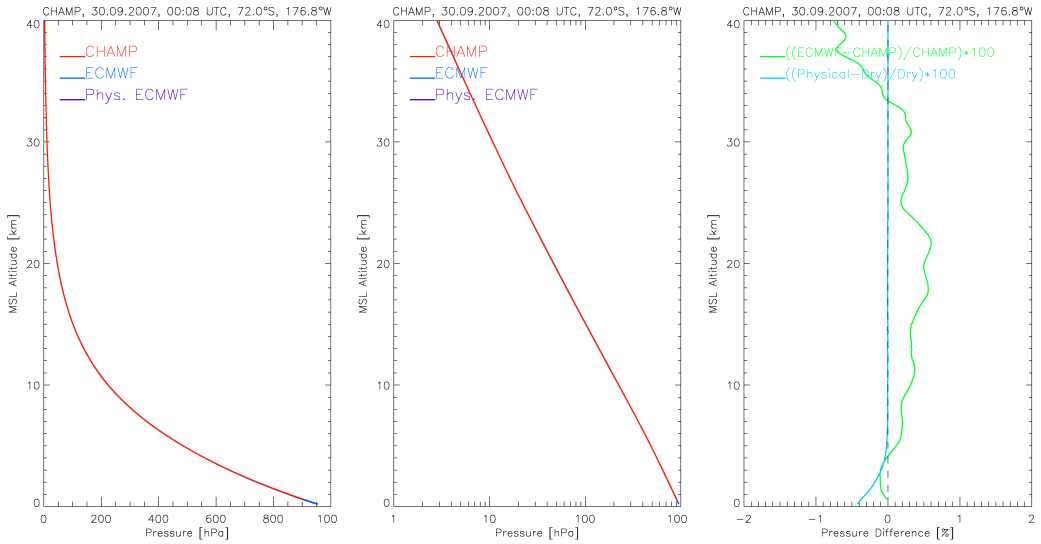

Figure 1.16: RO and ECMWF dry pressure and ECMWF physical pressure profiles (left: in linear space, middle: in logarithmic space) as a function of MSL altitude. The systematic difference between RO and ECMWF dry pressure as well as between ECMWF physical and dry pressure, both given in percent, are depicted in the right panel.

The profile of air density as a function of height can therefore be directly derived from the refractivity profile by

$$\rho_{\mathrm{dry}}(h) = N_{\mathrm{dry}}(h)\frac{M_{\mathrm{dry}}}{77.6R}. \tag{1.52}$$

The CHAMP dry density profile as a function of MSL altitude is shown in Figure 1.15 in linear space (left panel) and in logarithmic space (right panel). The logarithmic behavior of refractivity is propagated also in the dry density profile. Near the surface (at an altitude of 0.6 km), the atmospheric dry density amounts to 1.3 kg/m^3. Up to 40 km, atmospheric dry density decreases to approximately 3.9×10^{-3} kg/m^3.

Derivation of Dry Pressure

Under the assumption of hydrostatic equilibrium, the atmospheric pressure equals the weight of the overlying air column per area. This relationship is specified by the hydrostatic integral, which is the integral of acceleration of gravity as a function of geographic latitude and height $g(\phi, h)$ times density $\rho_{\mathrm{dry}}(h)$ yielding atmospheric

pressure:

$$p_{\mathrm{dry}}(h) = \int_{h}^{\infty} g(\phi, h')\rho_{\mathrm{dry}}(h')\mathrm{d}h' \tag{1.53}$$

The upper bound of the integral, which is theoretically infinity, is set to 120 km. The Earth's acceleration of gravity is derived from

$$g(\phi, h) = g_{\mathrm{surf}}(\phi)\left(\frac{r_{\mathrm{e}}(\phi)}{r_{\mathrm{e}}(\phi)+h}\right)^2, \tag{1.54}$$

where the acceleration of gravity at the surface is

$$g_{\mathrm{surf}}(\phi) = 9.780327\left(1 + 0.0053024\sin^2\phi - 0.0000058\sin^2(2\phi)\right) \tag{1.55}$$

and the Earth's radius r_{e} at latitude ϕ is (NIMA 2000)

$$r_{\mathrm{e}}(\phi) = \frac{r_{\mathrm{eq}}(1-f)}{\sqrt{1-f(2-f)\sin^2\phi}} = \frac{r_{\mathrm{p}}}{\sqrt{1-\epsilon^2\cos^2\phi}}, \tag{1.56}$$

where $r_{\mathrm{eq}} = 6378.137$ km is the Earth's equatorial radius, $r_{\mathrm{p}} = 6356.7523142$ km is the Earth's polar radius, $f = (r_{\mathrm{eq}} - r_{\mathrm{p}})/r_{\mathrm{eq}} = 1/298.257223563$ describes the Earth's flattening, and $\epsilon = \left(\sqrt{r_{\mathrm{eq}}^2 - r_{\mathrm{p}}^2}\right)/r_{\mathrm{eq}}$ is the Earth's numerical eccentricity (NIMA 2000).

Figure 1.16 shows the RO and ECMWF dry pressure profiles as well as the ECMWF physical pressure profile as a function of MSL altitude (again in linear and in logarithmic space, left and middle panel). The pressure, which also decreases exponentially with height, equals to approximately 906 hPa at 0.6 km and to 2.8 hPa at an altitude of 40 km.

The systematic difference between RO and ECMWF dry pressure (green line in the right panel of Figure 1.16) increases from the surface to approximately 22 km, where it yields its maximum value of approximately +0.6 %. It becomes smaller above 22 km, above 33 km it even becomes negative. This southern high latitude profile reveals the difference between physical and dry pressure (shown in light blue) being negligible above 6 km altitude where the water vapor content is small. Below 6 km altitude, however, water vapor partial pressure yields physical pressure being smaller than dry pressure. Therefore, the difference (physical minus dry pressure) is negative. It amounts to approximately −0.4 % near the surface.

In order to clarify the difference between physical and dry pressure, Figure 1.17 depicts this difference as a function of latitude (South Pole to North Pole) and altitude (surface up to 14 km) exemplarily for January 2005. Left panel shows

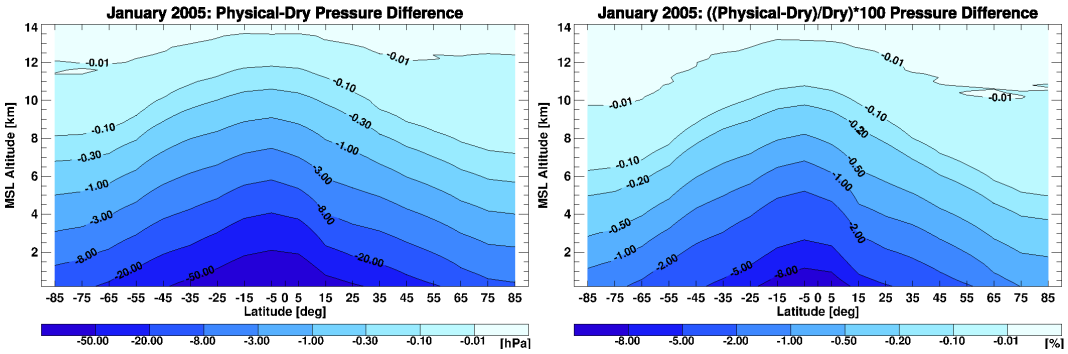

Figure 1.17: Difference between physical and dry pressure as a function of latitude and altitude. Absolute difference (in hPa, left panel) and relative difference (in %, right panel) are estimated from ECMWF data.

absolute differences given in hPa, the right panel depicts relative differences, given in %. Above 13 km at low latitudes and above approximately 10 km at high latitudes, the difference between physical and dry pressure is negligible (smaller than 0.01 %). At tropical latitudes near the surface, where water vapor content is largest, the difference between physical and dry pressure exceeds 8 %.

Derivation of Dry Temperature

Dry temperature is obtained by utilizing the ideal gas law:

$$T_{\mathrm{dry}}(h) = \frac{M_{\mathrm{dry}}}{R} \frac{p_{\mathrm{dry}}(h)}{\rho_{\mathrm{dry}}(h)}. \tag{1.57}$$

The temperature profile is smoothed by a Blackman window filter (cf. Equation 1.49) to eliminate numerical noise.

Vertical profiles of RO and ECMWF dry temperature and ECMWF physical temperature are depicted in Figure 1.18. Temperature does not decrease exponentially with height. It decreases from the Earth's surface to the tropopause (here at approximately 9 km), where minimal temperatures are recorded. In the stratosphere, however, the availability of ozone assures an increase of atmospheric temperature. The systematic difference between the RO and the co-located ECMWF dry temperature profile is slightly positive up to 21 km and negative above. The difference between physical and dry temperature remains smaller than 3 K.

Physical temperatures are always warmer than dry temperatures as long as water vapor content is not negligible. Figure 1.19 shows this relation as a function of latitude and altitude. It can be noticed that at altitudes above 9 km (polar summer)

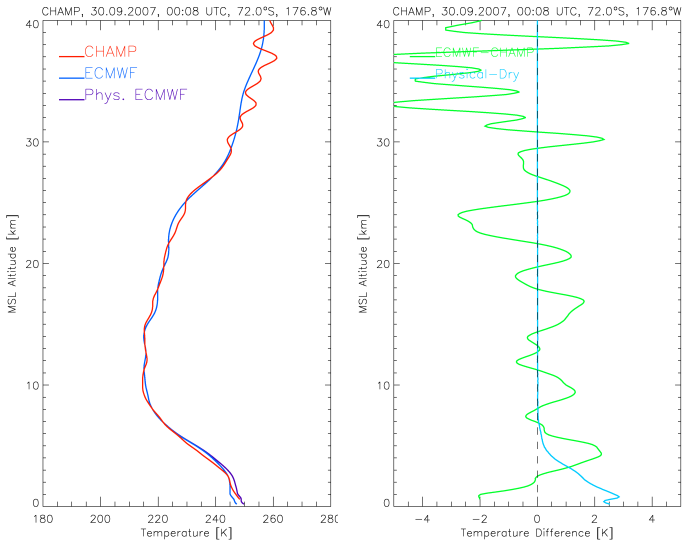

Figure 1.18: RO and ECMWF dry temperature and ECMWF physical temperature profiles as a function of MSL altitude (left). The systematic difference between RO and ECMWF dry temperature as well as between ECMWF physical and dry temperature are depicted in the right panel.

and 13 km (tropics) the difference is always below 0.1 K. In the tropical lower troposphere, however, it exceeds 30 K.

Derivation of Dry Geopotential Height on Dry Pressure Levels

The geopotential height can be calculated from

$$Z(h) = \frac{1}{g_{45}} \int_0^h g(\phi, h') \mathrm{d}h', \tag{1.58}$$

where $g_{45} = 9.80665\ \mathrm{m/s^2}$ is the mean acceleration of gravity at sea level at $\phi = 45°$ (Tyler 2001). Geopotential height itself is a non-meteorological parameter. However, it is possible to specify geopotential height as a function of pressure levels. Measurements of geopotential height at constant pressure levels can be used e.g., for detecting global warming (cf. Wallace et al. 1993). For that reason, geopotential height is interpolated to standard pressure altitude levels (termed "pressure altitude"), defined by

$$\text{pressure altitude} = -H_0 \ln\left(\frac{p}{p_0}\right), \tag{1.59}$$

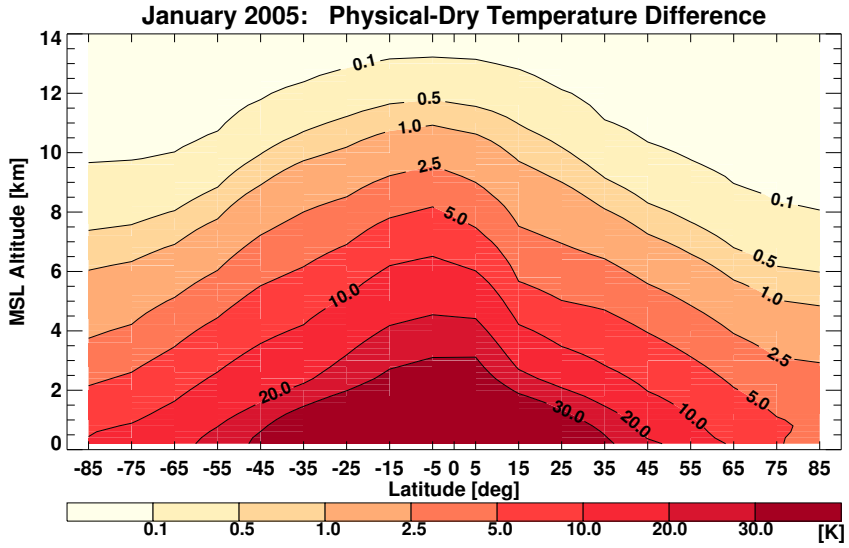

Figure 1.19: Difference between physical and dry temperature as a function of latitude and altitude estimated from ECMWF data.

where $H_0 = 7$ km is the tropospheric scale height, p is atmospheric pressure, and $p_0 = 1013.25$ hPa is the standard surface pressure.

Geopotential height as a function of pressure altitude and the systematic difference between the RO and ECMWF profile is shown in Figure 1.20. There is a nearly linear relationship between geopotential height and pressure altitude. The systematic difference between the RO and the ECMWF profile shows that ECMWF geopotential height is higher than RO geopotential height up to approximately 35 km and smaller above.

1.3.8 Quality Control

Quality checks are performed on a regular basis during the retrieval chain. Quality checks, which comprise technical aspects and data consistency, are called "internal" quality checks. Most of them are performed in the bending angle retrieval and have already been mentioned in the description of the corresponding retrieval steps. Not all quality checks performed during the retrieval affect the internal Quality Flag (QF) (e.g., the outlier removal of phase delay profiles).

"External" quality checks are applied to the retrieval results (refractivity and dry temperature profiles) where retrieved profiles are compared to co-located profiles extracted from ECMWF analysis fields with a T42L60 (until February 2006) or a T42L91 (since March 2006) resolution. Radio occultation refractivity profiles are

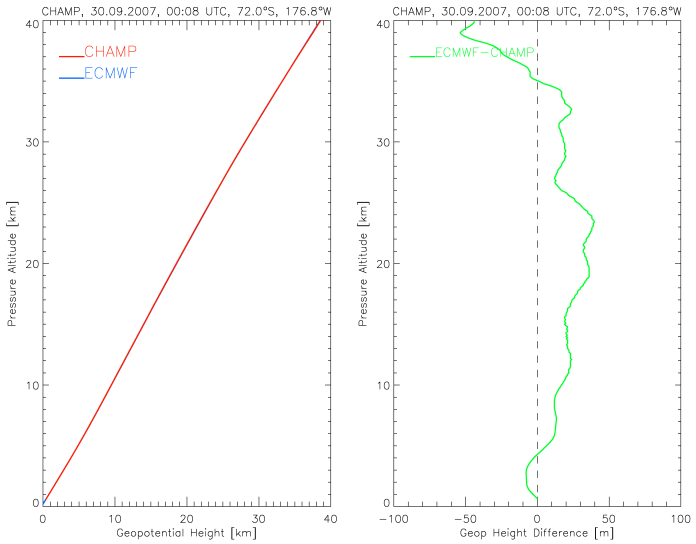

Figure 1.20: RO and ECMWF dry geopotential height profiles as a function of pressure altitude (left) and their systematic difference (right).

compared to co-located ECMWF refractivity profiles between 5 km and 35 km. RO profiles, which differ from co-located ECMWF profiles by more than 10 % (maximum allowed refractivity deviation) are assigned to a "bad" QF. Temperature profiles are checked between 8 km and 25 km. RO dry temperature profiles, which differ from co-located ECMWF profiles by more than 20 K (maximum allowed dry temperature deviation) are also assigned to a "bad" QF.

The quality flag is an integer number with two digits. The internal quality flag affects the one's place and the external quality flag affects the ten's place. Table 1.2 summarizes the internal QF and its meanings; Table 1.3 summarizes the external QF and its meanings. If, e.g., the QF is equal to 37 then the absolute value of the bending angle bias is larger than the estimated bending angle noise (internal QF = 7) and neither the temperature criterion nor the refractivity criterion is met (external QF = 30).

1.3.9 Reference to the Earth's Geoid

All atmospheric profiles are derived as a function of ellipsoidal height. The difference between the Earth's ellipsoid and the geoid amounts to −105 m south of India and 85 m around New Guinea. Atmospheric parameters derived by the OPSv54 retrieval are referenced relative to the Earth's geoid (i.e., MSL altitude) where

$$\text{MSL altitude} = \text{height} - \text{geoid undulation}. \tag{1.60}$$

Table 1.2: Internal quality flags and their meanings (modified from Gobiet (2005)).

internal QF	Meaning
QF = 0	All internal quality checks passed. Retrieval results are of high quality.
QF = 2	Less than 25 data points are available between 65 km and 75 km. The bending angle observational error was set to 50 μrad. Retrieval results should not be used (at least not above 25 km).
QF = 5	Negative (ionosphere-corrected) bending angles occur below 50 km. Profile is discarded, no useful results.
QF = 6	The bending angle noise is smaller than 0.5 μrad so that the observational error was set to 50 μrad or there are not enough data available to perform statistical optimization (i.e., no (useful) data available above 20 km impact height or no (useful) data available below 35 km impact height). Bending angle profile is not statistically optimized but it is used to derive refractivity and other atmosphere parameters. Retrieval results may not be used.
QF = 7	The absolute value of the bias is larger than the estimated bending angle noise. Bending angle profile is not statistically optimized but it is used to derive refractivity and other atmosphere parameters. Retrieval results may not be used.
QF = 8	The estimated bending angle noise is larger than 50 μrad. Bending angle profile is not statistically optimized but it is used to derive refractivity and other atmosphere parameters. Retrieval results may not be used.
QF = 9	The event is too short to yield a meaningful atmospheric profile (the event duration is shorter than 15 s) or there are no data available in PLL mode or there are no (useful) data available above 20 km or impact parameters are increasing with decreasing altitude in the uppermost part of the profile. Profile is discarded, no useful results.

Table 1.3: External quality flags and their meanings (modified from Gobiet (2005)).

external QF	Meaning
QF = 10	The difference between the retrieved RO temperature profile and the co-located ECMWF analysis temperature profile is larger than 20 K somewhere between 8 km and 25 km. Retrieval results may not be used.
QF = 20	The difference between the retrieved RO refractivity profile and the co-located ECMWF analysis refractivity profile is larger than 10 % somewhere between 5 km and 35 km. Retrieval results may not be used.
QF = 30	The profile does neither satisfy the temperature criterion nor the refractivity criterion. Retrieval results may not be used.
QF = 50	There are not enough data available to perform external quality control. Retrieval results may not be used.

The geoid undulation is extracted from a $3.75° \times 3.75°$ latitude-longitude grid and interpolated to the mean RO event location. If averaged over a lot of RO profiles between 50°E and 110°E (Indian Ocean), the difference between profiles, which are referenced to the geoid and those referenced to the ellipsoid amounts up to 0.3 K at low latitudes from 10 km to 14 km. If averaged over a lot of profiles between 110°E and 170°E (New Guinea), the difference amounts to −0.4 K at low latitudes from 10 km to 14 km altitude (Borsche 2008).

1.3.10 Derivation of Tropopause Parameters

The Lapse Rate Tropopause (LRTP) and the Cold Point Tropopause (CPTP) are determined from retrieved dry temperature profiles. The LRTP is found as the lowest level at which the lapse rate of the profile decreases to 2 K/km or less. Furthermore, the lapse rate average between that level and 2 km above has to be less than 2 K/km (WMO 1957). The CPTP is determined as the coldest point (local minimum) of the temperature profile (Highwood and Hoskins 1998). Because the stratosphere at high latitudes can be very cold (in particular in polar winter), the CPTP is technically defined to be lower than 20 km and higher than the LRTP (Borsche 2008).

The LRTP altitude of the RO profile depicted in Figure 1.18, amounts to 8.9 km (T = 215.6 K). The CPTP altitude of that profile is detected at 9.9 km (T = 214.6 K). The corresponding values for the ECMWF profile are 8.2 km (T = 217.3 K) and 11.0 km (T = 215.3 K) for the LRTP and CPTP, respectively.

Schmidt et al. (2004) and Borsche et al. (2007) performed a study on tropopause

characteristics at low latitudes investigating RO data from the CHAMP satellite. Schmidt et al. (2005) analyzed thermal tropopause parameters on a global basis utilizing RO data of the CHAMP and the Satélite de Aplicaciones Científicas C (SAC-C) satellite.

1.4 Beyond OPSv54: Further Improvements

The challenges of the OPS retrieval version beyond OPSv54 are

1. Use of FORMOSAT-3/COSMIC (F3C) Open Loop (OL) data and integration of a WO retrieval (Gorbunov 2002);
2. Integration of a moist air retrieval, i.e., a 1-Dimensional Variational (1D-Var) retrieval (Healy and Eyre 2000) to retrieve also physical atmospheric parameters and water vapor.
3. A new bending angle retrieval, which utilizes data of different satellites in a more transparent way;

While the new bending angle retrieval is only theoretically constructed, the integration of OL data, the implementation of the WO retrieval, and the 1D-Var retrieval are already implemented in the End-to-End Generic Occultation Performance Simulation and Processing System (EGOPS) software to a large extend.

1.4.1 F3C Open Loop Data and Wave Optics Retrieval

The OPSv54 retrieval is not able to handle phase delay data received in OL mode but the GPS receivers aboard the F3C satellites record GPS signals in the PLL mode only down to approximately 8 km and in the OL mode below.

Michael Gorbunov implemented a preprocessing of phase delay data received in OL mode. With these additional data, F3C measurements can be used down to the Earth's surface. The WO retrieval, which has also been implemented by Michael Gorbunov uses both, PLL and OL input data.

The OPSv55 retrieval output is a combined GO and WO bending angle profile. The blending of the GO and the WO bending angle is done with a half Gaussian transition somewhere between 7 km and 13 km impact height; the Gaussian half width amounts to 1.5 km.

Figure 1.21 shows the minimal impact height of all F3C/FlightModel (FM)-1 measurements recorded on September 5, 2007. Data, which have been obtained from GO retrieval are derived only with PLL data, whereas the WO retrieval uses both, PLL and OL data. WO bending angles stop at approximately 2 km impact height, which corresponds to the Earth's surface. The lower limit of GO bending angles

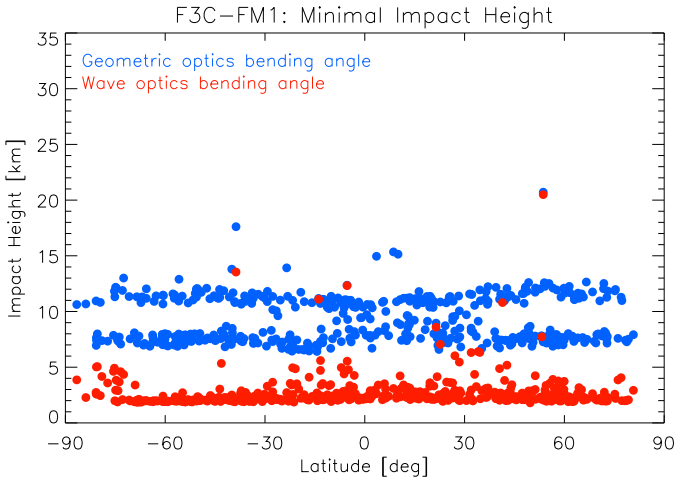

Figure 1.21: Minimal impact height of bending angle profiles. Data stem from one day of F3C/FM-1 data (September 5, 2007). GO bending angles (GO retrieval uses only phase delay data received in PLL mode) are compared to WO bending angles (retrieval also utilizes OL input data). WO bending angles stop at approximately 2 km impact height, which corresponds to the Earth's surface.

varies between 8 km for F3C setting occultation events and 12 km impact height for F3C rising occultation measurements.

1.4.2 Moist Air Retrieval (1D-Var)

Atmospheric profiles of physical temperature, physical pressure, and humidity (moist atmospheric quantities) can be retrieved applying a 1D-Var retrieval. It utilizes the measured refractivity or bending angle profile y_{obs}, the a priori knowledge of the state of the atmosphere (i.e., a background profile) x_{bg}, and their associated errors (i.e., observation and background covariance matrices, $\mathbf{O}$ and $\mathbf{B}$, respectively). The 1D-Var minimizes of a quadratic cost function J (GRAS SAF 2009)

$$J(x) = \frac{1}{2}\left(x - x_{\text{bg}}\right)^{\text{T}} \mathbf{B}^{-1}\left(x - x_{\text{bg}}\right) + \frac{1}{2}\left(y_{\text{obs}} - \mathbf{H}[x]\right)^{\text{T}} \mathbf{O}^{-1}\left(y_{\text{obs}} - \mathbf{H}[x]\right) \quad (1.61)$$

to retrieve the physical atmospheric state x. $\mathbf{H}[x]$ is the forward modeled observation. The GRAS/Satellite Application Facility (GRAS-SAF) developed the Radio Occultation Processing Package (ROPP), which also includes a 1D-Var retrieval. Current EGOPS developments include this ROPP 1D-Var software in the WEGC OPS retrieval.

1.4.3 New Bending Angle Retrieval

The aim of the new bending angle retrieval is to perform best for all RO data of different satellites but also for simulated RO and microwave (X/K band) measurements. It will be not implemented in the OPSv55 but in a later version of the OPS retrieval.

The improvements may comprise, but are not limited to:

- Atmospheric phase delay profiles will be analyzed and prepared in a more sophisticated way. This includes an enhanced method to detect outliers in the raw phase delay profile and new filter techniques (a Blackman-Window-Sinc filter and a Hamming-Window-Sinc filter in addition to the regularization filter), which will be established to filter phase delay profiles. Windowed-Sinc filters are known to be very stable. Also a new treatment of background profiles at phase level will be included.
- These improvements (i.e., the enhanced phase delay data preparation) should be sufficient to eliminate the artificial correction of the bending angle observational error (i.e., observational errors, which are set to 10 μrad or 50 μrad). This is one weakness of the OPSv54 retrieval.
- An extended search for the favored bending angle background at the level of statistical optimization, which should depend on the users needs.

1.5 Characteristics of Radio Occultation

The measurement principle itself, the use of microwave signals, and the specifications of the satellite orbits, which have been used for RO measurements so far, determine the characteristics of RO measurements and account for their potentials to be used for atmospheric sciences such as numerical weather prediction or climate monitoring.

Self-calibration and long-term stability: The information used in the retrieval process is not the phase profile itself, but the phase delay relative to the phase measured above the atmosphere. For that reason, the single assumption to call the measurement "self-calibrating" is that the atmosphere has to be stable within the measurement time of one or two minutes. This self-calibrating characteristics also implies that the measurements are long-term stable and do not contain biases or drifts. This feature is particularly important for RO data to be used for climate monitoring purposes since data of different satellites can be combined without the need of inter-calibration (Foelsche et al. 2008*b*).

Penetration of clouds and independence of sunlight: The frequency domain used for GNSS-signals enables measurements to be performed during virtually all

weather conditions. This comes true because the signals are able to penetrate through most of the clouds and the measurement, the excess phase delay, is not significantly degraded by clouds. In tropical regions, however, where atmospheric humidity is large, atmospheric multipath causes a severe degradation of the signal, which cannot be handled by a simple GO retrieval (need of a WO retrieval). Furthermore, GPS signals are not affected by the presence or absence of sunlight so that measurements can be performed during day and night.

Accuracy: The accuracy of RO measurements depends on the instruments quality (e.g., thermal receiver noise), ionospheric and atmospheric conditions (e.g., residual ionospheric errors, water vapor ambiguity, or atmospheric multipath errors), accuracy of orbit determination, horizontal drift of the tangent point, and inversion procedures (e.g., initialization errors of the Abelian integral) (Kursinski et al. 1997). Between 8 km and 30 km altitude, the temperature error is less than 1 K even in worst case scenarios (see Figure 1.22). As discussed by Kursinski et al. (1997), contributions from initialization errors of the Abelian integral, thermal noise, local multipath, and residual ionosphere limit the accuracy of temperature profiles at high altitudes. At low altitudes (especially at equatorial latitudes) the accuracy is limited by the uncertainty in water abundance.

Vertical and horizontal resolution: Limb sounding measurements are characterized by a high vertical but low horizontal resolution. The same holds true for RO measurements. The GO vertical resolution is limited by the diameter of the first Fresnel zone, which decreases with height. It amounts to about 1.4 km in the stratosphere and about 0.5 km near the Earth's surface. The horizontal resolution amounts to about 300 km (Kursinski et al. 1997).

Global coverage: The orbit's inclination of GPS satellites is fixed at $i = 55°$. For that reason, the inclination of the LEO satellite determines the geographical coverage of RO measurements. The higher the inclination of the satellites' orbit, the higher the latitudes which can be reached by RO measurements. Until now, RO measurements have only been performed by nearly polar orbiting satellites (with an inclination of at least 72°). The distance of the RO event to the LEO satellite is determined by the altitude of the LEO satellite (cf. Subsection 1.3.2). Satellites with orbit inclinations of 72° and 800 km orbit altitude are able to perform measurements at polar latitudes. So far, global coverage of RO events has been achieved by all RO missions.

Thus, GPS occultations offer independent, very precise, and accurate measurements of the UTLS region with a high vertical resolution. Measurements, which are available globally, are long-term stable and data, provided by different satellites, can be

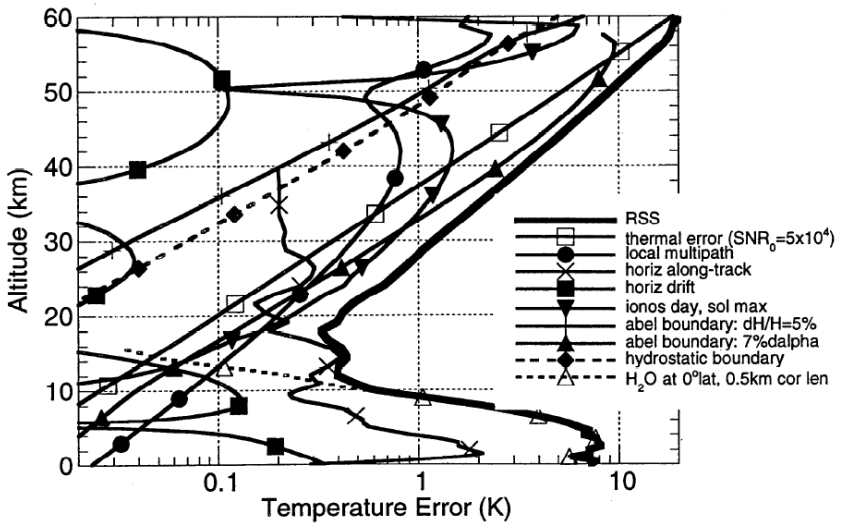

Figure 1.22: Summary of dry temperature errors as a function of altitude. Errors are found under daytime, solar maximum ionosphere conditions. Temperature accuracies are found to be better than 1 K between 8 km and 30 km altitude (from Kursinski et al. (1997)).

combined without the need of inter-calibration so that they can be used for global climate monitoring on a long-time scale.

1.6 Summary of Radio Occultation Retrieval

At the WEGC, University of Graz, the main utilization of RO data is to perform climate monitoring. Even though measurements are very accurate, precise, and long-term stable, atmospheric climatologies derived from different satellites can only be reasonably compared if the retrieval follows exactly the same algorithm. All data used in the following chapters of this thesis are derived from OPSv54. For this reason the main retrieval steps of OPSv54 are summarized in a flowchart shown in Figure 1.23; for a tabular summary see also Steiner et al. (2009).

Input data of the WEGC retrieval are provided by other data centers. They contain atmospheric phase delay and precise orbit information as a function of time. Currently most of these data are provided by UCAR/CDAAC, Colorado (CO), United States of America (USA) (all except MetOp-A data, which are provided by EUMETSAT and a selected set of CHAMP data, which is provided by GFZ).

After some plausibility checks and smoothing with a regularization filter, measurement data are used to derive atmospheric Doppler (time derivative of excess

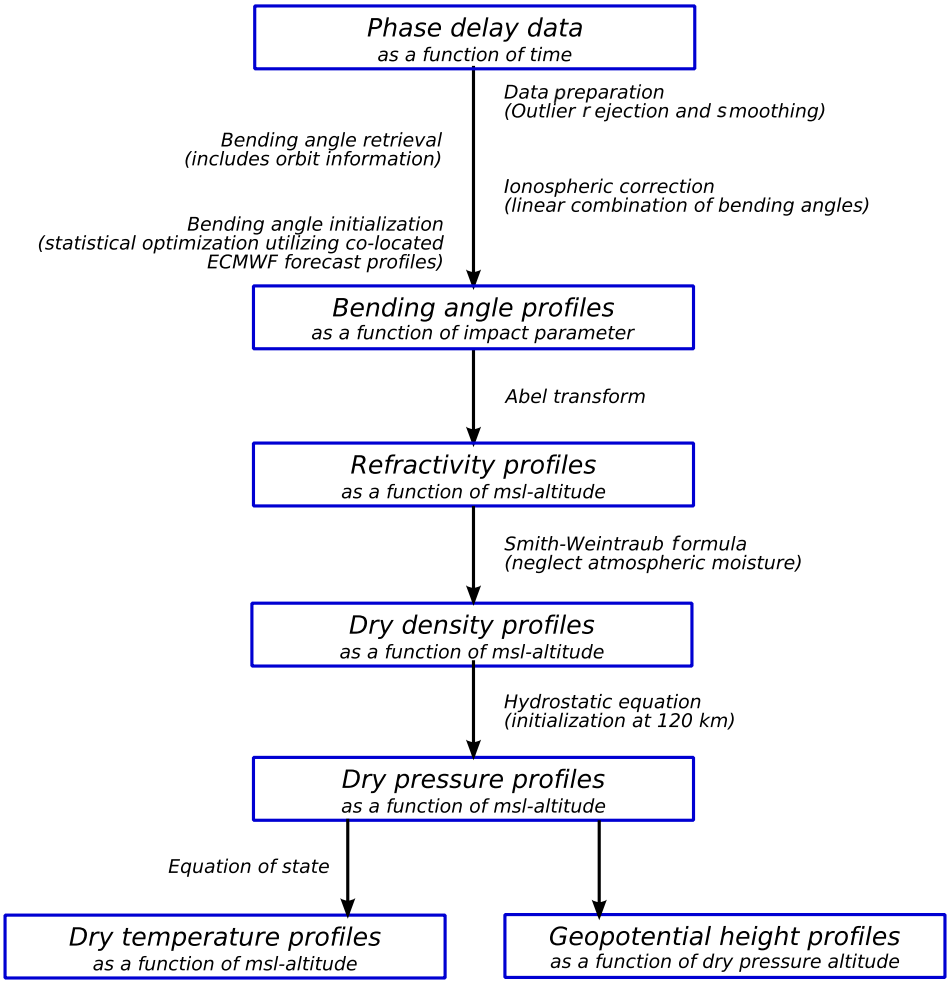

Figure 1.23: Summary the RO retrieval algorithm of the OPSv54 retrieval.

phase delays) as a function of time. Atmospheric Doppler profiles and orbit information (satellite positions are referred to the center of refraction) are utilized to calculate atmospheric bending angle profiles as a function of impact parameter. The retrieval utilizes the GO approach. The ionospheric influence on the measurement is removed by applying an ionospheric correction, where low-pass filtered L1- and L2-bending angle profiles are linearly combined. The L1 high pass contribution is added again after ionospheric correction. Bending angles at high altitudes (from 30 km to 120 km) are statistically optimized with background information. For that purpose co-located bending angle profiles are extracted from ECMWF forecast fields. Above their top level, ECMWF data are pieced together with MSIS data. The statistical optimization is performed by inverse covariance weighting. The statistically optimized bending angle is used for further calculations. Atmospheric refractivity as a function of MSL altitude is obtained from bending angle by an Abel transform. Atmospheric moisture is neglected when calculating dry density profiles from atmospheric refractivity via the Smith-Weintraub formula ("dry air retrieval"). The hydrostatic integral, which is initialized at 120 km and the equation of state deliver dry pressure and dry temperature profiles, respectively, both as a function of MSL altitude. Profiles of geopotential height as a function of dry pressure altitude are derived from interpolating the non-meteorological parameter geopotential height to pressure altitude. Additional retrieval results, such as tropopause parameters, are calculated subsequent to the retrieval algorithm.

Quality checks are performed regularly during the retrieval chain. Data are checked for technical aspects and data consistency. Furthermore, retrieved refractivity and dry temperature profiles are compared to co-located ECMWF analysis profiles. Data are considered reliable if RO and ECMWF refractivity profiles do not deviate by more than 10 % between 5 km and 35 km. Dry temperature profiles are checked between 8 km and 25 km. Data pass quality control if RO and ECMWF temperatures deviate by less than 20 K in that altitude range.

2 Characteristics of Radio Occultation Data from Different Satellite Missions

2.1 Radio Occultation Satellite Missions and Data Centers

The application of Radio Occultation (RO) on the Earth was established with the Global Positioning System/Meteorology (GPS/MET) mission onboard the Microlab-1 satellite in 1995 (Ware et al. 1996). The satellites Oersted (Escudero et al. 2001) and SUNSAT (Stellenbosch UNiversity SATellite) (Mostert and Koekemoer 1997), which were launched onboard the same rocket in 1999, had severe technical problems with their RO receivers and very little useful data was generated (Luntama 2009). From 2000 to 2002 four more RO satellite missions have been launched. While CHAMP (CHAllenging Mini-Satellite Payload) (Wickert et al. 2001), SAC-C (Satélite de Aplicaciones Científicas C) (RO instrument GOLPE, GPS Occultation and Passive reflection Experiment) (Hajj et al. 2002), and GRACE (Gravity Recovery And Climate Experiment) (Wickert et al. 2005) had/have their atmospheric focus on tropospheric and stratospheric measurements, the Ionospheric Occultation Experiment (IOX) mission onboard PICOSat focused on the ionosphere. In 2006 the first multi-satellite RO mission (FORMOSAT-3/COSMIC (F3C), six platforms, instrument GOX, GPS Occultation Experiment) and the first operational RO mission (MetOp-A (Meteorological Operational), GRAS (GNSS Receiver for Atmospheric Sounding)) have been launched. Since June 2007 the Terra Synthetic Aperature Radar (TerraSAR-X) satellite, which carries a GPS RO receiver is in orbit (Wickert et al. 2009). The Indian satellite Oceansat-2 has been launched in September 2009. Its instrument ROSA (Radio Occultation Sounder for Atmospheric Studies) will also perform RO measurements. Table 2.1 lists these—past and active—RO satellite missions and shows data availability at the Wegener Center for Climate and Global Change (WEGC).

Table 2.1: Past and active RO satellites missions tabulated according to their date of launch. Data availability at WEGC is given in the third column, the last column indicates the current status of the mission.

Spacecraft/Instrument	Launch	Data at WEGC	Status (Mar. 2010)
Microlab-1/GPS/MET	Apr. 3, 1995	1995, 1997	Decommissioned
Oersted	Feb. 23, 1999	–	Decommissioned
SUNSAT	Feb. 23, 1999	–	Decommissioned
CHAMP	Jul. 15, 2000	2001 to 2008	Inactive
SAC-C/GOLPE	Nov. 21, 2000	2001, 2002	Active
PICOSat/IOX	Sep. 29, 2001	–	Decommissioned
GRACE	Mar. 17, 2002	since 2007	Active
F3C/GOX	Apr. 15, 2006	since 2006	Active
MetOp-A/GRAS	Oct. 19, 2006	test data set	Active
TerraSAR-X	Jun. 15, 2007	–	Active
Oceansat-2/ROSA	Sep. 23, 2009	–	Comm. Phase

2.1.1 Radio Occultation Data Centers

Depending on the center conducting these satellite missions and on data level[1], data are archived at and distributed from different data centers:

- German Research Centre for Geosciences (GFZ) provides CHAMP, GRACE, and TerraSAR-X RO data (level 0 to level 2) (`http://isdc.gfz-potsdam.de/`).
- Jet Propulsion Laboratory (JPL)/Global Environmental & Earth Science Information System (GENESIS) (`http://genesis.jpl.nasa.gov`) disseminates RO data from CHAMP, GRACE, SAC-C (level 0 to level 2), and F3C (level 1 and level 2).
- University Corporation for Atmospheric Research/COSMIC Data Analysis and Archive Center (UCAR/CDAAC) provides RO level 0 to level 2 data of GPS/MET, CHAMP, SAC-C, GRACE, and the F3C satellites (`http://cosmic-io.cosmic.ucar.edu/cdaac/`).
- Data from the GRAS instrument onboard MetOp are disseminated by the European Organization for the Exploitation of Meteorological Satellites (EUMET-

[1] Data levels distinguish between raw measurement data (level 0), phase delay and orbit data (level 1), retrieved atmospheric parameter profiles (level 2), and derived climatological products (level 3). Note that this definition may differ from definitions used by individual data centers, see e.g., Löscher et al. (2009).

SAT) (levels 0 and 1) and by GRAS/Satellite Application Facility (GRAS-SAF) (levels 2 and 3) (`http://www.grassaf.org/`).

- The WEGC uses excess phase delay profiles and orbit information (level 1 data) provided by other data centers and performs its own RO inversion retrieval. Atmospheric profiles (level 2) and climatological products (level 3) of GPS/MET, CHAMP, SAC-C, GRACE, and F3C are disseminated by `https://www.globclim.org/`.

2.1.2 Radio Occultation Data Utilized at WEGC

To derive profiles of bending angle, refractivity, or temperature, the WEGC Occultation Processing System (OPS) uses excess phase delay profiles and orbit information provided by other data centers. Even though the RO technique itself is self-calibrating, different data processing schemes yield differences in atmospheric RO data products, which cannot be neglected (Ao et al. 2003; Engeln 2006; Löscher et al. 2009). For that reason WEGC Occultation Processing System Version 5.4 (OPSv54) uses atmospheric phase delay and orbit information provided by UCAR/CDAAC for all satellites except for MetOp, whose level 1 data are only provided by EUMETSAT. Systematic differences in level 1 processing are investigated applying the OPSv54 retrieval to a selected set of GFZ level 1 data as well.

GPS/MET: The first RO experiment was the GPS/MET "proof-of-concept" mission. UCAR/CDAAC now disseminates GPS/MET data with data version 2007.3200. The previous data version, also available at WEGC, was 2005.1720. Data are available for four measurement periods (prime times), April/May 1995, June/July 1995, October 1995, and February 1997, when Anti-Spoofing (AS)[2] was turned off. Data with data version 2007.3200 are also available for AS on periods but up to now these data have not been utilized at WEGC.

Only a small number of profiles is available from April 1995 until July 1995 (only 19 days with available RO data; on average 53 high quality profiles per day). The average number of high quality profiles per day in October 1995 and February 1997 (in total 29 days with RO data) amounts to 85. The GPS receiver onboard GPS/MET recorded setting occultations only.

CHAMP: The research satellite CHAMP is operated by GFZ Potsdam, Germany. Amongst other scientific instruments, it carries a GPS receiver and performs setting RO measurements. The RO instrument has been activated for the first time on February 11, 2001 (Wickert et al. 2001). Nearly continuous measurements are available from September 2001 until early October 2008, with a gap

[2] AS is the encryption of the Precision code (P-code) of GPS signals. When AS was turned on the signal quality was significantly degraded.

of about 6 weeks in July/August 2006. The CHAMP data set constitutes the first long-term record of RO measurements, which can be used for climatological studies (Steiner et al. 2009).

Up to retrieval version Occultation Processing System Version 5.3 (OPSv53) WEGC used input data provided by GFZ, since retrieval version OPSv54 WEGC operationally uses data provided by UCAR/CDAAC. The OPSv54 retrieval utilizes UCAR/CDAAC data versions 2007.1200 (May 19, 2001 to May 30, 2007), 2007.1700 (June 1, 2007 to July 31, 2007), and 2007.3200 (August 1, 2007 to October 4, 2008).

SAC-C: The SAC-C mission is an international project between Argentina (Comisión Nacional de Actividades Espaciales (CONAE)), the United States of America (USA) (National Aeronautics and Space Administration (NASA)), and other partners from Europe and South America. WEGC utilizes RO data provided by UCAR/CDAAC, data versions 2005.3090 (August 13, 2001 to October 14, 2002) and 2005.1720 (November 3, 2002 to November 15, 2002).

GRACE: GRACE is a joint project between the USA (NASA) and Germany (German Center for Air and Space Flight (Deutsches Zentrum für Luft und Raumfahrt (DLR)). The mission consists of two "twin" satellites (GRACE-A and GRACE-B), which are separated by about 220 km. The main focus of this mission lies on gravity field measurements but both satellites also carry a GPS RO receiver.

Continuous activation of GRACE-A measurements began on May 22, 2006. GRACE-B performed occultation measurements only on July 28, 2004 and July 29, 2004 (Wickert et al. 2005; Wickert et al. 2006) and in a short period between September 23, 2005 and September 30, 2005 (Wickert et al. 2009).

WEGC uses GRACE-A data delivered by UCAR/CDAAC (data versions 2007.3200 until May 31, 2009 and 2009.2650 since June 1, 2009). UCAR/CDAAC data are available since November 27, 2006 (WEGC uses data since March 1, 2007, when data stream became continuous). Even though both GRACE satellites are able to perform rising and setting occultation measurements, all data currently available at WEGC stem from setting occultations of GRACE-A. The data stream is expected to continue until at least 2013 (Wickert et al. 2009).

F3C: The F3C satellite constellation is a joint science mission between Taiwan and the USA (Rocken et al. 2000; Wu et al. 2005; Anthes et al. 2008). The constellation consists of six spacecraft (FlightModel (FM)), whose orbit planes are separated by about 30°. All satellites perform rising and setting RO measurements. The F3C constellation can track more than 2500 RO events per day.

Data are available since April 21, 2006 but UCAR/CDAAC strongly recommends not to use data before July 13, 2006 (because of different receiver firmware

versions (CDAAC Team 2010)). WEGC utilizes data since August 2006. UCAR/CDAAC data versions are 2007.3200 (until March 31, 2009) and 2009.2650 (since April 1, 2009). The F3C satellites are expected to perform measurements until 2013.

MetOp: MetOp-A is the first of three almost identical MetOp satellites. The satellites will be launched in a time interval of about 5 years. MetOp-A has been launched in October 2006, MetOp-B and MetOp-C will be launched in 2011 and 2016, respectively. Each satellite carries the same type of GPS receiver (a GRAS receiver), (Loiselet et al. 2000; Luntama 2006). The GRAS instrument has two rising and two setting channels, which means that it is able to perform two rising and two setting occultation measurements simultaneously. More than 600 occultation events can be tracked per day. High quality data of the MetOp series are expected to be delivered until 2020.

At WEGC, phase delay and orbit data of MetOp-A are available only from a nonofficial "test data set" from September 30, 2007 until October 31, 2007. This data set has been processed in offline-mode (C. Marquardt, EUMETSAT, pers. comm.) with processing version 0.6 (Marquardt 2009). Due to a small bug in the code, this GRAS level 1 prototype record does not contain any L2 excess phase delay of rising occultation measurements. For that reason WEGC utilizes only setting GRAS measurements. In general, bending angle profiles and derived atmospheric parameters are currently available at GRAS-SAF.

Figure 2.1 shows all data available at WEGC from 1995 to 2008. The long-term record of CHAMP data together with that of GPS/MET can be used for climate trend analyses (Steiner et al. 2009). With the launch of F3C in 2006 the number of available RO data has increased by a factor of ten, which enables RO data to be used not only for global climate studies but also for smaller-scale or even regional climate investigations.

2.2 Validation of Data Quality of a Selected Set from Each Satellite

The reliability of estimated atmospheric climate trends strongly depends on data quality. Even though the RO technique features high accuracy and high precision it is not possible to completely remove ionospheric effects in the neutral atmospheric retrieval. Since the ionospheric correction in the retrieval process only yields elimination of first order ionosphere terms, the ionosphere residual is larger during high solar activity than during low solar activity.

Furthermore, data quality is affected by the receiver quality and by the procedure applied to correct for potential clock errors. The latter is performed differently for

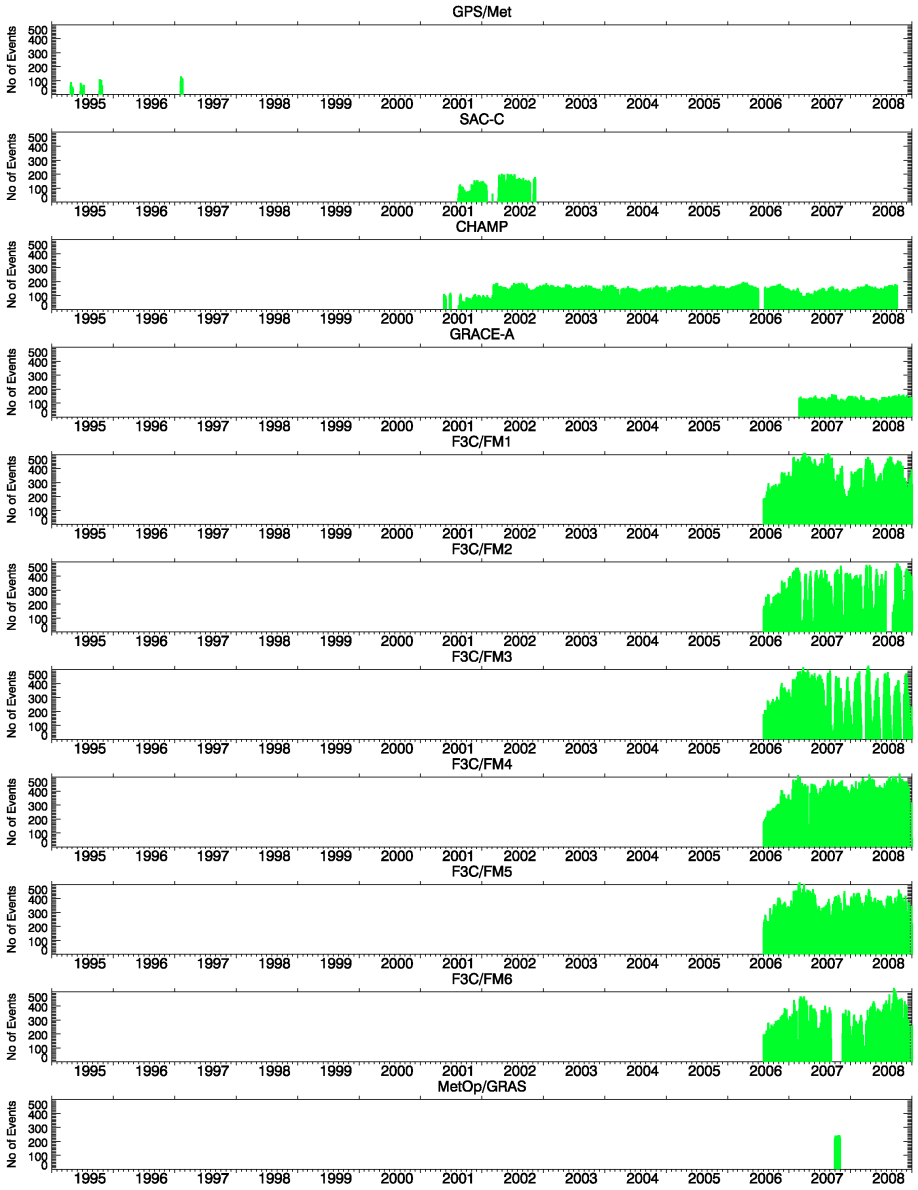

Figure 2.1: Number of high quality measurements derived from different RO satellites on a daily basis from 1995 to 2008. The total number of measurements significantly increased in 2006, when additional measurements performed by the six F3C satellites became available.

GPS/MET and GFZ CHAMP data (double differencing), for SAC-C, CDAAC CHAMP, and F3C data (single differencing), and for GRACE and MetOp data (zero-differencing) (W. Schreiner, UCAR, pers. comm. October 2009).

In this section the quality of a selected set of RO data is assessed. Quality flag statistics in general and data quality at high altitudes (between 50 km and 80 km) in particular are analyzed together with characteristics of refractivity and temperature data.

2.2.1 Overview of the Data Sets

The quality of RO data measured onboard GPS/MET, SAC-C, CHAMP, GRACE-A, F3C, and MetOp-A is analyzed. GPS/MET and SAC-C data are available for 1995/1997, and for 2001/2002, respectively. No RO data other than GPS/MET are available in 1995/1997. However, to give a first impression of data quality at same solar activity (same residual ionospheric noise), SAC-C data from September 2002 are compared to CHAMP data from September 2002. Data from CHAMP, GRACE-A, F3C, and MetOp-A are compared for September 2007. Since F3C/FM-6 did not provide any data from September 9, 2007 until November 13, 2007 (CDAAC Team 2010), F3C data are only investigated from FM-1, FM-2, FM-3, FM-4, and FM-5. The impact of level 1 processing on data characteristics is analyzed applying the OPSv54 retrieval to two different CHAMP records: one provided by GFZ and the other one provided by UCAR/CDAAC. Both data sets are taken exactly from the same period in 2007 (September 29, September 30, and October 1).

Table 2.2 gives an overview of all data analyzed in this section. To get a representative ensemble of profiles, data from GPS/MET, SAC-C, CHAMP, and GRACE-A are analyzed for three consecutive days (e.g., data from September 29, September 30, and October 1). F3C and MetOp-A data are only used from one single day. For September 30, 2007 EUMETSAT delivers 641 MetOp-A measurements recorded in Phase Locked Loop (PLL)-mode. Since 301 rising profiles do not contain any L2 phase delay, only 340 MetOp-A measurements are utilized in the WEGC retrieval.

2.2.2 Quality Flag Statistics

Assessment of data quality is applied on input data (technical aspects) within the retrieval at bending angle level (Internal Quality Control (IQC)), and after computation of atmospheric parameters where retrieved profiles of refractivity and temperature are compared to co-located profiles from European Centre for Medium-Range Weather Forecasts (ECMWF) analysis fields (External Quality Control (EQC)). Table 2.3 yields an overview of the number of retrieved profiles, which can be somewhat smaller than the number of input data (Table 2.2) because of retrieval failures. Furthermore, the number of high quality profiles and the number of profiles flagged

Table 2.2: Overview of selected data sets provided by each satellite. Investigated periods and the total number of available phase delay profiles are given in the second and third column.

Satellite	Investigated Period	Total number of input data
GPS/MET	Oct 12, 1995 to Oct 14, 1995	443
SAC-C	Sep 29, 2002 to Oct 1, 2002	537
CHAMP (CDAAC)	Sep 29, 2002 to Oct 1, 2002	653
CHAMP (GFZ)	Sep 29, 2007 to Oct 1, 2007	408
CHAMP (CDAAC)	Sep 29, 2007 to Oct 1, 2007	582
GRACE-A	Sep 29, 2007 to Oct 1, 2007	506
F3C/FM-1	Sep 30, 2007	449
F3C/FM-2	Sep 30, 2007	560
F3C/FM-3	Sep 30, 2007	275
F3C/FM-4	Sep 30, 2007	553
F3C/FM-5	Sep 30, 2007	558
MetOp-A	Sep 30, 2007	641 (340)

"bad" by IQC and/or EQC are given in Table 2.3.

The percentages of QF = 0 profiles ("good") and QF $\neq$ 0 profiles ("bad") refer to the number of retrieved profiles and not, as may be expected, to the number of OPS input data (phase delay profiles). This results in hardly any difference for GPS/MET, SAC-C, CHAMP, and GRACE because only few measurements cannot be retrieved. However, the more frequent failure of the retrieval of F3C measurements yields a significantly lower percentage of high quality profiles if it is referred to the number of input data. It decreases from 64.5 % to 57.5 % (FM-1), from 77.5 % to 68.9 % (FM-2), from 72.5 % to 60.4 % (FM-3), from 74.0 % to 65.5 % (FM-4), and from 79.7 % to 73.8 % (FM-5).

GRACE-A achieves the "best" QF statistics as more than 80 % of all data are of high quality. "Worst" QF statistics is achieved from F3C/FM-1. On average, about 70 % of all profiles, retrieved with the OPSv54 retrieval are of high quality.

It is clearly noticeable that most profiles are flagged bad by both, the internal QF and the external QF (last column). The reason is that bending angle profiles with internal QF $= 5, 6, 7, 8, 9$ are not statistically optimized. Instead of the statistically optimized bending angle, the raw bending angle is used to derive atmospheric refractivity and other atmospheric profiles. Hence, it is not surprising that the retrieved refractivity and dry temperature profiles do not match EQC requests.

MetOp data almost all fail due to IQC (80.3 %). 46 of these 98 profiles are flagged

Table 2.3: Quality flag statistics of the selected data sets provided by each satellite. Results are obtained from the OPSv54 retrieval.

Satellite	Retr. profiles	QF = 0 profiles	QF ≠ 0 profiles	IQC only	EQC only	IQC & EQC
GPS/MET	442	321 (72.6 %)	121 (27.4 %)	12	1	108
SAC-C	537	354 (65.9 %)	183 (34.1 %)	2	2	179
CHAMP (CDAAC)	653	436 (66.7 %)	217 (33.3 %)	22	5	190
CHAMP (GFZ)	408	283 (69.4 %)	125 (30.6 %)	22	6	97
CHAMP (CDAAC)	581	390 (67.1 %)	191 (32.9 %)	33	4	154
GRACE-A	505	410 (81.2 %)	95 (18.8 %)	14	10	71
F3C/FM-1	400	258 (64.5 %)	142 (35.5 %)	6	5	131
F3C/FM-2	498	386 (77.5 %)	112 (22.5 %)	18	13	81
F3C/FM-3	229	166 (72.5 %)	63 (27.5 %)	7	3	53
F3C/FM-4	489	362 (74.0 %)	127 (26.0 %)	18	3	106
F3C/FM-5	517	412 (79.7 %)	105 (20.3 %)	18	6	81
MetOp-A (setting)	340	218 (64.1 %)	122 (35.9 %)	98	2	22

bad because the number of data points between 65 km and 75 km is smaller than 25 (QF = 2). Probably, data of an operational MetOp processing will overcome that problem. However, 50 MetOp-A profiles are flagged bad because the absolute value of the bias is larger than the estimated bending angle noise (QF = 7). This reflects the superior quality of the MetOp-A receiver and the "insufficiency" of the OPSv54 retrieval to cope with such high data quality. To exploit the full potential of MetOp data, future generations of the OPS retrieval have to deal with such a data quality in a more appropriate manner.

2.2.3 Bending Angle Quality

Bending angle quality is validated from bending angle bias, bending angle noise, observational error, and zRAER50 values (impact height, where retrieval to apriori error ratio equals 50 %, cf. Chapter 1). Only high quality profiles (QF = 0) are used for bending angle validation. The bending angle bias and bending angle noise estimated between 65 km and 80 km impact height is shown in Figure 2.2 and Figure 2.3 (a zoom to -1 μrad to 5 μrad) as a function of geographic latitude. In both figures, the bending angle bias is depicted in gray, bending angle noise is colored in red, green, and blue according to its magnitude.

As can be seen in Figure 2.2, MetOp-A bending angle quality is superior to all the other satellite data. More than 95 % of all MetOp-A data exhibit a bending angle noise smaller than 5 μrad. Also GPS/MET bending angle data have very small noise

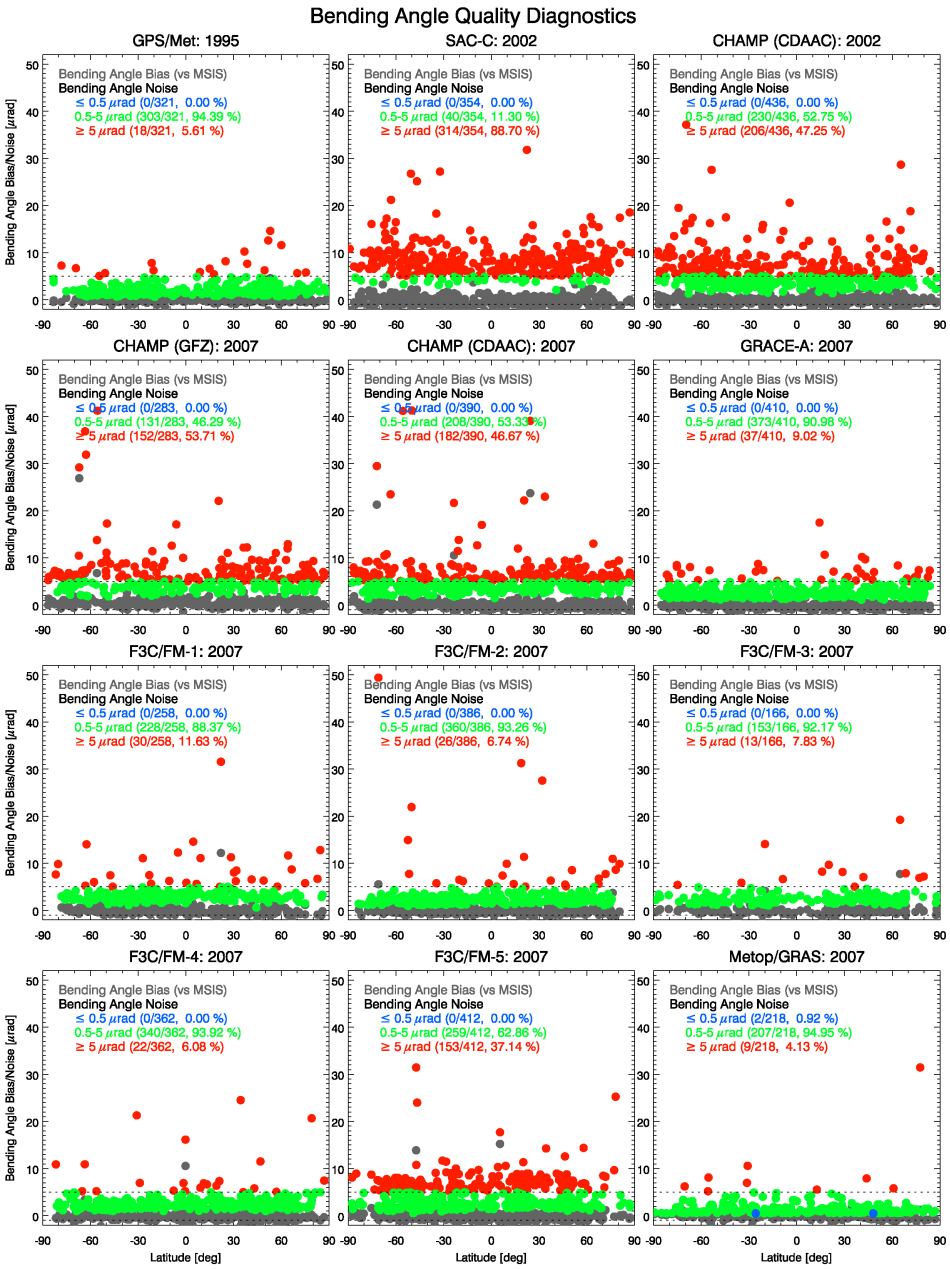

Figure 2.2: Bending angle bias and bending angle noise as a function of geographic latitude. Profiles with large data noise >5 μrad are colored in red, profiles with data noise between 0.5 μrad and 5 μrad are depicted in green, and profiles with very small bending angle noise, $\leq$0.5 μrad, are plotted in blue.

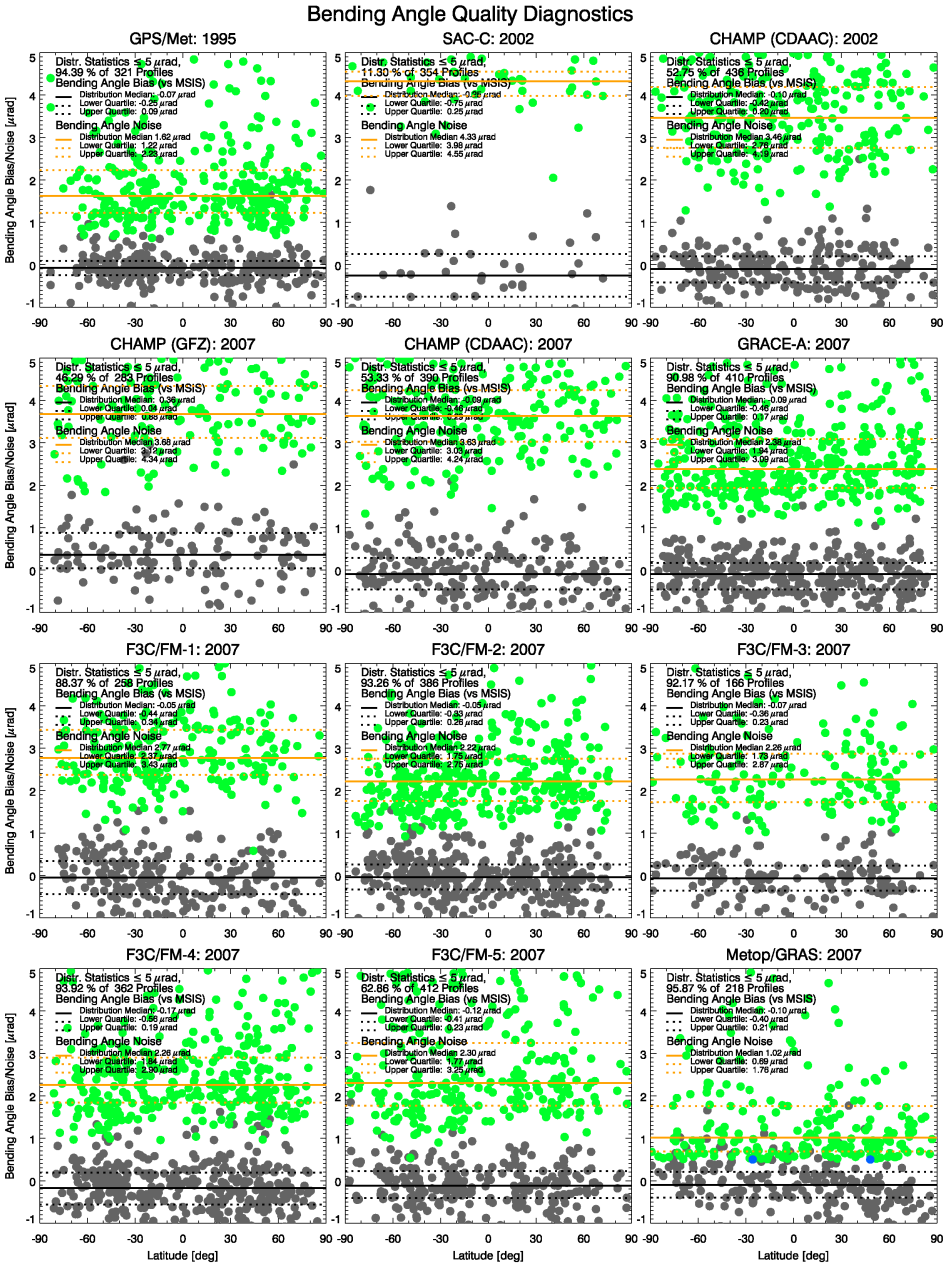

Figure 2.3: Bending angle statistics as a function of latitude for all RO data, same as Figure 2.2 but zoom into -1 μrad to 5 μrad. Colors have the same meaning as in Figure 2.2.

(data stem from "prime times"). F3C data do not show consistent measurement noise: 94 % of all FM-4 data feature bending angle noise smaller than 5 μrad but only 68 % of all FM-5 data exhibit such small bending angle noise. GRACE-A bending angles have similar characteristics as FM-2 and FM-3 bending angles. CHAMP data noise is similar in 2002 and 2007, less noise is observed for CDAAC CHAMP data than for GFZ CHAMP data. Worst quality is found for SAC-C data: only 11 % of all SAC-C data have bending angle noise smaller than 5 μrad.

Figure 2.2 reveals that neither the bending angle bias nor bending angle noise show any dependency on geographic latitude. Figure 2.3 confirms this independence from geographic latitude showing the same data as Figure 2.2 but zoomed in the range between -1 μrad and 5 μrad.

For climate applications it is very important that the bending angle bias is close to zero and very similar for all satellites (Foelsche et al. 2008*a*). This is actually true as can be seen from Figure 2.3. The bending angle bias relative to MSIS (Mass Spectrometer and Incoherent Scatter Radar) data is negative for nearly all satellites (median of the bias is between -0.05 μrad and -0.25 μrad). There is one single satellite record, which exhibits a positive bias (median of bias: $+0.36$ μrad). Since it concerns the CHAMP data set, whose level 1 processing has been done by GFZ, it reflects the impact of level 1 processing on the bending angle bias. Note that the medians of bending angle bias and bending angle noise are calculated only from those profiles whose bending angle noise is smaller than 5 μrad.

MetOp-A data exhibit the smallest bending angle noise (median: 1.02 μrad). This estimated bending angle noise is larger than that published, e.g., by Marquardt et al. (2009). The reason is that measurement profiles with bending angle noise smaller than 0.5 μrad and measurement profiles with a larger bending angle bias than bending angle noise are rejected (bad quality flag) in the OPSv54 retrieval. This low noise level seemed to be unrealistically small (we learned from MetOp-A data that this was a misapprehension). Two blue dots correspond to MetOp-A profiles, whose bending angle noise approximates to 0.5 μrad. Deactivating most internal quality control mechanisms results in lower bending angle noise (0.76 μrad, Foelsche et al. 2009*c*).

Currently, our MetOp-A data are better than that of GPS/MET by a factor of 1.6 (median: 1.62 μrad), better than F3C and GRACE-A data by about a factor of 2.3, and better than CHAMP by a factor of 3.6. The median of the bending angle noise of SAC-C data amounts to 4.33 μrad.

Figure 2.4 depicts observational errors as a function of latitude for the same data sets. Remember that the observational error is equal to observed bending angle noise, but if this noise cannot be determined appropriately the observational error is adjusted. The only important adjustments in this context are: if negative bending angles occur between 55 km and 65 km impact height, the observational error is set to 10 μrad and if negative bending angles occur between 50 km and 55 km, the

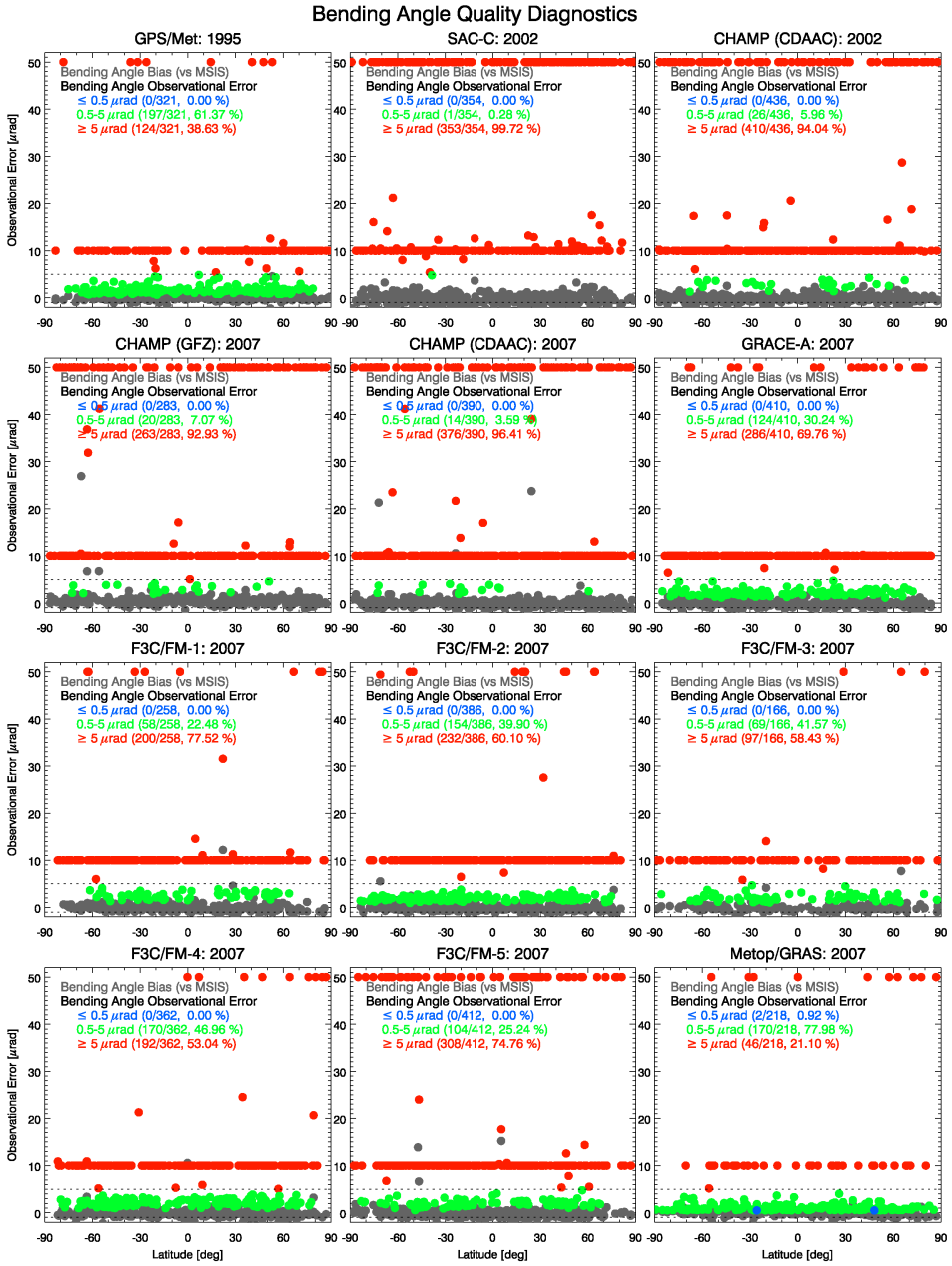

Figure 2.4: Bending angle bias and observational error as a function of geographic latitude. Colors have the same meaning as in Figure 2.2.

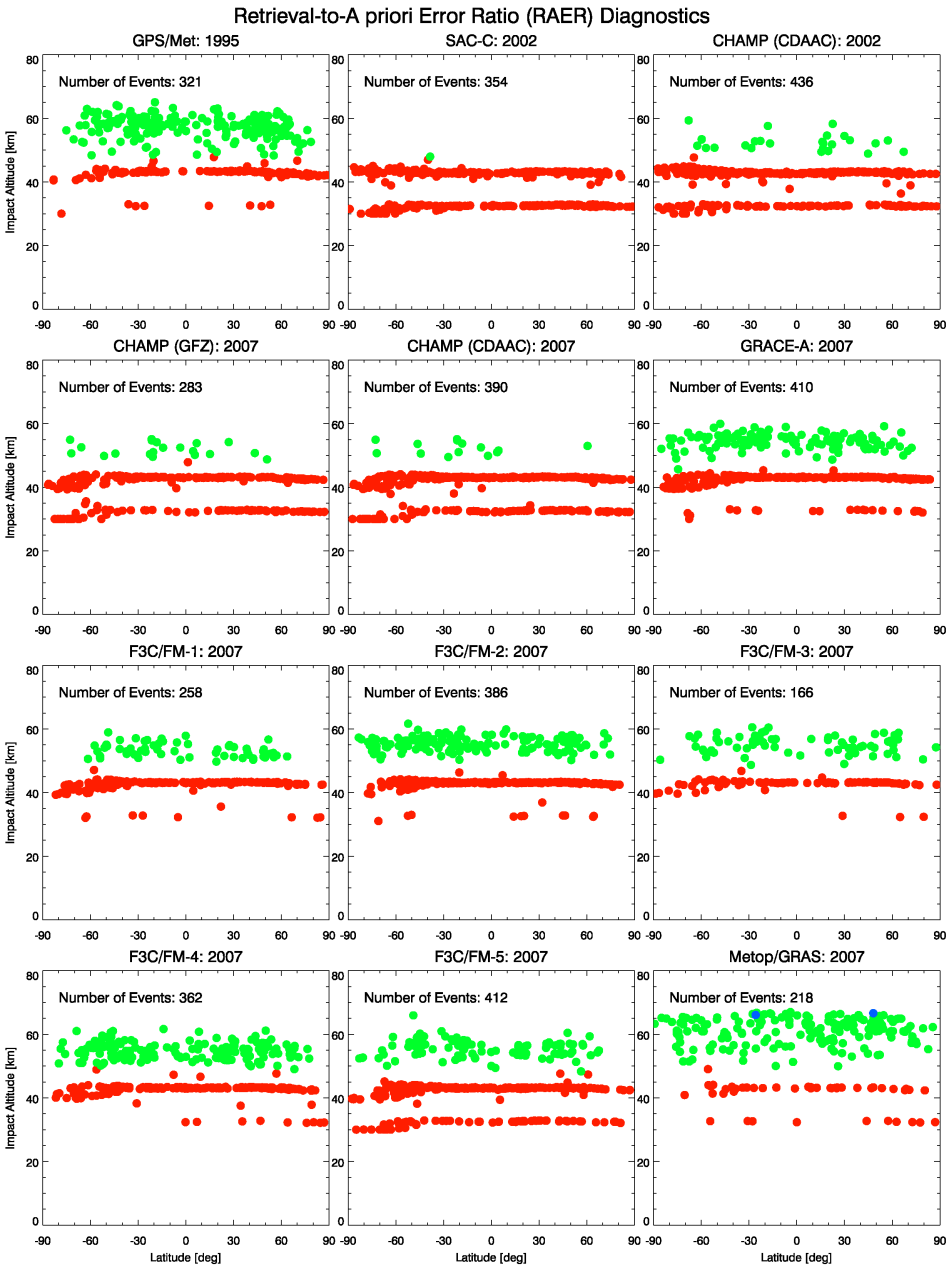

Figure 2.5: zRAER50 values as a function of geographic latitude. The correlation between the observational error and zRAER50 values is clearly revealed. Better data quality (smaller observational error) is reflected in higher zRAER50 values. The color corresponds to estimated observational errors shown in Figure 2.4

observational error is set to 50 μrad. Strict quality criteria approve high quality profiles only if the bending angle noise can be determined appropriately or one of these two constraints is applied. If the bending angle does not satisfy other quality criteria, the quality flag is set "bad".

After this Quality Control (QC), more than 90 % of all SAC-C and CHAMP data have observational errors larger than 5 μrad. The quality of the SAC-C receiver in September 2002 is worse: only one single SAC-C profile exhibits an observational error smaller than 5 μrad.

From September 29, 2007 to October 1, 2007, CDAAC provides about 40 % more CHAMP profiles than GFZ. However, less GFZ data are modified by IQC and there are more GFZ profiles with observational errors smaller than 5 μrad. The quality of GRACE-A, F3C, and MetOp-A data is better than that of CHAMP as less profiles have negative bending angles between 50 km and 55 km. MetOp-A data again show best quality (79 % of all MetOp-A profiles have observational errors smaller than 5 μrad).

Figure 2.5 shows zRAER50 values as a function of latitude. The color of the dots corresponds to the estimated observational errors shown in Figure 2.4. Profiles with very small observational errors ≤ 0.5 μrad have highest transition heights. As shown by Pirscher et al. (2007*a*) and Foelsche et al. (2009*c*), these zRAER50 values lie between 65 km and 75 km. Large observational errors (red dots) yield zRAER50 values to be as low as 30 km: observational errors of 50 μrad and 10 μrad correspond to zRAER50 values of about 30 km and 42 km, respectively.

High receiver quality of MetOp-A is reflected in highest zRAER50 values. Most MetOp-A profiles are observation dominated below 60 km whereas nearly all SAC-C profiles are background dominated down to 42 km. While background information begins to show up at altitudes of about 30 km when SAC-C and CHAMP data are used, this range is extended by more than 10 km using data from GRACE-A, F3C, and MetOp-A.

A remarkable feature is the latitude dependence of low zRAER50 values (red dots): at high southern latitudes these zRAER50 values are somewhat smaller than elsewhere. This characteristic may be due to the overestimated quality of ECMWF bending angles in winter polar regions. The error of the background profile was assumed to amount to 15 % of the background bending angle value, independent on latitude and altitude (cf. Chapter 1). Low temperatures in polar winter are associated with small bending angle values and for that reason with small bending angle errors. Since the error of the background bending angle is utilized in the Retrieval to Apriori Error Ratio (RAER) calculation process, it co-determines the zRAER50 value. The smaller the background bending angle error, the lower the associated zRAER50 because the profile is background dominated for a longer altitude range (Pirscher et al. 2007*a*).

Observational errors and zRAER50 values as shown in Figure 2.4 and Figure 2.5 are used in the inversion process of the operational OPSv54 retrieval. The historical

context of the OPS retrieval shows, that the retrieval was originally developed to perform best for CHAMP data. For that reason, some of the quality checks applied by IQC mechanisms may be obsolete for data other than CHAMP. In this way, the actual quality of GRACE-A, F3C, and MetOp-A data is currently not utilized to its full extent in the OPS retrieval.

2.2.4 Validation of Refractivity and Dry Temperature Profiles

Retrieved refractivity and dry temperature profiles are validated against co-located profiles provided by ECMWF. Except for GPS/MET, these co-located profiles are extracted from ECMWF analysis fields (with different vertical resolutions: 60 vertical levels in 2002 and 91 vertical levels in 2007). Since ECMWF analyses have been of comparatively bad quality in 1995 (see Chapter 3) ECMWF Re-Analysis (ERA)-40 data (Uppala et al. 2005) are used as reference to validate GPS/MET data quality.

The validation methodology is based on error characteristics of refractivity and dry temperature profiles. The difference profile is calculated for each corresponding pair of profiles:

$$\Delta x(z_j) = x_{\mathrm{RO}}(z_j) - x_{\mathrm{coloc}}(z_j), \tag{2.1}$$

where $\Delta x(z_j)$ denotes the difference of the retrieved profile x_{RO} and the co-located profile x_{coloc} at the altitude level z_j. The mean systematic difference $\overline{\Delta x(z_j)}$ is calculated by

$$\overline{\Delta x(z_j)} = \frac{1}{N(z_j)} \sum_{i=1}^{N(z_j)} \Delta x_i(z_j), \tag{2.2}$$

with $N(z_j)$ being the number of profiles at altitude level z_j. The number of profiles decreases with decreasing altitude because increasing humidity leads to atmospheric multipath and signal degradation.

The determination of the standard deviation of the difference profiles $\sigma(z_j)$ is based on

$$\sigma(z_j) = \sqrt{\frac{1}{N(z_j)-1} \sum_{i=1}^{N(z_j)} \left(\Delta x_i(z_j) - \overline{\Delta x(z_j)}\right)^2}. \tag{2.3}$$

The Root Mean Square (RMS) error profile is derived from

$$\mathrm{RMS}(z_j) = \sqrt{\overline{\Delta x(z_j)}^2 + \sigma(z_j)^2}. \tag{2.4}$$

The statistics is calculated for all profiles available between 90°S and 90°N.

Validation of Refractivity Profiles

Due to the roughly exponential decrease of refractivity with height, refractivity differences are shown in terms of relative quantities, which are derived by dividing the absolute quantities by the mean of all reference profiles at each altitude level. The decreasing number of profiles available at low altitudes causes some "abnormal" oscillations below 5 km, which are therefore not interpretable.

Figure 2.6 depicts the refractivity validation results of the selected satellite subsets. Systematic differences are displayed in green, standard deviations in gray, and RMS errors in black.

The first obvious peculiarity is that GPS/MET refractivity profiles feature a totally different systematic difference to ECMWF than the other satellites. It oscillates around zero only between 7 km and 14 km altitude but is persistently negative above. Largest deviations (-1.4 %) are found above 31 km. However, the systematic differences do not necessarily reflect defective retrieved profiles but result from deficiencies in the reference data set (analysis or reanalysis fields; different vertical resolution of the reference data sets). The reference profiles, which have been extracted from ERA-40 fields, exhibit significant biases within selected parts of the atmosphere (Randel et al. 2004).

Systematic differences between SAC-C/CHAMP RO data and ECMWF analyses in September/October 2002 look very similar. They are negative nearly everywhere below 38 km altitude and positive above. Two peaks occur close to 16 km and close to 35 km altitude, where the systematic difference comes close to or even exceeds -0.5 %. Standard deviations are also in good agreement for both satellite data. Its minima are located at 12 km (SAC-C) and at 13 km (CHAMP), above and below that level it increases. A local maximum can be found close to 16 km, where the systematic difference also shows a prominent peak.

Systematic differences of the other satellite data relative to ECMWF analyses in September/October 2007 show a significantly smoother behavior compared to the other investigated periods. Systematic differences are persistently negative and amount to approximately -0.3 % nearly everywhere. The difference between GFZ CHAMP and CDAAC CHAMP allows to estimate the impact of different level 1 processing on refractivity profiles. While GFZ CHAMP data show positive systematic differences already above 30 km, the other data set features positive systematic differences above approximately 38 km. Therefore, the impact of level 1 processing is largest at high altitudes. It is negligible below 20 km.

The standard deviation and the RMS error show a maximum between 15 km and 17 km. In September 2007 it is most pronounced in FM-2 data where it almost exceeds 1.0 %. In FM-5 and GRACE-A the RMS error yields 0.7 % to 0.8 %. CHAMP, FM-3, FM-4, and MetOp-A data do not show any special feature in that height region. The reason for the large standard deviation is unknown at the current stage and has

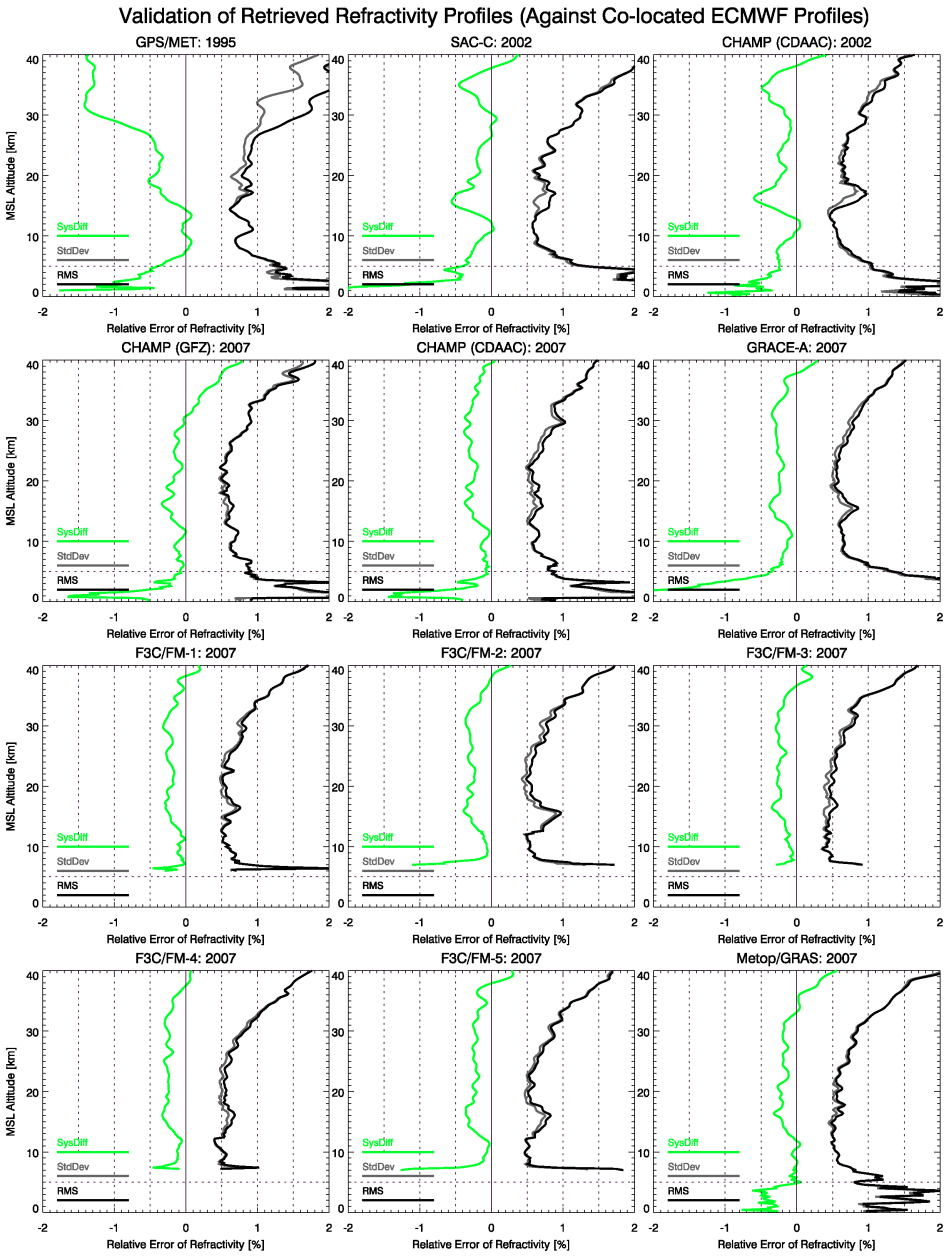

Figure 2.6: Refractivity validation results using the standard OPSv54 processing of a selected set from each satellite. Systematic differences (green), standard deviations (gray), and RMS errors (black) of the retrieved RO data vs. co-located reference profiles from the ERA-40 reanalyses/ECMWF analyses.

to be investigated in detail in a further study.

Validation of Dry Temperature Profiles

Dry temperature profiles are retrieved from refractivity profiles so that systematic differences between RO and ECMWF dry temperature reflect similar features to refractivity systematic difference but with different sign and somewhat different vertical structure (more details about the correlation of systematic differences of retrieved atmospheric parameters are given in Chapter 3).

Figure 2.7 shows dry temperature validation results. Compared to the other satellite data, GPS/MET dry temperature profiles again exhibit the largest systematic difference to ECMWF analyses. It is negative between 7 km and 29 km, where it amounts up to 1 K and positive above 30 km, exceeding 3.5 K at 40 km. As already mentioned in the last subsection, these huge systematical differences are mainly attributable to the ERA-40 validation data set.

Global mean RO temperature profiles of SAC-C and CHAMP in September/October 2002 are in good correspondence with ECMWF analyses (systematic differences smaller than 1 K) below approximately 33 km. Deviations relative to ECMWF are largest at approximately 38 km, where they exceed 2 K (CHAMP).

In 2007, the systematic differences of the RO satellite data relative to ECMWF are smaller than in 1995 and 2002. Systematic differences rarely exceed 1 K, and always stay smaller than 1.5 K. Largest deviations are observed between MetOp-A and ECMWF, where they exceed 1 K at 31 km. CHAMP, GRACE-A, and F3C data are in better agreement with ECMWF than MetOp-A.

Since MetOp-A data are of better quality, observation information is of higher importance for statistical optimization as compared to the other satellite data. The larger systematic difference of MetOp-A and ECMWF therefore points at the smaller degree of background information remaining in MetOp-A data at lower altitudes.

CHAMP systematic differences are similar to F3C but larger fluctuations are due to the smaller number of data going into the statistical calculation. GFZ CHAMP data feature a larger systematic difference relative to ECMWF than UCAR/CDAAC CHAMP data. While the systematic difference between GFZ CHAMP and ECMWF data is persistently positive above 13 km, it is persistently positive above 23 km between UCAR/CDAAC CHAMP and ECMWF.

Standard deviations and the RMS error of MetOp-A are slightly larger than for CHAMP, GRACE-A, and F3C but show similar characteristics.

2.3 Temporal Evolution of Data Quality

Section 2.2 showed some remarkable features of data quality of selected data sets provided by each satellite. However, since it is possible that some of these features

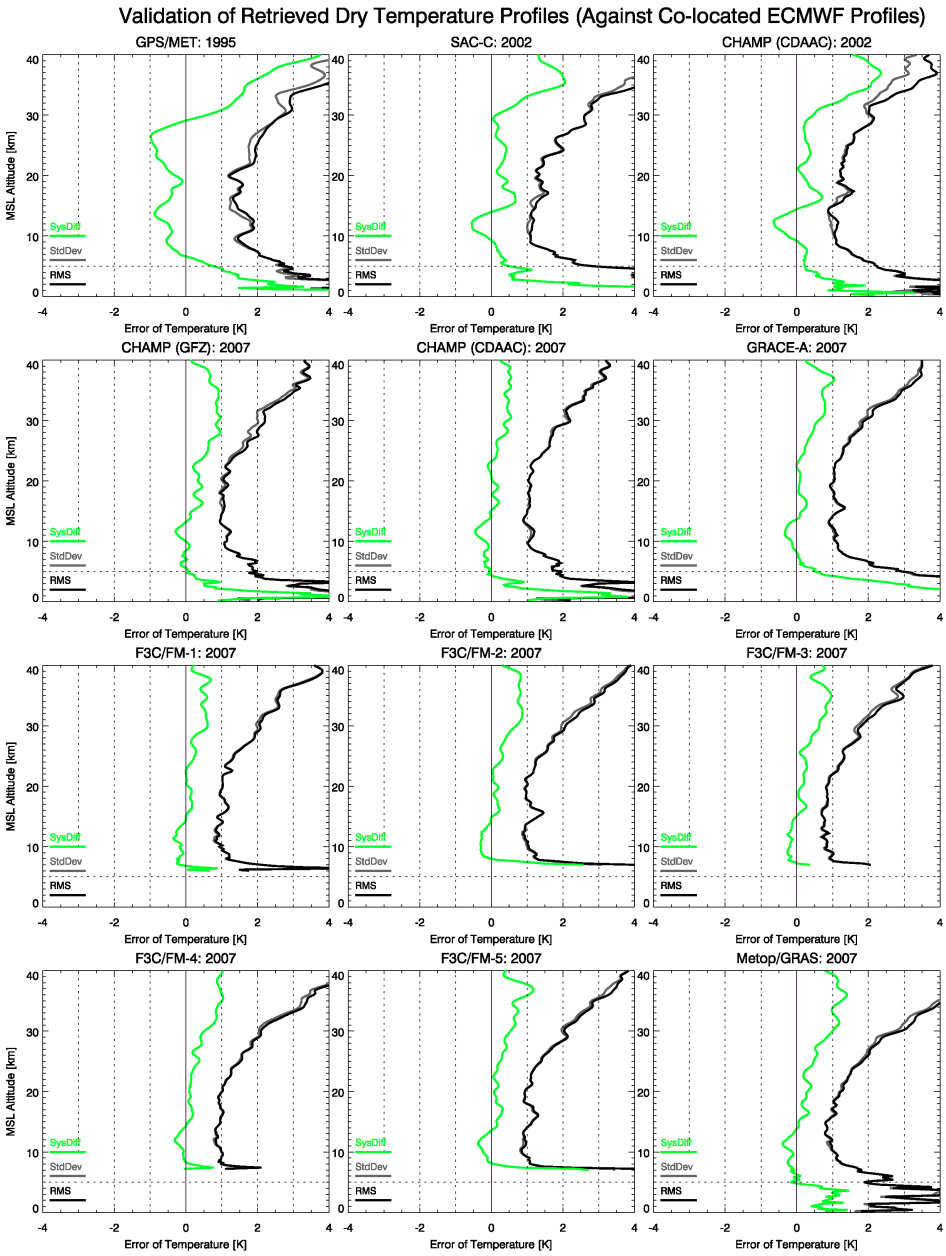

Figure 2.7: Dry temperature validation results using the standard OPSv54 processing of a selected set from each satellite. Systematic differences (green), standard deviations (gray), and RMS errors (black) of the retrieved RO data vs. co-located reference profiles from the ERA-40 reanalyses/ECMWF analyses.

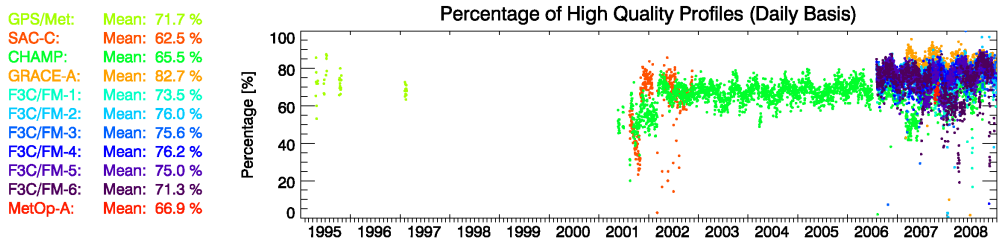

Figure 2.8: Percentage of high quality profiles as a function of time (1995 to 2008).

do not systematically occur in all data sets, the temporal evolution of the whole RO record available at WEGC is analyzed. The investigated period extends from 1995 to 2008.

2.3.1 Temporal Evolution of Quality Flag Statistics

The temporal evolution of the daily average percentage of high quality profiles (QF = 0) from 1995 to 2008 is shown in Figure 2.8. Different satellite data are depicted in different colors, the corresponding temporal mean is given on the left hand side of the panel. The percentage refers to the total number of profiles retrieved with the OPSv54 retrieval. Note, that given values somewhat overvalue the performance of F3C because of retrieval crashes and MetOp-A statistics only refers to setting occultations.

The temporal evolution of data quality mainly confirms the results obtained from selected data sets (Table 2.3). The highest percentage of high quality profiles is available from GRACE-A, which yields more than 80 % high quality profiles. The percentage of high quality profiles of F3C amounts to 71 % to 76 %. While the F3C/FM-1 statistics is better for the whole FM-1 record (73.5 % high quality profiles compared to 64.5 % high quality profiles on September 30, 2007) opposite behavior is observed for FM-5 (79.7 % high quality profiles on September 30, 2007, but only 71.3 % high quality profiles for the whole FM-5 record). Within intermittent periods in 2007 and 2008, FM-6 delivered comparatively many atmospheric measurements with bad data quality. The percentage of high quality profiles of GPS/MET, MetOp-A, CHAMP, and SAC-C amounts to approximately 72 %, 67 %, 66 %, and 62 %, respectively, which corresponds to the results obtained in Section 2.2.

2.3.2 Temporal Evolution of Bending Angle Quality

The temporal evolution of bending angle quality is investigated from the median of the bending angle bias (statistics is performed on a daily basis, i.e., uses all QF = 0 profiles available within one day), the median of bending angle noise, and the mean of the observational error used within statistical optimization.

Figure 2.9 shows the temporal evolution of the median of the bending angle bias relative to MSIS (top) and the solar radio flux (bottom) from 1995 to 2008. The solar radio flux is correlated with solar activity and therefore with solar Ultraviolet (UV) radiation and the level of ionization in the Earth's atmosphere at high altitudes.

The bending angle bias is slightly negative and very similar for all satellites. The temporal average value is largest for SAC-C (-0.18 μrad) and smallest for MetOp-A (-0.09 μrad in October 2007), GRACE-A, and GPS/MET (-0.11 μrad). Data from SAC-C, which is operated as "testbed" satellite, show largest temporal variability. The bending angle bias of all F3C satellites averages to -0.14 μrad (exception: F3C/FM-1 with -0.15 μrad). These numbers are larger than median values given in Figure 2.3. The reason is that here the median is calculated from all QF $= 0$ profiles available within one day, but in Figure 2.3 the median is calculated only from those profiles, whose bending angle noise is smaller than 5 μrad.

A closer look at the temporal evolution of the bending angle bias and the solar radio flux[3] reveals that there may be a correlation between both parameters. While the CHAMP bending angle bias slightly decreases from 2001 to 2008 the solar radio flux significantly decreased. However, due to large data variability the mathematical correlation is not significant. It also seems that an annual cycle is superimposed on the bending angle bias. The absolute value of the bias is larger during northern hemisphere winter than during northern hemisphere summer. This characteristic is noticeable in all satellite data but has to be investigated in more detail in a future study.

To better understand the nature of different RO records, Figure 2.10, top panel, depicts the temporal evolution of bending angle noise. Temporal mean values are again shown on the left hand side of the panel.

While smallest bending angle noise is found for MetOp-A (0.98 μrad), it is largest for SAC-C (5.13 μrad) and for CHAMP (4.66 μrad). As already noticed in the temporal evolution of the bending angle bias, SAC-C data quality varies significantly with time. While comparatively good data quality is obtained from October 2001 to July 2002 it is bad in from August 2001 until September 2001 and from August 2002 until November 2002.

CHAMP bending angle noise was smallest at the beginning of the observation period (until March/April 2002). After an update of the software onboard CHAMP in March 2002 (J. Wickert, GFZ, pers. comm. November 2009) the bending angle noise increased from approximately 3.5 μrad to 5 μrad, afterward it remained comparatively constant with time. However, from March to May 2007 it significantly increased to approximately 7 μrad. During this period there have been no updates

[3] Daily-mean solar radio flux at 10.7 cm wavelength. The F10.7 index is given in solar flux units (1 sfu $= 10^{-22}$ W/(m^{2}Hz)). F10.7 data are available from the National Geophysical Data Center at `ftp://ftp.ngdc.noaa.gov/STP/SOLAR_DATA/SOLAR_RADIO/FLUX/DAILYPLT.ADJ`, (October 2009).

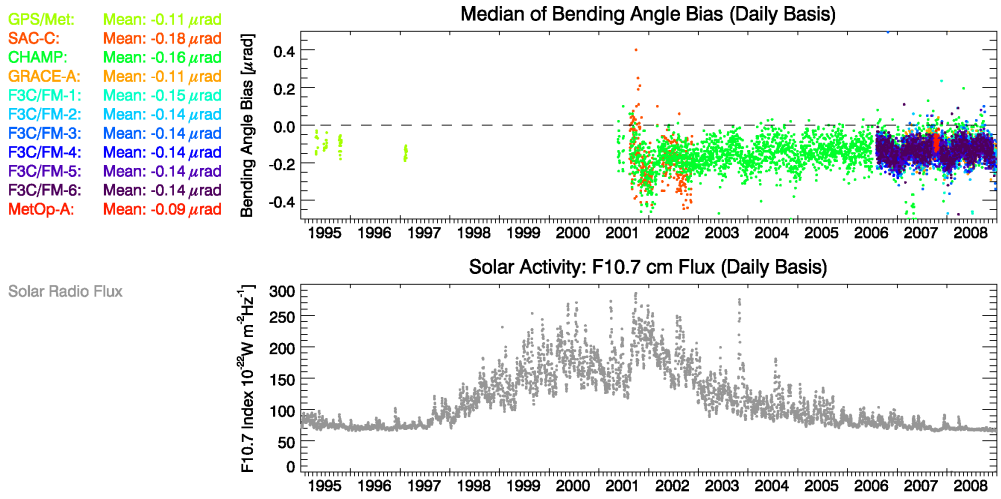

Figure 2.9: Time series of the daily median bending angle bias of different satellite data (top) and solar radio flux (bottom) from 1995 to 2008.

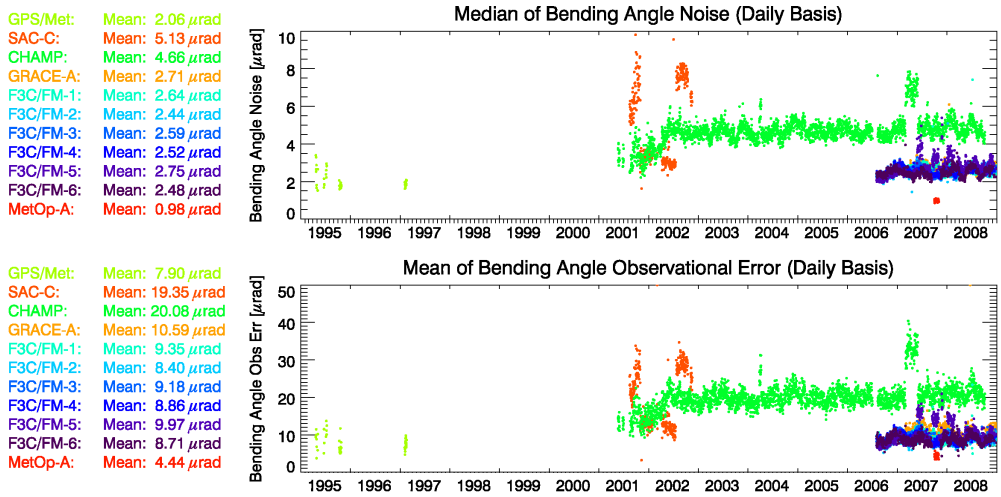

Figure 2.10: Time series of the daily median bending angle noise (top) and daily mean bending angle observational error (bottom) of different satellite data from 1995 to 2008. Note the different y-axis in both plots.

or changes in the GPS software (J. Wickert, GFZ, pers. comm. November 2009), which could explain this conspicuous feature. Neither UCAR nor WEGC data version changed within this period so that the reason for this sudden increase of bending angle noise is still unclear.

GRACE-A and F3C bending angle noise is very similar. If bending angle noise is averaged over the whole period, it yields 2.4 μrad to 2.7 μrad for these satellites. F3C/FM-5 bending angles exhibit significantly larger noise within some periods in 2007 and 2008 where it almost reaches the CHAMP noise level. The cause for this large noise may be that one Precise Orbit Determination (POD) navigation antenna of FM-5 has low L2 Signal to Noise Ratio (SNR) so that this satellite is operated only with a single POD antenna (CDAAC Team 2010).

The development of bending angle noise is clearly reflected in the bending angle observational error (bottom panel of Figure 2.10). Due to observational error adjustments, the observational errors are larger than bending angle noise by about a factor of four. While best data quality is again found for MetOp-A (with an average observational error of 4.4 μrad) worst quality is detected in SAC-C and CHAMP data (mean observational errors of 19 μrad and 20 μrad, respectively).

The temporal evolution of the observational error again shows variable data quality of SAC-C, the sudden increase of data quality in northern hemisphere spring in 2007 in CHAMP data, and worse data quality of F3C/FM-5 compared to the other F3C satellites.

2.3.3 Validation of Dry Temperature Climate Records

Bending angle data quality at high altitudes (between 50 km and 80 km impact height) determines the degree of background information at lower altitudes (e.g., at 30 km). Better data quality is reflected in higher transition heights, where background information equals observation information.

The temporal evolution of daily mean zRAER50 values is shown in the top panel of Figure 2.11. Nearly all CHAMP and SAC-C profiles are observation dominated below 41 km. zRAER50 values increase using GRACE-A, F3C, GPS/MET, and MetOp-A data. Their average zRAER50 values amount to 46 km, 47 km, 50 km, and 57 km, respectively. Note the remarkable GPS/MET data quality in 1995/1997.

The OPSv54 retrieval uses background information provided by ECMWF short-term forecasts. Studies evaluating the quality of ECMWF data (e.g., Gobiet et al. 2005; Borsche et al. 2007; Foelsche et al. 2008*b*) showed that ECMWF temperatures are somewhat cooler than RO temperatures at high altitudes (up to 1.5 K at an altitude of 30 km). RO profiles with lower background/observation transition heights are stronger affected by this bias than profiles with higher transition heights.

The middle and bottom panels of Figure 2.11 show monthly mean dry temperature deviations relative to the monthly satellite mean averaged between 20°S and 20°N

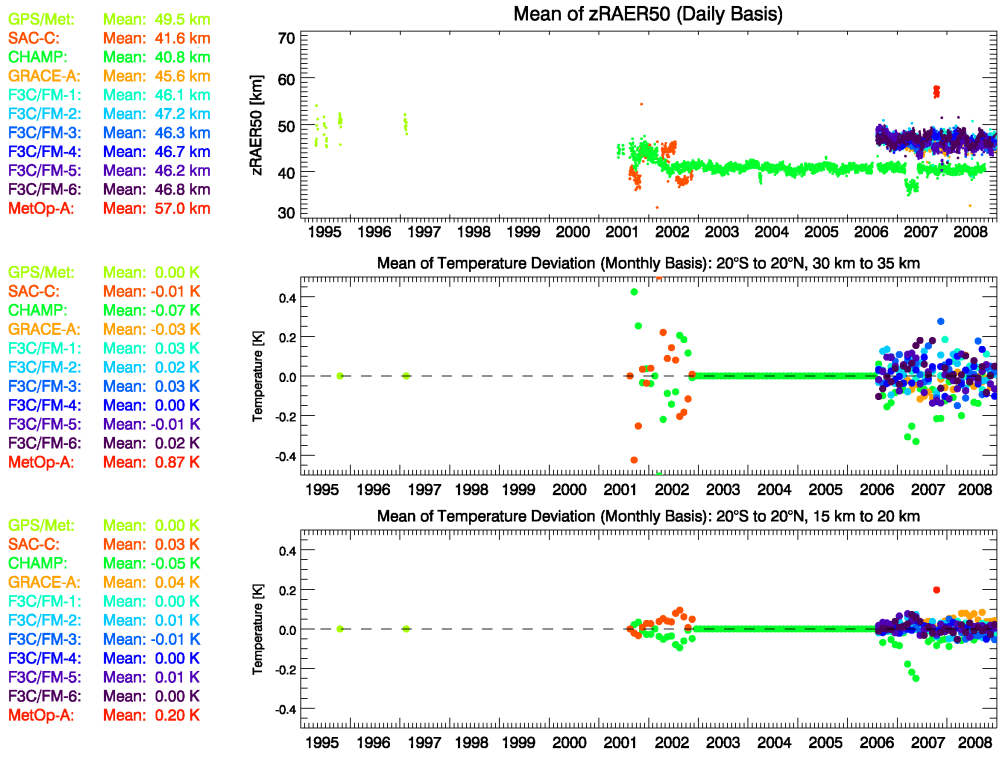

Figure 2.11: Time series of zRAER50 values of different satellite data (top panel) and deviations of dry temperatures from the satellite mean at low latitudes (20°S to 20°N) and two different height layers (between 30 km and 35 km, middle panel, and between 15 km and 20 km, bottom panel) from 1995 to 2008.

and between 30 km and 35 km[4] and between 15 km and 20 km, respectively. SAC-C and CHAMP records are compared for 2001 and 2002. During this period the satellite mean is computed only from these two satellite records, such that corresponding deviations always point in the opposite direction. Data from CHAMP and F3C are compared from August 2006 to December 2008, GRACE-A climatologies are available since March 2007, and one single MetOp-A climatology is computed from October 2007.

The effect of background information at high altitudes (30 km to 35 km) is clearly noticeable: CHAMP climatologies in 2001 and 2002 are slightly warmer than those of SAC-C if CHAMP background/observation transition height is higher compared to SAC-C. The situation is quite the opposite if zRAER50 values of SAC-C are larger than those of CHAMP. The difference between CHAMP and SAC-C monthly mean

[4]Deviations are derived as described in detail in Chapter 3 and Chapter 4.

climatologies exceeds 1 K in March 2002. The temporal mean difference (2001 to 2002) amounts to 0.2 K, where SAC-C temperatures are slightly cooler than those of CHAMP.

At high altitudes CHAMP climatologies from 2006 to 2008 are consistently slightly cooler than those of GRACE-A and F3C by up to 0.3 K from March to May 2007. Apart from this period differences amount to 0.1 K to 0.2 K. MetOp-A temperatures are significantly warmer than temperatures derived from other satellite data in October 2007. Between 30 km and 35 km the MetOp-A red dot is even out of the plot range. While F3C and GRACE-A data are very similar, CHAMP temperatures are coolest. Averaged from 30 km to 35 km altitude, the deviations from the satellite mean in October 2007 amount to −0.22 K (CHAMP), −0.12 K (GRACE-A), −0.08 K (FM-1), −0.09 K (FM-2), −0.11 K (FM-3), −0.13 K (FM-4), −0.12 K (FM-5), and +0.87 K (MetOp-A). These deviations may reflect better MetOp-A data quality but partly they can also stem from differences in level 1 processing (MetOp-A data are provided by EUMETSAT while other satellite data are provided by UCAR/CDAAC).

Differences between temperature climate records of different satellites decrease with decreasing altitude. In most cases, they are negligible (< 0.1 K) at altitudes below 20 km. However, very large temperature differences at high altitudes sometimes propagate downwards. Examples are distinctively cooler CHAMP temperatures compared to the satellite mean in March–April–May (MAM) 2007 (deviations still exceed −0.2 K) and distinctively warmer MetOp-A temperatures in October 2007. In October 2007 the temperature deviations relative to the satellite mean between 15 km and 20 km amount to −0.08 K (CHAMP), 0.00 K (GRACE-A), −0.04 K (FM-1), −0.01 K (FM-2), −0.04 K (FM-3), −0.01 K (FM-4), −0.03 K (FM-5), and +0.20 K (MetOp-A).

2.4 Summary of RO Data Characteristics

RO data from different satellites are available in intermittent periods in 1995 and 1997 (GPS/MET), and continuously since 2001 (CHAMP). The availability of F3C data since 2006 significantly increased the number of RO measurements globally available. Data provided by SAC-C (2001 to 2002), GRACE-A (since March 2007), and MetOp-A (October 2007) complete the RO record currently available at WEGC.

For climate studies, the evaluation and monitoring of data quality is of highest importance. Characteristics of RO data are investigated for selected sets of data from each satellite and for the whole RO record available until 2008. Data characteristics and data quality were found to depend on receiver quality and data processing. Furthermore they seem to depend on solar activity (ionospheric conditions).

Foelsche et al. (2008*a*) allude to the importance of a small and temporarily constant bending angle bias. They show that a severely biased bending angle profile

yields an undesired downward propagation of systematic errors. The bending angle bias relative to MSIS is slightly negative but very similar for all satellite data except for GFZ CHAMP data. The specific characteristics of the GFZ data set points at differences in level 1 processing. The temporal evolution of CHAMP bending angle bias yields that it may slightly decrease from 2001 until 2008. Since the solar cycle decreases from maximum to minimum solar activity at the same time, this suggests that solar activity somewhat affects the bending angle bias.

While bending angle biases are in good agreement for all satellite data, there are distinctive differences in bending angle noise. Best bending angle quality (smallest bending angle noise) is found for data from the European satellite MetOp-A. Good bending angle quality is also observed for GPS/MET, whose data stem from "prime times" (high GPS signal quality), F3C, and GRACE-A. The long CHAMP record shows relatively constant bending angle quality (except for MAM 2007) but very variable data quality is found for SAC-C, which is operated as "testbed" satellite.

RO data are observation dominated below 41 km/42 km (CHAMP/SAC-C), 46 km/47 km (GRACE-A/F3C), 49 km (GPS/MET), and 57 km (MetOp-A). This different degree of background information yields slightly cooler CHAMP climatologies and warmer MetOp-A climatologies. Differences are most pronounced at high altitudes (above 30 km), but they decrease with decreasing altitude. In most cases, they are negligible (< 0.1 K) at altitudes below 20 km but occasionally very large temperature differences at high altitudes can also propagate downwards.

3 Climatology Processing System (CLIPS)

In general, all atmospheric measurements globally available can be used to calculate climatologies. The quality of a climatology depends on the reliability of the measurements (accuracy and precision), on the number of data, on their sampling times and locations, and—if used—on the underlying model. Randel et al. (2004) performed a study evaluating the uncertainties of some representative middle atmosphere climatologies over altitudes from 10 km to 80 km. They analyzed global meteorological analyses and assimilations, climatologies derived from satellite data, historical reference atmosphere circulation statistics, rocketsonde data, and lidar measurements. They found notable differences between analyses for temperatures near the tropical tropopause and polar lower stratosphere.

The characteristics and quality of the Radio Occultation (RO) record allow the validation of other climate data sets and models provided that spatio-temporal RO sampling is well understood. This chapter deals with the calculation of RO climatologies and their characterization as well as their validation with climatologies derived from European Centre for Medium-Range Weather Forecasts (ECMWF) analysis and reanalysis fields. The Climatology Processing System (CLIPS) software, developed at the Wegener Center for Climate and Global Change (WEGC), enables the calculation of these RO climatologies and provides their error estimates.

3.1 CLIPS Input Data

RO measurements are utilized to create climatologies of bending angle, density, refractivity, dry pressure, dry geopotential height, and dry temperature (e.g., Borsche et al. 2006; Foelsche et al. 2008*b*). The validity of these climatologies depends on the measurement's retrieval (e.g., Ao et al. 2003; Hajj et al. 2004; Wickert et al. 2004; Ho et al. 2009), and on sampling times and locations resulting in the sampling error (Foelsche et al. 2003; Foelsche et al. 2006; Pirscher et al. 2007*b;* Foelsche et al. 2008*b*). Using RO data for climate studies it is of highest importance that data from the same data processing scheme are used (Foelsche et al. 2009*b*). All RO data used in this section follow from the WEGC Occultation Processing System Version 5.4 (OPSv54) retrieval.

3.1.1 Radio Occultation Profiles

RO measurements are irregularly distributed around the globe. Profiles of atmospheric parameters are available at geographic latitudes φ_i and geographic longitudes λ_i (spatialized at mean tangent point location). The mean state of the atmosphere (typical for a desired temporal and spatial resolution) is estimated from RO measurements by optimally averaging the profiles aiming at deriving representative atmospheric parameters at evenly distributed grid points.

The quality of RO measurements (accuracy and precision) is known to be very good (Kursinski et al. 1997; Schreiner et al. 2007) and retrieval differences of different processing centers are small (Ho et al. 2009).

The number of RO measurements depends on the number of transmitters, the number of receivers and antenna characteristics. Assuming optimal receiver software and antenna characteristics, one single Global Positioning System (GPS) RO antenna can record about 350 events per day. Due to insufficient data calibration and data quality not all of them can be translated to useful atmospheric phase delay profiles (e.g., Wickert et al. 2003; Wickert et al. 2006). Further quality control mechanisms during the retrieval narrow the number of measurements, which yields high quality refractivity, pressure, and temperature profiles. Within the WEGC retrieval, about 65 % to 75 % of all retrieved profiles yield atmospheric profiles of high quality (cf. Chapter 2). Only these profiles are used to compute atmospheric climatologies.

Figure 3.1 shows the F3C/FM-4 event locations of high quality profiles in January 2009. Initially, 17976 F3C/FM-4 occultation link data have been available at COSMIC Data Analysis and Archive Center (CDAAC). Their level 1 processing scheme yielded 17008 phase delay profiles, which have been used as input data in the WEGC OPSv54 retrieval. 11494 profiles[1] (67.6 %) passed quality control at WEGC.

At first sight the measurements seem to be quite uniformly distributed in the atmosphere but looking more closely reveals more profiles at mid- and higher latitudes and less profiles at low latitudes.

A detailed view to the event statistics as a function of latitude and longitude depicts Figure 3.2: it shows the number of RO events per 5° latitude band, per 10° longitude sector, and per 500 km × 500 km area (as a function of latitude and longitude, respectively).

The latitudinal distribution of RO events (left panels) is symmetric with respect to the equator. The latitudinal sampling can be explained by the orbit characteristics of F3C/FM-4 (72° inclination) and the GPS satellites (55° inclination) because satellites with high inclination quickly fly over low latitudes but stay for a comparatively long

[1] The retrieval of an RO measurement yields different atmospheric parameters. The number of profiles refers to each atmospheric parameter, i.e., there is always the same number of high quality profiles for bending angle, refractivity, dry pressure, dry temperature, and dry geopotential height.

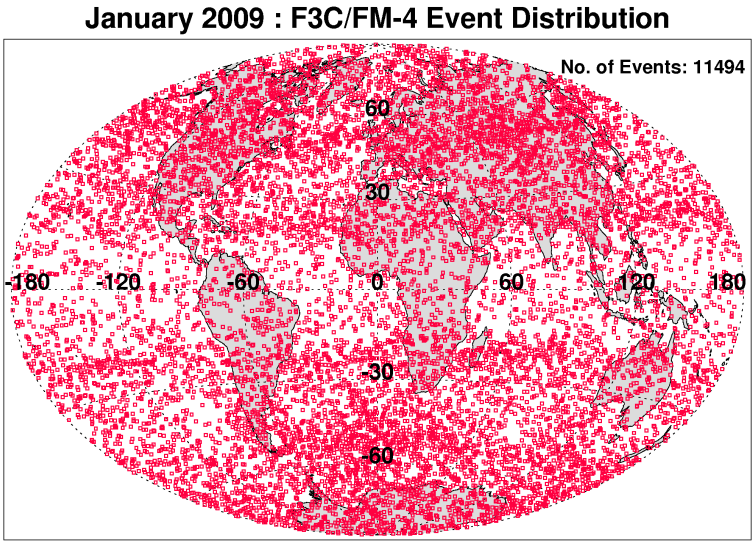

Figure 3.1: F3C/FM-4 RO event locations in January 2009. Each red square represents the mean latitude and mean longitude of a high quality RO measurement (Hammer-Aitoff equal area projection). The total number of profiles is 11494. Even though the event distribution seems to be quite uniform, there are more profiles available at mid-latitudes than, e.g., at low latitudes.

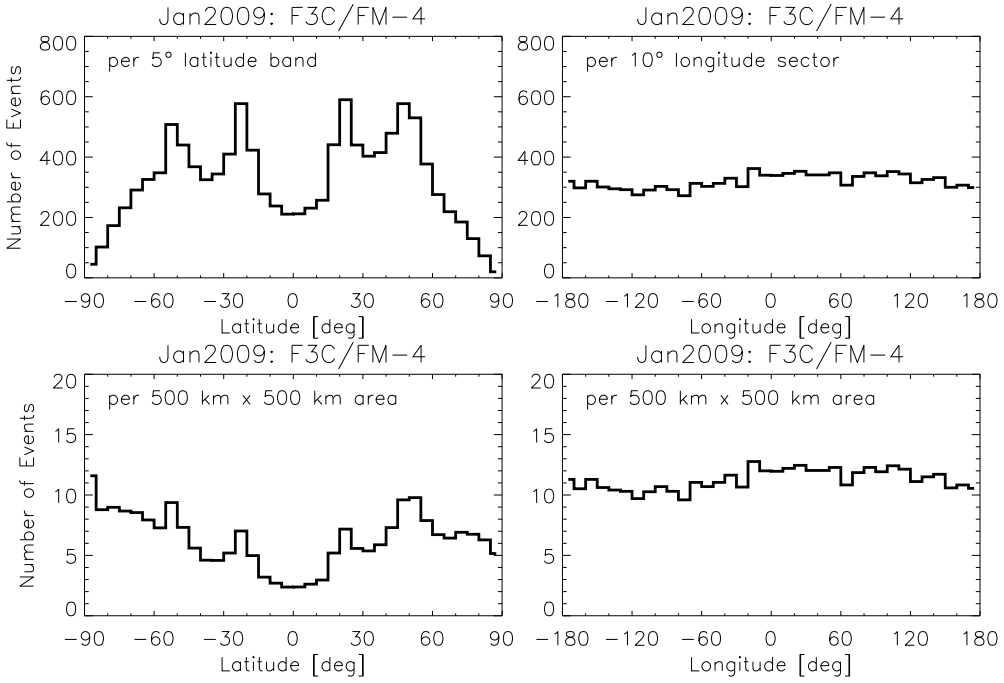

Figure 3.2: F3C/FM-4 RO event statistics in January 2009. The number of measurements is given per 5° latitude band (top left panel), per 10° longitude sector (top right panel), and per fixed surface area as a function of latitude and longitude, respectively (bottom). Note different y-axis in top and bottom panels.

time at high latitudes. The smaller dwell time of the satellites at low latitudes leads to a smaller number of measurements compared to mid latitudes. Local maxima occur at 25°N/S and at 50°N/S. Due to the non-polar orbit of F3C/FM-4, polar latitudes are rarely covered with RO measurements.

If the number of measurements is related to a fixed surface area, the number of high latitude events distinctively increases. This is because the Earth's surface area decreases with increasing latitude[2].

The meridional distribution of RO events (right panels) is rather uniform everywhere. The average event density is similar over the oceans and over land, including also remote regions like high mountains.

3.1.2 ECMWF Analysis Fields

ECMWF develops numerical models for medium-range weather forecasting and prepares medium-range weather forecasts for up to 10 days. The Integrated Forecasting System (IFS) of the ECMWF operationally generates global analysis fields for four time layers, 00 Universal Time Coordinated (UTC), 06 UTC, 12 UTC, and 18 UTC. An analysis is an estimate of the true atmosphere's state at a given time. Since data are not continuously available at any location (very sparse observations are, e.g., available at polar regions), background information and physical constraints are included to obtain an analysis close to the "true" atmospheric state. This analysis technique, which combines observational data and short-term forecasts is called data assimilation. Since November 25, 1997, global analyses follow from the 4-Dimensional Variational (4D-Var) analysis assimilation algorithm (Bouttier and Rabier 1997), before ECMWF used a 3-Dimensional Variational (3D-Var) assimilation technique. The model system and the amount and quality of observational data being incorporated in the assimilation process improved with time, resulting in better analysis (and forecasting) quality.

Since January 26, 2010 the horizontal resolution of ECMWF analysis fields is T1279 (spectral representation with triangular truncation at wave number 1279).

The vertical coordinate of ECMWF data is sigma levels. Close to the Earth's surface the levels follow the Earth's topography, at high altitudes, the levels are like constant pressure levels. From September 1991 until March 1999 ECMWF operational analyses had a vertical resolution of 31 levels. In March 1999 the vertical resolution was increased from 31 to 50 levels (Untch et al. 1998; Lalaurette 1999). In October 1999 ECMWF introduced an increase in the number of model levels to 60 (Jakob et al. 2000). In February 2006 the vertical resolution of ECMWF analysis fields increased from L60 (60 vertical levels) to L91 (91 vertical levels). This increase in vertical

[2] An example: the Earth surface area between the equator and 5° latitude amounts to 22 227 522 km^2, the Earth surface between 70° and 75° latitude amounts to 6 690 311 km^2, which is only about 30 % of the surface at low latitudes.

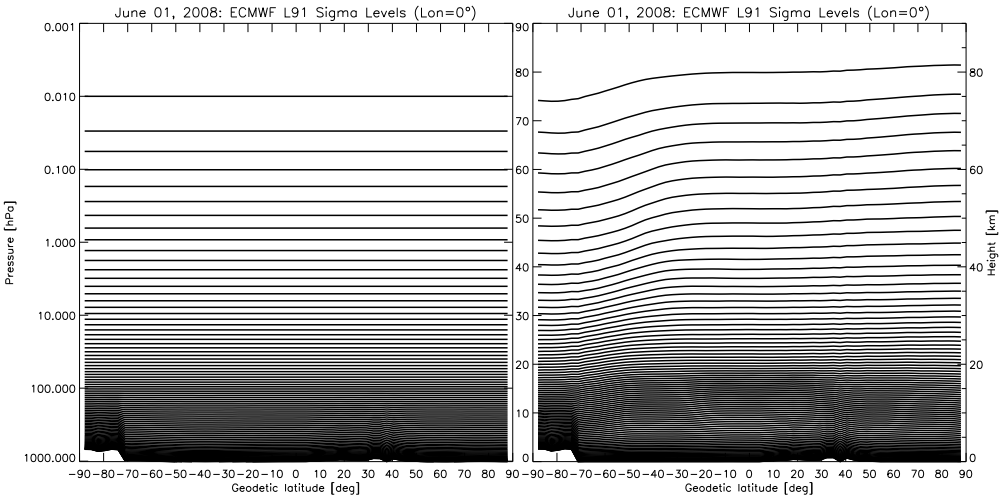

Figure 3.3: ECMWF sigma levels as a function of latitude and pressure (left) and as a function of latitude and ellipsoidal height (right).

resolution was accompanied with a raise of the model top from 0.1 hPa (about 60 km) to 0.01 hPa (about 80 km) (Untch et al. 2006). Figure 3.3 shows the vertical grid of the L91 ECMWF field. The left panel shows sigma levels as a function of latitude and pressure, the right panel shows sigma levels as a function latitude and ellipsoidal height[3]. The vertical grid of the model is very dense in the troposphere and becomes more transparent above.

Co-located ECMWF Profiles

For each RO profile, a co-located reference profile is extracted from an ECMWF analysis field. ECMWF fields are used at a reduced spatial resolution of T42, which corresponds to approximately 300 km. This horizontal resolution is selected to match the natural horizontal resolution of RO profiles, which is approximately 300 km as well.

Co-located reference profiles are extracted at times and locations of RO events. In a first step the time of the RO event is allocated to the nearest ECMWF time layer. The four ECMWF time layers do not represent an optimal sampling of all harmonics of the diurnal cycle. However, four time layers are sufficient to sample the diurnal cycle up to the second harmonics (the semidiurnal variations). Afterward

[3]Data have to be converted from sigma levels to pressure/altitude levels. This conversion necessitates the knowledge of geocentric latitude, surface geopotential, surface pressure, and the profiles of temperature and specific humidity (see e.g., DKRZ 1993).

the ECMWF field is spatially interpolated to the geographic event location, where the proxy RO profile is extracted.

Co-located ECMWF profiles are compared to RO profiles. To neglect, e.g., RO retrieval interpolation errors, co-located ECMWF profiles are derived in a similar way as RO profiles. The starting point is atmospheric refractivity, which is calculated directly from ECMWF analysis data. While integrated refractivity (Abel integral equation) yields atmospheric bending angle, dry density, dry pressure, dry temperature, and geopotential height (as a function of dry pressure altitude) follow from the dry air RO retrieval.

ECMWF Reference Field

The "full" ECMWF reference field is available on evenly distributed grid points with a horizontal resolution of $2.5° \times 2.5°$. It is derived from averaging over all analysis fields available within one month (i.e., data of all days and all time layers of the month). These data also pass through the RO retrieval chain by calculating atmospheric refractivity profiles from ECMWF analysis fields and deriving other atmospheric parameters. Currently at WEGC full ECMWF reference fields are available only for refractivity, dry temperature, and dry pressure, none are available for bending angle and geopotential height.

3.2 Averaging Strategy

The quality of a measurement cannot be improved by building a climatology. However, the quality of a climatology can be optimized by optimally averaging over all profiles and thereby minimizing the sampling error of a climatology. This section deals with an approach developed at WEGC how to calculate climatologies derived from RO measurements. This approach tries to reduce the effect of uneven sampling with latitude, longitude, and time.

3.2.1 Generation of Fundamental Climatologies

Global climatologies of atmospheric parameters are created from measurements gathered into "bins" (geographical cells). A bin corresponds to the spatial resolution of the climatology. In the WEGC standard setup, profiles are first gathered into "fundamental" bins, which are then aggregated to larger scale horizontal bins.

The spatial resolution of "fundamental" climatologies refers to non-overlapping bins with a horizontal resolution of 5° latitude $\times$ 60° longitude (i.e., 36 latitude bins from 90°S to 90°N, and 6 longitude bins). The longitudinal grid is chosen so that one longitudinal sector covers Europe and Africa (15°W to 45°E), the other longitudinal sectors are placed accordingly. The spatial resolution of $5° \times 60°$ leads

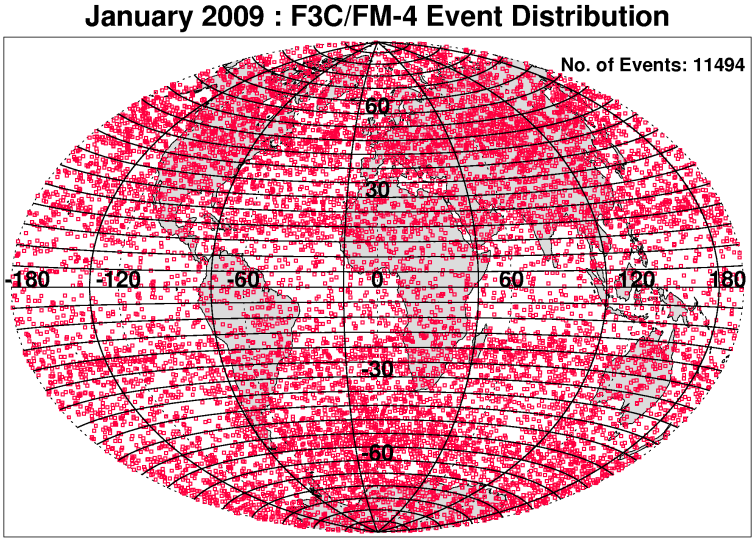

Figure 3.4: F3C/FM-4 RO events in January 2009 (red squares) and fundamental bins (boundaries of fundamental bins are depicted in black).

to a total number of 216 fundamental bins regularly distributed on the globe. By definition, fundamental climatologies have a temporal resolution of one month.

Figure 3.4 shows the F3C/FM-4 RO events in January 2009 and the fundamental bins (boundaries of fundamental bins are depicted in black). Each RO event is allocated to exactly one fundamental bin.

Fundamental climatologies of atmospheric parameters are derived by averaging over all profiles available within one fundamental bin. In doing so, all profiles are interpolated to a common 200 m altitude grid (top altitude is set to 80 km) and each single profile is weighted with the cosine of its geographic latitude. The cosine-weighting accounts for area changes between meridians at varying latitudes (Foelsche et al. 2008*b*), i.e., due to convergence of meridians towards the poles, the geographical area per latitude increment shrinks by $\cos\varphi$.

$$x(z_j, \varphi_u, \lambda_v) = \frac{1}{\sum_{i=1}^{N(z_j)} \cos(\varphi_i)} \sum_{i=1}^{N(z_j)} x(z_j, \varphi_i, \lambda_i) \cos(\varphi_i), \tag{3.1}$$

where $x(z_j, \varphi_u, \lambda_v)$ is the mean atmospheric parameter at altitude z_j, representing one fundamental bin with mean latitude φ_u and mean longitude λ_v. $N(z_j)$ is the total number of profiles available within the bin at altitude z_j. The number of profiles decreases with decreasing altitude because increasing humidity leads to atmospheric multipath and signal degradation. While almost 90 % of all high latitude F3C profiles

penetrate below 1 km, only 70 % of tropical F3C profiles penetrate the atmospheric boundary layer (Anthes et al. 2008).

Fundamental climatologies are calculated for RO profiles, co-located ECMWF profiles, and the ECMWF reference field. For the ECMWF reference field $N(z_j)$ corresponds to the total number of grid points of one fundamental bin, which is actually the same for all altitude levels.

3.2.2 Horizontal Aggregation of Fundamental Climatologies

The number of measurements within one month performed by single satellite RO missions is too small to get representative climatologies of atmospheric parameters in $5° \times 60°$ fundamental bins. Fundamental climatologies are only used to aggregate them to larger horizontal-scale climatologies. Currently the recommended basic resolution of single satellite climatologies is 10° latitude $\times$ 360° longitude (i.e., 10° zonal bands). They are derived from aggregating twelve fundamental bins. Multi-satellite climatologies are also useful with a smaller horizontal resolution (e.g., 5° zonal bands).

Longitudinal Aggregation

When expanding the horizontal resolution from fundamental $5° \times 60°$ bins to larger longitudinal bins, each profile, which represents the average atmospheric state of one fundamental bin is weighted with the number of profiles being available within the bin:

$$x(z_j, \varphi_u, \lambda_l) = \frac{1}{\sum_{v=1}^{L} N_v(z_j)} \sum_{v=1}^{L} x(z_j, \varphi_u, \lambda_v) N_v(z_j), \tag{3.2}$$

where $x(z_j, \varphi_u, \lambda_l)$ is the mean atmospheric parameter at altitude z_j, representing one aggregated bin with mean latitude φ_u and mean longitude λ_l. $N_v(z_j)$ is the number of profiles (number of grid points) within the fundamental bin v at altitude z_j, L is the number of aggregated longitudinal bins ($L = 6$ for zonal bands).

Latitudinal Aggregation

When expanding $5° \times 60°$ fundamental bins or aggregated longitudinal bins (e.g., 5° zonal bands) to larger latitudinal bins, each profile, representing the mean atmospheric state of one (fundamental) bin, is weighted with its corresponding bin area.

The area of one fundamental bin amounts to one sixth of the surface of a spherical layer. The area of such a surface at mean latitude φ_u is

$$A_{\text{zonal band}}(\varphi_u) = 2r_e^2 \pi (\sin \varphi_{u\text{top}} - \sin \varphi_{u\text{bot}}), \tag{3.3}$$

with r_e being the Earth's radius and $\varphi_{u\mathrm{top}}$ and $\varphi_{u\mathrm{bot}}$ characterizing the top and bottom latitudinal boundaries of the bin, respectively. The aggregation is calculated from

$$\begin{aligned} x(z_j, \varphi_k, \lambda_l) &= \frac{1}{\sum_{u=1}^{K} A_\mathrm{bin}(\varphi_u)} \sum_{u=1}^{K} x(z_j, \varphi_u, \lambda_l) A_\mathrm{bin}(\varphi_u) \\ &= \frac{1}{\sum_{u=1}^{K} (\sin\varphi_{u\mathrm{top}} - \sin\varphi_{u\mathrm{bot}})} \sum_{u=1}^{K} x(z_j, \varphi_u, \lambda_l)(\sin\varphi_{u\mathrm{top}} - \sin\varphi_{u\mathrm{bot}}) \end{aligned} \tag{3.4}$$

where $x(z_j, \varphi_k, \lambda_l)$ is the mean atmospheric parameter at altitude z_j, representing one aggregated bin with mean latitude φ_k and mean longitude λ_l. $\varphi_{u\mathrm{top}}$ and $\varphi_{u\mathrm{bot}}$ are the upper and lower latitude boundaries of the bin, K is the number of aggregated latitudinal bins.

Due to irregular sampling with latitude (cf. Figure 3.2) weighting with the number of profiles would introduce an error.

3.2.3 Temporal Aggregation of Larger-Scale Horizontal Climatologies

Climatologies of fundamental bins or corresponding larger-scale horizontal bins are calculated on a monthly time scale. Other temporal resolutions, e.g., seasonal or annual climatologies, are obtained from averaging over the corresponding number of months:

$$x(z_j, \varphi_k, \lambda_l) = \frac{1}{N_\mathrm{mon}} \sum_{i=1}^{N_\mathrm{mon}} x_i(z_j, \varphi_k, \lambda_l) \tag{3.5}$$

with N_mon being the number of months, which are averaged over (i.e., arithmetic time average). Seasonal climatologies are, e.g., March–April–May (MAM) or June–July–August (JJA), annual climatologies refer to the calender year, not to the meteorological year.

3.2.4 User Defined Binning

Regional climate change can be investigated in smaller regions as defined, e.g., by Giorgi and Francisco (2000). Since these regions have different latitudinal and longitudinal extensions, the fundamental binning strategy is not appropriate to calculate climatologies in these small-scale regions. Thaler (2009) developed a binning strategy for any user defined region with a minimum extension of $2.5° \times 2.5°$.

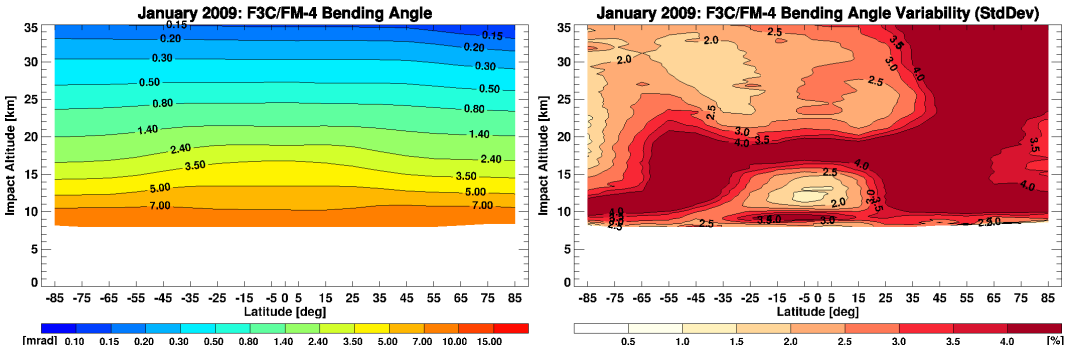

Figure 3.5: Monthly mean 10° zonal mean bending angle climatology of F3C/FM-4 (in mrad) and its variability (in %) in January 2009. The vertical coordinate is impact altitude.

3.2.5 Variability of Atmospheric Parameters

Atmospheric variability is represented by the standard deviation of atmospheric profiles. Since the standard deviation is a non-linear quantity it cannot be aggregated from fundamental bins to larger-scale horizontal bins but has to be calculated separately for each aggregated bin. The standard deviation $\sigma(z_j, \varphi_k, \lambda_l)$ is related to the aggregated mean $x(z_j, \varphi_k, \lambda_l)$. It is calculated from

$$\sigma(z_j, \varphi_k, \lambda_l) = \sqrt{\frac{\sum_{i=0}^{N(z_j)} \cos(\varphi_i)}{\left(\sum_{i=0}^{N(z_j)} \cos(\varphi_i)\right)^2 - \sum_{i=0}^{N(z_j)} \cos^2(\varphi_i)}} \cdot \sqrt{\sum_{i=1}^{N(z_j)} \left[x(z_j, \varphi_i, \lambda_i) - x(z_j, \varphi_k, \lambda_l)\right]^2 \cos(\varphi_i)}, \tag{3.6}$$

where $N(z_j)$ is the number of profiles available within the bin (φ_k, λ_l) at altitude z_j.

3.2.6 Example: F3C/FM-4 Climatologies in January 2009

Figure 3.5 to Figure 3.9 depict monthly mean 10° zonal mean climatologies derived from F3C/FM-4 data and their variability in January 2009 for bending angle, refractivity, dry temperature, dry pressure, and dry geopotential height.

All climatologies are shown as a function of latitude from south pole to north pole and appropriate altitude (impact altitude, Mean Sea Level (MSL) altitude, or dry pressure altitude). The altitude range expands from the surface to 35 km but F3C climatologies are cut off at 8 km because the current version of the Occultation

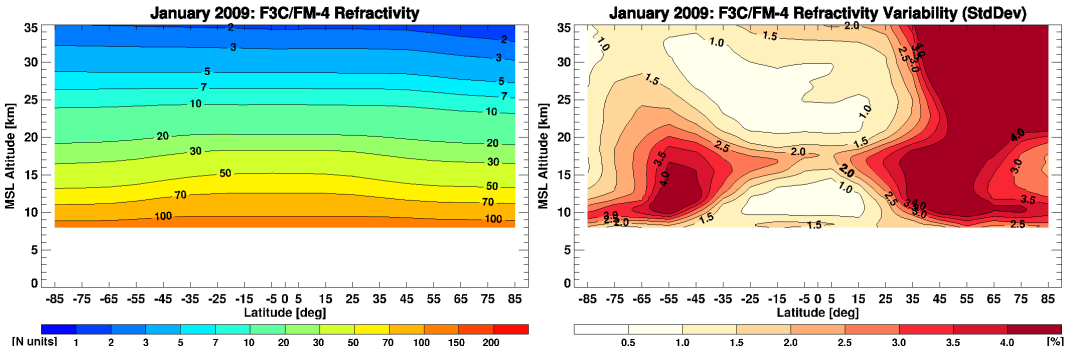

Figure 3.6: Monthly mean 10° zonal mean refractivity climatology of F3C/FM-4 (in N-Units) and its variability (in %) in January 2009.

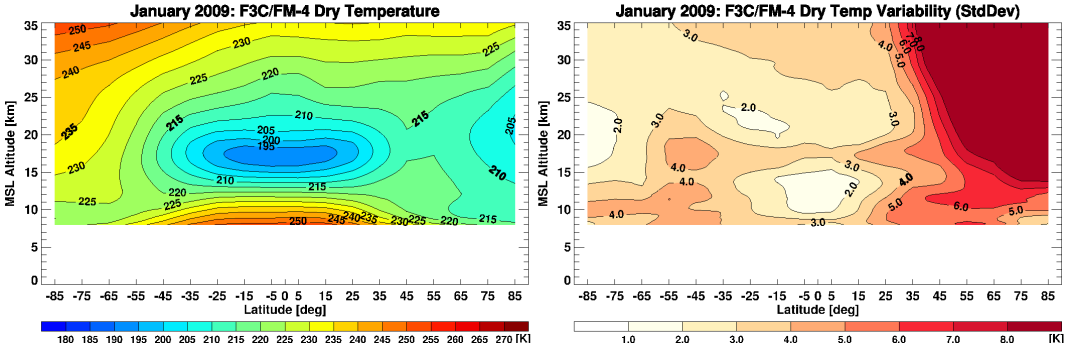

Figure 3.7: Monthly mean 10° zonal mean dry temperature climatology of F3C/FM-4 (in K) and its variability (in K) in January 2009.

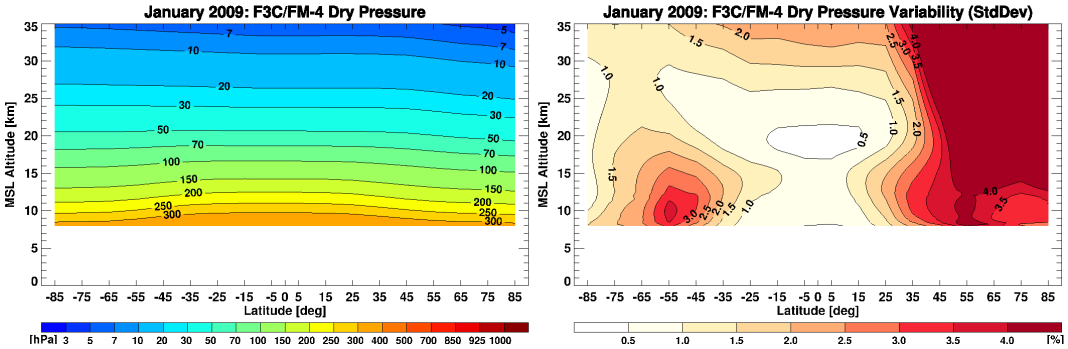

Figure 3.8: Monthly mean 10° zonal mean dry pressure climatology of F3C/FM-4 (in hPa) and its variability (in %) in January 2009.

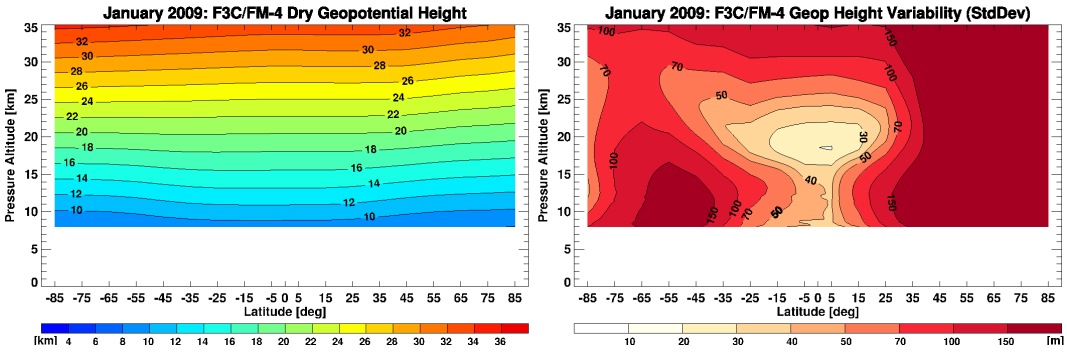

Figure 3.9: Monthly mean 10° zonal mean dry geopotential height climatology of F3C/FM-4 (in km) and its variability (in m) in January 2009. The vertical coordinate is dry pressure altitude.

Processing System (OPSv54) cannot handle F3C data received in Open Loop (OL) mode.

All depicted atmospheric parameters except dry temperature and dry geopotential height decrease exponentially with height. The dry temperature climatology shows distinctive features like the cold tropical tropopause region and the cold Arctic winter polar vortex. The variability of all atmospheric parameters (right panels) is most pronounced in the winter hemisphere at all altitudes but also comparatively strong in the tropopause region in other latitudinal regions. Less variability is observed at low latitudes below 15 km and above approximately 20 km as well as at mid- and high southern latitudes above 20 km.

3.3 Systematic Difference and Sampling Error

The quality of RO climatologies can be validated through comparison with other data sets. Lackner and Pirscher (2005) compared CHAllenging Mini-Satellite Payload (CHAMP) RO climatologies to ECMWF analyses, National Centers for Environmental Prediction (NCEP) reanalyses, and Mass Spectrometer and Incoherent Scatter Radar (MSIS) and COSPAR International Reference Atmosphere (CIRA) model data. These comparisons yielded smallest differences between RO and ECMWF data and somewhat larger differences between RO and NCEP data. Since MSIS/CIRA are long-term average atmosphere climatologies, which do not reflect the actual atmospheric state, the differences between monthly RO climatologies and MSIS/CIRA were comparatively large.

In this section, RO climatologies are compared to ECMWF analysis fields to estimate their systematic difference. ECMWF data are also used to estimate the sampling

error of RO climatologies.

3.3.1 Calculation of Systematic Difference and Standard Deviation of the Systematic Difference

The systematic difference between ECMWF and RO climatologies is estimated for each large-scale horizontal bin by calculating the difference between the mean co-located ECMWF profile and the mean retrieved RO profile:

$$\Delta x_{\mathrm{SysDiff}}(z_j, \varphi_k, \lambda_l) = x_{\mathrm{coloc}}(z_j, \varphi_k, \lambda_l) - x_{\mathrm{RO}}(z_j, \varphi_k, \lambda_l). \tag{3.7}$$

$x(z_j, \varphi_k, \lambda_l)$ is the mean atmospheric parameter of the bin (φ_k, λ_l) at altitude z_j. x_{coloc} and x_{RO} are calculated following the averaging strategy described in Section 3.2.

Since measurements are taken at the same location and at (nearly) the same time, it results in a comparison of the RO measurement method and the ECMWF model. Differences in sampling pattern are excluded. The systematic difference between two data sets cannot be reduced by enlarging a measurement sample.

The standard deviation of the systematic difference is a measure of difference profile variability. Just as the standard deviation of atmospheric profiles it cannot be aggregated from fundamental bins but has to be calculated separately for each aggregated bin. The standard deviation of the systematic difference $\sigma_{\mathrm{SysDiff}}(z_j, \varphi_k, \lambda_l)$ is related to the aggregated systematic difference $\Delta x_{\mathrm{SysDiff}}(z_j, \varphi_k, \lambda_l)$. It is calculated from

$$\sigma_{\mathrm{SysDiff}}(z_j, \varphi_k, \lambda_l) = \sqrt{\frac{\sum_{i=0}^{N(z_j)} \cos(\varphi_i)}{\left(\sum_{i=0}^{N(z_j)} \cos(\varphi_i)\right)^2 - \sum_{i=0}^{N(z_j)} \cos^2(\varphi_i)}} \cdot$$
$$\sqrt{\sum_{i=1}^{N(z_j)} \left[x_{\mathrm{coloc}}(z_j, \varphi_i, \lambda_i) - x_{\mathrm{RO}}(z_j, \varphi_i, \lambda_i) - \Delta x_{\mathrm{SysDiff}}(z_j, \varphi_k, \lambda_l)\right]^2 \cos(\varphi_i)}. \tag{3.8}$$

3.3.2 Systematic Difference Between ECMWF and F3C/FM-4 Data

This subsection exemplarily shows the systematic difference and the standard deviation of the systematic difference between ECMWF analyses and F3C/FM-4 climatologies of different atmospheric parameters in January 2009. Figure 3.10 to Figure 3.14 show latitude-height zonal means of the systematic difference (left) and the standard deviation of the systematic difference (right) for bending angle, refractivity, dry temperature, dry pressure, and dry geopotential height. Atmospheric parameters, which decrease exponentially with height (bending angle, refractivity, and dry pressure) are shown in terms of relative quantities. These are derived by dividing

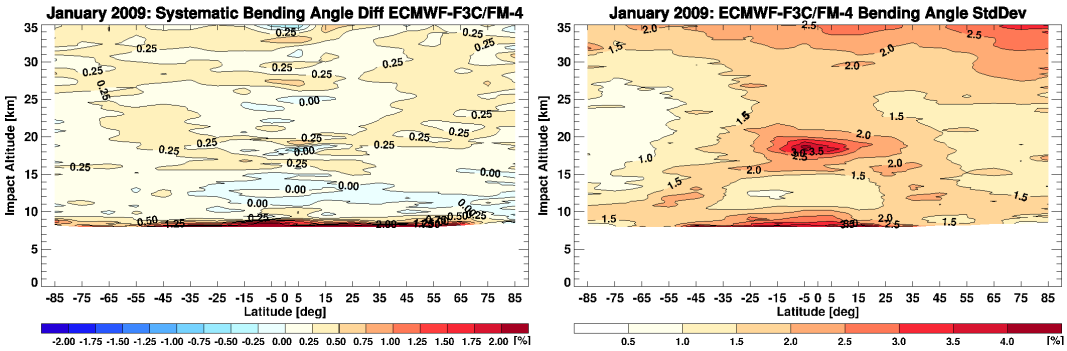

Figure 3.10: Systematic difference (left) and standard deviation of systematic difference (right) between ECMWF and F3C/FM-4 bending angle climatologies in January 2009.

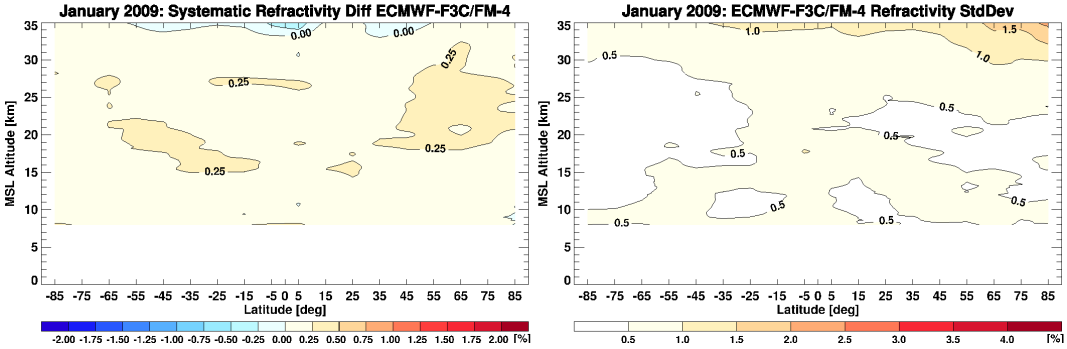

Figure 3.11: Systematic difference (left) and standard deviation of systematic difference (right) between ECMWF and F3C/FM-4 refractivity climatologies in January 2009.

the quantities by the mean of all RO data. Results of dry temperature and dry geopotential height are given in absolute quantities, Kelvin and meter, respectively.

It can be seen that a negative systematic difference in bending angle corresponds to a negative systematic difference in refractivity but to a positive systematic difference in dry temperature. This oppositional behavior of refractivity and dry temperature results from the fact that refractivity at microwave frequencies is inversely proportional to dry temperature (atmospheric humidity is neglected) (Rieder and Kirchengast 2001). Systematic differences of geopotential height and pressure generally show a smoother behavior than bending angle, refractivity, and dry temperature because of smoothing effects realized by the hydrostatic integral.

The systematic difference between ECMWF and F3C/FM-4 is very small for all at-

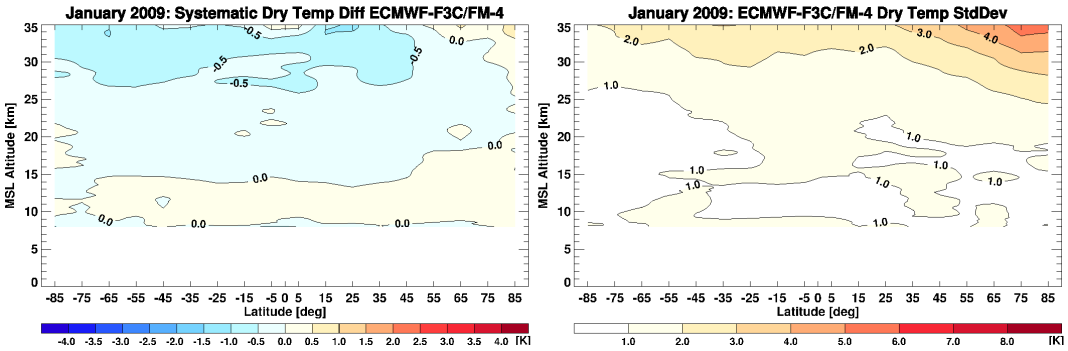

Figure 3.12: Systematic difference (left) and standard deviation of systematic difference (right) between ECMWF and F3C/FM-4 dry temperature climatologies in January 2009.

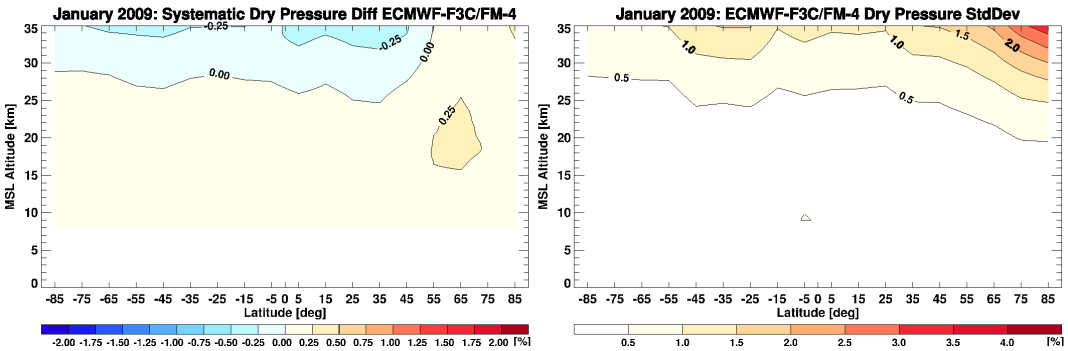

Figure 3.13: Systematic difference (left) and standard deviation of systematic difference (right) between ECMWF and F3C/FM-4 dry pressure climatologies in January 2009.

mospheric parameters, which partly results from the fact that ECMWF assimilates RO data since December 2006. For bending angle climatologies it amounts approximately to 0.25 % nearly everywhere between 10 km and 35 km. The corresponding standard deviation is most pronounced in the tropical tropopause, where it exceeds 3.5 %. Beside the tropical tropopause it increases with height yielding approximately 2.0 % above 30 km. It is not symmetric with respect to the equator but somewhat more pronounced in the northern winter hemisphere. Refractivity climatologies of ECMWF and F3C/FM-4 correspond to approximately +0.25 % nearly everywhere in the considered domain except for high altitudes (35 km), where the systematic difference becomes slightly negative. The standard deviation of the systematic difference remains within the limits of 1.0 % between 8 km and 30 km. The systematic dif-

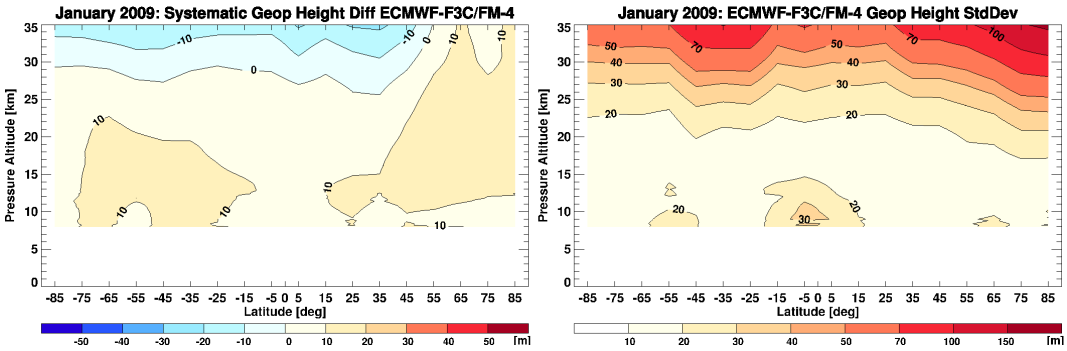

Figure 3.14: Systematic difference (left) and standard deviation of systematic difference (right) between ECMWF and F3C/FM-4 dry geopotential height climatologies in January 2009.

ference between dry temperature climatologies shows a height dependent pattern as it becomes larger than 0.5 K only above approximately 27 km. Beyond 50°N this increase with height cannot be observed but this region features a very large standard deviation (>3 K) above 30 km. Dry pressure climatologies correspond to ±0.25 % almost everywhere between 8 km and 35 km. The standard deviation remains smaller than 1.0 % in most parts between 8 km and 35 km. In the same region, the systematic difference of geopotential height is smaller than ±20 m. Within the core region of RO data (8 km to 30 km), the standard deviation of the systematic difference generally remains smaller than 40 m (exception: high northern winter hemisphere at high altitudes).

The excellent agreement between ECMWF analysis fields and F3C/FM-4 climatologies results from the fact that ECMWF assimilates RO data since December 12, 2006. However, as shown in the next section, there have been considerable changes of the systematic difference between ECMWF and RO data before December 2006.

3.3.3 Temporal Evolution of the Systematic Difference Between ECMWF and CHAMP Data

Figure 3.15 to Figure 3.16 depict latitude-height zonal bands of the systematic difference of bending angle (left) and dry temperature (right) between ECMWF and CHAMP for July from 2002 to 2008. The temporal evolution of the systematic difference shows some remarkable features from 2002 to 2006 but a significant decrease of the systematic difference is noticeable in 2007.

The first well pronounced feature is a wave-like bias structure, which appears during 2002 to 2005 in the southern winter polar vortex. It is most pronounced in 2003 (bending angle deviations exceeding ±4 %, dry temperature deviations oscillating

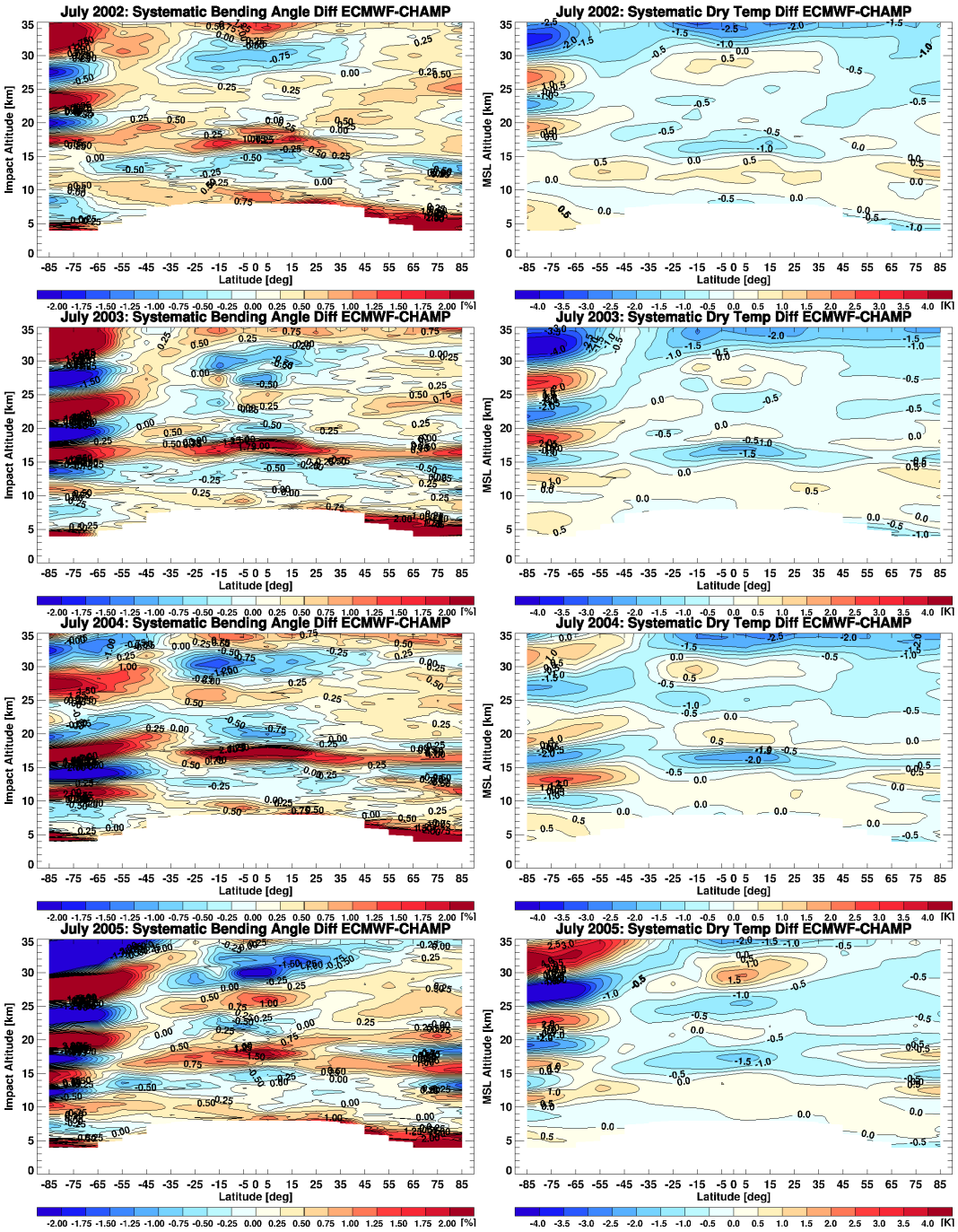

Figure 3.15: Systematic difference between ECMWF and CHAMP bending angle climatologies (left) and dry temperature climatologies (right) in July from 2002 to 2005.

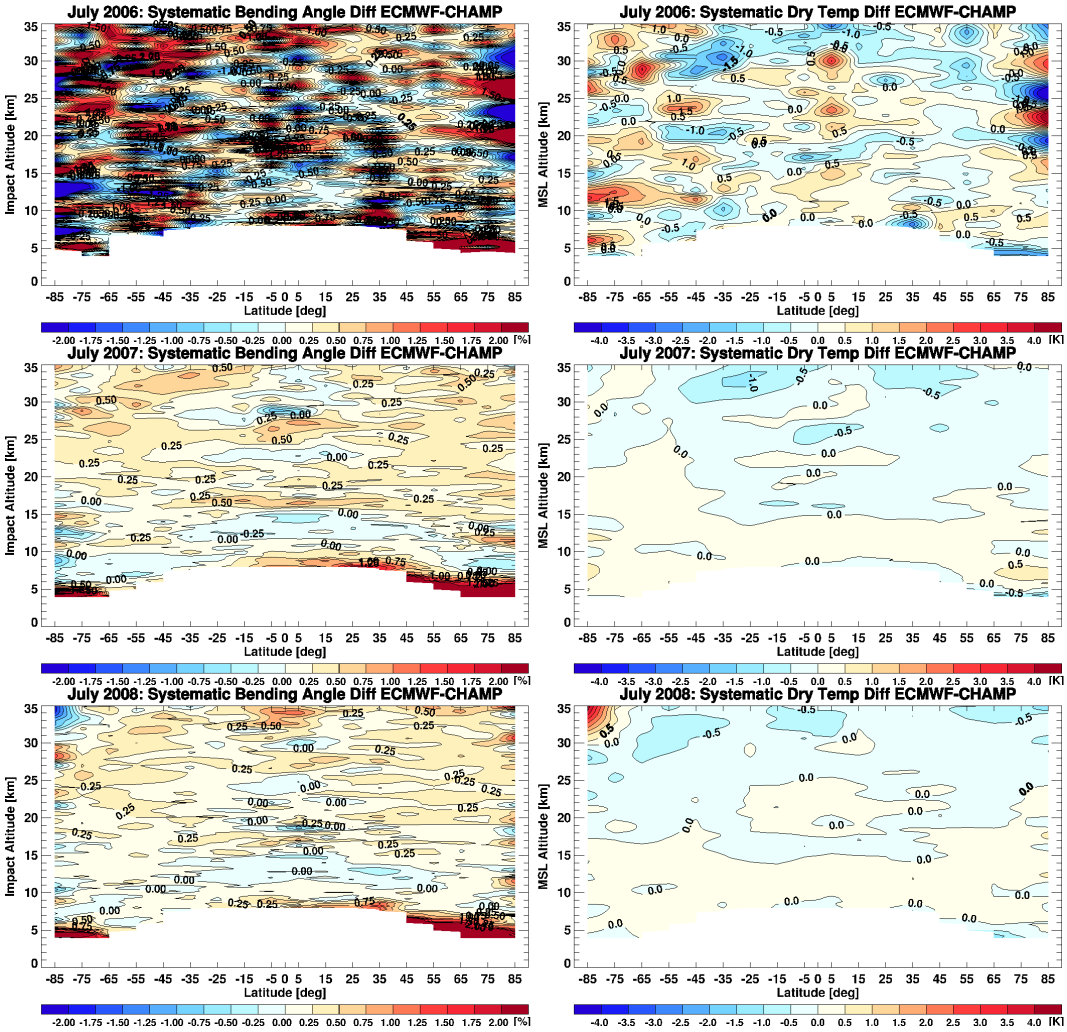

Figure 3.16: Systematic difference between ECMWF and CHAMP bending angle climatologies (left) and dry temperature climatologies (right) in July from 2006 to 2008.

between −4.5 K and +3 K) and 2005 (bending angle deviations exceeding −5 % and +6.5 %, dry temperature deviations exceeding −6.5 K and +5 K), when the phase changed its sign. Due to technical problems in July 2006 there are only few CHAMP data globally available (138 high quality profiles), which have been incorporated in the climatology. However, since the systematic difference does not depend on the number of measurements (it only affects its variability), it can be noticed that the wave-like bias almost disappeared in the southern hemisphere but a similar structure appeared in the northern hemisphere. The same result has been obtained by Foelsche et al. (2008*b*) and Foelsche et al. (2009*b*) who analyzed a combined record of CHAMP and Gravity Recovery And Climate Experiment (GRACE)-A data in JJA 2006. With the assimilation of RO data at ECMWF this conspicuous bias between ECMWF and CHAMP entirely disappeared.

Since changes in the systematic differences always were accompanied with changes in the assimilation system (changes in the assimilation scheme or additional data in the assimilation system) this bias can clearly be attributed to the ECMWF data. Furthermore, this feature is far beyond the error characteristics of RO data (Foelsche et al. 2008*b*). The wave-like bias was caused by deficiencies in the representation of the austral polar vortex in ECMWF analyses (Gobiet et al. 2005).

Another well pronounced systematic difference is visible in the tropical tropopause, where the systematic difference is positive in bending angle and negative in dry temperature until 2005. A negative dry temperature systematic difference corresponds to systematically warmer CHAMP temperatures than ECMWF temperatures. While the wave-like bias structure at high southern latitudes is observable only during southern hemispheric winter until 2005, the difference in the tropical tropopause can be noticed during all seasons until February 2006 when the ECMWF assimilation system increased its vertical resolution from L60 to L91. Consequently, this feature was caused by the weak representation of tropopause height variability in ECMWF operational analyses (Borsche et al. 2007).

The third conspicuous systematic difference between ECMWF analyses and CHAMP climatologies occurs at low latitudes between 28 km and 32 km. A negative bending angle systematic difference of −0.75 % to −2.0 % is accompanied with a positive dry temperature systematic difference of +0.5 K to +1.5 K. After the upgrade of the ECMWF model in February 2006 this feature also disappeared.

Above 32 km a further systematic deviation between ECMWF analyses and CHAMP climatologies can be detected. This systematic difference is the only one, which remains until 2008, even though its magnitude significantly decreased since RO data are assimilated at ECMWF. While the bending angle systematic difference exceeds +0.75 % until 2006, it only amounts to +0.25 % to +0.5 % afterward. Currently, the dry temperature systematic difference between ECMWF and RO data amounts to +0.5 K.

Differences to other documented systematic differences between ECMWF analyses

and CHAMP (Gobiet et al. 2005; Borsche et al. 2007; Foelsche et al. 2008*b;* Foelsche et al. 2009*b*) arise from different input data used in the OPS retrieval (University Corporation for Atmospheric Research (UCAR) input data rather than German Research Centre for Geosciences (GFZ) input data) and from different correlation lengths used within the statistical optimization of bending angle ($L_{\mathrm{bg}} = 10$ km and $L_{\mathrm{obs}} = 2$ km rather than $L_{\mathrm{bg}} = 30$ km and $L_{\mathrm{obs}} = 5$ km). These changes in particular affect the magnitude of systematic differences at high altitudes.

3.3.4 Systematic Difference Between ECMWF Analyses/Reanalyses and GPS/MET

The satellite mission Global Positioning System/Meteorology (GPS/MET) was the first RO mission, which probed the Earth's atmosphere. GPS/MET data are currently available within intermittent periods in 1995 and 1997. A large number of measurements, sufficient to build atmospheric climatologies is only available in October 1995 and February 1997. The number of high quality RO profiles in October 1995 amounts to 1092, in February 1997, 1374 profiles of high quality have been obtained[4].

From September 1991 until March 1999 operational ECMWF analysis fields had a vertical resolution of 31 levels. The top four levels were located at 10 hPa, 30 hPa, 50 hPa, and 70 hPa (Untch et al. 1998), which correspond to approximately 32 km, 25 km, 21 km, and 19 km, respectively. As already described in Chapter 1, ECMWF data are used for bending angle initialization at high altitudes. However, above the top-most level, data are pieced together with MSIS data, which are used up to 120 km. For this reason, the bending angle initialization with ECMWF L31 data (nearly) equals a bending angle initialization with MSIS.

Another data set available at ECMWF is ERA-40. This data set is available from 1957 to 2002 and has a vertical resolution of 60 levels. The top-most level is located at 0.1 hPa, which corresponds to approximately 60 km (cf. Figure 3.3).

Figure 3.17 and Figure 3.18 show the systematic difference (left) and the standard deviation of the systematic difference (right) between ECMWF operational analysis fields and GPS/MET climatologies (top) and between ERA-40 fields and GPS/MET climatologies (bottom) for dry temperature.

In October 1995 and in February 1997 the systematic difference between ECMWF operational analysis fields and GPS/MET climatologies is distinctively more pronounced than the systematic difference between ERA-40 fields and GPS/MET climatologies. This is primarily caused by the coarse vertical grid of operational analyses

[4]These numbers refer to the operational OPSv54 retrieval, where ECMWF Re-Analysis (ERA)-40 fields have been used for the initialization of bending angle. If operational ECMWF analysis fields have been used, the number of profiles is somewhat smaller (1084 high quality profiles in October 1995 and 1334 high quality profiles in February 1997).

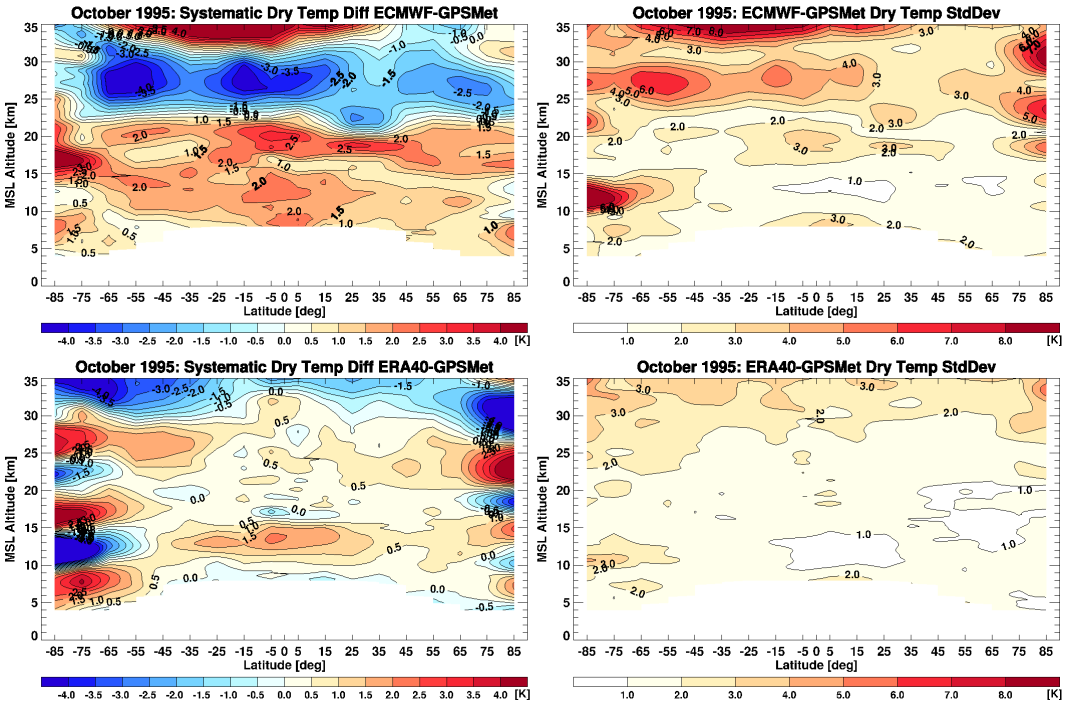

Figure 3.17: Systematic difference (left) and standard deviation of the systematic difference (right) between ECMWF and GPS/MET dry temperature climatologies in October 1995. The upper panels show deviations to ECMWF operational analysis fields, the bottom panels depict deviations to ERA-40 fields.

at that time and the resulting weak representation of atmospheric variability at high altitudes.

Analyzing different middle-atmosphere climatologies, Randel et al. (2004) found a cold temperature bias in the upper stratosphere and an oscillatory vertical bias structure in ERA-40 data, especially large over Antarctica. Both features can also be observed in Figure 3.17 and Figure 3.18 (top right panels), more pronounced in October 1995 than in February 1997. In October 1995 the temperature difference between ERA-40 and GPS/MET amounts up to -1.5 K at low latitudes above 33 km, it increases to more than -4 K at high southern latitudes. The wave-like bias structure (similar to that observed in CHAMP data) occurs at high southern and high northern latitudes in October and oscillates between $+4$ K and -4 K. In February 1997 the bias structure is only observed at high southern latitudes.

Compared to radiosonde data, Randel et al. (2004) found a (small) warm bias in ERA-40 data in the tropical tropopause region. The same bias is visible between

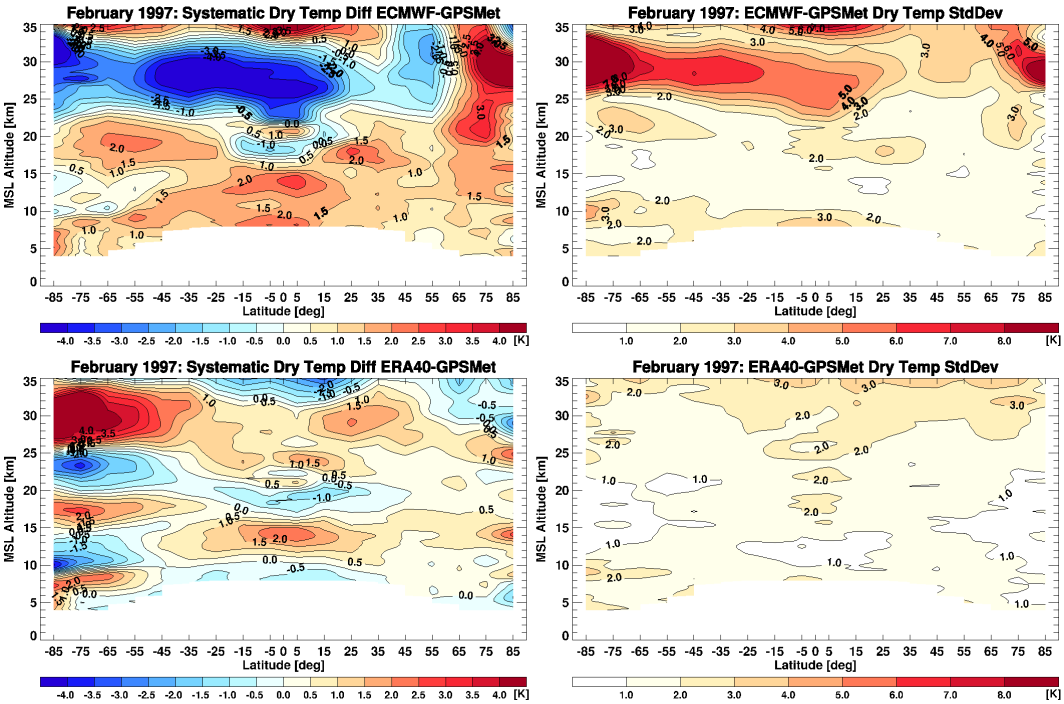

Figure 3.18: Systematic difference (left) and standard deviation of the systematic difference (right) between ECMWF and GPS/MET dry temperature climatologies in February 1997. The upper panels show deviations to ECMWF operational analysis fields, the bottom panels depict deviations to ERA-40 fields.

ERA-40 and GPS/MET. It amounts to 1.5 K in October 1995 and to 2.0 K in February 1997.

The standard deviation of the systematic difference is also more pronounced between ECMWF operational analyses and GPS/MET than between ERA-40 and GPS/MET. Again, this results from the low vertical resolution of ECMWF operational analysis fields in the nineties of the twentieth century.

Although GPS/MET data are the first RO data available from the Earth's atmosphere, these results underpin the reliability and utility of RO data to detect deficiencies in other climate data sets.

3.3.5 Calculation of the Sampling Error of RO Climatologies

Because of discrete sampling times and locations even perfect measurements (without any observational error) yield a sampling error in a climatology. The sampling error can be estimated, when the times and locations of RO events are known. The

use of an adequate reference atmosphere (e.g., ECMWF data) enables to estimate the sampling error even for future satellite missions knowing their orbit characteristics and therewith their measurement locations.

The sampling error of RO climatologies is computed separately for each bin in forming the difference between the average of all co-located ECMWF profiles within the bin, and the "true" reference mean of the bin (Foelsche et al. 2008*b*):

$$\Delta x_{\mathrm{SE}}(z_j, \varphi_k, \lambda_l) = x_{\mathrm{coloc}}(z_j, \varphi_k, \lambda_l) - x_{\mathrm{true}}(z_j, \varphi_k, \lambda_l). \tag{3.9}$$

$x_{\mathrm{coloc}}(z_j, \varphi_k, \lambda_l)$ and $x_{\mathrm{true}}(z_j, \varphi_k, \lambda_l)$ are calculated following the averaging strategy described in Section 3.2. Remember that the "true" reference mean was derived from 4D ECMWF fields using the complete spatial-temporal field.

The sampling error contains a random and a systematic component. The random component is caused by atmospheric variability, which is not adequately sampled by the satellite. High atmospheric variability (e.g., at high latitudes during wintertime) demands a large number of measurements to minimize the sampling error, whereas low atmospheric variability (e.g., in the tropics) is captured by a smaller number of measurements. The random component of the sampling error is increasingly reduced by averaging over longer timescales and/or larger spatial regions as well as by increasing spatial and temporal density of observations if so becoming available.

The systematic component of the sampling error results from systematic spatial and temporal undersampling. The spatial component stems from an inhomogeneous spatial sampling. To give an example, few measurements are taken between 85°N/S and 90°N/S. The reason for this is the small inclination of GPS satellites ($i \approx 55°$), which renders measurements beyond 85° latitude very sparse.

A detailed discussion about the sampling error (and its local time component) follows in Chapter 5. Here I only want to show some examples. One focus lies on the specific effect of "dry sampling", which is the main reason, why atmospheric climatologies are cut off at different height levels in the troposphere.

3.3.6 Dry Sampling Error

In the lower and middle troposphere the presence of water vapor limits the performance of the Geometric Optics (GO) retrieval, which is applied to extract atmospheric parameters from RO measurements. Since small-scale atmospheric structures effect refraction of radio waves, moist atmospheric conditions can only be inverted using a Wave Optics (WO) retrieval.

The analysis of the penetration depth of RO data from the OPSv54 GO retrieval yields a significant deeper penetration depth of RO profiles in dry atmosphere conditions compared to moist atmosphere conditions. Figure 3.19 exemplarily shows the penetration depth of CHAMP RO profiles in January 2008 (top panel) and the corresponding monthly mean total column water vapor (bottom panel) as provided by

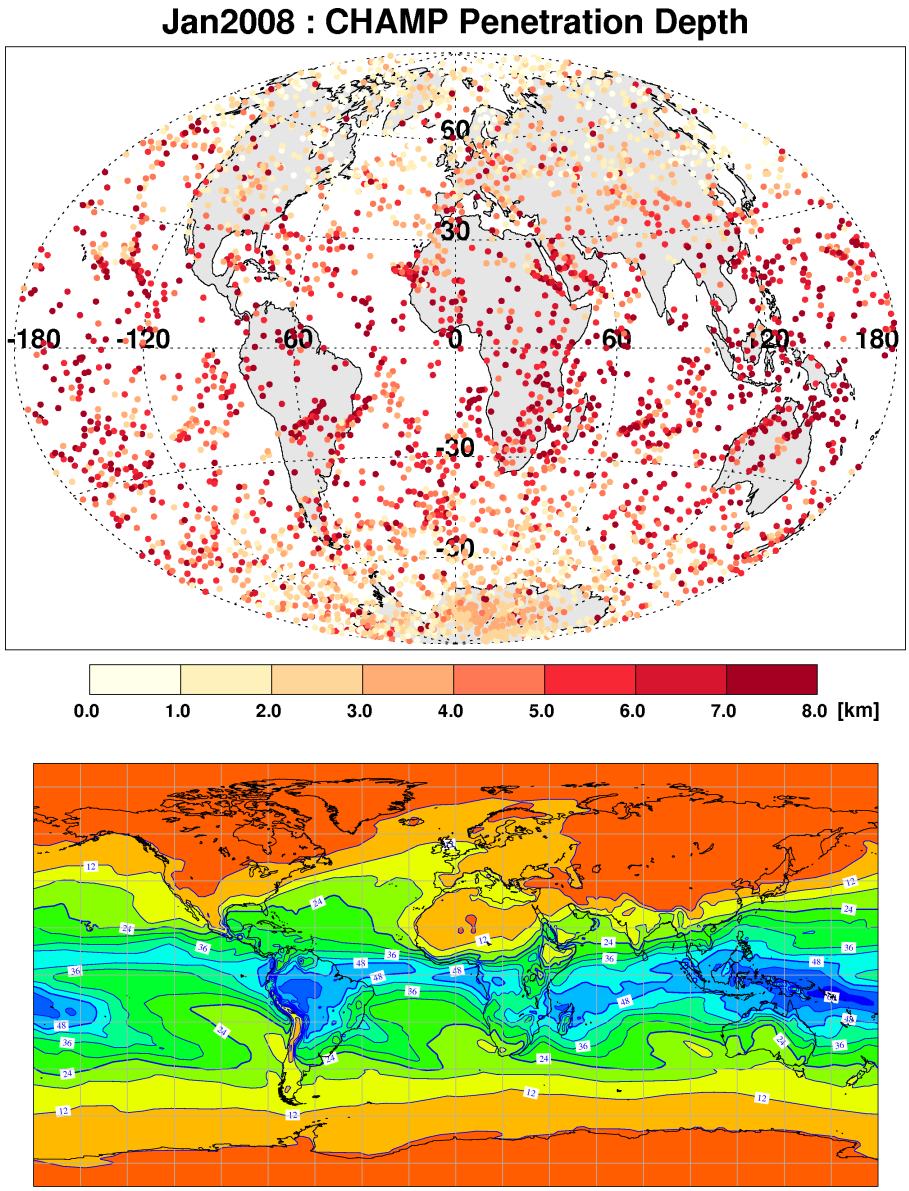

Figure 3.19: Penetration depth of CHAMP profiles (top) and total column water vapor as provided by ECMWF (bottom) in January 2008.

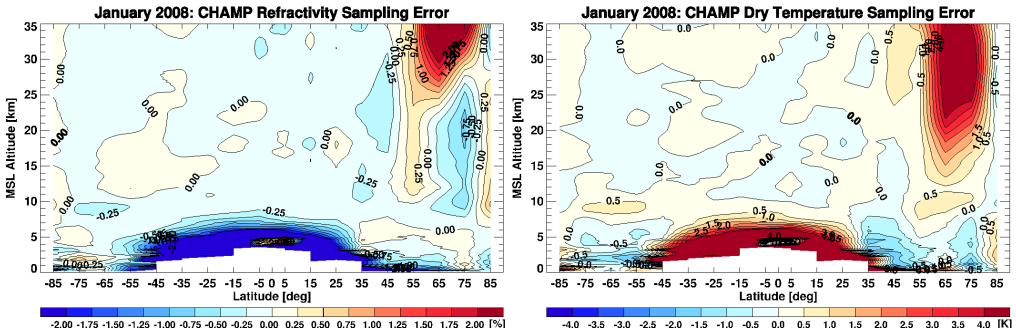

Figure 3.20: CHAMP refractivity and dry temperature sampling error in January 2008. The "dry air sampling error", which depends on atmospheric humidity and thus occurs in the lower troposphere, is negative in refractivity and positive in dry temperature.

ECMWF. While most profiles penetrate below 2 km at high latitudes (beyond 60°) where atmospheric humidity is small, low latitude profiles (equatorwards of 30°) rarely reach below 5 km. However, there are also some tropical profiles penetrating below 2 km. The comparison between the penetration depth of these profiles and the monthly mean total column water vapor yields that these profiles are located in drier atmospheric regions. In the Pacific ocean, westwards of South America, e.g., where the cold Humboldt current causes lower atmospheric moisture content, CHAMP profiles sometimes penetrate down to the lowest atmospheric layers.

If the lowest part of the atmosphere is sampled predominantly in dry air conditions rather than moist air conditions, the resulting climatology features a "dry sampling error". Since humid air conditions have larger refractivities than dry air conditions, this selective sampling results in a systematic under-representation of the "true" mean refractivity. The lowest part of the atmosphere is therefore biased towards smaller refractivities, which is equivalent to higher dry temperatures (Foelsche et al. 2008*b*).

Figure 3.20 depicts the CHAMP refractivity and dry temperature sampling error in January 2008. The sampling error is shown for all data available (i.e., all altitudes between the surface and 35 km). The increasing amount of moisture in the free atmosphere at low latitudes is reflected in a huge negative refractivity and a huge positive dry temperature sampling error. It exceeds −20 % and +15 K in the tropical lower troposphere in refractivity and dry temperature, respectively. At high latitudes, where atmospheric moisture is small, the "dry sampling error" becomes negligible.

The "dry sampling error" is the main reason for the climatologies to be cut-off. The cut-off altitude is not constant but rather depends on geographic latitude. It

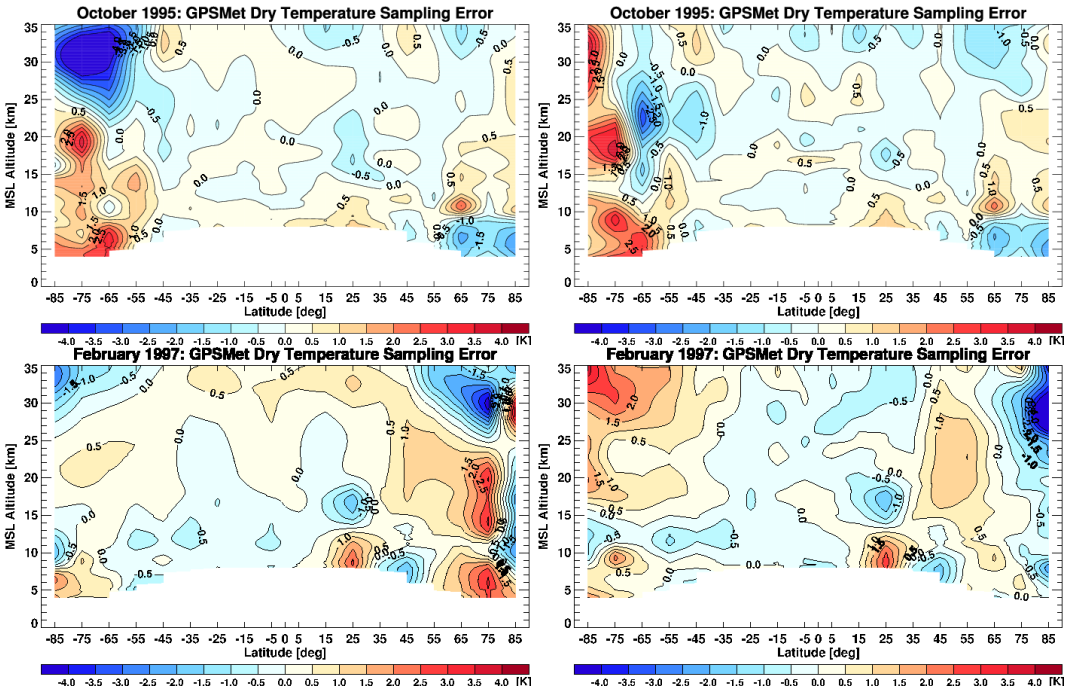

Figure 3.21: Sampling error of GPS/MET dry temperature climatologies in October 1995 and February 1997. The left panel shows sampling error estimation using operational analysis fields provided by ECMWF, the right panel depicts sampling error estimations from ERA-40 fields.

amounts to 8 km between 30°N and 30°S, 7.5 km between 30°N/S and 40°N/S, 6 km between 40°N/S and 50°N/S, 5 km between 50°N/S and 60°N/S, and 4 km between 60°N/S and 90°N/S.

3.3.7 Sampling Error of GPS/MET Climatologies

Despite the comparatively small number of RO measurements provided by GPS/MET, the sampling error of the climatologies is comparatively small. Figure 3.21 shows the sampling error of GPS/MET climatologies in October 1995 (top) and in February 1997 (bottom). Left panels depict the estimated sampling error using ECMWF operational analysis fields, right panels show the sampling error if it is estimated from ERA-40 fields.

At mid- and low latitudes the sampling error rarely exceeds 0.5 K in both months. However, at high latitudes the number of measurements is too small to capture atmospheric variability. The sampling error becomes significant beyond approximately 60°.

Interestingly, there is a remarkable difference between the sampling error estimation using ECMWF operational analysis and ERA-40 fields, which is most pronounced at high latitudes. This behavior points at differences in the models quality and performance (see Figure 3.17 and Figure 3.18).

GPS/MET data have been used in an atmospheric temperature change detection study by Steiner et al. (2009). They analyzed a combined record of GPS/MET and CHAMP data and investigated climate trends detected in GPS RO data from 1995 to 2008. To be independent from the sampling characteristics of both satellites, Steiner et al. (2009) subtracted the sampling error before piecing together temperature climatologies of GPS/MET and CHAMP and calculating trend statistics. Since the estimated GPS/MET sampling error significantly depends on the model used, they analyzed data only equatorwards of 50°.

3.3.8 Long-Term Stability of the Sampling Error

The number of RO measurements and their distribution in space and time primarily depend on the number of transmitters and receivers and on the orbit characteristics of Low Earth Orbit (LEO) and GPS satellites. While the number of GPS satellites increased from 27 in 2002 to 32 in 2008 (Suppan 2010), the orbit altitude of LEO satellites generally decreases with time due to atmospheric drag.

Suppan (2010) investigated the long-term stability of the sampling error due to orbit changes of the CHAMP satellite and changes in the GPS constellation from 2002 to 2008. He used the End-to-End Generic Occultation Performance Simulation and Processing System (EGOPS) software to simulate distributions of RO measurements for different orbit developments and estimated the sampling error using ECMWF analysis fields. His trend analysis did not reveal any significant trend in any simulation. He concluded that neither varying satellite orbits nor the increasing number of transmitter satellites yielded an influence on the long-term stability of the sampling error.

3.4 Summary of CLIPS

The CLIPS, developed at WEGC, provides RO climatologies of different satellites and their error estimations. It utilizes single RO measurements and combines them in an optimal way to compute climatologies of different atmospheric parameters. The averaging strategy aims at minimizing potential sampling errors, which are estimated using ECMWF analysis data. The common horizontal resolution of RO climatologies is 10° zonal bands.

Sampling errors are caused by uneven sampling in space and time as well as by the specific effect of “dry sampling”. The “dry sampling error”, which depends on the content of atmospheric humidity, manifests itself as negative refractivity

sampling error and positive temperature sampling error. It exceeds −20 % and +15 K in refractivity and dry temperature, respectively. The dry sampling error can be reduced applying a WO RO retrieval because that one is able to deal with signal degradation due to atmospheric multipath. However, a WO retrieval cannot "extend" a signal which is interrupted. Since the OPSv54 retrieval is a GO retrieval, the simple way we currently deal with the dry sampling error is to cut off atmospheric climatologies. The cut off altitude depends on geographic latitude (i.e., content of atmospheric humidity).

RO climatologies can be used to detect deficiencies in other climate data sets. The comparison of GPS/MET RO data and ECMWF analysis fields from 1995 and 1997 reveals erroneous atmospheric regions of ECMWF data. They result from the coarse vertical grid of operational analyses at that time and the resulting weak representation of atmospheric variability at high altitudes. Better agreement is obtained between GPS/MET RO and ERA-40 data but GPS/MET data reveal a cold temperature bias in the upper stratosphere and an oscillatory vertical bias structure at high latitudes in the ERA-40 data set.

The temporal evolution of systematic differences between ECMWF operational analyses and CHAMP RO data yields that changes in the systematic difference are always accompanied with changes in the assimilation system. Therefore, the bias can clearly be attributed to ECMWF data. Since December 2006 RO data are assimilated at ECMWF and RO data and ECMWF analyses are in excellent agreement. Largest temperature differences are observed at high altitudes (above 30 km), where they exceed 0.5 K.

4 Consistency of RO Climatologies

The understanding of differences of Radio Occultation (RO) data derived from different satellites is crucial when utilizing the RO record for climate studies. Previous studies investigated the consistency of sets of co-located single RO profiles. Hajj et al. (2004) compared co-located occultations observed by CHAllenging Mini-Satellite Payload (CHAMP) and Satélite de Aplicaciones Científicas C (SAC-C). After removal of expected atmospheric variability they found that single profiles agree to within 0.5 K between 5 km and 20 km altitude. Schreiner et al. (2007) compared co-located FORMOSAT-3/COSMIC (F3C) profiles and found that the refractivity Root Mean Square (RMS) difference between 10 km and 20 km is less than 0.2 %.

Foelsche et al. (2009*a*) and Foelsche et al. (2009*b*) analyzed systematic differences between seasonal mean 10° zonal mean climatologies from CHAMP and F3C. They found that after subtraction of the estimated respective sampling errors, climatologies from different F3C satellites agree to within 0.1 K almost everywhere between 8 km and 35 km altitude. Differences between F3C and CHAMP climatologies rarely exceed 0.2 K provided that data from the same processing center are used.

In the following the approach of Foelsche et al. (2009*a*) and Foelsche et al. (2009*b*) is applied to investigate systematic differences of refractivity and dry temperature climatologies between CHAMP, GRACE-A (Gravity Recovery And Climate Experiment), F3C, and MetOp-A (Meteorological Operational). Since at Wegener Center for Climate and Global Change (WEGC) MetOp-A data are currently only available from October 2007, the investigation focuses on this particular month. The focus lies on different features, which result from sampling pattern caused by orbit characteristics (e.g., orbit inclination) and data availability, from data quality at high altitudes, and from systematic retrieval differences. The latter is investigated primarily for CHAMP data provided by different data centers.

4.1 Differences Resulting from Sampling Patterns

The satellite orbit altitude and inclination determine the geographic locations of RO events. While the orbit altitude determines the distance from the mean tangent point location to the Low Earth Orbit (LEO) satellite, the orbit inclination determines the geographical coverage of RO measurements. Only near-polar orbiting satellites have the potential to perform RO measurements at high latitudes.

Table 4.1: Number of level 1 data, retrieved profiles, and high quality profiles retrieved from CHAMP, GRACE-A, F3C, and MetOp-A in October 2007.

	Input Data	Retr. Profiles	QF = 0 Profiles	Percentage of QF = 0 profiles	
CHAMP	5516	5509	3644	64.1 %	(66.1 %)
GRACE-A	4200	4191	3554	84.8 %	(84.6 %)
F3C/FM-1	4085	3552	2173	61.2 %	(53.2 %)
F3C/FM-2	15873	14223	11188	78.7 %	(70.5 %)
F3C/FM-3	10137	9043	7110	78.6 %	(70.1 %)
F3C/FM-4	17807	16055	12301	76.6 %	(69.1 %)
F3C/FM-5	15659	14204	10791	76.0 %	(68.9 %)
MetOp-A	10408	10381	6957	67.0 %	(66.8 %)

4.1.1 Spatial and Temporal Sampling

The monthly number of occultation measurements per spacecraft does not only depend on the satellite equipment (i.e., tracking only setting or both, setting and rising occultations) but also on the satellites' "health". In October 2007, e.g., the solar panels of F3C/FlightModel (FM)-3 were stuck, which limited the power and payload operation for this spacecraft. While orbit raising of FM-1[1] limited the number of occultation measurements of this satellite, there was no contact to F3C/FM-6 during this particular month (CDAAC Team 2010).

Table 4.1 shows the total number of profiles (input data of the Occultation Processing System Version 5.4 (OPSv54) retrieval, retrieved profiles, and high quality profiles) in October 2007 for CHAMP, GRACE-A, the F3C satellites (FM-1 to FM-5), and MetOp-A. Right columns specify the percentage of high quality profiles (referred to the number of retrieved profiles and referred to the number of input data in parentheses).

In October 2007 most measurements are available from FM-4, the smallest number of profiles is delivered from FM-1 (orbit raising). CHAMP provides distinctively more measurements than GRACE-A but since more CHAMP profiles are of bad quality the number of high quality profiles is similar to that of GRACE-A. The total number of MetOp-A measurements received in Phase Locked Loop (PLL) mode is 20362. Since 9954 measurements stem from rising occultations, which do not contain valid L2 excess phase delays, the number of MetOp-A input data amounts to 10408.

The geographic distribution (i.e., latitudinal and longitudinal event statistics) of

[1] In April 2006 all satellites were launched on a single launch vehicle into a parking orbit with 520 km orbit altitude. Afterward the satellites were consecutively raised to 800 km. In October 2007, FM-2, FM-4, FM-5, and FM-6 already were in their final orbits, FM-3 was at 710 km altitude.

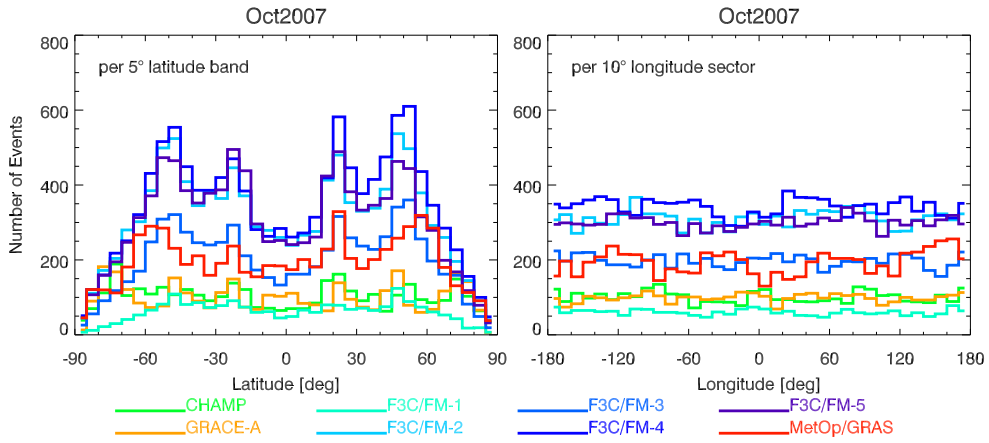

Figure 4.1: Event statistics as a function of latitude (number of RO events per 5° latitude band, left) and longitude (number of RO events per 10° longitude sector, right) in October 2007 for CHAMP, GRACE-A, FM-1, FM-2, FM-3, FM-4, FM-5, and MetOp-A.

high quality RO measurements performed in October 2007 is shown in Figure 4.1. The similar number of high quality profiles of CHAMP, GRACE-A, and F3C/FM-1 allows to investigate the impact of different orbit characteristics on the latitudinal distribution of RO events. While CHAMP and GRACE fly in an orbit with high inclination (87.2° and 89.0°, respectively), the F3C satellites are in orbits with only 72° inclination. The smaller inclination limits the number of RO events beyond 50°/55° latitude. While the number of F3C measurements continuously decreases beyond this latitude, it remains stable up to 80° latitude for CHAMP and GRACE-A . The latitudinal distribution of MetOp-A (orbit with 98.7° inclination) measurements, shows a peak at 60° latitude. The meridional event distribution (right panel) of all RO measurements is rather uniform.

Figure 4.2 depicts the daily number of high quality profiles in October 2007 for all satellites. While CHAMP and GRACE provide between 100 and 150 high quality profiles per day, the number MetOp-A profiles is somewhat larger than 200. Compared to the F3C satellites, CHAMP, GRACE, and MetOp-A continuously provide measurements in October 2007 and there is no single data gap. However, there are a lot of data gaps of FM-1 and FM-3. Each single F3C satellite is able to record about 400 high quality profiles per day.

All high quality profiles are used to build atmospheric climatologies. Differences between the satellites concerning spatial and temporal sampling are reflected in respective climatological sampling errors. Figure 4.3 depicts the sampling errors of CHAMP, GRACE-A, FM-1, FM-2, FM-3, FM-4, FM-5, and MetOp-A refractivity climatolo-

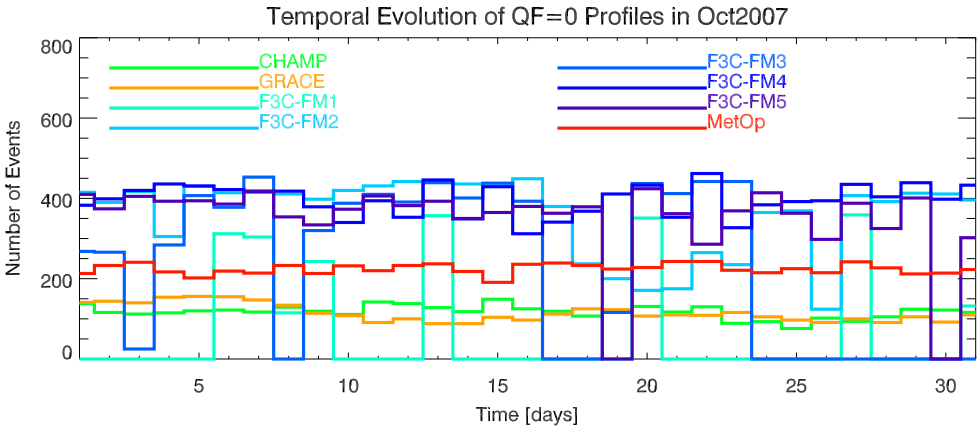

Figure 4.2: Daily number of high quality RO profiles in October 2007 for CHAMP, GRACE-A, FM-1, FM-2, FM-3, FM-4, FM-5, and MetOp-A.

gies. The sampling error is largest at high southern latitudes, where atmospheric variability is strong (southern hemisphere spring, breakdown of the polar vortex). While GRACE-A, FM-2, FM-3, and FM-5 refractivity sampling errors beyond 50°S are predominantly negative, the corresponding CHAMP, FM-1, and MetOp-A sampling errors are predominantly positive. To reveal the reasons for these different characteristics, it is necessary to have a closer look at temporal sampling at southern high latitudes.

The negative FM-3 sampling error exceeds −3.5 % at polar southern latitudes above 25 km. It results from uneven temporal FM-3 sampling because no measurements are performed at the end of the month (from October 24, 2007 until October 31, 2007). Compared to FM-3, sampling gaps of FM-1 are more homogeneously distributed in time. For that reason, the resulting sampling error remains within the limits of ±1 %.

At low latitudes all satellite climatologies feature sampling errors smaller than ±0.5 %. FM-4, which provides most atmospheric measurements during October 2007, features such a small sampling error in all geographic regions.

4.1.2 Differences in Refractivity and Dry Temperature Climatologies

Differences of monthly mean 10° zonal mean atmospheric climatologies derived from various RO satellite data from October 2007 are investigated relative to the satellite mean climatology. All utilized RO data stem from the same level 1 processing (University Corporation for Atmospheric Research (UCAR)/COSMIC Data Analysis and Archive Center (CDAAC), data version 2007.3200) except for MetOp-A, whose

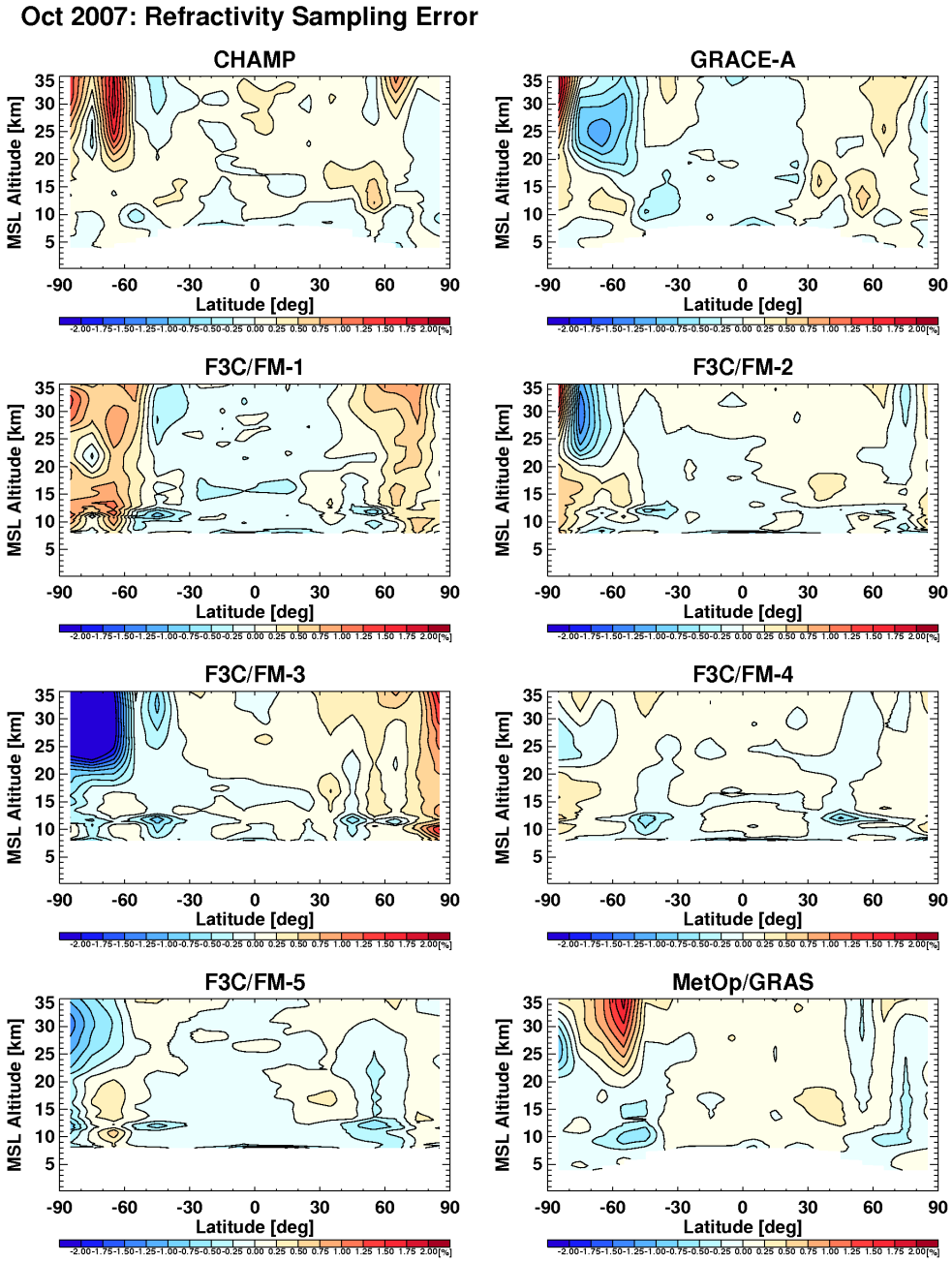

Figure 4.3: Refractivity sampling error in October 2007 for CHAMP, GRACE-A, FM-1, FM-2, FM-3, FM-4, FM-5, and MetOp-A.

Table 4.2: Mean disparities in refractivity climatologies with and without sampling error subtraction in October 2007. Mean values are calculated between 8 km and 35 km altitude. Last column represents deviations relative to the satellite mean with MetOp-A excluded.

	ΔN	$\Delta N^{\mathrm{SE\,sub}}$	$\Delta N^{\mathrm{SE\,sub}}$
CHAMP	0.10 %	−0.02 %	−0.01 %
GRACE-A	−0.06 %	−0.03 %	−0.02 %
F3C/FM-1	0.14 %	0.01 %	0.02 %
F3C/FM-2	−0.00 %	−0.01 %	0.00 %
F3C/FM-3	−0.15 %	0.01 %	0.02 %
F3C/FM-4	0.01 %	0.01 %	0.01 %
F3C/FM-5	−0.13 %	−0.03 %	−0.02 %
MetOp-A	0.10 %	0.06 %	—

level 1 data are only provided by the European Organization for the Exploitation of Meteorological Satellites (EUMETSAT). The comparison of CHAMP, GRACE, and F3C climatologies excludes retrieval differences going into the satellites' data disparities.

Figure 4.4 depicts latitude-height zonal bands of refractivity differences of CHAMP, GRACE-A, F3C, and MetOp-A relative to the satellite mean. Comparison with Figure 4.3 reveals that disparities are primarily caused by differences in sampling times and locations: first of all the deviations are determined by the sampling errors of each climatology.

The quantitative estimation of the sampling error allows to subtract it from a climatology. Systematic differences between data derived from different satellites are calculated from sampling error subtracted single satellites climatologies, which are compared to the sampling error subtracted satellite mean climatology.

Refractivity results are shown in Figure 4.5. Climatologies of all satellites agree to within 0.25 % everywhere between 8 km and 30 km altitude. Above 30 km, MetOp-A data feature somewhat higher refractivities (up to 0.5 %) compared to the satellite mean.

Table 4.2 shows mean refractivity deviations ΔN and $\Delta N^{\mathrm{SE\,subtracted}}$ of all satellites relative to the satellite mean averaged over the entire domain from 8 km to 35 km altitude. The last column represents mean deviations, which are calculated only from data following from the same processing chain (level 1 processing done by UCAR/CDAAC).

As expected, it is noticeable that the sampling error subtraction significantly reduces refractivity deviations. Strongest decrease is found for CHAMP, F3C/FM-1, and F3C/FM-3. After sampling error subtraction, refractivity climatologies are in

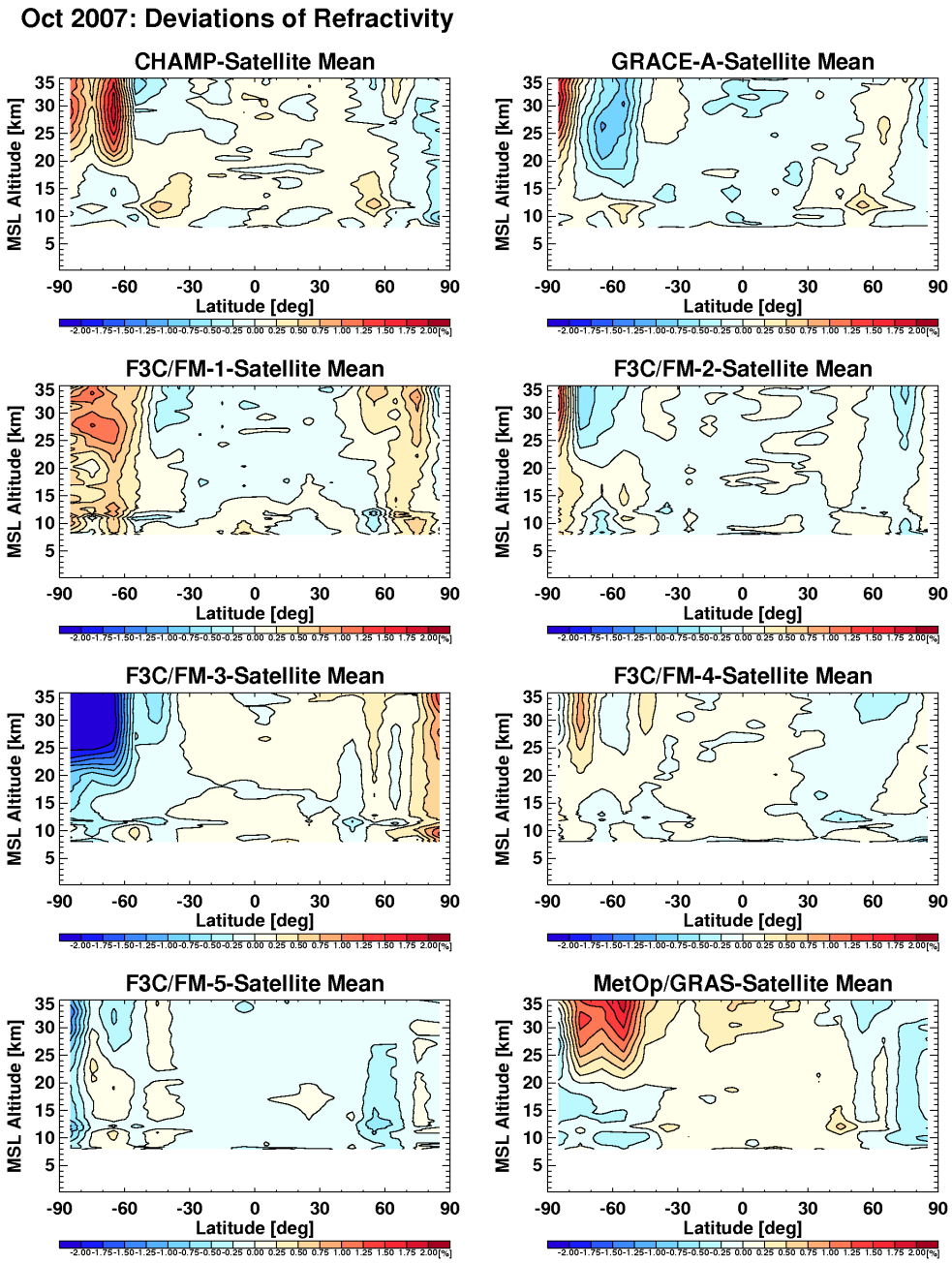

Figure 4.4: Differences between refractivity climatologies relative to the satellite mean climatology in October 2007. Results are shown for CHAMP, GRACE-A, FM-1, FM-2, FM-3, FM-4, FM-5, and MetOp-A.

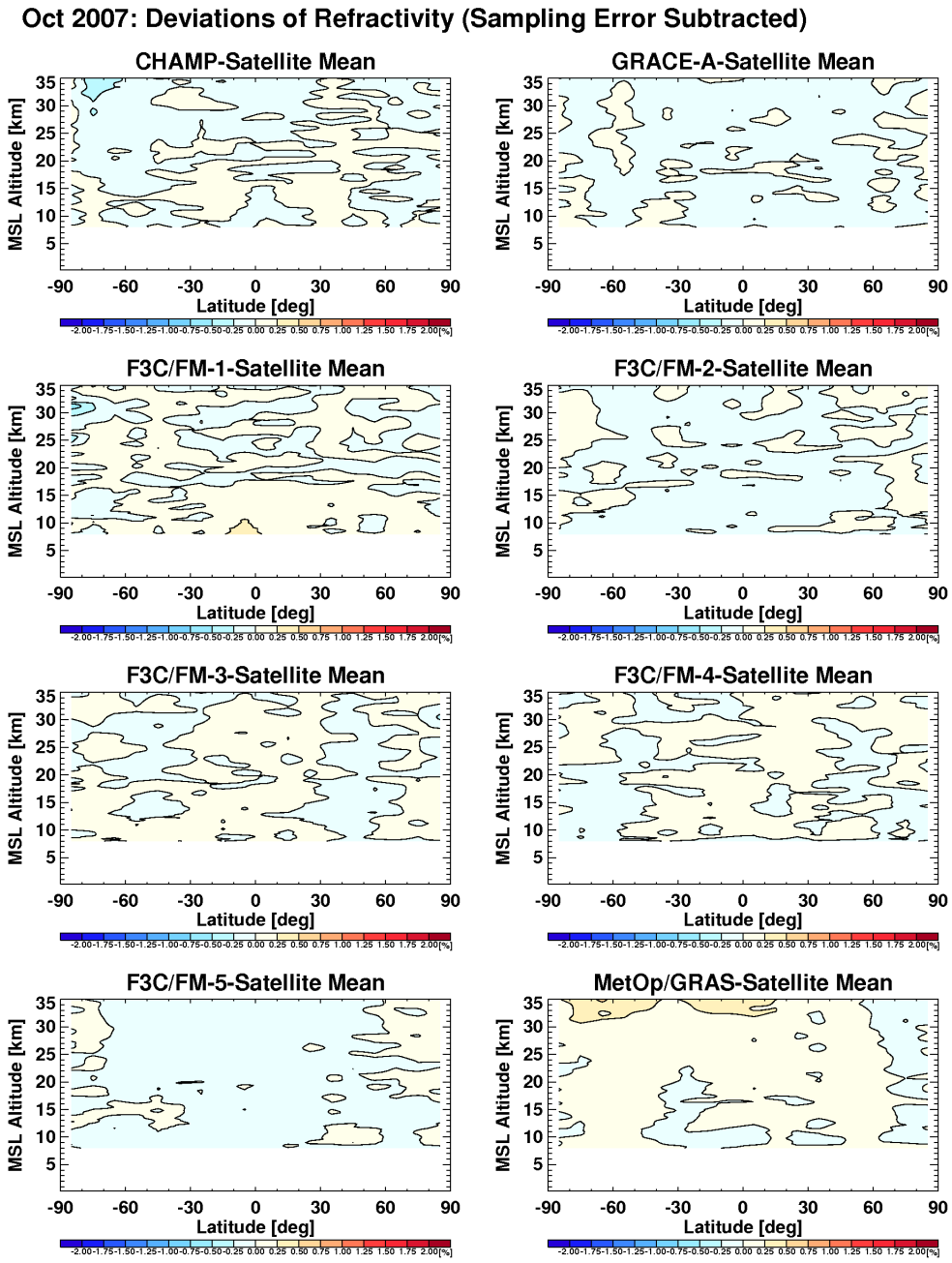

Figure 4.5: Differences between sampling error subtracted refractivity climatologies relative to the satellite mean climatology in October 2007. Results are shown for CHAMP, GRACE-A, FM-1, FM-2, FM-3, FM-4, FM-5, and MetOp-A.

Table 4.3: Mean disparities in dry temperature climatologies with and without sampling error subtraction in October 2007. Mean values are calculated between 8 km and 35 km altitude. Last column represents deviations relative to the satellite mean with MetOp-A excluded.

	ΔT	$\Delta T^{\mathrm{SE\,sub}}$	$\Delta T^{\mathrm{SE\,sub}}$
CHAMP	−0.02 K	−0.10 K	−0.07 K
GRACE-A	−0.03 K	−0.02 K	0.01 K
F3C/FM-1	−0.05 K	−0.04 K	−0.01 K
F3C/FM-2	−0.01 K	−0.00 K	0.03 K
F3C/FM-3	−0.14 K	−0.02 K	0.01 K
F3C/FM-4	0.01 K	0.00 K	0.03 K
F3C/FM-5	−0.05 K	−0.03 K	−0.00 K
MetOp-A	0.29 K	0.21 K	—

very good agreement with mean differences over the entire domain being smaller than 0.1 %. Larger refractivities as observed in MetOp-A climatologies at high altitudes (cf. Figure 4.5) are reflected in the largest mean value of 0.06 %. Excluding MetOp-A from these calculations, the differences between CHAMP, GRACE-A, and F3C data do not exceed ±0.02 %.

Figure 4.6 shows dry temperature deviations of all sampling error subtracted climatologies relative to the satellite mean. MetOp-A data feature a positive systematic difference from 90°S to 20°N and a negative systematic difference from 20°N to 90°N. These characteristics occur at all altitude levels but are most pronounced at highest altitudes (above 30 km), where they exceed 1 K. This very strong pronounced feature somewhat suppresses the differences between the other satellite data. However, it becomes apparent that CHAMP temperatures are slightly cooler than other satellite temperatures at high altitudes.

Table 4.3 specifies average differences in dry temperature climatologies calculated between 8 km and 35 km altitude. Interestingly, CHAMP dry temperature deviations relative to the satellite mean are larger after sampling error subtraction. The reason for that is that the temperature sampling error is mainly positive at high southern and high northern latitudes, which compensates negative systematic differences observed at high altitudes.

Large MetOp-A dry temperatures anomalies as observed in Figure 4.6 are reflected in a large mean disparity. Sampling error removed dry temperature climatologies of MetOp-A are warmer than those of CHAMP, GRACE-A, and F3C by 0.21 K. The other satellites are in very good agreement with each other. Especially F3C and GRACE climatologies are in excellent agreement. As mentioned above, CHAMP dry temper-

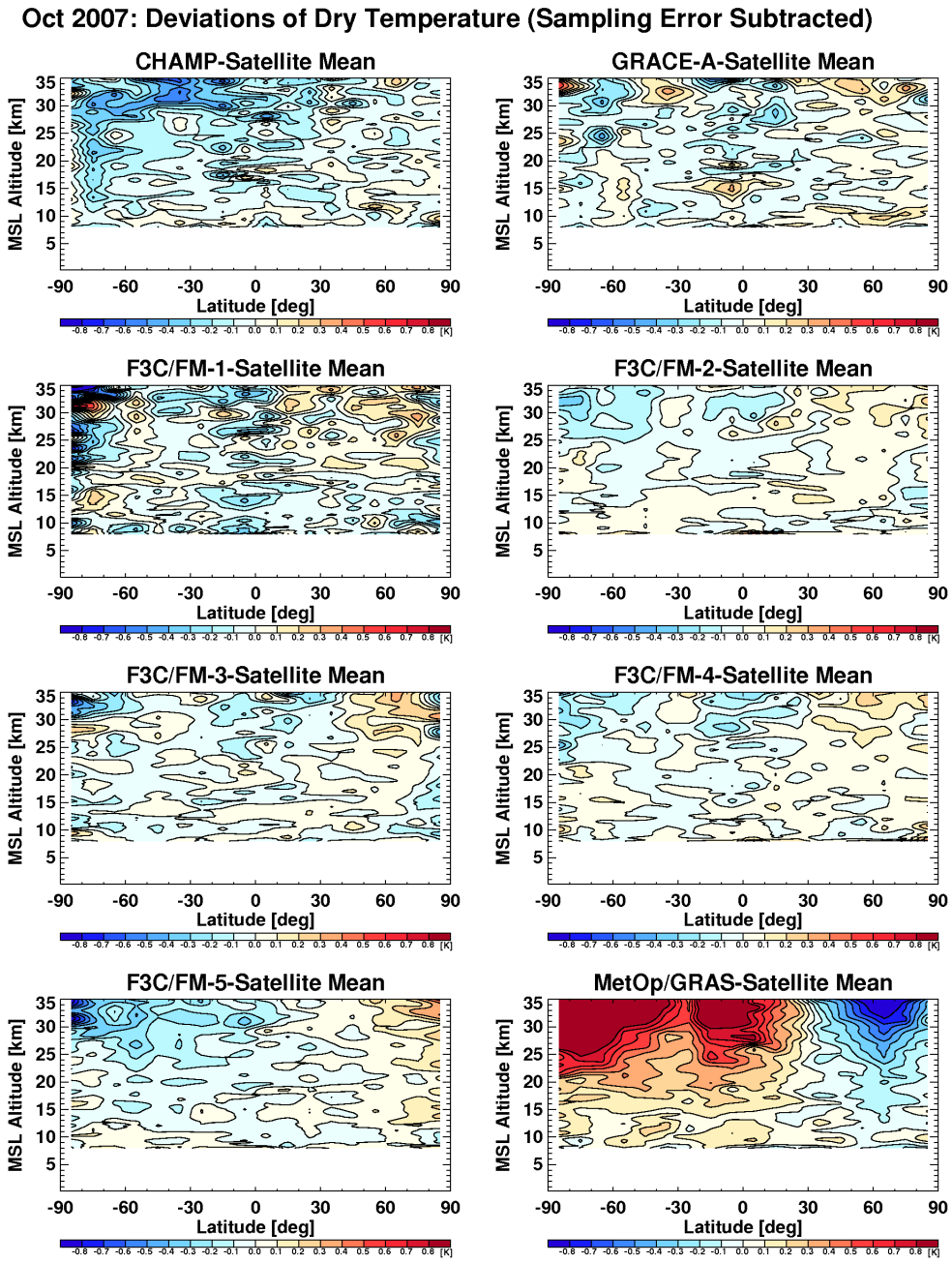

Figure 4.6: Differences between sampling error subtracted dry temperature climatologies relative to the satellite mean climatology in October 2007. Results are shown for CHAMP, GRACE-A, FM-1, FM-2, FM-3, FM-4, FM-5, and MetOp-A.

ature data are somewhat cooler than those of the other satellites. The reason for negative systematic difference of CHAMP compared to the other satellites is analyzed in the next section.

4.2 Data Quality at High Altitudes

As already mentioned several times, bending angle quality at high altitudes (50 km to 80 km) determines the degree of background information utilized in the retrieval (cf. Chapter 2).

The zRAER50 value is the transition (impact) height, where background information used for bending angle initialization equals observation information. Figure 4.7 depicts zonal mean zRAER50 values in October 2007 for all satellites. Background information penetrates towards lowest altitudes in the CHAMP data set where the mean transition height (averaged over all latitudes) lies at approximately 40 km. Mean zRAER50 values of the other satellites are 44 km (F3C/FM-5), 45 km (F3C/FM-1), 46 km (GRACE-A), 47 km (F3C/FM-2, F3C/FM-3, F3C/FM-4), and 57 km (MetOp-A). All satellite data feature lowest zRAER50 values at high northern latitudes. While MetOp-A data, e.g., are observation dominated below 60 km between 30°S and 40°S, the transition height decreases to 48 km at northern polar latitudes (between 80°N and 90°N). This may result from the fact that comparatively more bending angle profiles retrieved at high latitudes feature observational errors, which have been adjusted by internal quality control mechanisms (i.e., set to 10 μrad or 50 μrad, cf. Chapter 2, Figure 2.5).

The main result of zRAER50 values shown in Figure 4.7 is that background information penetrates towards lower altitudes (lower compared to the other satellite data) in the CHAMP data set. Furthermore, when concentrating on a given altitude level, lowest amount of background information is present in the MetOp-A data set. Please be aware that zRAER50 values are derived from bending angle data but the Abel integral and the hydrostatic integral applied in the inversion process propagate background information towards lower altitudes (approximately 1.5 scale heights) in derived atmospheric parameters (e.g., refractivity, temperature).

As seen in Chapter 3, European Centre for Medium-Range Weather Forecasts (ECMWF) data are somewhat cooler than RO data at high altitudes (the difference of ECMWF analyses to F3C RO data, e.g., amounts to 0.5 K at 35 km altitude, cf. Chapter 3, Figure 3.12). Since ECMWF data are used as background information for bending angle initialization (ECMWF short-term forecasts), this bias propagates further in RO data. This is the reason why CHAMP data are somewhat cooler than other satellite data at high altitudes. However, the cause for MetOp-A temperatures being warmer than other satellite temperatures in the southern hemisphere but colder at mid- and high latitudes in the northern hemisphere (most pronounced at

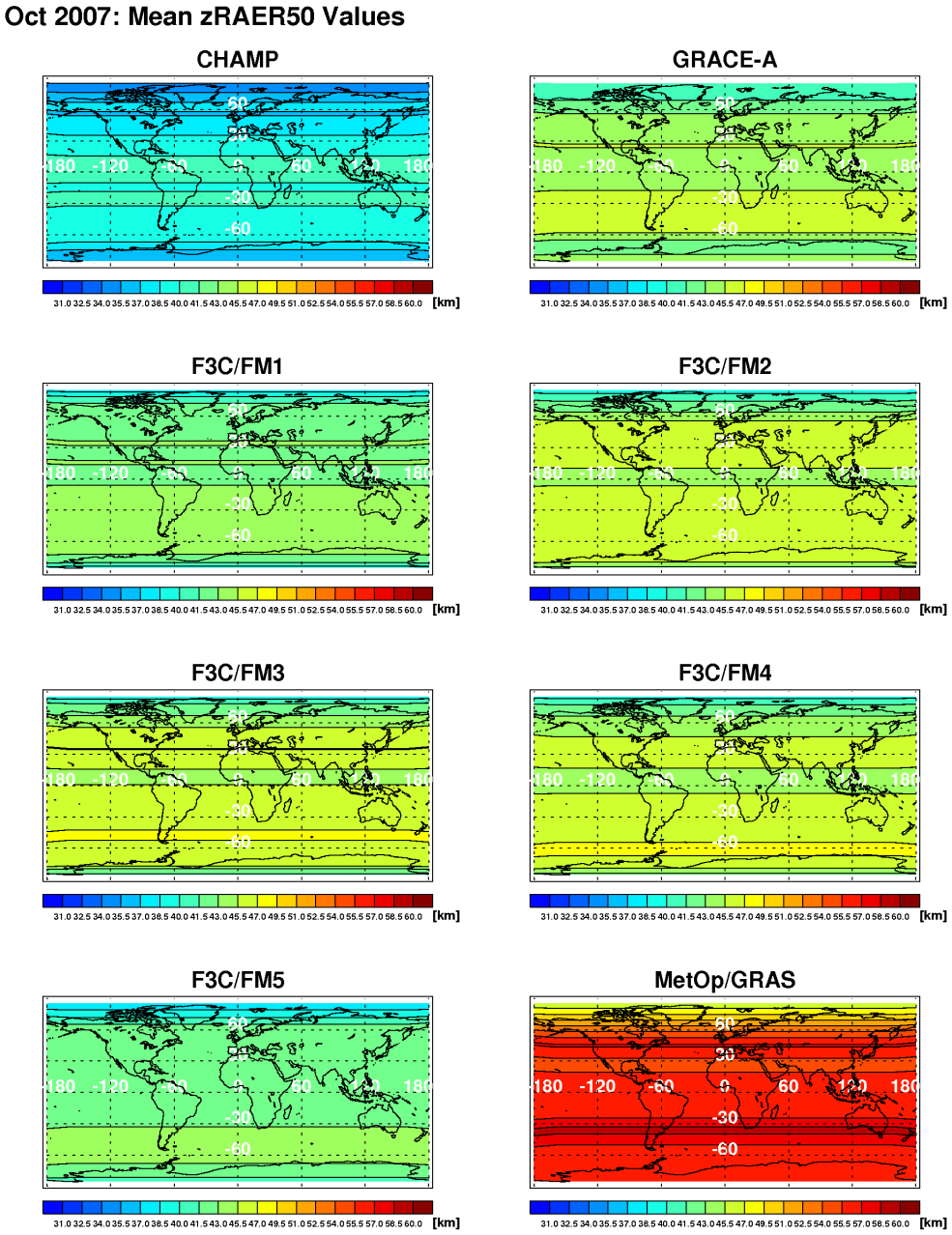

Figure 4.7: zRAER50 climatologies of CHAMP, GRACE-A, FM-1, FM-2, FM-3, FM-4, FM-5, and MetOp-A in October 2007.

Table 4.4: Disparities of sampling error subtracted dry temperature climatologies as a function of altitude in October 2007. Bottom rows represent deviations relative to the satellite mean with MetOp-A excluded.

	30 to 35 km	25 to 30 km	20 to 25 km	15 to 20 km	10 to 15 km
CHAMP	−0.21 K	−0.13 K	−0.10 K	−0.05 K	−0.04 K
GRACE-A	0.01 K	−0.05 K	−0.03 K	−0.01 K	−0.00 K
FM-1	−0.04 K	−0.03 K	−0.04 K	−0.02 K	−0.05 K
FM-2	−0.03 K	−0.02 K	−0.01 K	0.01 K	0.01 K
FM-3	−0.05 K	−0.00 K	−0.01 K	−0.03 K	−0.02 K
FM-4	−0.03 K	−0.02 K	0.01 K	0.02 K	0.02 K
FM-5	−0.11 K	−0.06 K	−0.02 K	−0.01 K	0.01 K
MetOp-A	0.45 K	0.31 K	0.20 K	0.09 K	0.06 K
CHAMP	−0.14 K	−0.09 K	−0.07 K	−0.04 K	−0.03 K
GRACE-A	0.07 K	−0.01 K	−0.00 K	0.00 K	0.01 K
FM-1	0.03 K	0.01 K	−0.01 K	−0.00 K	−0.04 K
FM-2	0.03 K	0.03 K	0.02 K	0.02 K	0.02 K
FM-3	0.02 K	0.04 K	0.02 K	−0.01 K	−0.01 K
FM-4	0.04 K	0.02 K	0.03 K	0.03 K	0.03 K
FM-5	−0.04 K	−0.02 K	0.00 K	0.00 K	0.02 K

high altitudes) is still unclear and has to be investigated in a further study.

Table 4.4 specifies average deviations of dry temperature relative to the sampling error subtracted satellite mean as a function of altitude (in 5 km steps). Most important are altitudinal characteristics of the CHAMP and MetOp-A dry temperature deviations. They significantly decrease with decreasing altitude, which mainly reflects the decreasing amount and therefore influence of background information. Below 20 km CHAMP dry temperatures are only 0.05 K cooler than the satellite mean, MetOp-A dry temperatures are 0.09 K warmer than the satellite mean. If MetOp-A data are excluded, the difference between CHAMP dry temperatures and the satellite mean amounts to −0.14 K between 30 km and 35 km altitude, it decreases to −0.04 K below 20 km altitude. Consistency of F3C data is tremendous. FM-2, FM-3, and FM-4, which feature the same average zRAER50 value agree to within 0.02 K also at high altitudes.

4.3 Data Processing

Inconsistencies in RO climatologies can also originate from a different implementation of the RO retrieval. These differences comprise (after Ho et al. (2009)):

- precise orbit determination and clock synchronization to eliminate the effects on the geometric Doppler and of the relative transmitter–receiver oscillator drift,
- conversion of geometric Doppler to bending angle,
- extrapolation of the ionospheric correction into the lower troposphere,
- the initialization of the bending angle profile at high altitudes, and
- the quality control algorithms used to distinguish high from bad quality data.

In the following, CHAMP RO climatologies provided by different RO processing centers are investigated in detail. The comparison of these climatologies does not separate the causes for different data characteristics but summarizes all causes mentioned above. To isolate the effect of precise orbit determination and clock synchronization (which is performed in level 1 processing) differences between German Research Centre for Geosciences (GFZ) and UCAR/CDAAC CHAMP data, which are used as input data for WEGC OPSv54 retrieval are analyzed. The effect of bending angles initialization at high altitudes is investigated by comparing Global Positioning System/Meteorology (GPS/MET) data initialized with ECMWF analysis fields with GPS/MET data initialized with ECMWF Re-Analysis (ERA)-40 data.

4.3.1 Comparison of CHAMP Climatologies Retrieved from Different Data Centers

Ho et al. (2009) performed an inter-comparison study estimating the uncertainty of RO data provided by different data centers. They examined the CHAMP refractivity record from 2002 to 2006 and found that absolute values of fractional refractivity anomalies among GFZ, Jet Propulsion Laboratory (JPL), UCAR, and WEGC are in general smaller than 0.2 % between 8 km and 25 km altitude.

In a follow-on study, GFZ, JPL, UCAR, WEGC, and also Danish Meteorological Institute (DMI) and EUMETSAT provide CHAMP climatologies of bending angle, refractivity, dry temperature, dry pressure, and dry geopotential height to investigate their systematic differences and to look for potential impacts on climate trends.

While GFZ, JPL, and UCAR perform their own level 1 processing, DMI and WEGC use UCAR phase delay and orbit data. Level 2 processing is performed separately by each processing center. UCAR/CDAAC (Doug Hunt) prepared monthly mean 5° zonal mean climatologies from retrieved high quality RO profiles (i.e., same level 3 climatology processing). To this day EUMETSAT did not provide single RO profiles so that their climatological product is currently not available. Processing versions of different centers were: OCC18.9.535 (DMI), POCS ATM vers. 005 (GFZ), v2fo_10Kp1N (JPL), 2009.2650 (UCAR), and OPSv54 (WEGC).

Table 4.5: Number of high quality profiles of CHAMP available at different processing centers in October 2007 as well as mean disparities in refractivity and dry temperature climatologies relative to the center mean. Mean values are calculated between 8 km and 35 km altitude (and between 8 km and and 30 km altitude in parenthesis) from 40°S to 40°N.

	High quality profiles	ΔN	ΔT
DMI	3602	0.00 % (0.00 %)	0.12 K (0.07 K)
GFZ	4054	0.21 % (0.10 %)	−0.16 K (0.08 K)
JPL	3883	−0.10 % (−0.04 %)	−0.44 K (−0.33 K)
UCAR	4127	−0.08 % (−0.04 %)	0.17 K (0.02 K)
WEGC	3644	−0.03 % (−0.02 %)	0.31 K (0.16 K)

Due to different quality control mechanisms[2], all processing centers provide a different number of high quality profiles per month. Table 4.5, first column, specifies the total number of high quality profiles obtained by each data center in October 2007. While most high quality profiles are available from UCAR/CDAAC (4127 profiles), least follow from DMI processing (3602). Top panel of Figure 4.8 depicts the latitudinal distribution of these measurements. Most measurements are obtained between 70°S and 75°S, 20°S and 25°S, 20°N and 25°N, 50°N and 55°N, and 70°N and 75°N. It is interesting to note that WEGC and UCAR provide more high quality profiles at low latitudes compared to the other data centers.

Figure 4.8 and Figure 4.9 depict refractivity and dry temperature deviations as a function of latitude and altitude for each of the five processing centers relative to the center mean. Both figures show largest differences at high southern latitudes, where atmospheric variability is strong and differences in spatio-temporal availability of high quality profiles yields largest sampling error differences. Since sampling error estimates of each data set are currently not available at WEGC (it is in preparation by UCAR), the focus lies on mid- and low latitudes (40°S to 40°N), where sampling issues are negligible.

The second and third column of Table 4.5 give mean refractivity and dry temperature deviations of each data center relative to the center mean. These differences are averaged between 8 km and 35 km altitude (and between 8 km and 30 km altitude given in parenthesis) and between 40°S and 40°N. Within 8 km and 35 km altitude, JPL refractivities are smaller than average by −0.10 %, GFZ refractivities are larger than average by 0.21 %. Dry temperature climatologies agree to within < 0.8 K (JPL temperatures are cooler than average by −0.44 K and WEGC temperatures are

[2]Detailed information about RO processing chains applied at different data centers can be found in Ho et al. (2009).

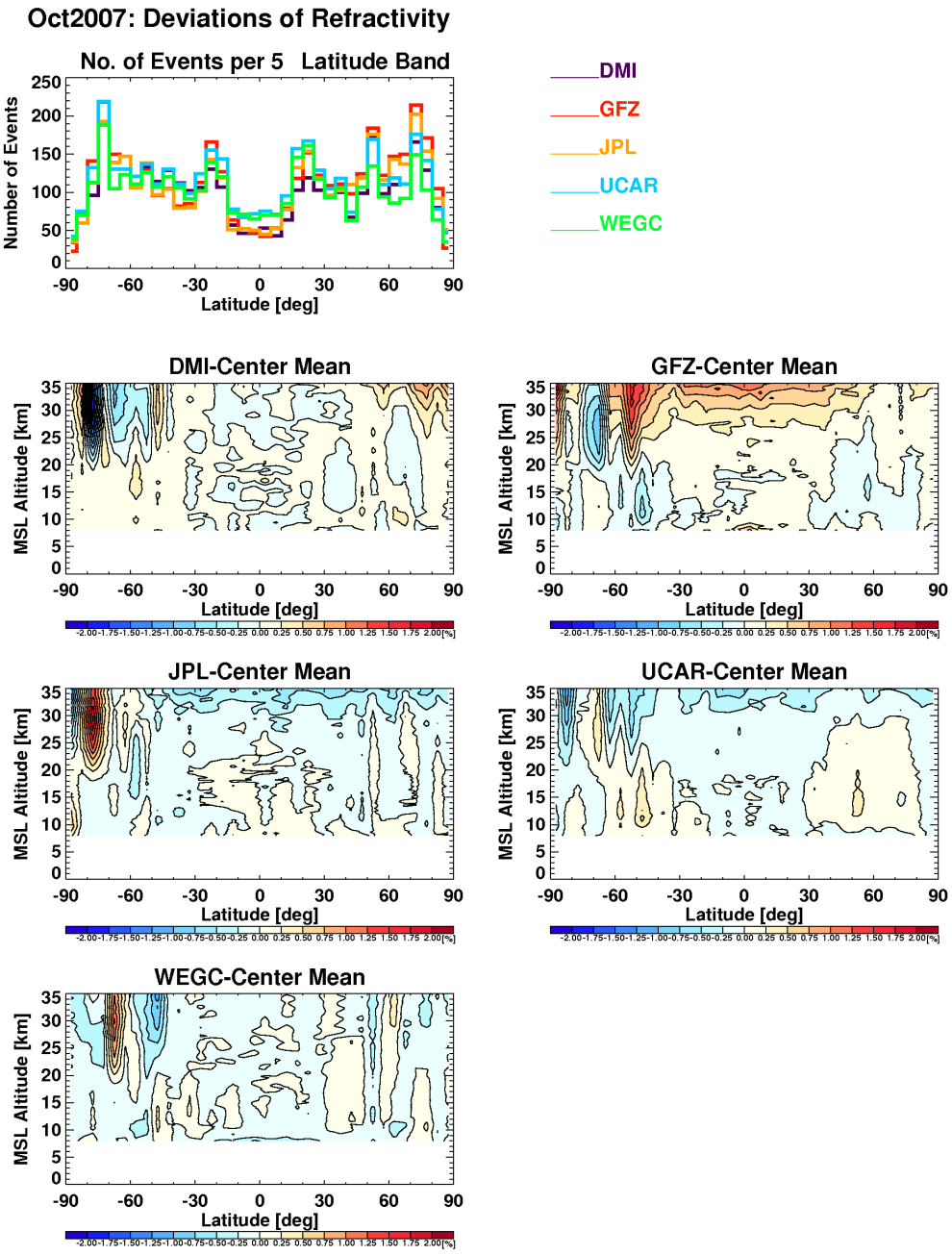

Figure 4.8: Differences between CHAMP refractivity climatologies obtained from different RO processing centers relative to the center mean climatology in October 2007.

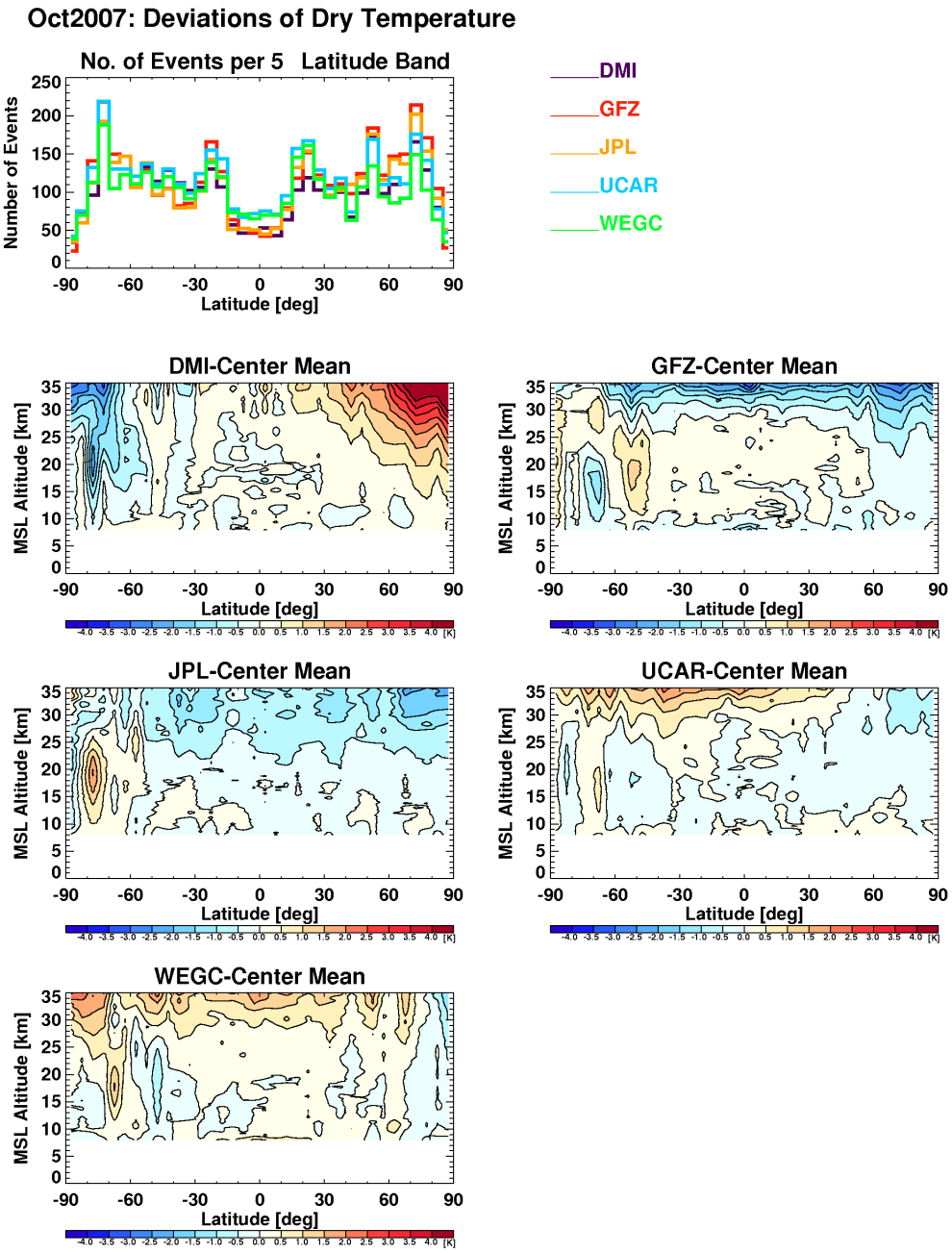

Figure 4.9: Differences between CHAMP dry temperature climatologies obtained from different RO processing centers relative to the center mean climatology in October 2007.

Table 4.6: Disparities of refractivity and dry temperature climatologies as obtained from different data centers relative to the center mean as a function of altitude in October 2007.

	30 to 35 km	25 to 30 km	20 to 25 km	15 to 20 km	10 to 15 km
DMI	−0.00 %	−0.00 %	0.02 %	0.00 %	0.00 %
GFZ	0.68 %	0.27 %	0.09 %	0.04 %	0.01 %
JPL	−0.35 %	−0.13 %	−0.03 %	−0.02 %	−0.03 %
UCAR	−0.27 %	−0.11 %	−0.07 %	−0.01 %	0.01 %
WEGC	−0.06 %	−0.03 %	−0.02 %	−0.01 %	0.00 %
DMI	0.36 K	0.17 K	0.05 K	0.05 K	0.01 K
GFZ	−1.20 K	0.04 K	0.23 K	0.12 K	0.06 K
JPL	−0.94 K	−0.74 K	−0.45 K	−0.16 K	−0.05 K
UCAR	0.83 K	0.15 K	0.02 K	−0.06 K	−0.05 K
WEGC	0.95 K	0.39 K	0.15 K	0.06 K	0.02 K

warmer than average by 0.31 K). A look at numbers given in parenthesis as well as at Figure 4.8 and Figure 4.9 yields that these differences primarily originate from high altitudes.

Table 4.6 specifies altitude dependent refractivity and dry temperature anomalies of all five processing centers relative to the center mean. Differences are quantified every 5 km. Differences at high altitudes (30 km to 35 km) exceed 0.6 % (GFZ), −0.3 % (JPL), and −0.2 % (UCAR). These large lower stratospheric refractivity differences may result from differences in bending angle initialization. While GFZ initializes RO bending angle with an MSIS (Mass Spectrometer and Incoherent Scatter Radar) climatology, JPL performs an exponential extrapolation of bending angles above 50 km, and UCAR uses a National Center for Atmospheric Research (NCAR) climatology for bending angle initialization (Ho et al. 2009). The significant decrease of refractivity differences with decreasing altitude yields them to be smaller than 0.1 % below 25 km. Overall, these results are in very good agreement with Ho et al. (2009), cf. Figure 2 therein.

In contrast to refractivity climatologies, the agreement of dry temperature climatologies is worse above 20 km. At high altitudes CHAMP GFZ and JPL temperatures are distinctively colder than those of the other data centers. Differences between warmest and coldest retrieved temperatures at 30 km to 35 km altitude exceed 2 K (−1.2 K for GFZ and 0.95 K for WEGC). They still exceed 0.6 K between 20 km and 25 km.

The disagreement between CHAMP refractivity and dry temperature climatologies derived from different RO processing centers distinctively exceeds differences

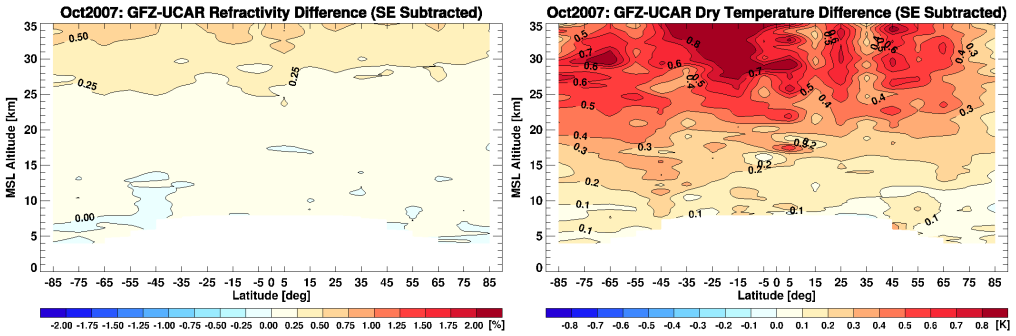

Figure 4.10: Difference between CHAMP climatologies, which results from different level 1 processing. Phase delay and orbit data are provided by GFZ and by UCAR. Left panel depicts the ((GFZ − UCAR)/UCAR)100 % refractivity difference (in percent), the right panel shows GFZ minus UCAR dry temperature difference.

observed between different RO satellites, which stem from the same data processing.

4.3.2 Level 1 Processing

Concerning level 1 processing (preparation of phase delay data, space- and velocity vectors of Global Positioning System (GPS) and LEO satellites) one important source of uncertainty results from precise orbit determination and clock synchronization (Ho et al. 2009), which is performed differently e.g., at GFZ and UCAR. While GFZ generates GPS and LEO orbits using GFZ's precise orbit determination software EPOS-OC (König et al. 2005), UCAR uses the Bernese 5.0 GPS data processing package (Dach et al. 2007) to generate CHAMP orbits and clocks. GPS orbits and clocks are obtained from International GNSS Service (IGS) final results. At GFZ, transmitter and receiver clocks are calibrated using the double-differencing technique, but UCAR applies a single differencing approach. To get more information about differences in data processing, it is referred to Ho et al. (2009).

The impact of the level 1 processing is investigated applying the OPSv54 retrieval to two different input data sets. One data set is provided by GFZ (version 2), the other one is provided by UCAR/CDAAC (version 2007.3200). Level 2 Occultation Processing System (OPS) and the level 3 Climatology Processing System (CLIPS) are performed at WEGC so that differences observed in RO climatologies are primarily caused by different input data. A slightly different number of high quality profiles only has a minor impact on the sampling error (which is subtracted from the climatologies anyway).

Figure 4.10 depicts the difference between sampling error subtracted refractivity and dry temperature climatologies. Mean GFZ refractivity is larger than that of

UCAR by up to 0.5 % at 35 km altitude. Below 25 km differences are smaller than 0.25 %. Mean GFZ dry temperature is warmer than UCAR temperature. The difference exceeds 0.8 K at low southern latitudes above 30 km[3]. It is larger than 0.2 K everywhere above 15 km. It may be suspicious that refractivity and dry temperature differences are of the same sign. However, the inspection of differences at altitudes above 35 km shows that GFZ dry temperature is colder than UCAR temperature above 40 km.

4.3.3 Impact of Background Atmosphere

Within the operational OPSv54 retrieval, bending angle initialization is performed with ECMWF short-term forecast fields. As already seen in Chapter 2 background information strongly affects atmospheric climatologies at high altitudes. In this section, some results, which show the effect of different background information used for bending angle initialization with the same data quality (i.e., same RO data set, initialized with the different background information) are presented.

Figure 4.11 shows the difference of refractivity and dry temperature climatologies resulting from different background information. At one time GPS/MET data are initialized with operational ECMWF analysis fields and at the other time they are initialized with ERA-40 data. Refractivity differences are given in terms of relative quantities (GPS/MET operational analyses minus GPS/MET ERA-40 divided by GPS/MET ERA-40).

It can be seen that refractivity data are in good agreement at all altitude levels up to 35 km at low and mid latitudes as well as at high northern latitudes. Beyond 50°S the difference becomes larger and exceeds 2 %. This is the same geographic region, where the sampling error (estimated from ECMWF operational analyses) becomes significant whereas it remains comparatively small if it is estimated from ERA-40 data (cf. Subsection 3.3.7). Differences in sampling error estimation do not only result from different background data utilized but also from the slightly different number of profiles incorporated into climatologies. While the retrieval yields 1092 high quality RO profiles, if GPS/MET bending angles are initialized with ERA-40 data, only 1084 high quality profiles are available if bending angles are initialized with operational ECMWF analyses fields. The remaining eight profiles are all located at high southern latitudes (e.g., five profiles between 60°S and 70°S, two profiles between 50°S and 60°S).

The sampling error subtraction somewhat improves the data agreement at high southern latitudes but it also increases the difference in other parts of the atmosphere. This results from different sampling errors subtracted from both climatologies (cf. Subsection 3.3.7).

[3]Mean zRAER50 values agree to within 1 km in all latitude regions.

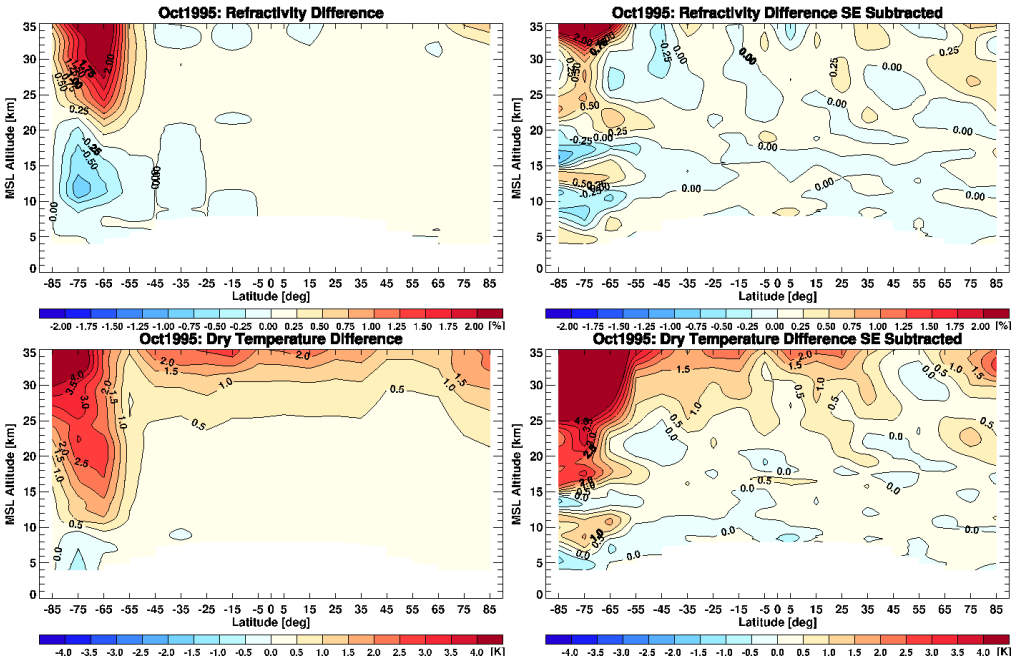

Figure 4.11: Difference of GPS/MET climatologies, which results from bending angle initialization: The difference is calculated from GPS/MET climatologies, whose profiles are initialized with operational ECMWF analysis fields minus GPS/MET climatologies, whose profiles are initialized with ERA-40 data.

Dry temperature differences are distinctively larger between both data sets. While differences exceed 1 K to 2 K at an altitude to 30 km, they decrease with decreasing altitude. The 0.5 K contour line is located at an altitude of approximately 25 km. Differences become distinctively smaller below that height level.

The application of the hydrostatic integral within the processing chain is responsible that the background information propagates further downward in the Lower Stratosphere (LS) region so that dry temperature differences are much larger than refractivity differences. This underpins the particular importance to use high quality background information for bending angle initialization. A "bad" initialization of bending angles at highest altitudes results in errors in retrieved atmospheric profiles, which reach down as far as 25 km.

4.4 Summary of Consistency of Different RO Climatologies

This section showed that inconsistencies of RO climatologies can mainly result from differences in

1. spatio-temporal sampling of RO measurements,

2. data quality at high altitudes, and

3. data processing.

Knowledge of the spatio-temporal distribution of RO measurements enables the quantitative estimation of the sampling error. While LEO and GPS orbit characteristics primarily determine the location of RO events, the number of measurements depends on the satellite's equipment and the satellite's health. The sampling error is estimated using an adequate (ECMWF) reference atmosphere.

After subtraction of the estimated respective sampling errors, climatologies derived from different satellites (CHAMP, GRACE, F3C, and MetOp) show very good agreement. Mean absolute differences of refractivity climatologies over the entire domain between 8 km and 35 km are smaller than 0.1 %, mean temperature differences do not exceed 0.3 K in the same domain.

Largest climatological disagreements are found at high altitudes (30 km to 35 km), where the impact of background information is non-negligible, especially for CHAMP data because background information penetrates towards lowest altitudes in this data set. Since ECMWF data, used as background information, feature a negative temperature bias at 35 km and above (ECMWF temperatures are cooler than RO data), this bias propagates further down within CHAMP data. At one specific altitude level, less background information is present in GRACE-A and F3C data, which are therefore slightly warmer than CHAMP data. Since MetOp data exhibit least background information corresponding temperatures are warmest. However, since MetOp temperatures are inconsistent in the northern and southern hemisphere this data set has to be looked at in more detail in a further study.

Inconsistencies of RO climatologies derived from different satellites significantly decrease with decreasing altitude. Below 15 km CHAMP dry temperatures are cooler than the satellite mean by 0.05 K, MetOp data are warmer than the satellite mean by 0.09 K. Consistency of F3C climatologies is tremendous. Climatologies, which are derived from data with same quality agree to within 0.02 K also at high altitudes.

Largest climatological disagreements arise when comparing data from different processing schemes. Mean differences of CHAMP climatologies among five processing centers (DMI, GFZ, JPL, UCAR, and WEGC) amount to 0.15 % and 0.5 K in refractivity and dry temperature, respectively (averaged from 40°S to 40°N and from 8 km to 30 km). Again, differences are largest at high altitudes. Note that climate time series of refractivity and temperature changes agree much closer (Ho et al. 2009; Steiner et al. 2009).

Level 1 processing and bending angle initialization are found to make a major contribution in data inconsistencies. Utilizing GFZ and UCAR level 1 data in WEGC OPS,

respective climatologies differ by more than 0.5 K at all latitudes above 30 km. Bending angle initialization is responsible for dry temperature deviations being larger than 1 K above 30 km.

5 Local Time Influence in Radio Occultation Climatologies

This chapter, which mainly shows results of Pirscher et al. (2007*b*) and Foelsche et al. (2009*a*), focuses on the Sampling Error (SE) of Radio Occultation (RO) climatologies as obtained from satellites in Low Earth Orbit (LEO), in particular on the effect of local times at which RO profiles have been taken. While Pirscher et al. (2007*b*) analyzed the local time influence in single-satellite RO climatologies (Meteorological Operational (MetOp) and CHAllenging Mini-Satellite Payload (CHAMP)), Foelsche et al. (2009*a*) included an investigation of the local time error, which results from FORMOSAT-3/COSMIC (F3C) local time sampling.

5.1 Satellite Orbits and Their Effects on Local Time Sampling

The satellite orbits of transmitters and receivers determine the global distribution of RO events and the local time when measurements are taken (Pirscher et al. 2007*b*). A Global Positioning System (GPS) receiver mounted on a LEO satellite with high inclination allows for measurements to be performed at every position on the globe. During one revolution, the LEO sub-satellite track crosses each geographical latitude at two different local times. At the equator, the local times are separated by twelve hours, but the higher the latitude the more asymmetric are the sub-satellite points in local time.

Sun-synchronous satellites are a particular type of LEO satellites. They are characterized by unchanging equator crossing times (Larson and Wertz 1997). The equator crossing times of non sun-synchronous satellites change depending on their rate of nodal precession. For this reason only non sun-synchronous satellites are able to entirely sample at all local times. Satellites with very slow drifting rates (some hours within some years) are most unfavorable in regard to local time sampling and climate trend detection. As experience with Microwave Sounding Unit (MSU) climate time series has shown, such a long-term drift can pretend a false trend in the time series (Mears and Wentz 2005).

5.1.1 Satellite Drifting Rates and Their Dependency on Altitude and Inclination

The Earth's oblateness is the main reason for the secular drift of satellite orbit planes. Assuming a circular orbit (i.e., eccentricity $e = 0$), an orbit's precession rate $\dot{\Omega}$ (in rad/s) can be calculated as (Hofmann-Wellenhof et al. 1997; Larson and Wertz 1997; Boain 2005)

$$\dot{\Omega} = -\frac{3}{2} J_2 \left(\frac{a_\mathrm{e}}{a}\right)^2 n \cos i \tag{5.1}$$

where $J_2 = 1082.63 \times 10^{-6}$ is the negative of the second zonal coefficient of spherical harmonics describing the Earth's polar oblateness, $a_\mathrm{e} = 6378137$ m is the mean equator radius of the Earth (NIMA 2000), a is the semi-major axis of the satellite's orbit (in m), i its inclination (in rad), and $n = \sqrt{GM_\mathrm{e}/a^3}$ is the mean motion of the satellite (in rad/s), where $G = 6.674 \times 10^{-11}$ m^3/(kg s^2) is the gravitational constant (Mohr et al. 2008) and $M_\mathrm{e} = 5.9733 \times 10^{24}$ kg the mass of the Earth (NIMA 2000).

The orbit parameters i and a can be chosen in a way that the precession rate of the satellite equals to the mean motion of the Earth on the way around the sun. This mean motion amounts to $360°/365.242199\ \mathrm{d} = 0.9856°/\mathrm{d}$, where 365.242199 d corresponds to one tropical year[1]. To calculate the nodal precession rate of the orbit with respect to the sun, $\dot{\Omega}_\odot$ has to be referred to the sun:

$$\dot{\Omega}_\odot = 0.9856°/\mathrm{d} - \dot{\Omega}. \tag{5.2}$$

If $\dot{\Omega} = 0.9856°/\mathrm{d}$, the satellite circuits on a sun-synchronous orbit and $\dot{\Omega}_\odot^{\mathrm{SunSynch}}$ is equal to 0. A sun-synchronous orbit can be obtained by different possible combinations of a and i, whereby a higher orbital altitude requires a slightly lower inclination (cf. Eq. (5.1)). If $\dot{\Omega}$ is greater or less than $0.9856°/\mathrm{d}$, the satellite drifts in local time.

Table 5.1 summarizes the orbit characteristics of three satellites, which carry a GPS receiver and perform RO measurements: the sun-synchronous satellite MetOp and the non sun-synchronous satellites CHAMP and F3C. The equator crossing time of sun-synchronous satellites remains constant. MetOp's equator crossing (descending node) is at 09:30 a.m. local time. The orbit will be maintained to ±5 minutes accuracy at the nominal local time within the satellite's lifetime.

CHAMP's altitude of 400 km is the mean altitude of the satellite because atmospheric drag caused a decrease of the orbit altitude from 454 km in July 2000 to less than 330 km in March 2009. All six satellites of the F3C constellation have been at an initial orbit altitude of about 520 km but they were consecutively raised to 800 km (see Subsection 5.1.2).

[1] "The tropical year is defined as the time interval needed for the mean tropical longitude of the sun to increase by 360°" (Meeus and Savoie 1992).

Table 5.1: Altitude h, inclination i, resulting drifting rate $\dot{\Omega}$, and drifting rate with respect to the sun $\dot{\Omega}_\odot$ of MetOp, CHAMP, and F3C.

	h (in km)	i (in °)	$\dot{\Omega}$ (in °/d)	$\dot{\Omega}_\odot$ (in °/d)
MetOp	823	98.7	+0.9856	0.0
CHAMP	400	87.2	−0.3934	1.3791
F3C	800	72.0	−2.0361	3.0218

Drifting rates of non sun-synchronous satellites can also be specified in units of hours per day or hours per month, which may be more comprehensible. If the drifting rate of a satellite amounts to 1.3791°/d (CHAMP), the satellite drifts one hour within 10.9 days or 2.8 hours within one month (30 days). Since RO measurements can be performed during day and night, CHAMP drifts through all local times at low latitudes within about 130 days. Due to the limb sounding measurement principle, the effective repeat period is obtained every 108 days (Zeng et al. 2008). That implies that neither a monthly nor a seasonal period suffices to entirely sample over all local times. A drifting rate of 3.0218°/d (F3C) means that the satellite drifts one hour within 5.0 days and 6 hours within one month. One single F3C satellite samples through all local times within two months at low latitudes.

The single difficulty in calculating the drifting rates of satellites is to use the appropriate units.

5.1.2 Example: Drifting Rates of F3C Satellites as a Function of Time

The dependency of drifting rate from orbit altitude and inclination has been utilized to achieve the plane separation of the six F3C satellites (Anthes et al. 2008).

The satellites have been launched on the same rocket in April 2006. They have reached an orbital altitude of 520 km and an inclination of 72°, yielding an orbital precession rate of $\dot{\Omega} \approx -2.34°/\text{d}$ and $\dot{\Omega}_\odot \approx 3.33°/\text{d}$. Consecutive orbit raising from 520 km to 800 km (Figure 5.1, top left panel), with constant inclination (Figure 5.1, top right panel), yielded a change in drifting rate to $\dot{\Omega} \approx -2.04°/\text{d}$ and $\dot{\Omega}_\odot \approx 3.02°/\text{d}$ (Figure 5.1, bottom left panel) and a desired orbit separation of 30° (Figure 5.1, bottom right panel). In June 2006 the first satellite separated from the others, it was FlightModel (FM)-5. In December 2007 the final constellation should have been developed, but since the solar panels of FM-3 were stuck, its orbit raising has been halted at an altitude of 710 km in July 2007.

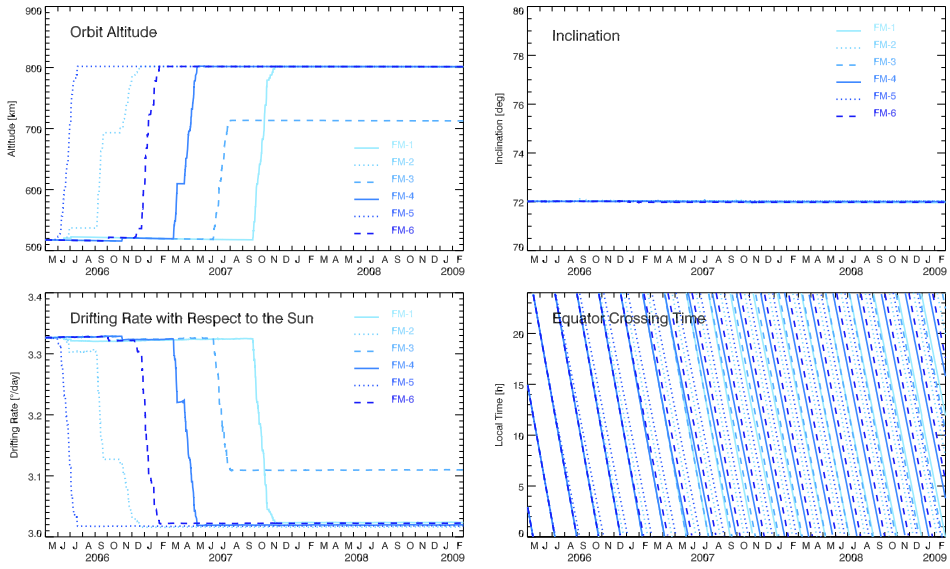

Figure 5.1: F3C orbit: altitudes and inclinations (top panels), resulting drifting rates with respect to the Sun $\dot{\Omega}_{\odot}$, and equator crossing times (bottom panels) from May 2006 to February 2009.

5.1.3 Hour Angles of Single Satellites and Satellite Constellations

The hour angles η_{a} (ascending branch) and η_{d} (descending branch) of a satellites' orbit depend on the nodal precession rate of the orbit with respect to the sun $\dot{\Omega}_{\odot}$, the time t (usually measured on daily or monthly timescales), the initial ascending node crossing time ϕ (with respect to midnight local time), and the sounding offset time $\psi(\varphi)$, which depends on the geocentric latitude φ and on i, the inclination of the satellite (Leroy 2001):

$$\eta_{\mathrm{a}} = \dot{\Omega}_{\odot} t + \phi + \psi(\varphi) \tag{5.3}$$

and

$$\eta_{\mathrm{d}} = \dot{\Omega}_{\odot} t + \phi + \pi - \psi(\varphi) \tag{5.4}$$

with

$$\psi(\varphi) = \arcsin\left(\frac{\tan\varphi}{\tan i}\right). \tag{5.5}$$

Hour Angles of Single Satellites

Since RO measurements can be performed during day and night, soundings are available from both the ascending and the descending branch of the orbit.

Table 5.2: Hour angles of the ascending and descending branch (in hours) of the orbit at $t = 0$ and $t = 1$ (i.e., one month later). Results are shown for MetOp, CHAMP, and one single F3C satellite (FM-1). $\varphi = 98.7°$ refers to the inclination of MetOp; this is equivalent to $\varphi = 81.3°$.

$t = 0$	$\varphi = 0°$		$\varphi = 60°$N		$\varphi = 72°$N		$\varphi = 87.2°$N		$\varphi = 98.7°$N	
Satellite	η_a	η_d	η_a	η_d	η_a	η_d	η_a	η_d	η_a	η_d
MetOp:	0.0	12.0	−1.0	13.0	−1.9	13.9	–	–	6.0	6.0
CHAMP:	0.0	12.0	0.3	11.7	0.6	11.4	6.0	6.0	–	–
F3C/FM-1:	0.0	12.0	2.3	9.7	6.0	6.0	–	–	–	–
$t = 1$	$\varphi = 0°$		$\varphi = 60°$N		$\varphi = 72°$N		$\varphi = 87.2°$N		$\varphi = 98.7°$N	
Satellite	η_a	η_d	η_a	η_d	η_a	η_d	η_a	η_d	η_a	η_d
MetOp:	0.0	12.0	−1.0	13.0	−1.9	13.9	–	–	6.0	6.0
CHAMP:	2.8	14.8	3.1	14.4	3.3	14.2	8.8	8.8	–	–
F3C/FM-1:	6.0	18.0	8.3	15.8	12.0	12.0	–	–	–	–

Table 5.2 shows the hour angles of the ascending and the descending branch of the orbit at different latitudes and at the definite times $t = 0$ and $t = 1$ (i.e., one month (30 days) later) for MetOp, CHAMP, and one single F3C satellite (FM-1). The initial ascending node crossing time ϕ was assumed to be zero for all satellites (which is an appropriate starting point).

At the equator the ascending nodes and the descending nodes of all satellites are separated by exactly 12 hours. It can be seen that the sun-synchronous satellite MetOp is constant in terms of local sampling as its hour angles stay constant with time. At 60° both branches of the orbit move approximately two hours together. Compared to the equator, soundings of the ascending branch occur approximately one hour earlier and soundings of the descending branch occur one hour later. When latitude equals the inclination of the satellite, the hour angles of the ascending and descending branch are the same.

CHAMP and F3C are non sun-synchronous satellites with drifting rates of 2.8 hours per month and 6.0 hours per month, respectively. The difference of the hour angles of the ascending and descending branch of the CHAMP orbit remains close to 12 h up to 70°. Both branches come close and finally together only at highest latitudes. Local time sampling of one single F3C satellite is asymmetric by approximately 5 h at 60°N as the soundings of the ascending branch occur 2.3 h later and soundings of the descending branch occur 2.3 h earlier compared to the equator.

Table 5.3: Hour angles of the ascending and descending branches (in hours) of the orbits of six F3C satellites at $t = 0$ and at $t = 1$ (i.e., 1 month later) under the assumption of an ideal orbit configuration with 30° plane separation.

$t = 0$	$\varphi = 0°$		$\varphi = 60°$N		$\varphi = 72°$N	
Satellite	η_a	η_d	η_a	η_d	η_a	η_d
FM-1	0.0	12.0	2.3	9.7	6.0	6.0
FM-2	2.0	14.0	4.3	11.7	8.0	8.0
FM-3	4.0	16.0	6.3	13.7	10.0	10.0
FM-4	6.0	18.0	8.3	15.7	12.0	12.0
FM-5	8.0	20.0	10.3	17.7	14.0	14.0
FM-6	10.0	22.0	12.3	19.7	16.0	16.0
$t = 1$	$\varphi = 0°$		$\varphi = 60°$N		$\varphi = 72°$N	
Satellite	η_a	η_d	η_a	η_d	η_a	η_d
FM-1	6.0	18.0	8.3	15.8	12.0	12.0
FM-2	8.0	20.0	10.3	17.8	14.0	14.0
FM-3	10.0	22.0	12.3	19.8	16.0	16.0
FM-4	12.0	24.0	14.3	21.8	18.0	18.0
FM-5	14.0	2.0	16.3	23.8	20.0	20.0
FM-6	16.0	4.0	18.3	1.8	22.0	22.0

Hour Angles of a Satellite Constellation

The orbital plane spacing of the six F3C satellites was designed to be 30°, which implies that the initial ascending node crossing times ϕ are separated by 30°. Application of Eqs. (5.3) and (5.4) allows the calculation of hour angles of each single F3C satellite.

Table 5.3 shows these calculated hour angles at $\varphi = 0°$, $\varphi = 60°$N and $\varphi = 72°$N at $t = 0$ and $t = 1$ (i.e., one month later). Figure 5.2 supplements the consideration of the orbital configuration showing the satellite orbits as functions of local time and latitude over a period of one month. The bottom panel of Figure 5.2 shows the orbital tracks of the entire F3C satellite configuration (consisting of all six FM).

The ascending branch and descending branch of the orbit are separated by 12 hours only at low latitudes, which allows the orbit configuration to sample at all local times within 10 days. At high latitudes, however, the orbital plane separation of 30° is not sufficient to achieve adequate local time sampling within one month.

At $\varphi = 72°$ latitude and $t = 0$ the local time sampling gap of the satellite tracks stretches out over 14 hours. While it takes about four months for one single F3C satellite to scan at all local times at high latitudes, all six satellites together need

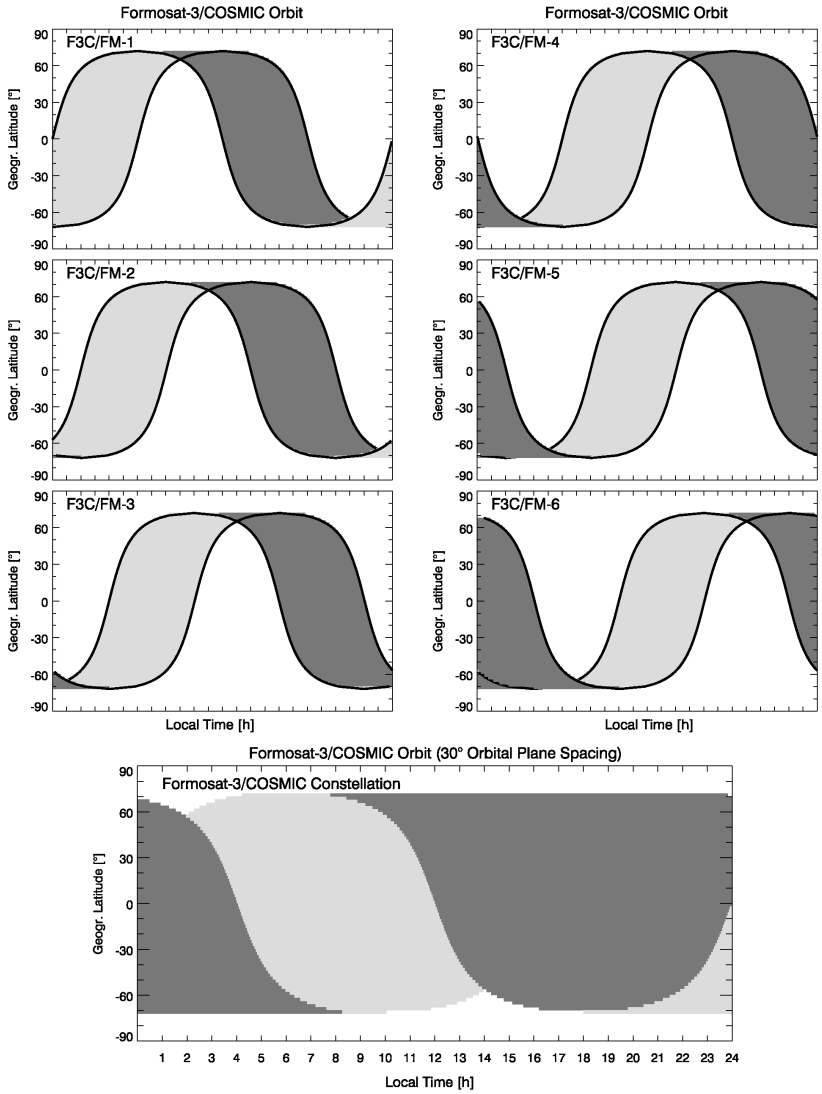

Figure 5.2: F3C orbits as a function of local time and latitude over a period of one month. The ascending branches of the orbits are depicted in light gray, the descending branches are shown in dark gray. The development of the local time sampling of the entire F3C configuration is shown in the bottom panel.

somewhat more than two months. If data are averaged over one month, the gap of local time sampling drifts with the same rate as the satellites themselves (6 hours within one month).

In this context it is important to notice that the RO technique is a limb sounding technique. Dependent on the altitude of the LEO satellite, measurements can be performed more than 2000 km away from the satellite. Thus, the range of local times, which can actually be sampled by the satellites is larger than the range of local times, which is covered by the satellite tracks only.

5.1.4 Local Time Sampling

Knowledge of a satellites' orbit characteristics allows to simulate the distribution (time and location) of RO events. RO event distributions of MetOp, CHAMP, and F3C were simulated using the End-to-End Generic Occultation Performance Simulation and Processing System (EGOPS) software (Kirchengast et al. 2004) with appropriate satellite orbit element files.

Figure 5.3 illustrates the RO event locations (black dots) and the sub-satellite points (in blue) of simulated MetOp (simMetOp) (top), simulated CHAMP (simCHAMP), one single simulated F3C (simF3C) satellite (FM-1) and the whole simF3C constellation with 30° orbit plane separation (bottom) in July 2005 (plotted at each time when an RO event occurred). The middle and right columns show the number of northern hemispheric and southern hemispheric RO events as a function of local time for one month (July 2005, dark gray) and one season (June–July–August (JJA) 2005, light gray).

The local time of MetOp's descending node (equator crossing time) remains constant at 09:30. The stability of the sun-synchronous orbit and its asymmetry regarding local time sampling at high latitudes leads to an unequal weighting of day and night in the northern and southern hemisphere. Even though the limb sounding of RO measurements somewhat spreads the local times at which measurements are performed, the majority of the measurements at mid and high northern latitudes is performed during daytime, whereas at mid and high southern latitudes most of them take place during nighttime. At 60°N, for example, the local times of MetOp's sub-satellite points are at about 10:30 and 20:20, respectively, but the measurements take place from 07:30 to 22:30.

MetOp stays stationary in local time sampling so that independent of the considered time interval (month or season), the event's local time will be the same—only the number of measurements will change.

Within July 2005, CHAMP's local time of the descending node shifted from 05:00 to 02:00 while F3C/FM-1's descending node shifted from 15:00 to 09:00. The local time drift of CHAMP and F3C/FM-1 causes a more even distribution of RO events in local time when extending the time-span from month to season. The northern and

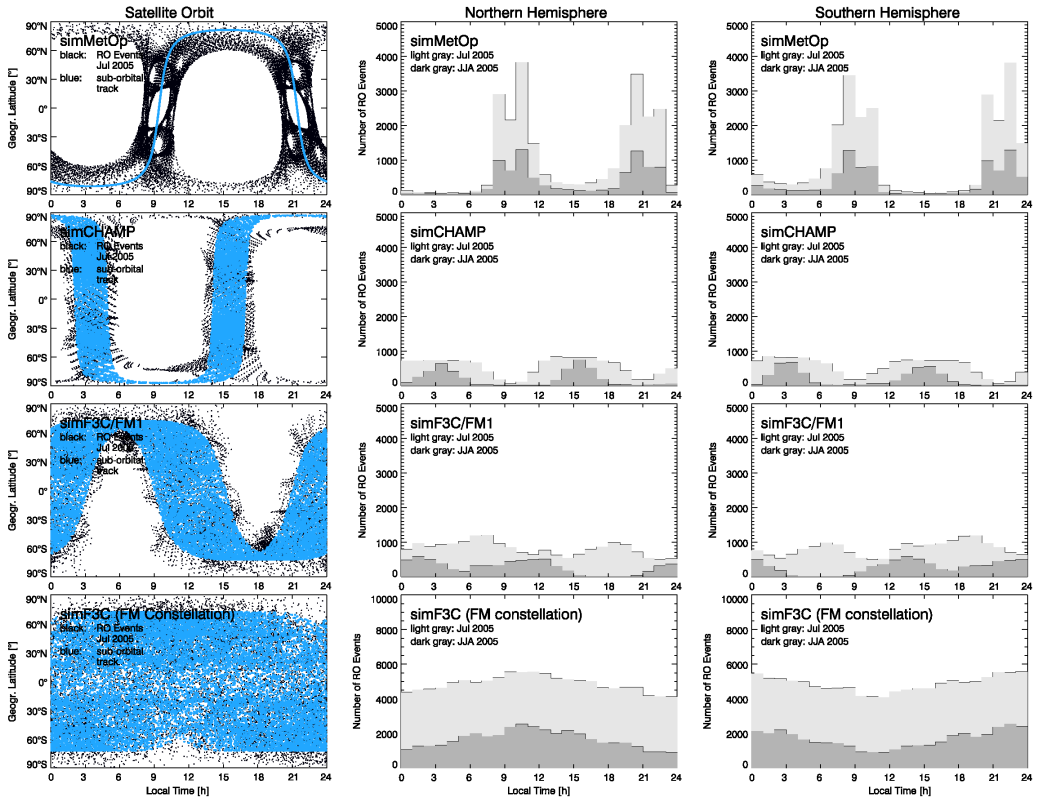

Figure 5.3: Occultation locations (black dots) and satellite sub-orbital tracks (in blue) are shown for July 2005 as a function of local time and latitude (left panels); the number of northern hemispheric measurements (middle panels) and southern hemispheric measurements (right panels) as function of local time in July 2005 (dark gray) and JJA 2005 (light gray) of simMetOp (top), simCHAMP, simF3C/FM-1, and the simF3C constellation (bottom). Note the different y-axis in the middle and right bottom panels (the number measurements performed by six satellites is considerable larger than the number of measurements performed by one single satellite.

southern hemisphere local time distributions of RO events performed by all six F3C satellites show the same pattern for one month and one season. This is because the depicted month is the central month of the season and the local time drift of the satellites amounts to 6 hours per month[2].

The considerable difference of total event numbers of MetOp, CHAMP, and F3C results from CHAMP only observing setting occultations (only one aft-looking antenna) whereas MetOp and each single F3C satellite observe about twice as many occultations, performing setting and rising measurements (one front- and one aft-looking antenna).

5.2 Sampling Error and Local Time Component

The measurement's local time strongly affects the SE of a climatology. The SE's Local Time Component (LTC) is caused by incomplete sampling of the diurnal cycle. It strongly depends on the geometry of the satellite orbits.

The SE of a climatology and its LTC can be estimated without any RO retrieval information beside the time and location of RO events. The use of a proxy data set (co-located profiles provided by the European Centre for Medium-Range Weather Forecasts (ECMWF) are compared to a regular ECMWF field) separates sampling information from observation information so that the SE is independent from RO observational errors.

The SE and its LTC are estimated for real CHAMP (realCHAMP) (i.e., all RO events where real CHAMP RO data passed the quality control within the Occultation Processing System (OPS) CHAMP retrieval), and for simMetOp, simCHAMP, and simF3C. The event distribution of realCHAMP is similar to the one of simCHAMP but the number of realCHAMP events is evidently reduced because of the restriction to events where real CHAMP profiles of high quality exist. The investigations were performed based on a period of two years from January 2004 until December 2005[3], a time span sufficiently long to also test for any potential longer-term secular components in the sampling characteristics.

The satellite orbit-dependent influence on local time sampling has already been investigated in relation to global cloud imagery data (Salby and Callaghan 1997) and to brightness temperatures (Kirk-Davidoff et al. 2005); an extensive theoretical study was also performed by Leroy (2001). Here, the focus lies on temperature data as obtainable from RO, i.e., gathered at times and locations of GPS RO events.

[2]The number of measurements performed in June 2005 and in August 2005 sums up to uniform local time sampling.

[3]This means that realCHAMP RO event locations as well as all simulations are based on this time period. Furthermore the ECMWF proxy data set stems from the period from January 2004 to December 2005.

5.2.1 Estimation of the SE and its LTC

The calculation of the SE of a climatology is described in detail in Subsection 3.3.5. To sum it up, the SE is defined as the difference between the mean of all co-located ECMWF profiles (co-located to the mean RO event location) of a bin and the mean of all data at all grid points available within the bin:

$$\Delta T(z_j, \varphi_k, \lambda_l)^{\mathrm{SE}} = T(z_j, \varphi_k, \lambda_l)^{\mathrm{coloc}} - T(z_j, \varphi_k, \lambda_l)^{\mathrm{true}}, \tag{5.6}$$

where $T(z_j, \varphi_k, \lambda_l)$ is the mean atmospheric parameter (temperature) at altitude z_j, representing one bin with mean latitude φ_k and mean longitude λ_l (derived either by co-located ECMWF profiles or the full ECMWF reference field). The averaging strategy used in this study generally follows Section 3.2 with the exception that larger horizontal-scale climatologies are aggregated from 5° zonal bands rather than $5° \times 60°$ fundamental bins. The vertical resolution of these climatologies corresponds to 500 m.

The LTC of a climatology stems from systematic undersampling of the diurnal cycle. In order to estimate the LTC (i.e., essentially the influence of the diurnal and semi-diurnal cycles) as part of the SE, the SE of the co-located ECMWF temperature profiles is taken as basis from which the non-local time SE calculated from ECMWF profiles taken at the same location at the same day, but at randomized times of the day is subtracted:

$$\Delta T(z_j, \varphi_k, \lambda_l)^{\mathrm{LTC}} = \Delta T(z_j, \varphi_k, \lambda_l)^{\mathrm{SE}} - \Delta T(z_j, \varphi_k, \lambda_l)^{\mathrm{SE\,rand}}. \tag{5.7}$$

The artificially randomized distribution is flat over all local times, i.e., well mimics a baseline sampling without local time selectiveness (Pirscher et al. 2007*b*).

The "region-average" mean SE and LTC are obtained from the calculation of direct region-average values. The magnitudes of the "region-average" mean SE and mean LTC $\Delta T(z_{j'}, \varphi_{k'}, \lambda_{l'})^{\mathrm{RegionMean\ SE}}$ and $\Delta T(z_{j'}, \varphi_{k'}, \lambda_{l'})^{\mathrm{RegionMean\ LTC}}$ are estimated via averaging the SE and the LTC from all relevant climatology grid points,

$$\Delta T(z_{j'}, \varphi_{k'}, \lambda_{l'})^{\mathrm{RegionMean\ SE}} = \frac{1}{N_{\mathrm{grid}}} \sum_{j=1}^{N_h} \sum_{k=1}^{N_\varphi} \sum_{l=1}^{N_\lambda} \Delta T(z_j, \varphi_k, \lambda_l)^{\mathrm{SE}}, \tag{5.8}$$

$$\Delta T(z_{j'}, \varphi_{k'}, \lambda_{l'})^{\mathrm{RegionMean\ LTC}} = \frac{1}{N_{\mathrm{grid}}} \sum_{j=1}^{N_h} \sum_{k=1}^{N_\varphi} \sum_{l=1}^{N_\lambda} \Delta T(z_j, \varphi_k, \lambda_l)^{\mathrm{LTC}}, \tag{5.9}$$

where N_{grid} specifies the number of grid points within a defined larger region. The region-average mean SE and LTC enable to quantify the effect of averaging over different large space-time domains.

The magnitudes of the "resolution-specific" mean SE $\Delta T(z_{j'}, \varphi_{k'}, \lambda_{l'})^{\mathrm{ResolMean\ SE}}$ and "resolution-specific" mean LTC $\Delta T(z_{j'}, \varphi_{k'}, \lambda_{l'})^{\mathrm{ResolMean\ LTC}}$ are estimated via

averaging the absolute values of $\Delta T(z_j, \varphi_k, \lambda_l)^{\mathrm{SE}}$ and $\Delta T(z_j, \varphi_k, \lambda_l)^{\mathrm{LTC}}$ from all relevant climatology grid points,

$$\Delta T(z_{j'}, \varphi_{k'}, \lambda_{l'})^{\mathrm{ResolMean\ SE}} = \frac{1}{N_{\mathrm{grid}}} \sum_{j=1}^{N_h} \sum_{k=1}^{N_\varphi} \sum_{l=1}^{N_\lambda} \left| \Delta T(z_j, \varphi_k, \lambda_l)^{\mathrm{SE}} \right|, \tag{5.10}$$

$$\Delta T(z_{j'}, \varphi_{k'}, \lambda_{l'})^{\mathrm{ResolMean\ LTC}} = \frac{1}{N_{\mathrm{grid}}} \sum_{j=1}^{N_h} \sum_{k=1}^{N_\varphi} \sum_{l=1}^{N_\lambda} \left| \Delta T(z_j, \varphi_k, \lambda_l)^{\mathrm{LTC}} \right|, \tag{5.11}$$

where N_{grid} again specifies the number of grid points within a defined larger region. These quantities represent typical values, which have to be expected within selected geographical sub-domains when looking at a monthly climatology resolved in 18 zonal bands and fixed height gridding. The high southern latitude region, for example, ranges from 60°S to 90°S. With 10° latitudinal sampling (bin size), and from an altitude of 15.5 km to 35.0 km (Lower Stratosphere (LS)) with 500 m vertical sampling, this yields a total number of grid points $N_{\mathrm{grid}} = 120$.

5.2.2 Features of the SE and the LTC

Figure 5.4 depicts the temperature SE (left) and its LTC (right) in January 2005 to illustrate the SE and LTC of a single month at the basic climatological resolution (10° zonal bands). The SE shapes of simMetOp, simF3C, simCHAMP, and realCHAMP are quite similar but the magnitude is different. In general, the latitudinal behavior of the SE is associated with the extent of underlying temperature variability. At low latitudes temperature variations are less pronounced but the higher the latitudes, the larger are the temperature variations and thus the larger are generally the effects on the SE (Foelsche et al. 2006; Foelsche et al. 2008*b*). The salient positive SE at mid and high northern latitudes in January 2005 is attributable to the under-sampling of the polar vortex, where spatio-temporal variability is particularly strong. The considerably smaller SE of simF3C is attributable to the distinctively larger number of measurements performed by six satellites and the resulting reduction of under-sampling of temperature variability.

The measurements' local time is associated with the satellite's equator crossing time. The equator crossing time of the sun-synchronous satellite MetOp remains constant at 09:30 (descending node). While CHAMP's equator crossing time shifted from approximately 09:40 to 06:45 in January 2005, all F3C measurements are spread over all local times at low and mid latitudes. The northern hemispheric local time sampling gap of simF3C measurements was located at noon. At high southern latitudes local time sampling was insufficient around midnight.

The close similarity of MetOp's and CHAMP's LTC can be attributed to the similar equator crossing times during this particular month. The absolute magnitude of

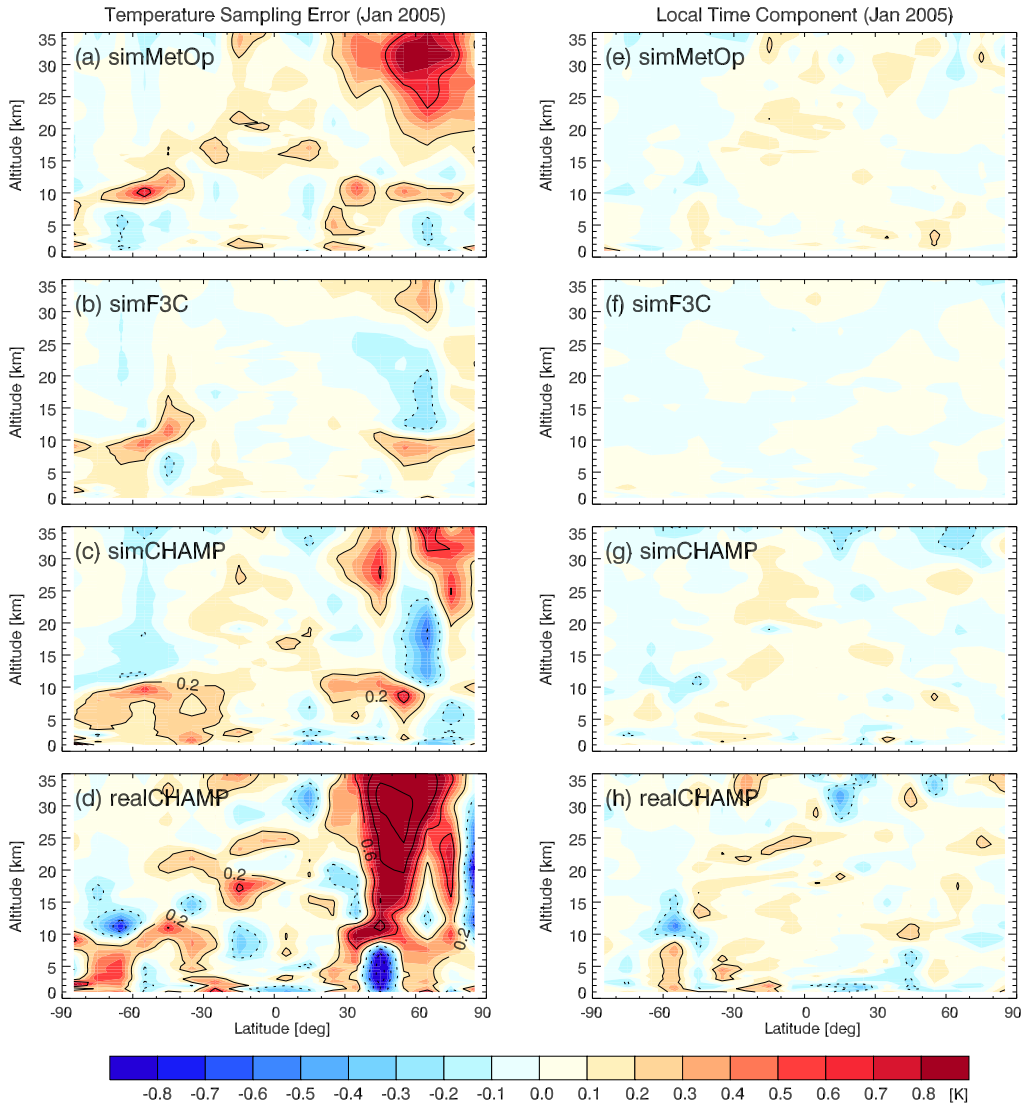

Figure 5.4: Monthly zonal mean temperature SE (left) and respective LTC of the error (right) in January 2005 for simMetOp, simF3C, simCHAMP, and realCHAMP (top to bottom).

the LTC is, in general, less than 0.1 K. realCHAMP's maximum values are larger and regions with a more pronounced LTC are somewhat wider spread than in case of simCHAMP. This is due to the reduced number of real measurements, since an increase in the number of profiles reduces the random component of the SE's LTC. The LTC of simF3C measurements is smallest in the whole atmosphere.

In order to show the systematic behavior of the SE and its LTC in the Tropics (TRO) (20°S to 20°N) and in the Southern Hemisphere Subtropics and Mid-latitudes (SHSM) (20°S to 60°S), Figure 5.5 and Figure 5.6 depict the temporal evolution of region-average SE and region-average LTC for the full two years simulated (Figure 5.5 shows results of simMetOp and simF3C, Figure 5.6 depicts results of simCHAMP and realCHAMP).

The tropical SE of simMetOp stays mainly positive with some increase of the SE between an altitude of 16 km and 20 km around the tropopause (at some spots exceeding 0.2 K). Apart from 6 km to 13 km, simF3C's low latitude SE is also small positive but no remarkable increase at the tropopause level can be observed. CHAMP's tropical SE resembles a pattern with sinusoidally varying positive and negative deviations, most pronounced between an altitude of 5 km and about 25 km. Above a height of about 27 km it is predominantly negative.

The increase in tropopause region variability is very clearly visible in the SE in the SHSM region for all four data sets, at altitudes from about 8 km to 13 km. This region shows a SE > 0.2 K observable during almost the whole observation period. This results from the comparatively larger temperature variability around the tropopause (Borsche et al. 2007). The feature is readily identifiable as well in simMetOp's tropical SE (Figure 5.5, top panels) and in simCHAMP's and realCHAMP's SE at low latitudes (Figure 5.6) but in case of CHAMP the overlay of the LTC is sufficiently strong that the positive deviation is cyclically broken when the measurement's local time results in a negative LTC.

Larger temperature variability at mid and high latitudes causes the SE to be more pronounced than at low latitudes. This SE, which occurs in hemispheric winter months, is also recognizable in Figure 5.5 and Figure 5.6 in the SHSM region. The largest SE occurs in the winter polar region, but it rarely exceeds ± 1.0 K (realCHAMP).

In general, the local time dependent part of the SE is well discernible in the respective SE in the tropics. At low latitudes the sun-synchronous satellite MetOp almost everywhere remains a slightly positive LTC (smaller than $+0.1$ K) during the whole observation period. This results from the equator crossing times of MetOp, which are at 09:30/21:30 (descending and ascending node). For this reason most events take place between 08:00/20:00 and 11:00/23:00 and no events occur between 0:00/12:00 and 07:00/19:00. Thus the skew-symmetric diurnal temperature cycle causes the LTC to be slightly positive compared to full local time sampling. This systematic bias can be expected to be persistent over the lifetime of MetOp.

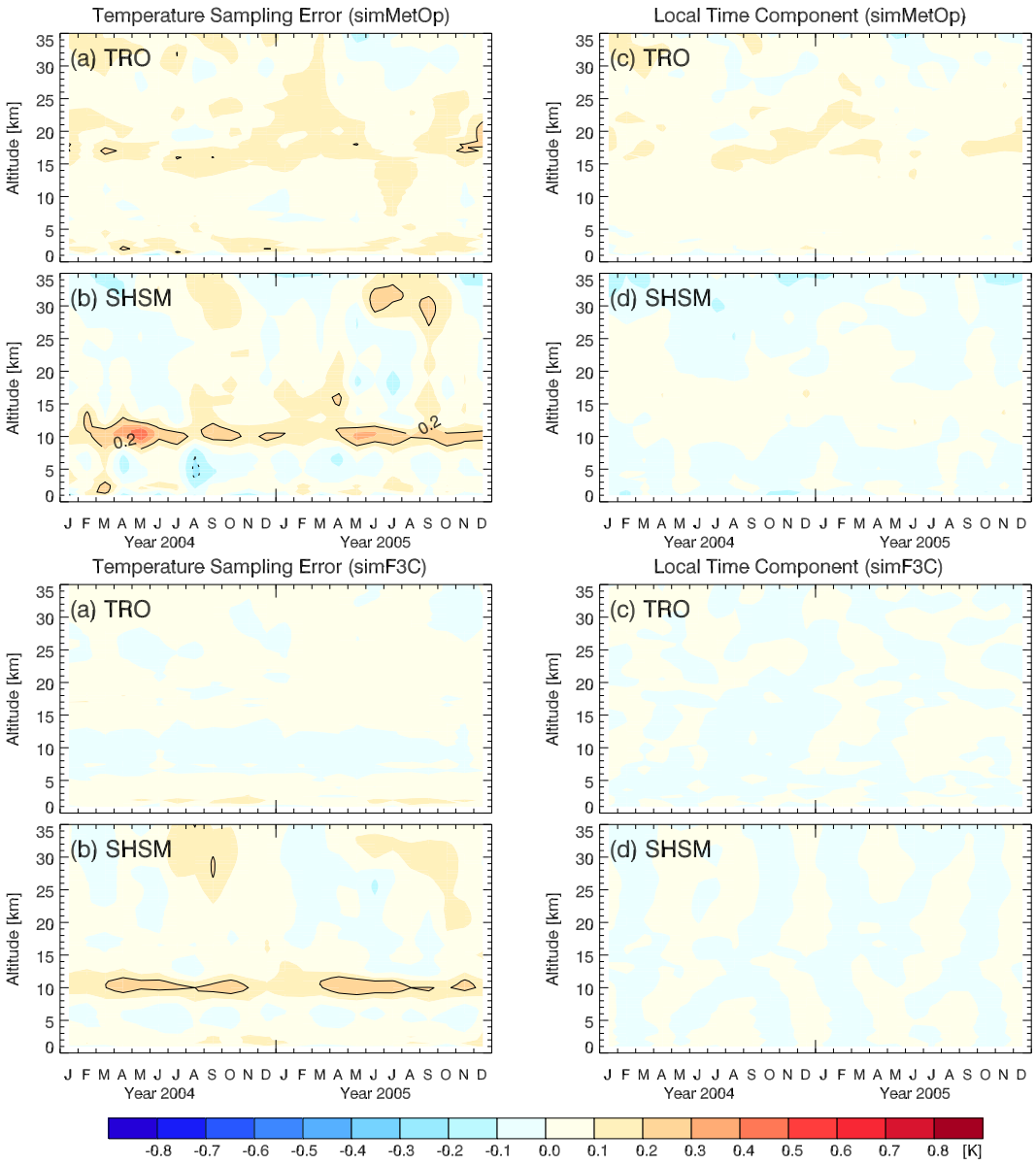

Figure 5.5: Time series of the monthly region-average temperature SE (left) and the LTC of the error (right) of simMetOp (top) and simF3C (bottom). TRO corresponds to the tropical band from 20°S to 20°N, SHSM represents the region from 20°S to 60°S.

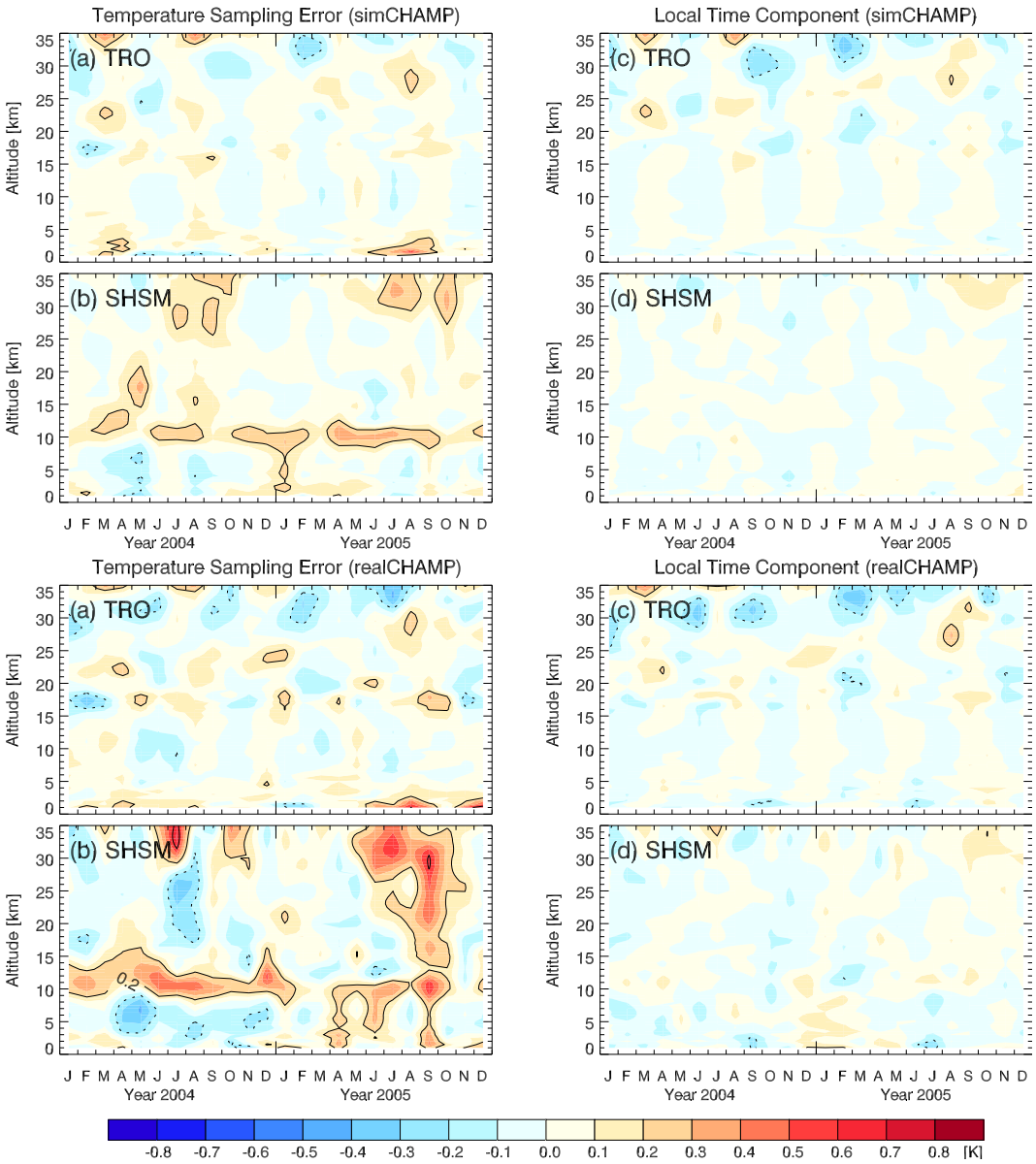

Figure 5.6: Time series of the monthly region-average temperature SE (left) and the LTC of the error (right) of simCHAMP (top) and realCHAMP (bottom).

Since F3C local time at low latitudes is quite uniform, no local time component remains in the SE.

In case of realCHAMP, whose measurements drift in local time, the tropical LTC shows a cyclic positive and negative deviation within ±0.1 K, a full cycle spanning about four months. This pattern is synchronous with the local time drift of CHAMP RO profiles, aligned with the drifting CHAMP orbit and determined by the 130 days period per one full diurnal cycle.

MetOp's LTC is different in the extratropical northern and the southern hemisphere. The northern hemispheric LTC is affected by more RO events during daytime (cf. Figure 5.3, middle left), which results in a positive LTC (generally smaller than +0.1 K though), whilst the counterpart behavior is formed in the southern hemisphere (see Figure 5.5), where the oversampling during nighttime yields a systematic negative contribution outside of 10 km to 20 km (smaller than −0.1 K though). This shows that the first harmonic of the diurnal cycle (period of 24 hours) cannot be removed completely at high latitudes due to the systematic asymmetry in observational time following from the satellite's sun-synchronous orbit (Leroy 2001). Due to the stability of the orbit, the LTC remains highly correlated overall within the latitudinal region also in the long term (Kirk-Davidoff et al. 2005).

The six F3C satellites do not uniformly sample local time at high latitudes and a LTC remains in the SE. However, the LTC does not really depend on local times when measurements are taken, it rather depends on the measurement's gap (i.e., on local times, when measurements are not taken). The local time sampling gap drifts with the same drifting rate as the satellites themselves. Averaging over monthly F3C measurements the local time sampling gap needs four months to drift through all local times. Because the gap is asymmetric on the northern and southern hemisphere, the LTC's sign is opposite on both hemispheres (Foelsche et al. 2009*a*).

CHAMP's LTC part of the SE diminishes at higher latitudes. Partly this results from the strong temperature variability, which exceeds the LTC, and partly it results from a decrease of the LTC with latitude. The geometry of the orbits allows for measurements to be performed within a larger range of local times at high latitudes, which may contribute to this decrease of LTC. Furthermore amplitudes of atmospheric thermal tides are distinctively stronger in the tropics compared to mid- and high latitudes (cf. Chapter 6). CHAMP's general LTC behavior outside the tropics in both hemispheres is characterized by quasi-random positive and negative deviations (smaller than ±0.1 K) during the observation period.

5.2.3 Absolute Magnitude of SE and LTC

The "resolution-specific" mean SE and mean LTC (absolute magnitude of the SE and LTC) represent typical values, which have to be expected within geographical subdomains when looking at a monthly climatology resolved into 18 zonal bands (10°

Table 5.4: Two-years average of resolution-specific SE (in K) and resolution-specific LTC of the error (in K) in five different latitude regions (SHP, SHSM, TRO, NHSM, NHP) for three different height regions (LS, UT, LT) of realCHAMP, simCHAMP, simMetOp, and simF3C.

	SHP		SHSM		TRO		NHSM		NHP	
	SE	LTC	SE	LTC	SE	LTC	SE	LTC	SE	LTC
realCHAMP										
LS	0.44	0.11	0.24	0.09	0.15	0.14	0.22	0.08	0.35	0.07
UT	0.31	0.11	0.27	0.12	0.10	0.05	0.28	0.10	0.35	0.09
LT	0.61	0.21	0.26	0.14	0.16	0.10	0.32	0.13	0.40	0.11
simCHAMP										
LS	0.31	0.07	0.16	0.06	0.12	0.11	0.14	0.06	0.21	0.05
UT	0.19	0.06	0.19	0.07	0.08	0.05	0.21	0.06	0.22	0.07
LT	0.40	0.14	0.17	0.09	0.14	0.09	0.23	0.10	0.24	0.07
simMetOp										
LS	0.33	0.06	0.12	0.05	0.11	0.09	0.12	0.06	0.26	0.05
UT	0.20	0.05	0.16	0.06	0.07	0.05	0.20	0.06	0.20	0.06
LT	0.36	0.10	0.13	0.06	0.11	0.05	0.18	0.07	0.23	0.06
simF3C										
LS	0.19	0.04	0.08	0.03	0.04	0.03	0.06	0.02	0.11	0.03
UT	0.12	0.03	0.12	0.02	0.03	0.01	0.13	0.02	0.15	0.03
LT	0.30	0.07	0.09	0.03	0.06	0.02	0.11	0.04	0.12	0.04

latitudinal width) and 500 m (or smaller) height gridding.

Typical Values for Some Sub-Domains

Figure 5.7 depicts the temporal variations of the resolution-specific SE and the resolution-specific LTC of the error for simMetOp (red), realCHAMP (blue), and simF3C (green), respectively, for a range of sub-domains of the global atmosphere. Table 5.4 supplements these graphical results with numerical values, showing the two year average in all different latitudinal regions and different height ranges considered.

The domains NHP/SHP represent 60°N/S to 90°N/S, NHSM/SHSM denote 20°N/S to 60°N/S, and TRO means the tropical region between 20°N and 20°S. The height ranges are divided into LS (height range between 15 km and 35 km), UT (5 km to 15 km), and LT (1 km to 5 km), respectively.

The comparison between realCHAMP and simCHAMP values allows for conclusions concerning the influence of the number of measurements, which are incorporated in the SE calculations. The same in principle applies for a comparison between

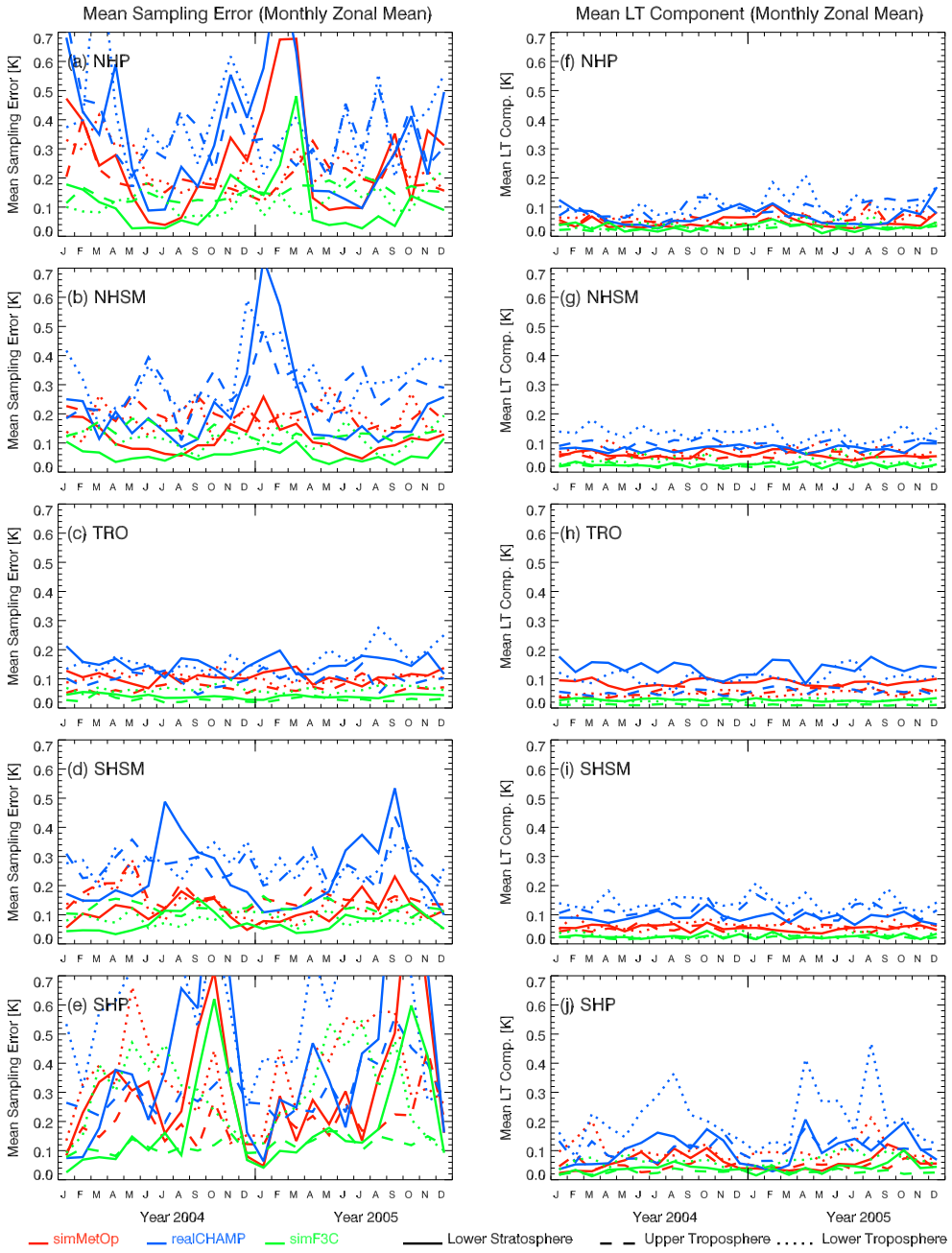

Figure 5.7: Time series of the resolution-specific mean SE (left) and the resolution-specific mean LTC of the error (right) in five different latitudinal regions (panel rows) for three different height regions (linestyles).

simCHAMP, simF3C, and simMetOp data but these satellites also differ in their orbital characteristics.

Figure 5.7 and Table 5.4 show that the resolution-specific SE's and LTC's temporal development as well as their magnitudes are in general similar for all satellites. Nevertheless, it is evident that a larger number of observations decreases both the SE and its LTC (the number of simF3C measurements is larger by a factor of 12 than simCHAMP and larger by a factor of six than simMetOp). A significant difference between the SE and the LTC of the sun-synchronous satellite MetOp and the non sun-synchronous satellite CHAMP cannot be observed but it has to be kept in mind that CHAMP is far from covering one full diurnal cycle within one month. Thus, the additional decrease in SE and LTC from simCHAMP to simMetOp is mostly attributable to the increase in the number of measurements. Climatologies of F3C measurements, which are available at all local times at low and mid latitudes within one month, show distinctively smaller SE and LTC in the respective latitude regions.

Figure 5.7 and Table 5.4 also show that the SE has a relatively symmetric appearance with respect to the equator. Seasonal temperature variations amplify the error in hemispheric winter, whereas it is lowest in the tropical region. In general, no remarkable height dependent pattern is noticeable. Sole exception is the SHP/LT region where large SE values can be found. The reason for this special SE is the presence and topography of the Antarctic continent, which allows only few RO profiles to extend to sea level and cuts many near 4 km height above the Antarctic plateau. The few low-reaching profiles are systematically warmer than the full average, resulting in that comparatively larger deviation.

The temporal behavior of the LTC error part of the SE (Figure 5.7, right column) is different from the SE. Even though a seasonal cycle is observable at high latitudes (larger LTC in hemispheric winter), comparatively large LTC magnitudes also occur at tropical latitudes, where the diurnal tide is most pronounced. In the tropical lower stratosphere (TRO/LS) the estimated LTC is even about the same size as the respective SE.

Typical Values for the Global UTLS

The study of SE properties was continued by investigating the error in the Upper Troposphere–Lower Stratosphere (UTLS) region in the altitude range between 5 km and 35 km: resolution-specific SE and LTC were calculated in a monthly 60° longitudinal UTLS sector (between 15°W and 45°E, i.e., in total one-sixth of the global area), and in the monthly and seasonally global UTLS region. The latitudinal resolution corresponds to the standard resolution of 10°, the vertical resolution still is 500 m (5 km to 35 km) in any case. Seasonal climatologies cover the period from December–January–February (DJF) 2003/04 until September–October–November (SON) 2005. Figure 5.8 depicts the results and Table 5.5 summarizes the two-year average values.

Table 5.5: Two-years average of resolution-specific SE (in K) and resolution-specific LTC of the error (in K) calculated in the UTLS region with different spatial and temporal resolutions of the climatological data.

	realCHAMP		simCHAMP		simMetOp		simF3C	
	SE	LTC	SE	LTC	SE	LTC	SE	LTC
Monthly 60° Sector	0.38	0.17	0.27	0.12	0.24	0.09	0.12	0.04
Monthly Zonal	0.25	0.10	0.17	0.07	0.17	0.06	0.09	0.03
Seasonal Zonal	0.18	0.06	0.12	0.04	0.12	0.05	0.06	0.01
Annual Zonal	0.11	0.03	0.07	0.02	0.08	0.04	0.04	0.01

In Table 5.5 also the values for the average annual mean have been added.

Overall the climatologies are of high accuracy with average SE smaller than 0.3 K and average LTC smaller than 0.15 K, respectively. The comparison between the monthly 60° sector mean and the monthly zonal mean allows to see the spatial resolution dependency of the mean SE. Insight into its temporal resolution dependency can be gained by comparing monthly, seasonal, and annual zonal means. The influence of the number of profiles on the errors can be best seen at any given resolution, from the difference between realCHAMP and simCHAMP. The satellite's orbit characteristics are reflected in different decreases in the resolution-specific SE and its LTC for F3C, CHAMP, and MetOp, respectively.

The resolution-specific SE decreases by about two thirds from the coarsest to the most detailed resolved data set. The spatial enlargement from the 60° sector mean to the global mean constitutes about the same degree of error reduction as the temporal extension of the averaging period from month to year.

Since CHAMP nearly samples one full diurnal cycle within one season and nearly three diurnal cycles within one year the LTC reduces most strongly for CHAMP: it decreases by more than a factor of two from monthly 60° sector to seasonal zonal means. The stability of simMetOp's orbit is reflected in the comparatively small decrease in LTC when increasing the averaging period. This small decrease is in this case to be attributed to the increasingly larger number of profiles which enters the SE calculation. Because of the comparatively even local time sampling, the LTC of F3C climatologies is very small in all spatial and temporal resolutions.

The resolution-specific SE and LTC of seasonal means and annual means are similar for CHAMP and MetOp but it is evident that a larger number of profiles further reduces the LTC of a drifting satellite, whereas it "saturates" to a residual small long-term constant bias for sun-synchronous satellites (about 0.04 K in annual mean for MetOp).

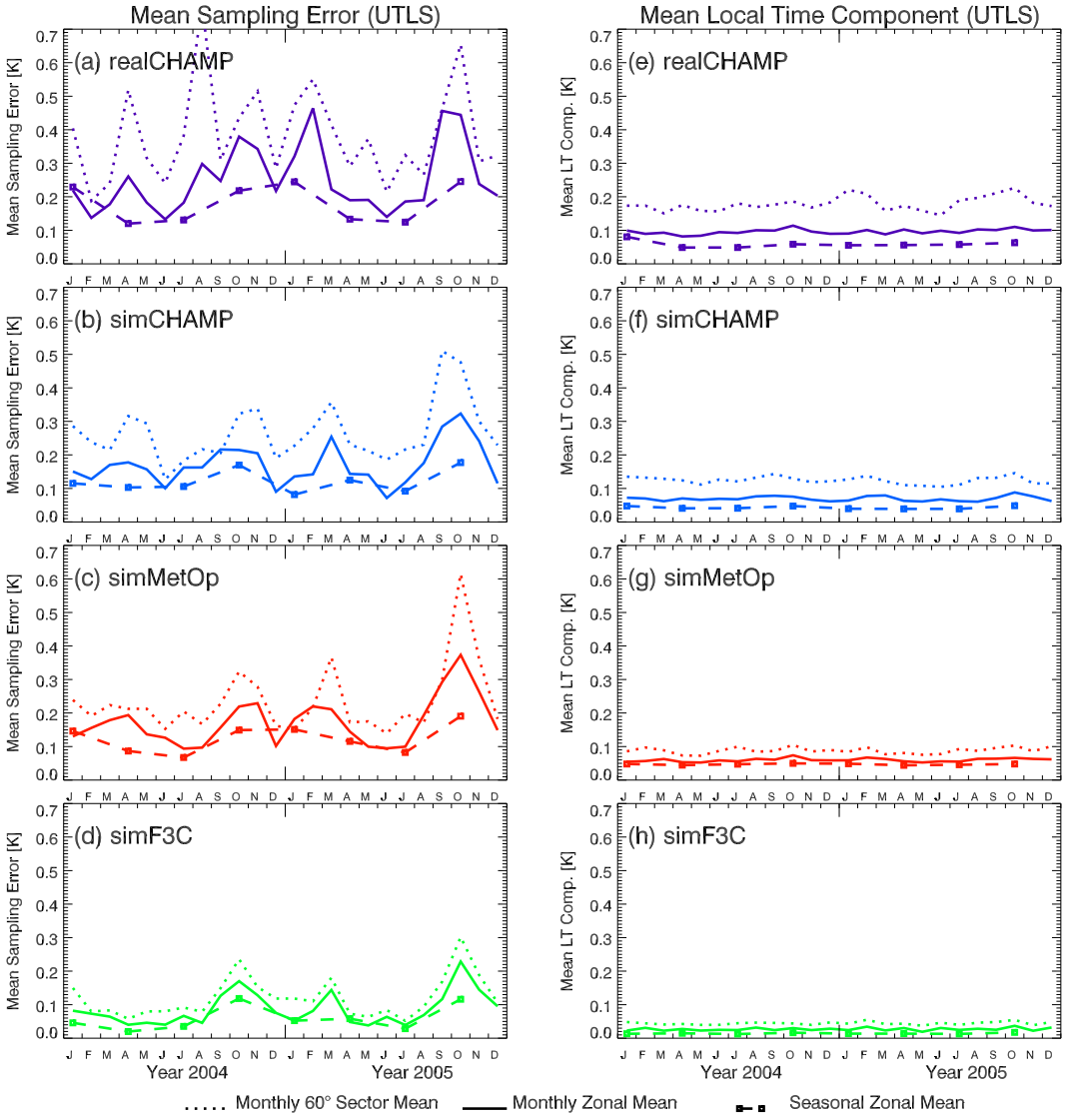

Figure 5.8: Time series of the UTLS region resolution-specific mean SE (left) and the resolution-specific mean LTC of the error (right) for monthly averages in a 60° longitudinal sector (dotted), monthly zonal averages (solid), and seasonal zonal averages (dashed), respectively.

5.2.4 Influence of Spatial and Temporal Climatological Resolution

Beyond the focus on the resolution-specific mean SE and LTC, the implications of averaging over of larger spatial regions have been studied. These parameters enable to quantify how the average errors approach zero, or a residual systematic bias, when averaging over increasingly larger space-time domains.

The two-years average of region-averaged SE and region-averaged LTC, calculated for the same geographical regions as used for the resolution-specific estimation in Section 5.2.3, are shown in Table 5.6. As the most salient (and expected) feature, essentially random errors are averaged out, so that region-averaged values are significantly smaller compared to resolution-specific ones.

The two-years average of the region-averaged SE is slightly positive for all satellites in all regions following from the positive SE arising at high latitudes predominantly in winter and from the systematic positive SE in the tropopause region. Since the SE depends on temperature variability, strongest variations occur at high latitudes. MetOp's SE in the tropical lower stratosphere is significantly larger compared to F3C and CHAMP, which is essentially zero (0.01 K is considered the limit of accuracy for quantitative interpretation, i.e., 0.01 K and below is "essentially zero"). It originates mainly from its LTC.

The region-averaged LTC shows the difference between the sun-synchronous satellite MetOp and the non sun-synchronous satellites F3C and CHAMP in the lower stratosphere. The two-years average of the region-averaged LTC of MetOp is negative in the southern hemisphere but positive in the tropics (most pronounced) and the northern hemisphere, while the two-years average of F3C's and CHAMP's region-averaged LTC is essentially zero.

Two-years averages for the whole global UTLS region yield a region-averaged SE of 0.05 K (realCHAMP), 0.04 K (simCHAMP and simF3C), and 0.07 K (simMetOp), respectively. These positive SE again can be attributed to the positive SE around the tropopause and especially to the positive SE in hemispheric winter. The UTLS two-years average LTC of realCHAMP, simCHAMP, and simF3C is found zero (0.00 K), while MetOp's LTC settles down at the stable non-zero value of 0.04 K, due to the residual hemispheric asymmetry of the LTC as noted above and seen in Table 5.6.

5.3 Summary of the Local Time Influence in RO Climatologies

The local time influence in RO climatologies is investigated for the sun-synchronous satellite (MetOp) and non sun-synchronous satellites CHAMP and F3C. The results showed that the local time of RO events has a minor but appreciable and clearly understandable influence on the SE of large-scale RO climatologies. The characteristics

Table 5.6: Two-years average and standard deviation of region-average SE (in K) and region-average LTC of the error (in K) in five different latitude regions for three different height regions of realCHAMP, simCHAMP, simMetOp, and simF3C.

	SHP		SHSM		TRO		NHSM		NHP	
	SE	LTC	SE	LTC	SE	LTC	SE	LTC	SE	LTC
realCHAMP										
LS_{mean}	0.06	0.00	0.05	0.00	0.00	−0.02	0.07	0.00	0.16	0.00
UT_{mean}	0.01	0.01	0.03	0.00	0.00	0.00	0.03	0.00	0.03	0.00
LT_{mean}	0.02	0.00	0.00	0.00	0.01	0.00	0.01	0.00	0.00	0.00
LS_{stddev}	0.35	0.06	0.13	0.05	0.06	0.06	0.14	0.03	0.27	0.03
UT_{stddev}	0.07	0.02	0.03	0.01	0.02	0.01	0.03	0.01	0.06	0.01
LT_{stddev}	0.03	0.02	0.02	0.01	0.01	0.01	0.02	0.01	0.05	0.01
simCHAMP										
LS_{mean}	0.13	0.00	0.05	0.00	0.01	−0.01	0.02	0.00	0.08	0.00
UT_{mean}	0.00	0.00	0.03	0.00	0.00	0.00	0.03	0.00	0.02	0.00
LT_{mean}	−0.01	0.00	0.00	0.00	0.01	0.00	0.02	0.00	−0.01	0.00
LS_{stddev}	0.25	0.02	0.06	0.03	0.06	0.07	0.07	0.03	0.14	0.03
UT_{stddev}	0.03	0.01	0.01	0.01	0.02	0.01	0.02	0.01	0.03	0.01
LT_{stddev}	0.01	0.01	0.01	0.01	0.01	0.00	0.01	0.00	0.03	0.01
simMetOp										
LS_{mean}	0.10	−0.03	0.03	−0.01	0.08	0.06	0.07	0.04	0.12	0.03
UT_{mean}	0.02	0.00	0.03	0.00	0.02	0.02	0.05	0.01	0.03	0.01
LT_{mean}	0.00	0.00	0.00	0.00	0.01	0.00	0.01	0.00	0.00	0.00
LS_{stddev}	0.28	0.02	0.05	0.02	0.03	0.02	0.06	0.02	0.22	0.01
UT_{stddev}	0.04	0.01	0.01	0.01	0.01	0.00	0.01	0.00	0.03	0.00
LT_{stddev}	0.02	0.01	0.01	0.00	0.00	0.00	0.01	0.00	0.03	0.00
simF3C										
LS_{mean}	0.12	0.00	0.04	0.00	0.02	0.00	0.01	0.00	0.06	0.00
UT_{mean}	0.02	0.00	0.03	0.00	0.00	0.00	0.03	0.00	0.03	0.00
LT_{mean}	0.00	0.00	0.00	0.00	0.01	0.00	0.01	0.00	0.01	0.00
LS_{stddev}	0.17	0.03	0.04	0.02	0.01	0.01	0.04	0.02	0.10	0.03
UT_{stddev}	0.01	0.00	0.01	0.00	0.00	0.00	0.01	0.00	0.01	0.00
LT_{stddev}	0.01	0.00	0.00	0.00	0.00	0.00	0.01	0.00	0.01	0.00

of the LTC are strongly dependent on the satellite's orbit.

The RO events' local time from satellites in sun-synchronous orbits remains constant and the resulting error is influenced by the event local times. For the sun-synchronous satellite MetOp the LTC remains constant during the whole observation period such that the magnitude of the local time errors in monthly mean or longer-term mean RO climatologies is generally lower than ± 0.1 K. Except for potential long-term effects of global warming on the diurnal cycle, which might require calibration, this small LTC is stable on decadal timescales and is mainly positive in the northern hemisphere and at low latitudes, whereas it is mainly negative in the southern hemisphere. These features are attributable to a slight orbit-determined asymmetry in local time sampling. The typical (temporally stable) local time error of an annual mean MetOp climatology resolved into 18 zonal bands amounts to approximately 0.04 K.

Non sun-synchronous satellites are able to sample at all local times if the averaging period is long enough. For the non sun-synchronous satellite CHAMP the local time error component in monthly mean RO climatologies is also small (up to about ± 0.15 K) but more variable (about zero mean) at mid and high latitudes. At low latitudes it results in sinusoidally varying positive and negative deviations with a several-months period, resulting from the local time drift of the satellite. The magnitude of local time errors is slightly larger compared to MetOp since the monthly averaging period is too short for CHAMP to entirely sample a diurnal cycle; a longer averaging period further decreases CHAMP's LTC. An annual mean climatology resolved into 18 zonal bands shows for CHAMP a typical local time residual error component of about 0.03 K.

At low latitudes, the satellite constellation F3C samples at all local times within 10 days so that the resulting LTC in monthly mean RO climatologies is very small (0.03 K). The orbital plane separation of 30° is not sufficient to achieve adequate local time sampling at high latitudes within one month and a residual error component remains. It primarily depends on the local time sampling gap, which drifts with the same drifting rate as the satellites themselves. The high latitude LTC yields sinusoidally varying positive and negative deviations with a two-months period. Averaging over larger geographical regions, the SE's local time dependent part becomes very small and even negligible (< 0.01 K). An annual mean climatology resolved into 18 zonal bands shows for F3C a typical local time residual error component of 0.01 K.

All estimated values of the LTC error represent a lower limit because the allocation of co-located ECMWF profiles to one of four Universal Time Coordinated (UTC) time layers broadens the respective local time distribution in the estimation process. However, since the diurnal cycle up to the second harmonics (semi-diurnal variations) is captured by the estimation, any residual delta error is expected to be of first order (10 % level) only.

The overall evidence is that monthly zonal mean climatologies of high accuracy (SE smaller than 0.3 K), with the LTC being a minor part (smaller than 0.1 K to 0.15 K), can be obtained. Also subtraction of the SE from RO climatologies is very effective to mitigate the SE in the climatologies (cf. previous Chapter 4). This underpins the utility of RO data for long-term monitoring of global climate variability and change.

6 Atmospheric Thermal Tides

The Local Time Component (LTC) of the Sampling Error (SE) (cf. Chapter 5) does not only depend on the drifting rate of the satellite but also on the characteristics and the magnitude of the diurnal cycle of an atmospheric parameter. For that reason it is of highest importance to monitor the diurnal cycle not only at the surface but also within the free atmosphere.

Within the scientific community the diurnal cycle of parameters in the free atmosphere refers to "atmospheric tides", which are observed as regular fluctuations in temperature, wind, pressure, or density. Atmospheric tides are global-scale waves, which can be classified into thermal and gravitational tides (Chapman and Lindzen 1970). While gravitational tides are excited by the gravitational field pull of the moon and the sun (cf. ocean tides), thermal tides are excited by insolation of the atmosphere and absorption of solar radiation as well as tropospheric heat release. These atmospheric thermal tides are mainly generated in the troposphere and stratosphere but as they are able to propagate away from these source regions and ascend into the upper atmosphere, they can also be observed in the mesosphere and thermosphere.

Within the Upper Troposphere–Lower Stratosphere (UTLS) region, atmospheric tides can be detected with Radio Occultation (RO) data. The orbit design of the FORMOSAT-3/COSMIC (F3C) constellation allows the determination and also monitoring of atmospheric tides on a monthly basis, at least up to 50°N/S.

6.1 Introduction to Atmospheric Thermal Tides

Atmospheric tides are primarily forced by daily variations in solar insolation. Lunar and solar gravitationally forced atmospheric tides are distinctively weaker than thermal atmospheric tides (Lindzen 1979). The amplitudes of gravitational tides are too small to be observed with RO data. For that reason this study focuses on atmospheric thermal tides.

6.1.1 Classical Tidal Theory

The classical tidal theory, which describes the basic characteristics of atmospheric tides is described by Chapman and Lindzen (1970), a review of the theory is given by Forbes (1995). This section mainly follows a summary, written by Oberheide (2006).

The classical tidal theory assumes that the motion of atmospheric waves can be considered as linear perturbations of an initially motionless zonal mean state, which is horizontally stratified and isothermal. Mechanical forcing and dissipation are neglected (Oberheide 2006).

Linearized Equations for Perturbations

According to Holton (1975), the linearized equations for perturbations (primed variables in Eq. (6.1) to (6.4)) in a spherical isothermal atmosphere are (1) two equations, which describe the horizontal momentum conservation (in the zonal and meridional direction)

$$\frac{\partial u'}{\partial t} - 2\Omega \sin\varphi v' + \frac{1}{r_\mathrm{e} \cos\varphi} \frac{\partial \Phi'}{\partial \lambda} = 0 \tag{6.1}$$

$$\frac{\partial v'}{\partial t} + 2\Omega \sin\varphi u' + \frac{1}{r_\mathrm{e}} \frac{\partial \Phi'}{\partial \varphi} = 0, \tag{6.2}$$

(2) the equation, which describes the energy conservation

$$\frac{\partial^2 \Phi'}{\partial t \partial z} + N^2 w' = \frac{\kappa J'}{H}, \tag{6.3}$$

and (3) the continuity equation

$$\frac{1}{r_\mathrm{e} \cos\varphi} \left(\frac{\partial u'}{\partial \lambda} + \frac{\partial (v' \cos\varphi)}{\partial \varphi} \right) + \frac{1}{\rho_0} \frac{\partial (\rho_0 w')}{\partial z} = 0, \tag{6.4}$$

with u, v, w the eastward zonal, the northward meridional, and the upward vertical wind, respectively, t the time, Ω the angular velocity of the Earth's rotation, λ and φ longitude and latitude, respectively, r_e the radius of the Earth, $\Phi = \int g(z, \varphi) \mathrm{d}z$ the geopotential with g the gravity acceleration as a function of altitude z and latitude φ. N^2 is the square of the Brunt-Väisälä (buoyancy) frequency, $\kappa = R/c_p \approx 2/7$ with R the gas constant for air and c_p the specific heat capacity at constant pressure p, J the heating rate per unit mass, H the constant scale height, and ρ_0 the air density, which decreases exponentially with height.

Equations (6.1) to (6.4) can be solved for longitudinally propagating waves with zonal wavenumbers k and frequencies f. In this subsection, zonal wavenumbers k are positive integer values so that positive values for f correspond to eastward propagating waves and negative values correspond to westward propagating waves (Oberheide 2006). This nomenclature is different to the one used throughout the remainder of this chapter where frequencies are always positive and positive/negative values of k represent westward/eastward propagation.

Variables can be separated by

$$\hat{\Phi} = \Theta(\varphi)G(z), \tag{6.5}$$

where $\Theta(\varphi)$ describes the latitudinal structures and $G(z)$ accounts for vertical structures.

Laplace's Tidal Equation

Laplace's tidal equation (also called horizontal structure equation) is a differential equation, which describes the latitudinal structure of the tides (by determining $\Theta(\varphi)$):

$$\mathcal{L}\hat{\Theta} + \epsilon\hat{\Theta} = 0 \tag{6.6}$$

Equation (6.6) is an eigenfunction-eigenvalue problem, which means that tides are eigenmodes or eigenoscillations of the atmosphere. A complete orthogonal set of eigenfunctions Θ_n (Hough functions[1]) and eigenvalues ϵ_n can be found for all specified wavenumbers k and frequencies f.

The Laplace operator $\mathcal{L}$ is given by

$$\mathcal{L} = \frac{\partial}{\partial\mu}\left[\frac{(1-\mu^2)}{(\eta^2-\mu^2)}\frac{\partial}{\partial\mu}\right] - \frac{1}{\eta^2-\mu^2}\left[-\frac{k}{\eta}\frac{(\eta^2+\mu^2)}{(\eta^2-\mu^2)} + \frac{k^2}{1-\mu^2}\right] \tag{6.7}$$

where $\mu = \sin\varphi$ and $\eta = f/(2\Omega)$.

The eigenvalues ϵ_n of Eq. (6.6) are given by

$$\epsilon_n = \frac{(2\Omega r_\mathrm{e})^2}{gh_n}, \tag{6.8}$$

where h_n is the separation constant (also called equivalent depth). It couples the horizontal structure of the tides with their vertical structure.

Vertical Structure Equation

The vertical structure equation for an isothermal atmosphere in its canonical form is

$$\frac{\partial^2 G_n^\star}{\partial x^2} + \alpha_n^2 = F_n(x) \tag{6.9}$$

[1] Hough functions are defined as an infinite sum of associated Legendre polynoms (Oberheide 2006).

where

$$G_n^\star = \frac{G_n \rho_0^{1/2}}{N}, \tag{6.10}$$

$$x = \frac{z}{H}, \tag{6.11}$$

$$\alpha_n^2 = \frac{\kappa H}{h_n} - \frac{1}{4}, \tag{6.12}$$

$$F = -\frac{1}{\rho_0^{1/2} i f N} \frac{\partial(\rho_0 J_n)}{\partial x}. \tag{6.13}$$

At altitudes above the source region, Eq. (6.9) has three solutions (for bounded solutions)

$$G_n^\star(x) \sim \begin{cases} \mathrm{e}^{-|\alpha_n|x} : \alpha_n^2 < 0, \\ \mathrm{e}^{i\alpha_n x} : \alpha_n^2 > 0, \\ \mathrm{e}^{(\kappa-1/2)x} : h_n = H/(1-\kappa), F_n(x) = 0, \forall x \end{cases} \tag{6.14}$$

The first solution ($\alpha_n^2 < 0$) leads to evanescent or trapped waves, the second solution ($\alpha_n^2 > 0$) leads to propagating waves, and the third solution leads to Lamb waves (free solutions).

Vertically propagating waves ($\alpha_n^2 > 0$) move into regions of lower density. If the tide is not dissipating, its kinetic energy must be conserved. Decreasing density with height yields increasing amplitudes of atmospheric tides. The waves' amplitude at height z can be described by

$$A = A_0 \exp\left(\frac{z}{2H}\right), \tag{6.15}$$

with A_0 being the initial amplitude of the wave. While amplitudes of diurnal tides at tropical latitudes are about 1 K at an altitude of 30 km (e.g. Alexander and Tsuda 2008), they become larger than 25 K in the lower thermosphere (Zhang et al. 2006).

The vertical wavelength $\lambda_{z,n}$ is given by

$$\lambda_{z,n} = \frac{2\pi H}{\alpha_n} = \frac{2\pi H}{\sqrt{\frac{\kappa H}{h_n} - \frac{1}{4}}} \tag{6.16}$$

with α_n/H being the vertical wavenumber. The vertical group velocity $c_{gz,n}$ for propagating waves is

$$c_{gz,n} = H \frac{\partial f}{\partial \alpha_n}. \tag{6.17}$$

Upward energy propagation $c_{gz,n} > 0$ is achieved only if $\alpha_n > 0$ for westward propagating waves ($f < 0$) or if $\alpha_n < 0$ for eastward propagating waves ($f > 0$). The wave maximizes at a given height $x = z/H$ if

$$k\lambda + \alpha_n x - ft = 0. \tag{6.18}$$

Focusing on a fixed longitude λ, Eq. (6.18) always results in downward phase progression as time progresses.

6.1.2 Genesis of Thermal Tides

The well pronounced temperature diurnal cycle, which can be observed on the surface, results from solar radiation, which irradiates on the Earth and is absorbed by the ground and the sea. Turbulence and infrared radiative transfer convey radiation to the adjacent atmosphere (Chapman and Lindzen 1970). However, these diurnal surface oscillations can only be observed in temperature, humidity, and wind, but not, e.g., in surface pressure.

This can be confirmed when looking at Figure 6.1, which shows surface temperature and surface pressure variations over a period of 20 days at two different stations. One meteorological station is located in the tropics, on the island of St. Helena, 15.9°S and 5.7°W, the other one is located in the mid-latitudes, in Graz, Austria, 47.0°N and 15.4°E. Surface temperature is higher at the tropical station than at the mid-latitude (winter) station but both time series show the well pronounced temperature diurnal cycle. The surface pressure at the tropical station also shows some distinctive oscillations but their period is different from one day. Surface pressure in Graz is characterized by irregular variations, which are associated with weather changes. However, looking into detail, reveals also some small oscillations in the mid-latitude surface pressure.

Figure 6.2 shows surface temperature and surface pressure recorded in St. Helena and in Graz only for two days from February 18, 2009 until February 19, 2009. Within these days the weather in Graz was quite stable and surface temperature and surface pressure oscillations are similar in Graz and St. Helena (apart from their different magnitudes, note the different y-axis ranges in the plots). Two temperature maxima can be found within these two days, which are connected with the diurnal cycle caused by thermal excitation due to exchange of heat with the ground. Four maxima in surface pressure point at a semi-diurnal cycle. This semi-diurnal cycle of surface pressure is not connected with exchange of heat with the ground. The underlying generation mechanism relies on thermal excitation due to direct absorption of insolation by atmospheric constituents.

Absorption of solar radiation by tropospheric water vapor, stratospheric ozone, and thermospheric molecular oxygen and molecular nitrogen as well as tropospheric

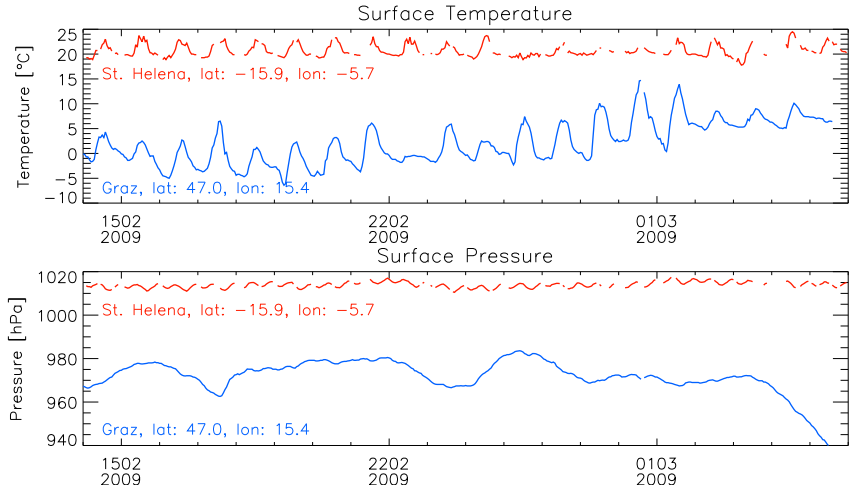

Figure 6.1: Surface temperature (top) and surface pressure (bottom) at two different meteorological stations from February 14, 2009 until March 6, 2009. While the meteorological station in St. Helena represents a typical tropical station, the station in Graz is a representative mid-latitude station.

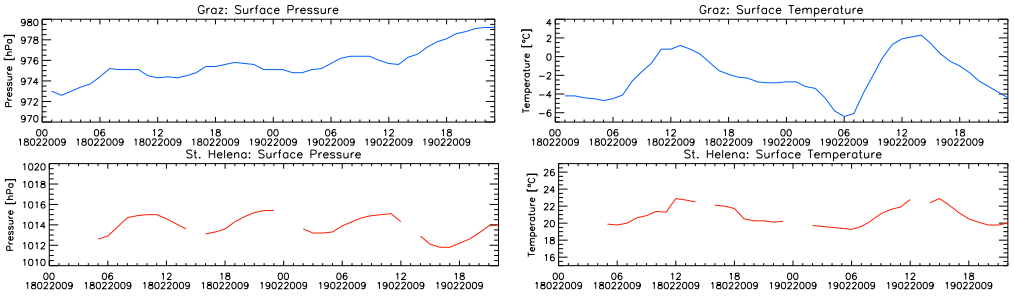

Figure 6.2: Surface pressure (left) and surface temperature (right) in Graz (top) and St. Helena (bottom) from February 18, 2009 until February 19, 2009. Note the different y-axes in the plots.

heat release generate atmospheric thermal tides (Hagan 1996; Hagan and Forbes 2002; Hagan and Forbes 2003).

However, solar energy penetrates the Earth's atmosphere only at daytime so that atmospheric heating by the sun occurs with a period of 24 hours. Since solar heating of the atmosphere occurs in an approximate square wave profile, the tides' periods equal the harmonics of one solar day. Diurnal tides occur with periods of 24 hours, semi-diurnal tides have periods of 12 hour, and the periods of terdiurnal tides amount to 8 hours.

Migrating thermal tides (e.g., Hagan 1996) move westward with the apparent motion of the sun. Zonal wavenumbers k of migrating tides (where positive wavenumbers correspond to westward motion) therefore equal their frequencies, f, in cycles per day (e.g., DW1 (westward migrating diurnal tide) $k = 1$ and $f = 1$ cycle per day, SW (westward migrating semi-diurnal tide) $k = 2$ and $f = 2$ cycles per day).

Any longitudinal variation in the absorbing medium such as large-scale regional cloudiness, diurnally varying latent heat release (convective heating), including variations in the Earth's surface (including land-sea contrast and topography) gives rise to additional non-migrating tidal components. Non-migrating tides have the same periods as migrating tides but they do not follow the apparent motion of the sun. Instead, they do not propagate horizontally, they propagate eastward, or they propagate westward, with a different speed relative to the sun ($k \neq f$, e.g., DE) (e.g., Tsuda and Kato 1989; Lieberman 1991; Williams and Avery 1996).

The most prominent atmospheric tidal mode in the whole atmosphere is the sun-synchronous migrating diurnal tide. In the UTLS region, its amplitude is just about the size to be very well observable. Since amplitudes increase with increasing altitude, other tidal components are better visible in the upper atmosphere, e.g., in the Mesosphere and Lower Thermosphere (MLT). At 115 km, for example, the amplitude of the migrating diurnal tide is larger than 20 K, the amplitude of the migrating semi-diurnal tide amounts to approximately 16 K, and the amplitude of the eastward propagating diurnal wave with wavenumber 3 (DE3) is approximately 8 K (Zhang et al. 2006).

6.1.3 Migrating Thermal Tides

Tidal equations can be solved for different sources of excitation—atmospheric migrating thermal tides are excited by the heating rate J. Tropospheric water vapor and stratospheric ozone are the main sources of excitation of atmospheric migrating thermal tides. Chapman and Lindzen (1970) calculated diurnal and semi-diurnal temperature and pressure oscillations due to water vapor and ozone excitation. They assumed that thermal excitation due to water vapor exists in an approximately 18 km thick layer, which is centered about 1.5 scale heights above the Earth's surface. Excitation due to stratospheric ozone was found to exist in an approximately 40 km

Table 6.1: Equivalent depths h_n for diurnal and semi-diurnal modes (after Lindzen 2008).

Diurnal Mode	h_n	Semi-diurnal Mode	h_n
+1	+ 0.69 km	+2	+7.85 km
+3	+ 0.12 km	+4	+2.11 km
+5	+ 0.05 km	+6	+0.96 km
−2	−12.27 km		
−4	− 1.76 km		

thick layer, which is centered at about 6 scale heights above the Earth's surface.

Table 6.1 shows the most important equivalent depths h_n for the diurnal and the semi-diurnal mode. Modes associated with positive equivalent depths h_n have most of their amplitude confined to latitudes equatorwards of 30°. Sufficient small positive equivalent depths are associated with vertical propagation (i.e., propagation of the disturbance away from the region of excitation). Modes associated with negative equivalent depths have most of their amplitude confined to latitudes polewards of 30°. Negative equivalent depths are associated with vertical trapping (Chapman and Lindzen 1970).

Migrating Diurnal Tides

The diurnal heating functions H^{D} for ozone and water vapor yield (Lindzen 2008)

$$H^{\mathrm{D}}_{\mathrm{O}_3} = 1.63\Theta^{\mathrm{D}}_{-2} - 0.51\Theta^{\mathrm{D}}_{-4} + \cdots + 0.54\Theta^{\mathrm{D}}_{1} - 0.14\Theta^{\mathrm{D}}_{3} + \ldots$$
$$H^{\mathrm{D}}_{\mathrm{H_2O}} = 0.16\Theta^{\mathrm{D}}_{-2} - 0.06\Theta^{\mathrm{D}}_{-4} + \cdots + 0.62\Theta^{\mathrm{D}}_{1} - 0.016\Theta^{\mathrm{D}}_{3} + \ldots$$

Most of the forcing goes into trapped modes with negative equivalent depths. However, because modes with positive equivalent depths are able to propagate vertically with short wavelengths, migrating diurnal tides are also able to move through the free atmosphere. The main propagating mode with an equivalent depth of $h_n = 0.69$ km has a vertical wavelength of about 25 km. The ozone excitation is generated in a layer of approximately 40 km depth. Thus, waves excited at one level can destructively interfere with waves excited at another level. Since the region of water vapor excitation is only 18 km thick, water vapor excitation is more important than ozone excitation for generating migrating diurnal tides (Chapman and Lindzen 1970).

Migrating Semi-Diurnal Tides

The semi-diurnal heating functions for ozone and water vapor are (Lindzen 2008):

$$H_{O_3}^{SD} = 0.25\Theta_2^{SD} + 0.065\Theta_4^{SD} + 0.036\Theta_6^{SD} + \dots$$
$$H_{H_2O}^{SD} = 0.03\Theta_2^{SD} + 0.008\Theta_4^{SD} + 0.005\Theta_6^{SD} + \dots$$

The equivalent depth of main mode Θ_2^{SD} amounts to $h_n = 7.85$ km, which yields an extremely long vertical wavelength of about 150 km. Since ozone excitation occurs over a greater depth and at higher altitudes than water vapor excitation, ozone is more important in generating semi-diurnal tides than water vapor excitation. Ozone excitation causes surface pressure to occur as a semi-diurnal variation (cf. left panels of Figure 6.2).

6.2 Observation of Atmospheric Thermal Tides

The diurnal tide of temperature is investigated in the UTLS region using RO data of the F3C satellite constellation. The main focus lies on the analysis of migrating diurnal and semi-diurnal tides at low- and mid-latitudes. Results will be published soon by Pirscher et al. (2010).

Studies on diurnal tides within the UTLS region have been performed by, e.g., Tsuda et al. (1997); Seidel et al. (2005); Alexander and Tsuda (2008); Huang et al. (2009) using radiosonde data and by, e.g., Revathy et al. (2001); Riggin et al. (2002) using radar data. These ground-based data contain global and local signatures of atmospheric tides and it is not possible to separate migrating from non-migrating diurnal tides. Zeng et al. (2008) used CHAllenging Mini-Satellite Payload (CHAMP) RO measurements to detect migrating diurnal tides within the tropics. The single satellite RO mission CHAMP yields the longest available RO data set with data available from 2001 to 2008. The design of the CHAMP orbit leads to a local-time drift of three hours within one month (cf. Chapter 5). Consequently it is not possible to observe diurnal tides within one month or one season. For that reason it is necessary to synthetically merge data from a number of years. This study advances the work of Zeng et al. (2008) by investigating F3C RO data and applying the same method to isolate atmospheric tides (space-time spectral analysis). The main advantages of the F3C data set are the large number of measurements performed by six evenly distributed satellites and the resulting high local-time resolution of diurnal tide analyses, which is possible on a continuous monthly scale.

To provide valuable context, comparisons are drawn to migrating diurnal tides analyzed in European Centre for Medium-Range Weather Forecasts (ECMWF) and National Centers for Environmental Prediction (NCEP) data. In an early study, Hsu and Hoskins (1989) have shown that ECMWF analyses contain diurnal and semi-

diurnal tides below 50 hPa. Since RO data are operationally assimilated at ECMWF and NCEP, the investigation is based on short-term forecasts (24 h to 45 h forecasts) rather than analyses, which avoids direct inter-dependencies and investigates the models' dynamics.

6.2.1 Data Basis

Diurnal tides of temperature are estimated on a continuous monthly scale from January 2007 until December 2008. RO data and ECMWF short-term forecasts are used between 8 km and 35 km altitude with a vertical gridding of 0.2 km; NCEP forecast data have been available on 26 pressure levels from which 10 pressure levels (300 hPa and above) have been used.

F3C RO Data

The Wegener Center for Climate and Global Change (WEGC) retrieval (cf. Chapter 1) uses phase delay and orbit data provided by UCAR/CDAAC. The retrieval utilizes co-located ECMWF short-term forecasts as background information above an altitude of 30 km (24 h/30 h forecasts, four time layers; co-location means nearest time layer and spatial interpolation to mean occultation event location). Dependent on the quality of the F3C measurements, most atmospheric profiles are observation dominated below 40 km (cf. Chapter 2). However, some background information remains in the refractivity profile as far down as 30 km and it propagates further downwards when calculating atmospheric pressure using the hydrostatic integral. For that reason diurnal tides detected with WEGC RO data are partially influenced by ECMWF short-term forecasts.

UCAR/CDAAC F3C dry temperature data have been used to quantify this effect. Within the high-altitude initialization, CDAAC uses a background model, which is based on a National Center for Atmospheric Research (NCAR) climatology exponentially extrapolated to 150 km (Randel et al. 2002, Section 4). The initialization process involves with the optimal mixing of the observed and background bending angle, which is described in Kuo et al. (2004). The background NCAR climatology does not possess any diurnal variation.

Dependent on the satellites' health, the F3C satellite constellation performs between 1500 and 2500 measurements per day. At WEGC on average, about 75 % of these measurements are of high quality (cf. Chapter 2). Between January 2007 and December 2008 more than 40 000 high quality RO profiles per month have been available.

The orbit characteristics and the local time sampling of the F3C satellite constellation has been discussed in Section 5.1. The principal points have been that (1) for the entire F3C constellation (with 30° orbit plane separation) it takes about 10 days

to sample all local times at low latitudes and (2) at high latitudes the constellation is not able to sample all local times within one month because a small gap of measurements remains. Averaging over monthly data, this gap of measurements drifts with the same rate as the satellites themselves.

ECMWF and NCEP Data

Because of the high quality in the UTLS region and their global availability, RO data have significant impact on global/regional weather analysis and prediction (Kuo et al. 2000; Liu et al. 2001; Healy and Thepaut 2006). Since December 12, 2006 RO data are operationally assimilated at ECMWF (Healy 2007), since May 1, 2007 the assimilation of RO profiles became operational at NCEP (Cucurull and Derber 2008), rendering the operational analyses not independent of RO profiles any more. For that reason ECMWF and NCEP short-term forecast data have been investigated to look for diurnal tides.

To obtain ECMWF forecast data at eight equally distributed Universal Time Coordinated (UTC) time layers (00 UTC, 03 UTC, 06 UTC, 09 UTC, 12 UTC, 15 UTC, 18 UTC and 21 UTC), forecasts of 24 h to 45 h (initial analysis at midnight) have been extracted with a horizontal resolution of approximately $2.5° \times 2.5°$ at 91 vertical levels (T42L91). These 91 vertical levels, which range up to approximately 80 km, are interpolated to a regular 200 m grid (only used between 8 km and 35 km).

Dry temperature, which is used to estimate atmospheric tides from ECMWF data, is approximated from physical temperature T (in K) and specific humidity q (in kg/kg) (Foelsche et al. 2008*b*) by

$$T_{\mathrm{dry}} \approx T(1 - 12.4q). \tag{6.19}$$

Operational Global Forecast System (GFS) forecasts are provided by the data archive at the National Climatic Data Center (NCDC)/NOAA Operational Model Archive and Distribution System (NOMADS). To be on a par with ECMWF, 24 h to 45 h forecasts (3 h forecast interval) with initial analysis at midnight have been used. The data are provided on a regular $0.5° \times 0.5°$ horizontal latitude-longitude grid, with 26 vertical standard pressure levels (GFS 004 domain). Data at [10, 20, 30, 50, 70, 100, 150, 200, 250, 300] hPa have been used. The main focus of this study is the lower stratosphere region, where dry temperature is essentially equal to physical temperature (negligible water vapor). Therefore the analysis of NCEP diurnal tides is restricted to physical temperature.

6.2.2 Methodology Used to Extract Atmospheric Tides

Information on global atmospheric waves is present in RO data. The spatial and temporal scales of the waves as well as characteristics of the data set determine the

method used to extract the waves. This section describes the methodology used to obtain information on atmospheric diurnal tides using F3C RO and model data.

Diurnal tides are investigated in different latitudinal regions, where the mean atmospheric profile of each region has to represent typical atmospheric characteristics and the variation of corresponding single measurements must not be too large. Therefore, the optimal extent of the regions to detect diurnal tides is a tradeoff between a sufficiently large number of RO profiles and small atmospheric variability. A sufficient number of measurements and reasonably similar atmospheric characteristics have been found, in selecting 5° zonal bands. These bands range from 90°S to 90°N resulting in 36 zonal bands. At low- and mid-latitudes the number of profiles available within one band varies between 1000 and 2500; at high latitudes, the number of profiles is significantly less.

Monthly averaged local-time variations of dry temperature ("diurnal temperature variations") enable a first view of diurnal tides (Pirscher et al. 2009). First of all, in data preparation for this purpose, any RO event is allocated to the appropriate 5° zonal bin. To remove synoptic atmospheric variability, the daily-mean 5° zonal mean ECMWF forecast profile is subtracted from each single F3C profile. Finally, diurnal temperature variations are calculated by averaging over all profiles belonging to the same local-time bin (eight local-time bins with three hours width) and subtracting the mean profile of all local-time bins. This approach does not contain any confining assumption but it strongly depends on the number of profiles and atmospheric variability. Furthermore, it does not split particular modes of total oscillation but represents the superposition of all waves.

Figure 6.3 shows diurnal temperature variations of WEGC F3C and ECMWF data. Northern hemispheric winter is accompanied by strong atmospheric variability. An unequally distributed number of profiles for each local-time bin (Figure 6.3 left panels) results in inhomogeneous diurnal temperature variations. Otherwise, a regular number of measurements and comparably low variability unveil patterns, which are similar to diurnal tides determined with a more sophisticated method.

The space-time spectral analysis method (Hayashi 1971) is used to decompose atmospheric tides into zonal wavenumber and direction (space) and period (time). The space dimension of the data set covers zonal bands with 5° width and is analyzed with respect to wavenumbers k. 64 grid points in longitude (spatial resolution: 5.625°) are used for the RO data sets and 32 grid points for the model data sets (spatial resolution: 11.25°). Time is gridded in 64 points in the RO data sets (UTC resolution: 0.375 h) and 8 points (only 8 time layers available, UTC resolution: 3 h) in the model data sets. To sum up, the RO data set $X_\varphi(\lambda, t)$ with geographic latitude φ, longitude λ, and time t, is gridded into 64×64 points and the forecast model data are gridded into 32×8 points. Sensitivity tests with different resolutions showed that the results of space-time spectral analysis are stable with these resolutions, i.e., changes of grid density have little effect (± 0.05 K) on the analysis results (cf. Figure 6.4).

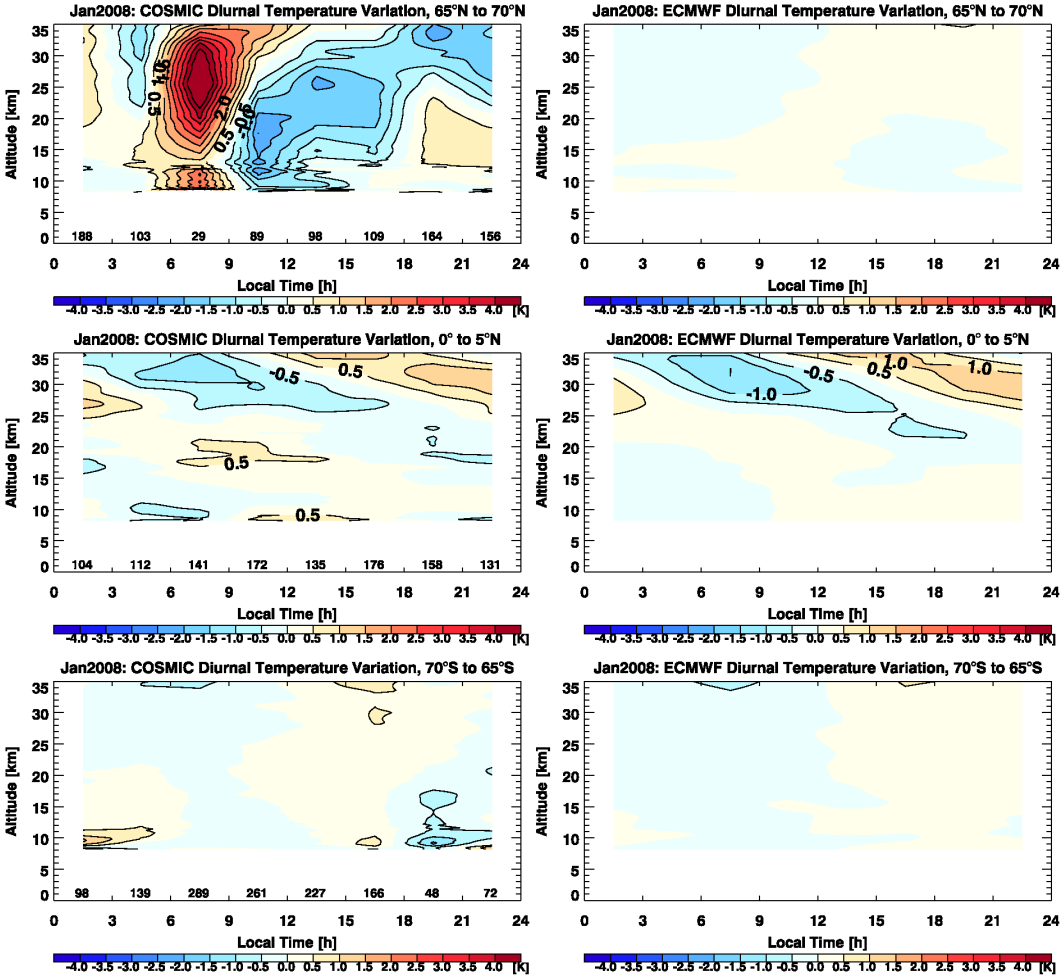

Figure 6.3: Diurnal temperature variation of F3C (left) and ECMWF (right) at 65°N to 70°N (top), 0° to 5°N (middle), and 65°S to 70°S (bottom) in January 2008. For F3C (left) the number of averaged RO profiles per local-time bin is shown as a bottom line in the panels.

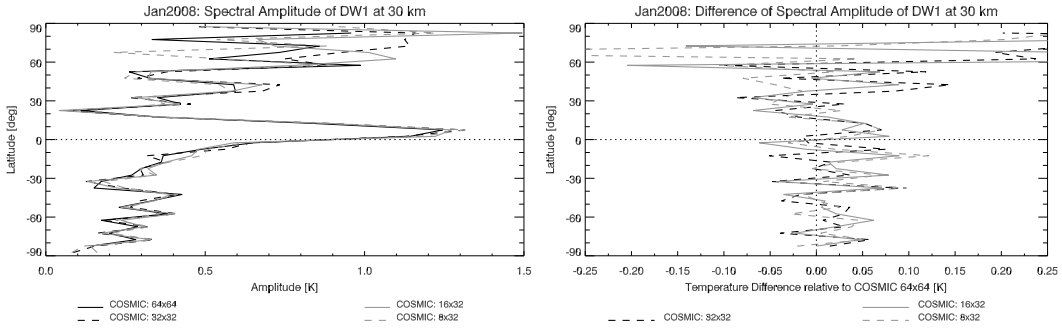

Figure 6.4: Spectral amplitudes of diurnal tide resulting from different longitude-UT fields (left) and corresponding differences. Space-time spectral analysis is performed for 64×64, 32×32, 32×16, and 32×8 longitude-UT fields. The differences between different resolutions are, in general, very small. Due to the failure of spectral analysis at high northern latitudes (winter), differences of spectral amplitudes are largest in this region.

Space-time spectral analysis is applied separately for each month, each zonal latitude band, and each height level. Again, the daily mean ECMWF forecast profile is subtracted from each single F3C profile. The mean longitude-UT field is calculated by averaging over all profiles, which are available in each grid cell. Grid cells, which do not contain any data, are filled applying bilinear interpolation from neighborhood cells. Mean longitude-UT fields of ECMWF and NCEP are calculated in the same way.

The space dimension is analyzed with Fourier analysis for each single time step t. A data set $x_t(\lambda)$ consisting of N grid points can be represented by adding together a series of $N/2$ harmonic functions,

$$x_t(\lambda) = \overline{x} + \sum_{k=1}^{N/2} \left\{ C_t(k) \cos\left[\frac{2\pi k\lambda}{N}\right] + S_t(k) \sin\left[\frac{2\pi k\lambda}{N}\right] \right\}, \tag{6.20}$$

where $C_t(k)$ and $S_t(k)$ are Fourier coefficients corresponding to the data series $x_t(\lambda)$.

Each single time step yields $N/2$ real and $N/2$ imaginary Fourier coefficients and computation of all time steps yields two time-series of real and imaginary Fourier coefficients (two matrices $C(k,t)$ and $S(k,t)$ with the dimensions $k = N/2$ and $t = M$). Examination of temporal variations of one wavenumber (k fixed) enables to find temporal periodic behavior. Fourier analyses of the time series $C_k(t)$ and $S_k(t)$ yield the frequency components of the data set:

$$C_k(t) = \overline{c} + \sum_{\omega=1}^{M/2} \left\{ A_k(\omega) \cos\left[\frac{2\pi\omega t}{M}\right] + B_k(\omega) \sin\left[\frac{2\pi\omega t}{M}\right] \right\}, \tag{6.21}$$

$$S_k(t) = \overline{s} + \sum_{\omega=1}^{M/2} \left\{ a_k(\omega) \cos\left[\frac{2\pi\omega t}{M}\right] + b_k(\omega) \sin\left[\frac{2\pi\omega t}{M}\right] \right\}. \tag{6.22}$$

After the computation of temporal variations of all wavenumbers, the Fourier coefficients of $C(k,t)$ are represented by the matrices $A(k,\omega)$ and $B(k,\omega)$, combined in the complex quantity F_c; the Fourier coefficients of $S(k,t)$ are represented by the matrices $a(k,\omega)$ and $b(k,\omega)$, combined in the complex quantity F_s.

The power spectra $P_\omega(C) = F_\mathrm{c}^\star F_\mathrm{c}$ and $P_\omega(S) = F_\mathrm{s}^\star F_\mathrm{s}$ (* denotes the complex conjugate), and the quadrature spectrum (imaginary part of the cross spectrum) $Q = \mathrm{Im}(F_\mathrm{s}^\star F_\mathrm{c})$ enable the calculation of the power spectra of the separated waves:

$$P_{+\omega} = \frac{1}{4}\left(P_\omega(C) + P_\omega(S) + 2Q_\omega(C,S)\right) \tag{6.23}$$

$$P_{-\omega} = \frac{1}{4}\left(P_\omega(C) + P_\omega(S) - 2Q_\omega(C,S)\right). \tag{6.24}$$

$P_{+\omega}$ is the power spectrum for westward traveling waves and $P_{-\omega}$ for eastward traveling ones. The corresponding waves' phase is calculated from

$$\varphi_{k,+\omega} = \tan^{-1}\left[\frac{-B(k,\omega) - a(k,\omega)}{A(k,\omega) - b(k,\omega)}\right], \tag{6.25}$$

$$\varphi_{k,-\omega} = \tan^{-1}\left[\frac{+B(k,\omega) - a(k,\omega)}{A(k,\omega) + b(k,\omega)}\right], \tag{6.26}$$

where phase denotes local-time of maximum temperature, (i.e., phase of wave crests).

The RO data set is decomposed into 32 wavenumbers and 32 frequencies and the ECMWF and NCEP model data are decomposed into 16 wavenumbers and 4 frequencies (recall that corresponding longitude-UT resolutions have been 64×64 and 32×8 for the RO and the model data sets, respectively). Waves with wavenumber $k = +1$ and period $T = 24$ h (frequency $f = 1$ cycle/d) travel westward and are called migrating diurnal tides, DW1. The SW2 wave is equal to the migrating semi-diurnal tide, wavenumber $k = +2$ traveling westward with the period $T = 12$ h (frequency $f = 2$ cycles/d).

A Hovmöller diagram shown in Figure 6.5a, presents the temperature anomaly of F3C data in January 2008 at an altitude of 30 km between the equator and 5°N. This 64×64 longitude-UT field is decomposed with spectral analysis. The dashed line corresponds to midnight local-time. It is obvious that the positive temperature anomalies lie close to the dashed line. This corresponds to the tide DW1 with temperature maximum close to midnight. Confirmation is obtained by calculating the spectrum (Figure 6.5b). The wave with $k = 1$ and $T = 24$ h, DW1, exhibits the

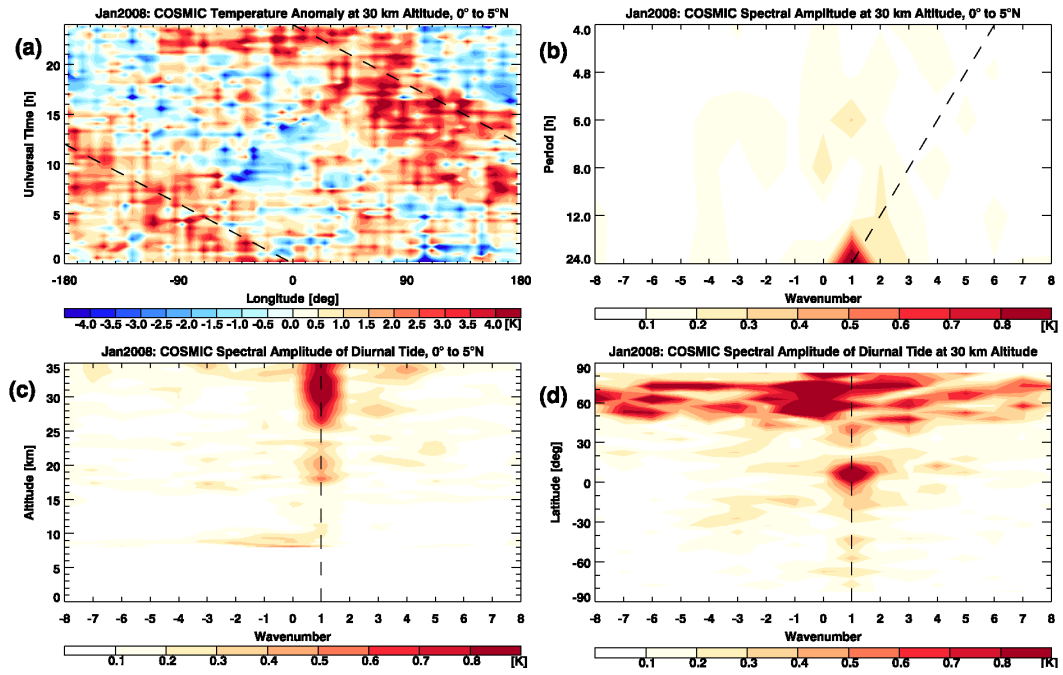

Figure 6.5: Temperature anomaly at an altitude of 30 km as a function of longitude and UT (a). This field, the zonal band between 0° and 5°N is spectrally analyzed. Spectral amplitude as a function of wavenumber and period at 30 km (b), and spectral amplitude of diurnal tide (period of 24 h) as a function of wavenumber and height (c), respectively of wavenumber and latitude (d), the latter involving all 5° bands. Migrating tides are located along the dashed line.

maximum spectral amplitude, all other components show negligible contribution. Figure 6.5c and Figure 6.5d depict the diurnal tides ($T = 24$ h) in terms of altitude and latitude dependence, respectively. In Figure 6.5c, the height cross-section near the equator shows that the spectral amplitude of DW1 increases with height and all other components yield a negligible spectral amplitude at all height levels. Figure 6.5d shows that beyond 50°N, spectral amplitude is large for all wavenumbers $-8 \leq k \leq 8$. This only means, however, that atmospheric waves cannot be isolated because the spectral analysis fails. This indicates that high atmospheric variability during wintertime and the comparatively low number of measurements at high latitudes yield significant aliasing errors.

To estimate the errors associated with F3C sampling, we extract profiles from ECMWF forecast fields, which are co-located to times and locations of F3C events. These profiles are used to estimated atmospheric tides using ECMWF data from a non-optimally sampled field. The sampling error of our atmospheric tides is esti-

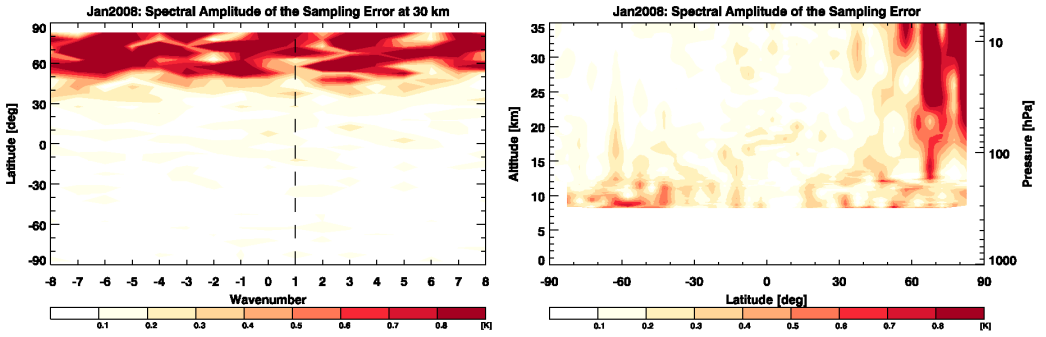

Figure 6.6: Spectral amplitude of the sampling error with $T = 24$ h as a function of wavenumber and latitude (left) and spectral amplitude of the sampling error with $k = 1$ and $T = 24$ h as a function of latitude and height (right) in January 2008.

mated from the spectral components of the difference field, the co-located longitude-UT ECMWF field minus the full longitude-UT ECMWF field.

Figure 6.6 depicts the spectral amplitude of the sampling error with $T = 24$ h as a function of wavenumber and latitude (left) and spectral amplitude of the sampling error with $k = 1$ and $T = 24$ h as a function of latitude and height (right) for January 2008. We find strongest spectral amplitudes of the sampling error in regions with high atmospheric variability (in winter polewards of 50° latitude). Non-negligible sampling errors occur also at mid and high latitudes below approximately 13 km. Spectral phase (not shown) does not show any regular pattern.

Because of these findings we focus our analysis of diurnal and semi-diurnal tides equatorwards of 50°, where the sampling error generally remains smaller than 0.2 K.

The systematic retrieval error of radio occultation measurements does not yield any error in spectral amplitudes and phases because it is eliminated when performing spectral analysis. However, the systematic difference originating from different retrieval algorithms is quantified comparing two F3C data sets from such different retrievals (CDAAC and WEGC).

6.2.3 Characteristics of DW1 in the UTLS

Amplitudes (Figure 6.7) and phases (Figure 6.8) of DW1 are shown as a function of latitude and altitude for January 2008, April 2008, July 2008, and October 2008 for WEGC F3C (left) and ECMWF (right).

In both data sets maximum amplitudes are observed at high altitudes for all months. Maximum tropical diurnal amplitudes show a latitudinal shift with height. Below approximately 27 km, they follow the movement of the inter-tropical convergence zone (which is always located in the summer hemisphere) whereas they shift

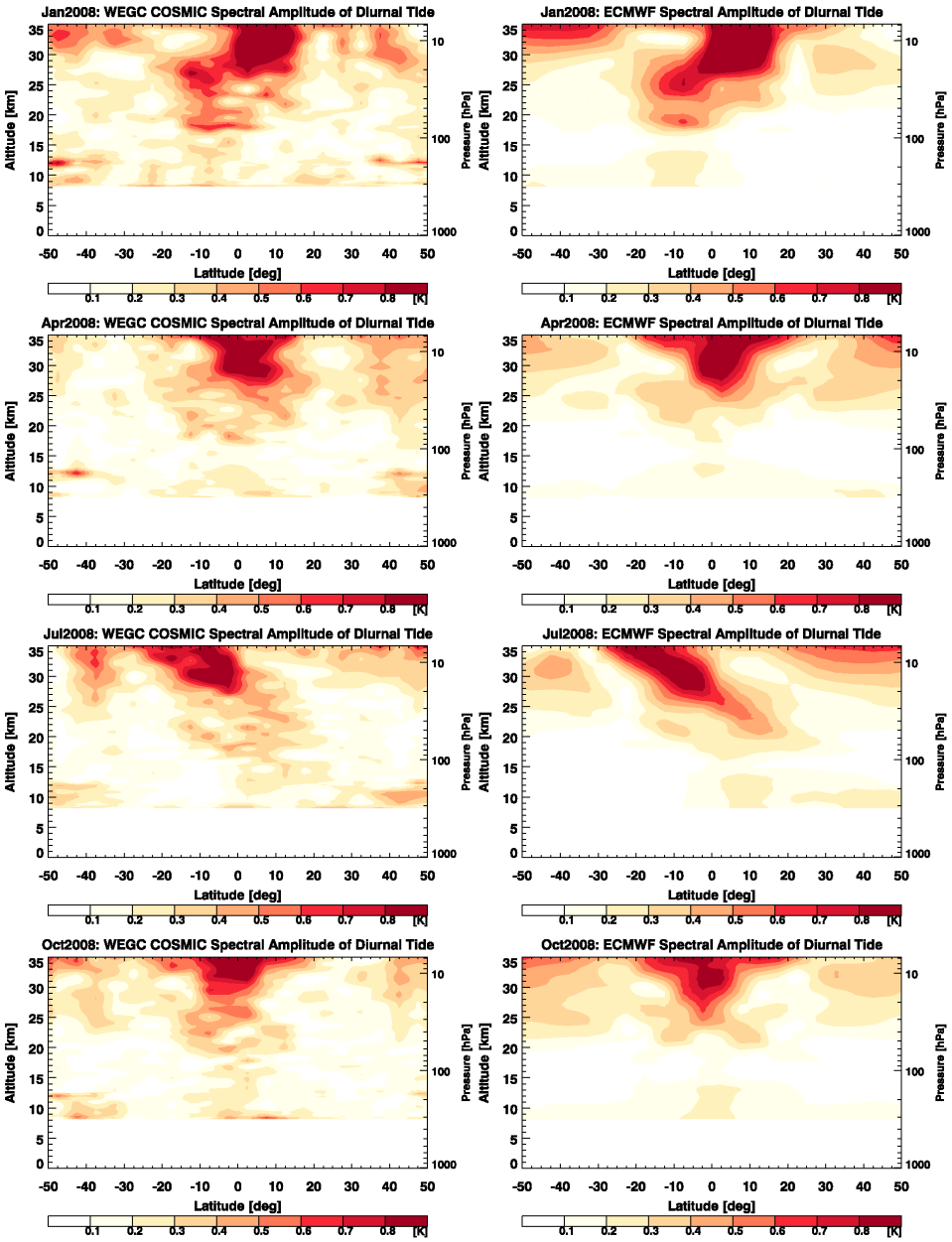

Figure 6.7: Spectral amplitude of DW1 detected with WEGC F3C data (left) and ECMWF data (right) in January 2008, April 2008, July 2008, and October 2008 (top–down).

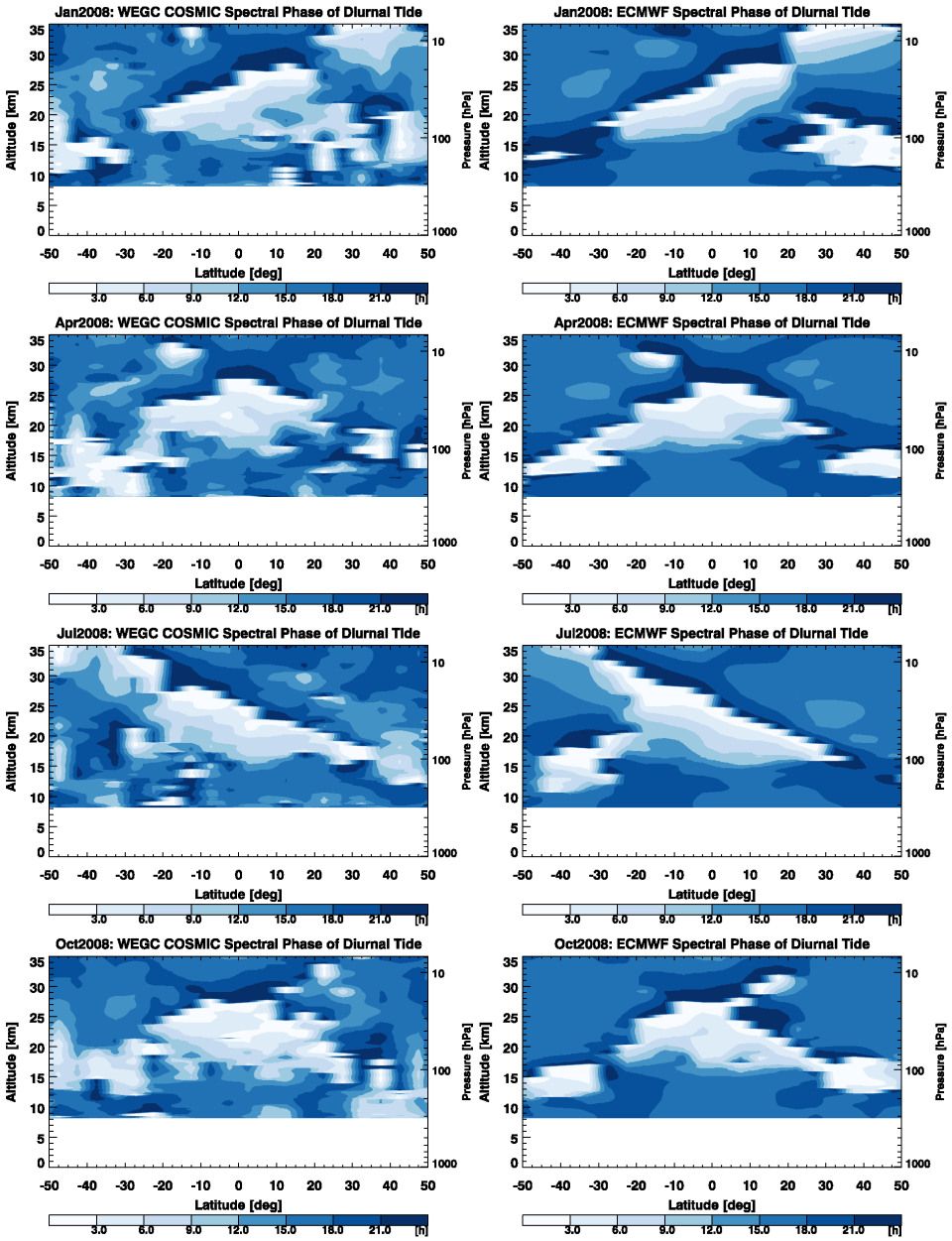

Figure 6.8: Spectral phase of DW1 detected with WEGC F3C data (left) and ECMWF data (right) in January 2008, April 2008, July 2008, and October 2008 (top–down).

to the opposite hemisphere at higher altitudes. During spring and autumn (equinox) spectral amplitude is nearly symmetric to the equator. This temporal changing vertical structure agrees well with that observed in CHAMP data (Zeng et al. 2008). A similar latitude-height structure of the amplitude of the diurnal tide was found in the Canadian Middle Atmosphere Model (CMAM) as shown by McLandress (2002*a*, Figures 3c and 3f therein). McLandress (2002*b*) attributed this seasonal variation to the interference of the latitudinal symmetric and antisymmetric vertically propagating modes, which have different vertical wavelengths.

Extra-tropical amplitudes are clearly observable above an altitude of 30 km. They are visible in both data sets (smoother in the ECMWF model data) and more pronounced in the summer hemisphere. F3C data occasionally show large amplitudes in the extra-tropics, which are not visible or at least not as pronounced in the ECMWF data set.

While model amplitudes are accompanied by relatively smooth phase as well, F3C phase shows a more irregular pattern. These large amplitudes and irregular phases in the observational data sets have already been attributed to insufficient F3C sampling of atmospheric variability and resulting failure of space-time spectral analysis (Figure 6.5d). Tropical diurnal phase exhibits symmetric characteristics with respect to the equator during equinox, where maximum temperatures are observed in the late afternoon at an altitude of 15 km, in early morning at an altitude of 20 km, and again in the late afternoon at an altitude of 35 km. In January and July (solstice) the vertical structure of the tropical diurnal phase is asymmetric about the equator. Extra-tropical phases, which are well-defined in the model data set, predominantly amount to 15 h to 18 h.

6.2.4 Comparison of DW1 Detected with Four Data Sets

Figure 6.9 shows amplitudes and phases as a function of altitude/pressure at different latitudes in January 2008 (left) and July 2008 (right) for all four data sets. Altitude-pressure conversion (necessary since NCEP data are only available at pressure levels) is done using the barometric formula $p = p_0 \exp(-(h - h_0)/H)$ with a scale height of $H = 7$ km and a surface pressure of $p_0 = 1013.25$ hPa. This basic approximation does not account for seasonal pressure variations but works reasonably well for the purpose.

Observational and model data show the same characteristics with small differences between the data sets. Vertical profiles of amplitude clearly show an increase of amplitude with altitude, which results from wave energy conservation and the decrease in density with height, yielding increasing tidal amplitudes with altitude (e.g., Chapman and Lindzen 1970).

Vertical profiles of amplitudes and phases in mid-latitude winter (30°N to 35°N in January 2008 and 30°S to 35°S in July 2008) are similar in both hemispheres.

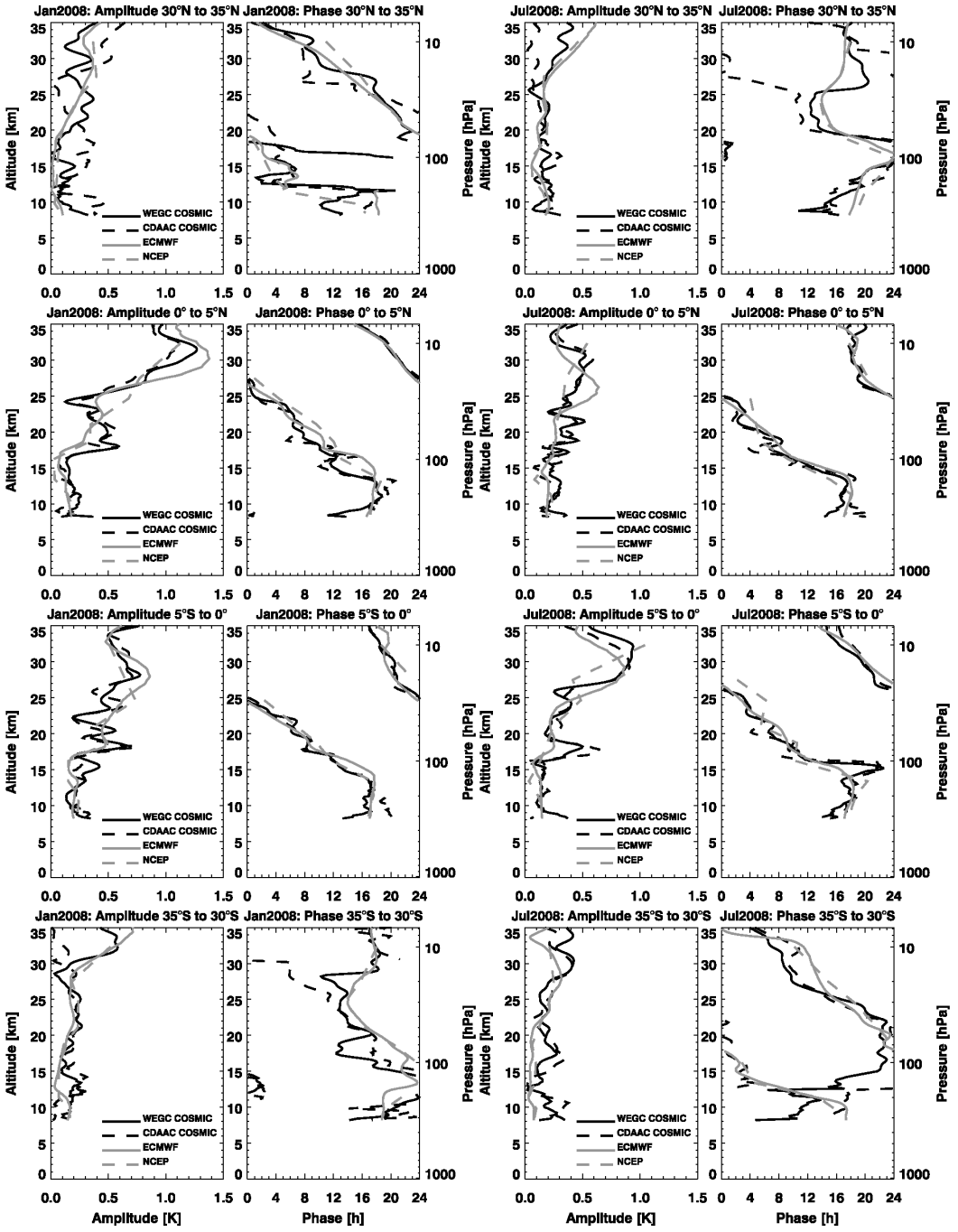

Figure 6.9: Spectral amplitude and phase of DW1 as a function of altitude at mid- and low latitudes (North–South, top to bottom) for January 2008 (left) and July 2008 (right).

Amplitudes of observational data sets are more variable with height than amplitudes of model data. Strong variability blurs the altitude level where the increase of amplitude is established. NCEP amplitudes almost coincide with ECMWF data, despite the lower vertical resolution and the approximated pressure-altitude conversion. ECMWF/NCEP show increasing amplitudes above 16 km/19 km in January 2008 and above 21 km/19 km in July 2008, respectively. Magnitudes of these tidal amplitudes are in good agreement with those of the Global Scale Wave Model (GSWM)-00 (Hagan et al. 2001) and GSWM-02, (Hagan and Forbes 2002; Hagan and Forbes 2003) as shown by Huang et al. (2009). Diurnal phase in mid-latitude winter is decreasing with height. Downward propagation of phase corresponds to upward propagation of wave energy. This is one of the fundamental properties of gravity waves, which reveals that phase fronts of gravity waves progress nearly perpendicular to group velocity (energy transport) (Lindzen 1990). The vertical wavelength, which can be approximated by inspection of the phase plots, amounts to 20 km. WEGC F3C phase detaches from the other data sets at an altitude of 20 km. The cause of this WEGC F3C phase characteristic is unclear at this stage.

In mid-latitude summer (30°N to 35°N in July 2008 and 30°S to 35°S in January 2008) amplitudes of DW1 observed in model data are more pronounced than amplitudes of DW1 detected in observational data above 27 km. WEGC F3C amplitudes are smaller than model amplitudes but stronger than CDAAC F3C amplitudes. CDAAC F3C data do not show significant amplitudes in mid-latitude summer. Differences in WEGC and CDAAC F3C data sets reflect the influence of retrieval differences, in particular the impact of high-altitude initialization of bending angles on diurnal tides detected with RO data. As noted above (see Section 6.2.1), WEGC bending angle profiles were initialized using ECMWF short-term forecasts (4 time layers) above 30 km. Therefore, WEGC F3C and ECMWF data sets are not fully independent, though background information in WEGC F3C data is far below 50 % at 30 km (Gobiet et al. 2007). CDAAC F3C data are initialized by an NCAR climatology, which does not contain tidal information. Assuming that ECMWF overestimates amplitudes of DW1, some information is transferred to WEGC F3C and these data may also overestimate amplitudes of diurnal tides. On the other hand, CDAAC F3C data may underestimate them because the initialization using an NCAR climatology tends to suppress any tidal information. Differences between WEGC and CDAAC F3C decrease with decreasing altitude. Below 30 km, WEGC and CDAAC F3C diurnal amplitudes correspond to 0.2 K.

Maximum temperatures of diurnal tide in mid-latitude summer are always observed in the afternoon or at night. This is consistent with the phase of the GSWM-00 model, shown by Huang et al. (2009) (though only up to 25 km). Phase increases from noon to midnight from 8 km up to 14 km/17 km (January 2008/July 2008). Above, it decreases to noon again and after a small increase it remains constant at 17 h. The amplitude observed in CDAAC F3C data is so small above 25 km in

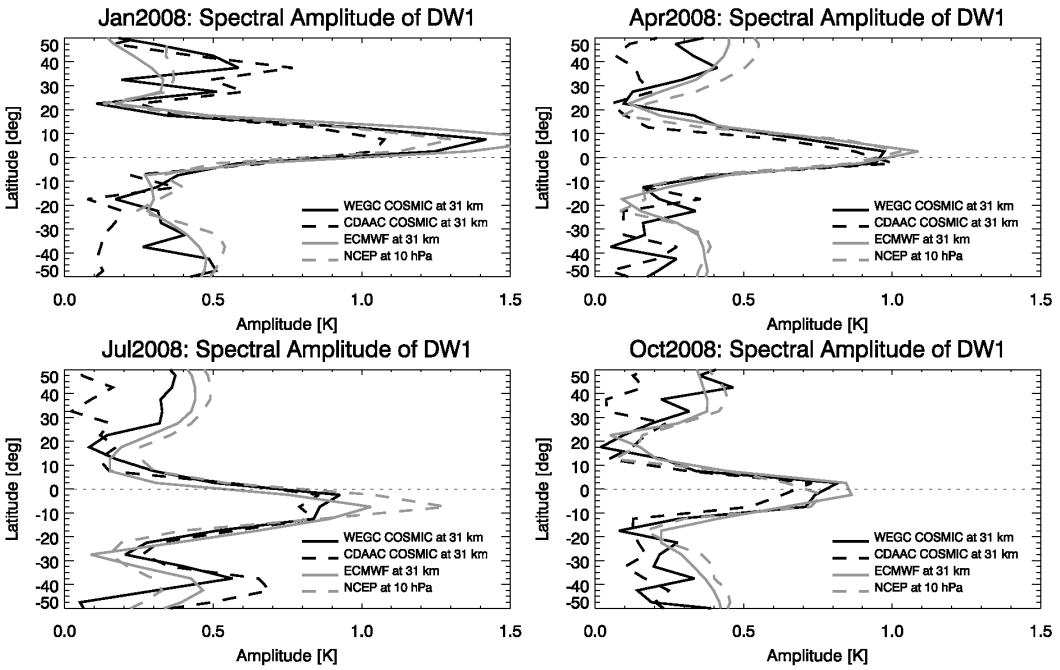

Figure 6.10: Spectral amplitude of DW1 as a function of latitude for January 2008 (top left), April 2008 (top right), July 2008 (bottom left), and October 2008 (bottom right) at 31 km/10 hPa.

July 2008 (amplitude smaller than 0.1 K) that space-time spectral analysis looses the signal and the phase separates from the other data sets.

Tropical amplitudes and phases show best agreement of all data sets as profiles closely shadow each other. Amplitudes are very small (0.1 K to 0.2 K only) from 8 km up to 16 km. Above the tropopause, amplitudes increase and amount up to 1.4 K between 0° and 5°N (ECMWF amplitude in January 2008) and become even larger. Below 15 km, phase shows a trapped wave structure, which peaks in the afternoon; above 15 km, phase shows downward progression of waves with a vertical wavelength of 20 km. These results are in good agreement with Alexander and Tsuda (2008) and Zeng et al. (2008).

Figure 6.10 depicts amplitude as a function of latitude. Here 31 km have been chosen, since pressure climatologies based on RO data show that the 10 hPa level (of NCEP data) corresponds to 31 km altitude in mid- and low latitudes. Note, that 10 hPa corresponds to 32.3 km using the barometric formula as mentioned above. Table 6.2 summarizes the amplitude values below 50° latitude.

Tropical spectral amplitudes are more pronounced in the model data sets than in the F3C data sets. Differences are strongest in the summer and winter months,

Table 6.2: WEGC F3C, CDAAC F3C, ECMWF, and NCEP amplitudes of DW1 at 31 km/ 10 hPa at low- and mid-latitudes in January 2008, April 2008, July 2008, and October 2008.

WEGC F3C	Jan2008	Apr2008	Jul2008	Oct2008
30°N to 50°N	0.4	0.3	0.3	0.3
15°N to 30°N	0.3	0.2	0.2	0.1
0° to 15°N	1.2	0.7	0.3	0.5
0° to 15°S	0.4	0.5	0.9	0.6
15°S to 30°S	0.3	0.2	0.3	0.2
30°S to 50°S	0.4	0.2	0.3	0.2
CDAAC F3C	Jan2008	Apr2008	Jul2008	Oct2008
30°N to 50°N	0.5	0.1	0.1	0.1
15°N to 30°N	0.4	0.1	0.1	0.2
0° to 15°N	1.0	0.6	0.3	0.4
0° to 15°S	0.4	0.5	0.8	0.4
15°S to 30°S	0.1	0.2	0.4	0.2
30°S to 50°S	0.1	0.2	0.5	0.2
ECMWF	Jan2008	Apr2008	Jul2008	Oct2008
30°N to 50°N	0.3	0.4	0.4	0.4
15°N to 30°N	0.3	0.2	0.3	0.2
0° to 15°N	1.4	0.8	0.2	0.5
0° to 15°S	0.4	0.5	0.9	0.6
15°S to 30°S	0.3	0.2	0.4	0.3
30°S to 50°S	0.5	0.4	0.4	0.4
NCEP	Jan2008	Apr2008	Jul2008	Oct2008
30°N to 50°N	0.4	0.5	0.5	0.4
15°N to 30°N	0.3	0.2	0.4	0.2
0° to 15°N	1.1	0.7	0.4	0.4
0° to 15°S	0.4	0.5	1.1	0.6
15°S to 30°S	0.3	0.2	0.2	0.3
30°S to 50°S	0.5	0.4	0.3	0.4

whereas they are comparatively small at equinox. Largest amplitudes are observed in January 2008 in all data sets; the amplitude of ECMWF DW1 is most pronounced and amounts to 1.7 K between 5°N and 10°N. In the same region, the other data sets show smaller amplitudes, WEGC F3C by approximately 16 %, CDAAC F3C by approximately 35 %, and NCEP by approximately 22 %. Tropical amplitudes are smallest in October 2008. Model data sets exhibit maximum amplitude (ECMWF: 0.9 K, NCEP: 0.8 K) in the southern hemisphere between 0° and 5°S, but observational data sets show maximum amplitudes in the northern hemisphere between 0° and 5°N (WEGC F3C: 0.8 K, CDAAC F3C: 0.7 K).

Extra-tropical amplitudes of DW1 are distinctively smaller than tropical amplitudes (cf. also Table 6.2). Between 30°N/S and 50°N/S at 31 km/10 hPa, amplitudes amount to 0.3 K to 0.5 K in the model data sets. A comparison between ECMWF and NCEP forecast model data yields that extra-tropical amplitudes of DW1 are more pronounced in NCEP data than in ECMWF data. In the same region, CDAAC F3C amplitudes are very small, except for January and July 2008 in the winter hemispheres, respectively.

6.2.5 Characteristics of SW2 in the UTLS

Amplitudes (Figure 6.11) and phases (Figure 6.12) of SW2 are shown as a function of latitude and altitude for January 2008, April 2008, July 2008, and October 2008 for WEGC F3C (left) and ECMWF (right).

Amplitudes of semi-diurnal tides are distinctively weaker than those of diurnal tides. Maximum amplitudes, observed at high altitudes for all months, are located at extra-tropical latitudes, between approximately 10°S/N and 30°S/N. They are more pronounced in the ECMWF data set, where they are, in general, smaller than 0.5 K at 35 km altitude. Apart from northern hemispheric winter, when maximum amplitudes are observed in the northern hemisphere, spectral amplitudes are always more pronounced in the southern hemisphere.

Spectral phase of SW2 confirms that our space-time spectral analysis results are robust.

6.2.6 Monitoring of Diurnal Tide DW1 and Semi-Diurnal Tide SW2

Figure 6.13 depicts amplitudes of diurnal (top) and semi-diurnal (bottom) migrating tides in WEGC F3C and ECMWF data at an altitude of 30 km as function of time. Tropical diurnal tides show a distinctive annual cycle, where maximum amplitudes are observed in hemispheric winter. This annual variation is similar to what has been observed with CHAMP data (Zeng et al. 2008) but different to what has been observed with SABER (Sounding of the Atmosphere using Broadband Emission Radiometry) data in the upper atmosphere (Zhang et al. 2006; Mukhtarov et al. 2009),

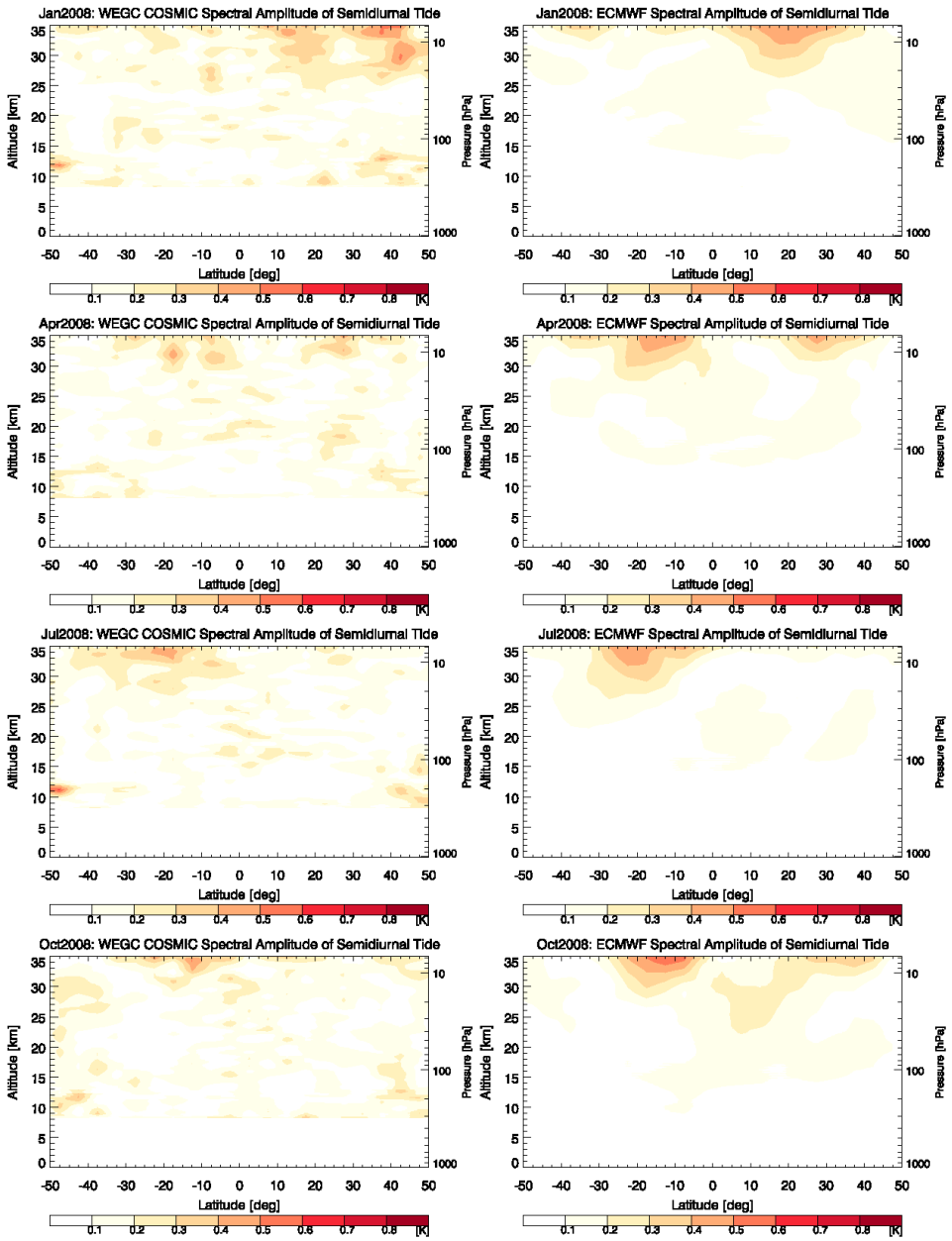

Figure 6.11: Spectral amplitude of SW2 detected with WEGC F3C data (left) and ECMWF data (right) in January 2008, April 2008, July 2008, and October 2008 (top–down).

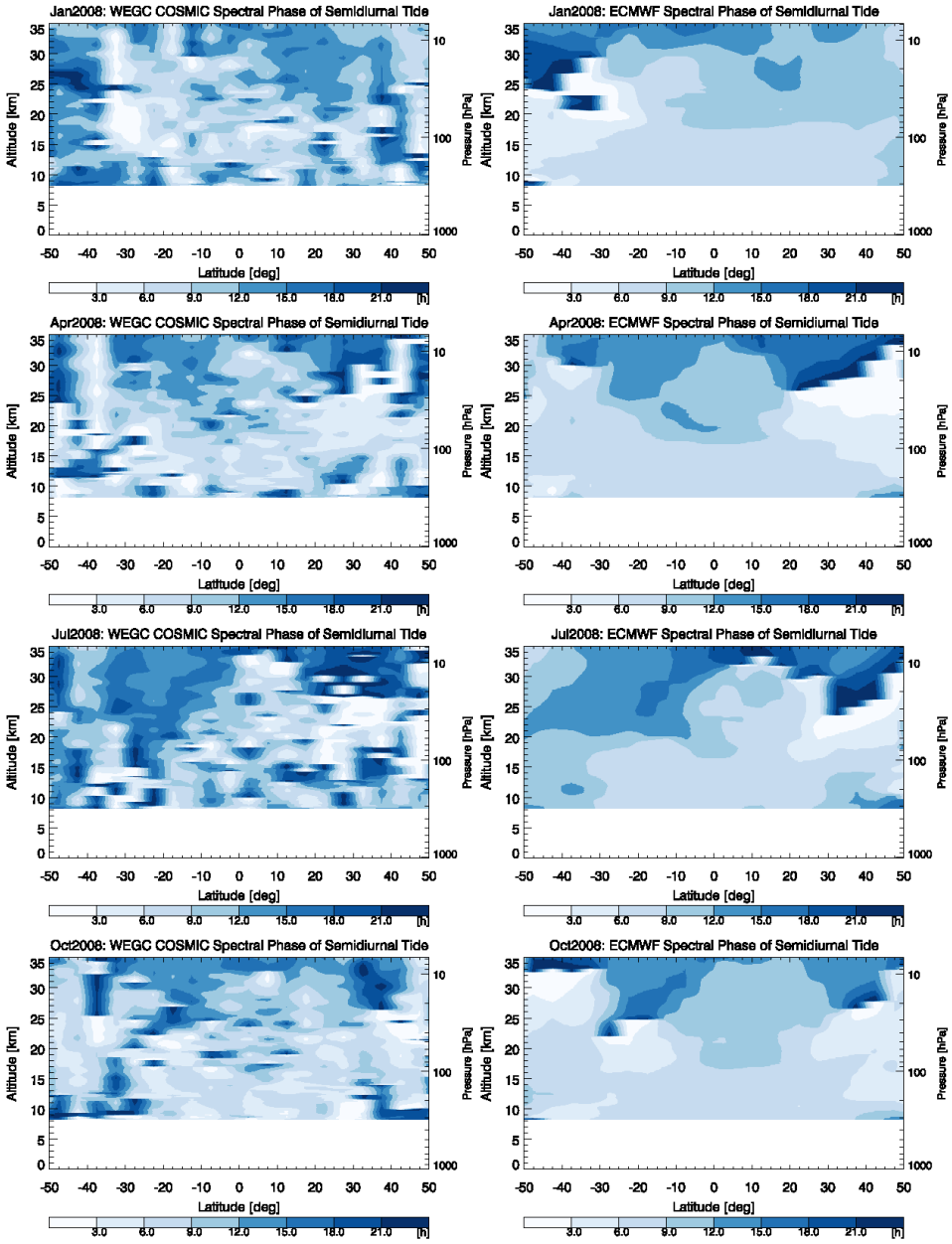

Figure 6.12: Spectral phase of SW2 detected with WEGC F3C data (left) and ECMWF data (right) in January 2008, April 2008, July 2008, and October 2008 (top–down).

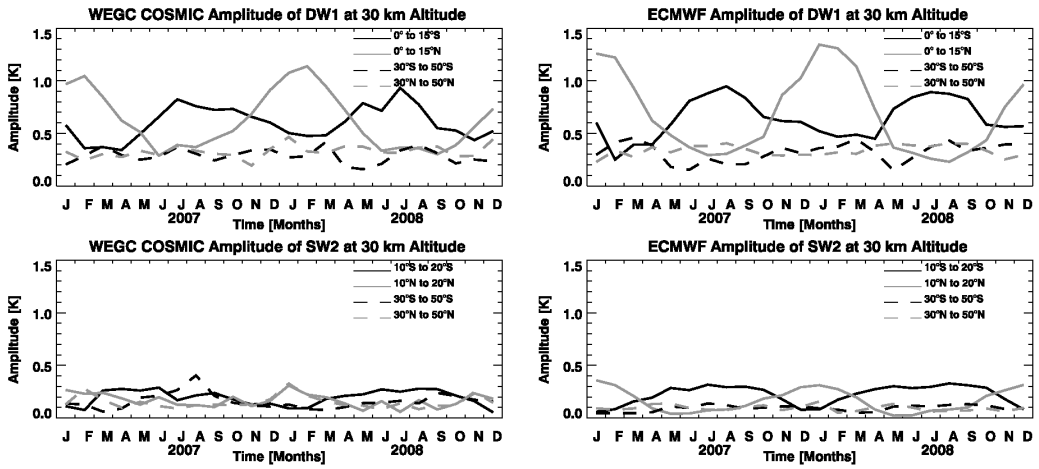

Figure 6.13: Spectral amplitude of diurnal tide DW1 (top) and semi-diurnal tide SW2 (bottom) at 30 km altitude for different latitude regions (see in-panel legends). WEGC F3C (left) and ECMWF (right) for all months from January 2007 to December 2008.

where maxima occur around equinox. This annual cycle results from latitudinal shift of maximum temperature with time at a constant altitude level (cf. Figure 6.7). The annual cycle in the northern hemisphere is more pronounced (higher maximum and smaller minimum amplitudes) than that observed in the southern hemisphere. Extra-tropical amplitudes of diurnal tides also show an annual cycle (the amplitudes of this annual cycle are above uncertainty level only in the ECMWF data set) but it is less pronounced than that of tropical diurnal tides and their maximum values are observed in hemispheric summer.

The semi-diurnal tide also shows maximum amplitudes (about 0.3 K) at low latitudes (10°S/N to 20°S/N). The annual cycle is similar to that observed in the tropical diurnal tide, with maximum amplitudes in winter.

Figure 6.14 shows the temporal evolution of diurnal and semi-diurnal tides at all latitudes and at an altitude of 30 km. Local time sampling at high latitudes is roughly the same every four months. These sampling problems of F3C are clearly noticeable in winter beyond about 40° to 50° latitude. Extra-tropical amplitudes shown in Figure 6.13 therefore contain small but non-negligible residual sampling errors (< 0.2 K) in hemispheric winter. ECMWF data feature small amplitudes of the semi-diurnal tide (up to 0.4 K), which are symmetric to the equator; they can barely be seen in the F3C data set.

Differences in amplitudes of diurnal tides between 2007 and 2008 are very small. Table 6.3 summarizes mean values of amplitudes in 2007 and 2008 at an altitude of

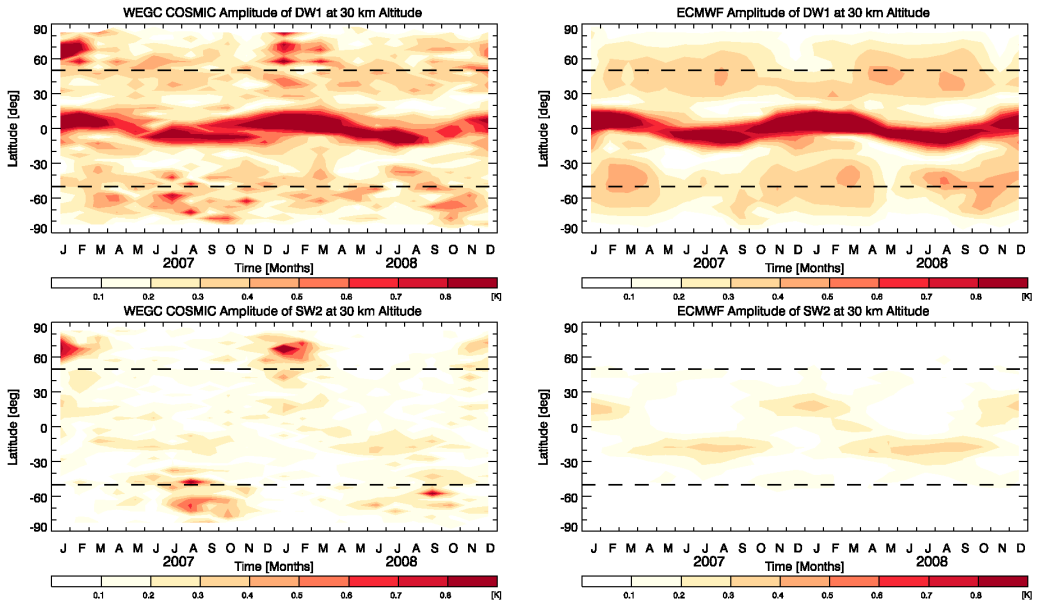

Figure 6.14: Spectral amplitude of diurnal tide (top) and semi-diurnal tide (bottom) at 30 km altitude. WEGC F3C (left) and ECMWF (right) for all months from January 2007 to December 2008. The dashed black bounds delimit the "core" region of the investigations (50°S to 50°N).

30 km at low- and mid-latitudes. Tropical diurnal tides are stronger in the ECMWF data set than in the WEGC F3C data set by up to 0.2 K, but amplitudes of both data sets do not differ significantly between 2007 and 2008. Amplitudes of extra-tropical diurnal tides are also larger in the model data set. ECMWF diurnal tides at mid-latitudes are stronger in 2008 but WEGC F3C data show a stronger diurnal tide at southern mid-latitudes in 2007. That may be due to worse local time sampling in 2007 than in 2008 because F3C satellites orbit separation was not fully developed yet.

6.3 Summary of Atmospheric Thermal Tides

The orbit design of the F3C satellite constellation allows the determination of diurnal tides in the UTLS region on a monthly basis equatorwards of about 50° latitude. Beyond 50° latitude, atmospheric variability in the winter hemisphere is too strong and F3C sampling too sparse to adequately resolve the tides. Within 50°S and 50°N the error associated with F3C sampling was estimated to be less than 0.2 K nearly everywhere.

Table 6.3: Mean amplitudes of DW1 in 2007 and 2008 at mid-latitudes (30°N/S to 50°N/S) and in the tropics (0° to 15°N/S) at an altitude of 30 km.

	WEGC F3C		ECMWF	
	2007	2008	2007	2008
30°N to 50°N	0.3	0.4	0.3	0.3
0° to 15°N	0.6	0.6	0.7	0.7
0° to 15°S	0.6	0.6	0.6	0.7
30°S to 50°S	0.3	0.3	0.3	0.4

This study yielded the migrating diurnal tide (DW1) to be the most pronounced spectral component in F3C RO observation data, and ECMWF and NCEP model data. Typical features of diurnal tides are found in all data sets and they are consistent with the theory of diurnal tides (Chapman and Lindzen 1970). On the one hand, this agreement confirms the utility of F3C RO data for monitoring diurnal tide dynamics, on the other hand it confirms that tidal dynamics is appropriately captured in the models, which is important for other (middle/upper) atmosphere models relying on ECMWF or NCEP dynamics.

Best agreement is found at low latitudes. The ECMWF and NCEP model data show a more homogeneous diurnal tide at all latitudes than F3C observational data. Spectral amplitudes are largest at high altitudes since tidal amplitudes generally increase with altitude. At an altitude of 30 km, typical amplitudes of migrating diurnal tides at tropical latitudes amount to 0.7 K to 1.0 K but occasionally they can also become up to 1.5 K (in ECMWF data only).

During solstice months tropical diurnal tides are characterized by a latitudinal shift with height. Below 27 km, maximum diurnal amplitudes follow the inter-tropical convergence zone (summer hemisphere); above that altitude maximum amplitudes shift to the other (winter) hemisphere. During equinox months, amplitudes are symmetric with respect to the equator. Focusing on a single confined low latitude band and on a constant altitude level, this latitudinal shift appears as an annual cycle of maximum amplitude. Below 27 km this cycle follows the annual cycle of the inter-tropical convergence zone, which is more pronounced in the northern hemisphere than in the southern hemisphere, above 27 km it is opposed to that.

The phase at low latitudes shows the typical feature of downward progression of wave fronts, which corresponds to upward propagation of wave energy. The vertical wavelength seen in observational and model data sets amounts to about 20 km.

Extra-tropical diurnal tides are most pronounced in the model data sets with amplitudes up to 0.5 K at 30 km. At mid-latitudes, the RO data sets reflect the influence of retrieval differences on diurnal tides: CDAAC F3C data (high-altitude

initialized with a climatology, which does not contain tidal information) do not show noticeable amplitudes of diurnal tide, while WEGC F3C data show a tide similar to that detected in the ECMWF data (initialized with ECMWF forecasts). Assuming that ECMWF overestimates the amplitude, the actual amplitude of the extra-tropical diurnal tide lies between both observational data sets. The difference between WEGC F3C and CDAAC F3C increases with height. At 30 km it reaches values of 0.2 K to 0.3 K.

Semi-diurnal tides become more apparent in the ECMWF data set than in the WEGC F3C data set, which is likely due to larger amplitudes in the model data set in general, and under-sampling problems in the observational data.

6.4 Climatological Impact of this Study

The SE and its LTC strongly affect the quality of a climatology. The LTC of a climatology does not only depend on the drifting rate of a satellite but also on characteristics—shape and magnitude—of diurnal tides. In a climatological context it is important to monitor a satellite's orbit and the diurnal tide of atmospheric parameters but also to know both, the impact of a temporal changing diurnal tide on the LTC of a climatology and the impact of a very slowly drifting satellite on the LTC if the diurnal cycle is constant.

In the recent past, discussion about temperature trends in the free atmosphere derived from Microwave Sounding Unit (MSU)/Advanced MSU (AMSU) satellite data received much attention. Discrepancies in sign and magnitude of the trends arose from incorrect inter-calibration and correction procedures between the different satellites (e.g., Karl et al. 2006). RO data, however, are self-calibrated, and inter-calibration between measurements of different satellites is, in principle, not needed (Foelsche et al. 2009*a*). Continuous RO data, available since 2001, are thus suitable to perform climate monitoring and related change analyses such as of the diurnal tide, because the data are expected to be stable on a long term basis (Foelsche et al. 2008*b*).

The diurnal cycle of atmospheric parameters is well known on the Earth's surface. Nearly continuous measurements at synoptic land stations, ships, and buoys allow an adequate determination of the diurnal tide of atmospheric parameters at the surface. Some of these data are available since the end of the 19th century. From 1950 until 2004 a decrease in the diurnal surface temperature range occurred due to a steeper increase in daily minimum surface temperatures than in daily maximum surface temperatures (Vose et al. 2005; Easterling et al. 2006). If data are used only since 1979, however, no change in temperature range is observed (Trenberth et al. 2007).

The number of measurements and the spatial density in the UTLS region was very sparse in the pre-satellite era (before 1979), since radiosonde, lidar, and radar data

were the only measurements available in the free atmosphere. That lack of long term measurements prevents the examination of a possible climate change impact on diurnal tides in the free atmosphere.

However, long-term changes of the diurnal tide in the upper atmosphere can be estimated with climatological models, such as the ECMWF–MPI-M Hamburg (ECHAM)5 model. If the characteristics of temporally changing diurnal tides of a model data set are well known (e.g., by applying a space-time spectral analysis and analyzing the results), it is possible to investigate the impact of that climate change signal on the LTC of a climatology. A long-term simulation of RO events performed by a sun-synchronous satellite and the extraction of model profiles co-located to RO measurements enables the estimation of the temporally changing LTC.

It is also possible to investigate the impact of a very slowly drifting satellite on the LTC component of a climatology with a simulation study: A temporally constant diurnal tide can simply be sampled with a sun-synchronous satellite with different equator crossing times. Such a simulation is equivalent to a slowly drifting satellite.

7 Summary and Conclusions

Radio Occultation (RO) measurements are of particular utility for observing global climate within the Upper Troposphere–Lower Stratosphere (UTLS) region. The RO technique is based on measurements of the path of radio waves passing through the atmosphere. The signal transmitted by a Global Positioning System (GPS) satellite and received onboard a Low Earth Orbit (LEO) satellite is modified by the Earth's atmosphere being in between. The signal's modifications are utilized to derive atmospheric characteristics like temperature, pressure, or humidity.

Because the fundamental observable, the phase delay of the occulted GPS signal, is traceable to the international standard for the second, RO measurements can serve as climate benchmark within their core region between about 8 km and 30 km. The RO data set delivers consistent, accurate, and long-term stable measurements. Observations are performed during virtually all weather conditions, are available globally, and offer a very high vertical resolution. The self-calibrating nature of RO measurements theoretically enables to combine data from different sensors and different occultation missions without the need for inter-calibration or overlap.

However, several calculation procedures are necessary to process RO phase delay measurements into vertical profiles of atmospheric parameters. The main objective of this thesis was to investigate fundamental atmospheric parameters of RO data provided by different satellites. Characteristics, consistency, uncertainty, and orbit-dependent features of RO climatologies are analyzed.

RO data are available in intermittent periods in 1995 and 1997 (GPS/MET, Global Positioning System/Meteorology), and continuously since 2001 (CHAMP (CHAllenging Mini-Satellite Payload), SAC-C (Satélite de Aplicaciones Científicas C), GRACE-A (Gravity Recovery And Climate Experiment), F3C (FORMOSAT-3/COSMIC), and MetOp-A (Meteorological Operational)).

The analysis of RO profiles yielded that data characteristics at high altitudes (65 km to 80 km) depend on solar activity (ionospheric conditions), receiver quality, and data processing. The results showed that the bending angle bias relative to Mass Spectrometer and Incoherent Scatter Radar (MSIS)[1] is in very good agreement for all satellite data, provided that the same processing scheme is used. The temporal mean of the bending angle bias of all satellite data (processing of University Corporation

[1] Note that neither RO nor MSIS bending angles are bias free. However, a large bias in the RO bending angle profile at high altitudes yields an undesired downward propagation of systematic errors in derived atmospheric profiles (Foelsche et al. 2008*a*).

for Atmospheric Research (UCAR) and European Organization for the Exploitation of Meteorological Satellites (EUMETSAT) phase delays) available from 1995 to 2008 amounts to -0.14 μrad. A positive bending angle bias could only be identified in the German Research Centre for Geosciences (GFZ) data set, which points at differences in the raw data ("level 1") processing.

The investigation of the temporal evolution of the bending angle bias indicates that its magnitude is affected by solar activity. UCAR phase delays yield a negative bending angle bias during high solar activity, while it approximates to zero (still slightly negative) during low solar activity.

Satellite data provided by different satellites exhibit distinctive differences in bending angle noise (numbers here apply to a vertical resolution of 2 km to 3 km). Best receiver quality (i.e., smallest bending angle noise between 65 km to 80 km) is found for data from the MetOp-A satellite (mean bending angle noise smaller than 1 μrad). Good bending angle quality is also observed for GPS/MET (2 μrad), whose data stem from "prime times" (high GPS signal quality), F3C (2.5 μrad), and GRACE-A (2.7 μrad). The long CHAMP record shows relatively constant bending angle noise (temporal mean: 4.7 μrad) except for March–April–May (MAM) 2007, when bending angle noise significantly increased to approximately 7 μrad. Very variable data quality is found for SAC-C (temporal mean: 5.1 μrad), which is operated as "testbed" satellite.

RO climatologies are obtained from single measurements by combining them in an optimal way (aiming at minimizing potential sampling errors[2]). Inconsistencies of RO climatologies of different satellites were found to originate from differences in spatio-temporal sampling, data quality at high altitudes (i.e., bending angle noise), and data processing.

After subtraction of the estimated respective sampling errors, climatologies derived from different satellites (CHAMP, GRACE-A, F3C, and MetOp-A) show very good agreement with mean temperature disparities being smaller than 0.3 K within 8 km and 35 km. Excluding MetOp-A climatologies in this comparison (MetOp-A data stem from a test data set) yields mean temperature differences being even smaller than 0.1 K. Largest disagreements are found at high altitudes, where the impact of background information used within RO data processing (initialization of the Abel integral) is non-negligible. The amount of background information penetrating downward to 30 km depends on the signal quality at highest altitudes[3]. Results show that a large amount of background information yields somewhat cooler temperatures than a small amount of background information. Simultaneously to the amount of background information, these inconsistencies significantly decrease with decreasing

[2] Sampling errors are caused by uneven sampling in space and time.

[3] While low bending angle noise implies a low amount of background information, high bending angle noise leads to a large amount of background information.

altitude. Below 15 km they are smaller than 0.1 K. Climatologies, which are derived from data with same quality agree to within 0.02 K also at high altitudes.

Largest disagreements of RO climatologies arise when comparing data from different processing schemes. Mean absolute differences of CHAMP climatologies among five processing centers (Danish Meteorological Institute (DMI), GFZ, Jet Propulsion Laboratory (JPL), UCAR, and Wegener Center for Climate and Global Change (WEGC)) amount to 0.5 K in dry temperature (averaged from 40°S to 40°N, 8 km to 30 km) while climate time series of temperature changes agree much closer. Again, differences are largest at high altitudes (30 km and 35 km), where disagreements of temperature data exceed 2 K. Level 1 processing and bending angle initialization were again found to make a major contribution.

The local time influence in RO climatologies depends on the satellite's orbit. For the sun-synchronous satellite MetOp the local time error remains constant with time. Its magnitude is generally smaller than ±0.1 K in monthly mean climatologies. The typical local time error of an annual mean MetOp climatology resolved into 18 zonal bands amounts to approximately 0.04 K. For non sun-synchronous satellites the local time error component in monthly mean climatologies decreases with increasing satellite drifting rate. At low latitudes for example, the satellite constellation F3C samples at all local times within 10 days so that the resulting Local Time Component (LTC) in monthly mean RO climatologies is very small (0.03 K). CHAMP local time drift is distinctively smaller (130 days to sample at all local times), which results in sinusoidally varying positive and negative deviations in the order of 0.1 K. An annual mean climatology resolved into 18 zonal bands shows for F3C and CHAMP a typical local time residual error component of 0.01 K and 0.03 K, respectively.

The overall evidence is that consistent monthly mean zonal mean RO climatologies of different satellites can only be obtained if (1) data from the same processing scheme are used, (2) data quality is monitored and corresponding amount of background information is provided and considered, and (3) spatio-temporal sampling is well understood. Results underpin the utility of RO data for long-term monitoring of global climate variability and change.

As a final application the utilization of RO data in atmospheric physics has been performed by investigating atmospheric tides. The orbit design of the F3C satellite constellation allows the determination of diurnal tides in the UTLS region on a monthly basis equator-wards of about 50° latitude. Beyond 50° latitude, atmospheric variability in the winter hemisphere is too strong and F3C sampling too sparse to adequately resolve the tides. This study yielded the migrating diurnal tide to be the most pronounced spectral component in F3C RO observation data. Spectral amplitudes are largest at high altitudes since tidal amplitudes generally increase with altitude. At an altitude of 30 km, typical amplitudes of migrating diurnal tides at tropical latitudes amount to 0.8 K to 1.0 K. The phase at low latitudes shows the typical feature of downward progression of wave fronts, which corresponds to upward

propagation of wave energy. The vertical wavelength amounts to about 20 km.

Bibliography

Alexander, S. P. and T. Tsuda (2008). "Observations of the diurnal tide during seven intensive radiosonde campaigns in Australia and Indonesia." In: *Journal of Geophysical Research* 113, D04109. DOI: 10.1029/2007JD008717.

Anthes, R. A. et al. (2008). "The COSMIC/FORMOSAT-3 mission: Early results." In: *Bulletin of the American Meteorological Society* 89.3, pp. 313–333. DOI: 10.1175/BAMS-89-3-313.

Ao, C. O., W. B. Schreiner, and J. Wickert (2003). *First report on the CHAMP radio occultation intercomparison study.* JPL publication 03-016. JPL.

Bertiger, W. I. et al. (1994). "GPS precise tracking of TOPEX/POSEIDON: Results and implications." In: *Journal of Geophysical Research* 99.C12, pp. 24449–24464.

Boain, R. J. (2005). "A-B-Cs of Sun-synchronous orbit mission design (AAS 04-108)." In: *Spaceflight Mechanics 2004–Part I.* Ed. by S. L. Coffey, A. P. Mazzoleni, K. K. Luu, and R. A. Glover. San Diego, CA: Univelt, Inc., pp. 85–104.

Born, M. and E. Wolf (1999). *Principles of Optics. Electromagnetic theory of propagation, interference and diffraction of light.* 7th ed. Cambridge, New York: Cambridge University Press.

Borsche, M. (2008). *Global atmospheric climatologies from radio occultation data and derivation of diagnostic parameters for climate monitoring (Ph.D. Thesis).* Austria: Wegener Center Verlag Graz. ISBN: 978-3-9502308-6-5.

Borsche, M., A. Gobiet, A. K. Steiner, U. Foelsche, G. Kirchengast, T. Schmidt, and J. Wickert (2006). "Pre-operational retrieval of radio occultation based climatologies." In: *Atmosphere and Climate: Studies by Occultation Methods.* Ed. by U. Foelsche, G. Kirchengast, and A. K. Steiner. Berlin Heidelberg: Springer, pp. 315–324.

Borsche, M., G. Kirchengast, and U. Foelsche (2007).
"Tropical tropopause climatology as observed with radio occultation measurements from CHAMP compared to ECMWF and NCEP analyses."
In: *Geophysical Research Letters* 34, L03702. DOI: 10.1029/2006GL027918.

Bouttier, F. and F. Rabier (1997). "The operational implementation of 4D-Var."
In: *ECMWF Newsletter* 78, pp. 2–5.

CDAAC Team (2010). *COSMIC Status Update.*
URL: http://cosmic-io.cosmic.ucar.edu/cdaac/index.html (visited on Feb. 10, 2010).

Chapman, S. and R. S. Lindzen (1970). *Atmospheric Tides.*
Dordrecht, The Netherlands: D. Reidel, p. 201.

Christy, J. R. and R. W. Spencer (2005). "Correcting temperature data sets."
In: *Science* 310, pp. 972–973.

Cucurull, L. and J. C. Derber (2008). "Operational implementation of COSMIC observations into NCEP's global data assimilation system."
In: *Weather and Forecasting* 23.4, pp. 702–711.
DOI: 10.1175/2008WAF2007070.1.

DKRZ (1993). *The ECHAM3 atmospheric general circulation model.* Report 6.
Deutsches Klimarechenzentrum, Modellbetreuungsgruppe, p. 189.

Dach, R., U. Hugentobler, P. Fridez, and M. Meindl, eds. (2007).
User manual of the Bernese GPS software version 5.0.
Astron. Inst., Univ. of Bern. Bern, Switzerland.

Diamond, B. L. and M. E. Austin (1975).
The ARIES program: Coordinates, transformations, trajectories and tracking.
Technical note 1975-15, distributed by National Technical Information Service. Massachusetts Institute for Technology, p. 90.

Dixon, T. H. (1991). "An introduction to the Global Positioning System and some geological applications." In: *Reviews of Geophysics* 29.2, pp. 249–276.

Easterling, D. R., B. Gleason, R. S. Vose, and R. J. Stouffer (2006).
A comparison of model produced maximum and minimum temperature trends with observed trends for the 20th and 21st centuries.
18th Conference on Climate Variability and Change, Session 5: Climate Modeling: Studies of Climate Change on 01.02.2006, Am. Meteorol. Soc. extended abstract. Atlanta, GA.

Engeln, A. von (2006). "A first test of climate monitoring with radio occultation instruments: Comparing two processing centers."
In: *Geophysical Research Letters* 33, L22705. DOI: 10.1029/2006GL027767.

Escudero, A., A. C. Schlesier, A. Rius, A. Flores, F. Rubek, G. B. Larsen, S. Syndergaard, and P. Høeg (2001). "Ionospheric tomography using Ørsted GPS measurements—preliminary results."
In: *Physics and Chemistry of the Earth, Part A: Solid Earth and Geodesy* 26.3, pp. 173–176. DOI: 10.1016/S1464-1895(01)00042-4.

Eshleman, V. R. (1973).
"The radio occultation method for the study of planetary atmospheres."
In: *Planetary and Space Science* 21, pp. 1521–1531.
DOI: 10.1016/0032-0633(73)90059-7.

Feng, D. D. and B. M. Herman (1999). "Remotely sensing the Earth's atmosphere using the Global Positioning System (GPS)—The GPS/MET data analysis."
In: *Journal of Atmospheric and Oceanic Technology* 16.8, pp. 989–1002.
DOI: 10.1175/1520-0426(1999)016<0989:RSTESA>2.0.CO;2.

Fjeldbo, G. and V. R. Eshleman (1968). "The atmosphere of Mars analyzed by integral inversion of the Mariner IV occultation data."
In: *Planetary and Space Science* 16.8, pp. 1035–1059.
DOI: 10.1016/0032-0633(68)90020-2.

Fjeldbo, G., A. J. Kliore, and V. R. Eshleman (1971). "The neutral atmosphere of Venus as studied with the Mariner V radio occultation experiments."
In: *The Astronomical Journal* 76.2, pp. 123–140. DOI: 10.1086/111096.

Fleming, E. L., S. Chandra, J. J. Barnett, and M. Corney (1990).
"Zonal mean temperature, pressure, zonal wind, and geopotential height as functions of latitude." In: *Advances in Space Research, COSPAR International Reference Atmosphere: 1986, Part II: Middle Atmosphere Models* 10.12, pp. 11–59.

Foelsche, U. (1999). "Tropospheric water vapor imaging by combination of ground-based and spaceborne GNSS sounding data." PhD Thesis. University of Graz, Austria: Institute for Geophysics, Astrophysics, and Meteorology.

Foelsche, U., G. Kirchengast, and A. K. Steiner (2003).
"Global climate monitoring based on CHAMP/GPS radio occultation data." In: *First CHAMP Mission Results for Gravity, Magnetic and Atmospheric Studies.* Ed. by C. Reigber, H. Lühr, and P. Schwintzer. Heidelberg: Springer, pp. 397–407.

Foelsche, U., A. Gobiet, A. K. Steiner, M. Borsche, J. Wickert, T. Schmidt, and G. Kirchengast (2006). "Global climatologies based on radio occultation data: The CHAMPCLIM project."
In: *Atmosphere and Climate: Studies by Occultation Methods.*
Ed. by U. Foelsche, G. Kirchengast, and A. K. Steiner.
Berlin Heidelberg: Springer, pp. 303–314.

Foelsche, U., G. Kirchengast, A. K. Steiner, L. Kornblueh, E. Manzini, and L. Bengtsson (2008*a*). "An observing system simulation experiment for climate monitoring with GNSS radio occultation data: Setup and test bed study."
In: *Journal of Geophysical Research* 113, D11108. DOI: 10.1029/2007JD009231.

Foelsche, U., M. Borsche, A. K. Steiner, A. Gobiet, B. Pirscher, G. Kirchengast, J. Wickert, and T. Schmidt (2008*b*). "Observing upper troposphere-lower stratosphere climate with radio occultation data from the CHAMP satellite."
In: *Climate Dynamics* 31, pp. 49–65. DOI: 10.1007/s00382-007-0337-7.

Foelsche, U., B. Pirscher, M. Borsche, G. Kirchengast, and J. Wickert (2009*a*). "Assessing the climate monitoring utility of radio occultation data: From CHAMP to FORMOSAT-3/COSMIC."
In: *Terrestrial, Atmospheric and Oceanic Science* 20.1, pp. 155–170.
DOI: 10.3319/TAO.2008.01.14.01(F3C).

Foelsche, U., B. Pirscher, M. Borsche, A. K. Steiner, G. Kirchengast, and C. Rocken (2009*b*). "Climatologies based on radio occultation data from CHAMP and Formosat-3/COSMIC."
In: *New Horizons in Occultation Research: Studies in Atmosphere and Climate.*
Ed. by A. K. Steiner, B. Pirscher, U. Foelsche, and G. Kirchengast.
Berlin Heidelberg: Springer, pp. 181–194.
DOI: 10.1007/978-3-642-00321-9_15.

Foelsche, U., B. Pirscher, M. Borsche, J. Fritzer, M. Pock, and G. Kirchengast (2009*c*). "The potential of GRAS to contribute to climate monitoring."
In: *Proc. of the 2nd EPS/Metop RAO Workshop.* SP-675/CD.
Noordwijk, NL: ESA/ESTEC Publ. Division.

Forbes, J. M. (1995). *Tidal and Planetary Waves.* Vol. 87.
Geophysical Monograph. 67–87: American Geophysical Union.

Fritzer, J., G. Kirchengast, and M. Pock (2009).
End-to-End Generic Occultation Performance Simulation and Processing System Version 5.5 (EGOPS5.5) Software User Manual.
Tech. rep. WEGC–EGOPS–2009–TR01. Version 1.
University of Graz, Austria: Wegener Center for Climate and Global Change and Institute for Geophysics, Astrophysics, and Meteorology.

GCOS (2004). *Global climate observing system implementation plan for the global observing system for climate in support of UNFCCC.* WMO-TD. Geneva: WMO, p. 136.

– (2009). *Implementation plan for the global observing system for climate in support of the UNFCCC.* WMO-TD. Draft v1.0. Geneva: WMO, p. 149.

GRAS SAF (2009). *The radio occultation processing package (ROPP) user guide, part II: Forward model and 1dVar modules.* User Guide. DMI ECMWF IEEC MetO, p. 79.

Giorgi, F. and R. Francisco (2000). "Uncertainties in regional climate change prediction: a regional analysis of ensemble simulations with the HADCM2 coupled AOGCM." In: *Climate Dynamics* 16, pp. 169–182.

Gobiet, A. (2005). *Radio occultation data analysis for climate change monitoring and first climatologies from CHAMP (Ph.D. Thesis).* Austria: Wegener Center Verlag Graz. ISBN: 3-9502126-3-9.

Gobiet, A. and G. Kirchengast (2004). "Advancements of Global Navigation Satellite System radio occultation retrieval in the upper stratosphere for optimal climate monitoring utility." In: *Journal of Geophysical Research* 109, D24110. DOI: 10.1029/2004JD005117.

Gobiet, A., U. Foelsche, A. K Steiner, M. Borsche, G. Kirchengast, and J. Wickert (2005). "Climatological validation of stratospheric temperatures in ECMWF operational analyses with CHAMP radio occultation data." In: *Geophysical Research Letters* 32, L12806. DOI: 10.1029/2005GL022617.

Gobiet, A., G. Kirchengast, G. L. Manney, M. Borsche, C. Retscher, and G. Stiller (2007). "Retrieval of temperature profiles from CHAMP for climate monitoring: Intercomparison with Envisat MIPAS and GOMOS and different atmospheric analyses." In: *Atmospheric Chemistry and Physics* 7, pp. 3519–3536.

Gorbunov, M. E. (2002). "Canonical transform method for processing radio occultation data in lower troposphere." In: *Radio Science* 37.5. DOI: 10.1029/2000RS002592.

Hagan, M. E. (1996). "Comparative effects of migrating solar sources on tidal signatures in the middle and upper atmosphere." In: *Journal of Geophysical Research* 101, D16, pp. 21213–21222.

Hagan, M. E. and J. M. Forbes (2002). "Migrating and nonmigrating diurnal tides in the middle and upper atmosphere excited by tropospheric latent heat release." In: *Journal of Geophysical Research* 107, D24. DOI: 10.1029/2001JD001236.

– (2003). "Migrating and nonmigrating semidiurnal tides in the upper atmosphere excited by tropospheric latent heat release."
In: *Journal of Geophysical Research* 108, A2. DOI: 10.1029/2002JA009466.

Hagan, M. E., R. G. Roble, and J. Hackney (2001).
"Migrating thermospheric tides." In: *Journal of Geophysical Research* 106, A7, pp. 12739–12752.

Hajj, G. A. and L. J. Romans (1998).
"Ionospheric electron density profiles obtained with the Global Positioning System: Results from the GPS/MET experiment." In: *Radio Science* 33.1, pp. 175–190.

Hajj, G. A., E. R. Kursinski, L. J. Romans, W. I. Bertiger, and S. S. Leroy (2002).
"A technical description of atmospheric sounding by GPS occultation."
In: *Journal of Atmospheric and Solar-Terrestrial Physics* 64.4, pp. 451–469.
DOI: 10.1016/S1364-6826(01)00114-6.

Hajj, G. A., C. O. Ao, P. A. Iijima, D. Kuang, E. R. Kursinski, A. J. Mannucci, T. K. Meehan, L. J. Romans, M. de la Torre Juarez, and T. P. Yunck (2004).
"CHAMP and SAC-C atmospheric occultation results and intercomparisons."
In: *Journal of Geophysical Research* 109, D06109. DOI: 10.1029/2003JD003909.

Hayashi, Y. (1971).
"A generalized method of resolving disturbances into progressive and retroprogressive waves by space Fourier and time cross-spectral analyses."
In: *Journal of the Meteorological Society of Japan* 49.2, pp. 125–128.

Healy, S. B. and J. R. Eyre (2000).
"Retrieving temperature, water vapour and surface pressure information from refractive-index profiles derived by radio occultation: A simulation study."
In: *Quarterly Journal of the Royal Meteorological Society* 126.566, pp. 1661–1683.

Healy, S. B. and J. N. Thepaut (2006).
"Assimilation experiments with CHAMP GPS radio occultation measurements."
In: *Quarterly Journal of the Royal Meteorological Society* 132.615, pp. 605–623.
DOI: 10.1256/qj.04.182.

Healy, S. (2007).
"Operational assimilation of GPS radio occultation measurements at ECMWF."
In: *ECMWF Newsletter* 111, pp. 6–11.

– (2009). *Refractivity coefficients used in the assimilation of GPS radio occultation measurements.* GRAS SAF Report 9. GRAS SAF, p. 18.

Hedin, A. E. (1991). "Extension of the MSIS thermosphere model into the middle and lower atmosphere." In: *Journal of Geophysical Research* 96, A2, pp. 1159–1172.

Hestenes, M. R. and E. Stiefel (1952). "Methods of conjugate gradients for solving linear systems." In: *Journal of Research of the National Bureau of Standards* 49.6, pp. 409–436.

Highwood, E. J. and B. J. Hoskins (1998). "The tropical tropopause." In: *Quarterly Journal of the Royal Meteorological Society* 124.549, pp. 1579–1604. DOI: 10.1002/qj.49712454911.

Ho, S.-P. et al. (2009). "Estimating the uncertainty of using GPS radio occultation data for climate monitoring: Intercomparison of CHAMP refractivity climate records from 2002 to 2006 from different data centers." In: *Journal of Geophysical Research* 114, D23107. DOI: 10.1029/2009JD011969.

Hocke, K. (1997). "Inversion of GPS meteorology data." In: *Annales Geophysicae* 15.4, pp. 443–450.

Hocke, K., G. Kirchengast, and A. K. Steiner (1997). *Ionospheric correction and inversion of GNSS occultation data: problems and solutions.* IGAM/UG Technical Report for ESA/ESTEC No. 2. Institute for Geophysics, Astrophysics, and Meteorology.

Hocke, K., K. Igarashi, and T. Tsuda (2003). "High-resolution profiling of layered structures in the lower stratosphere by GPS occultation." In: *Geophysical Research Letters* 30.8. DOI: 10.1029/2002GL016566.

Hofmann-Wellenhof, B., H. Lichtenegger, and J. Collins (1997). *GPS Theory and Practice.* Wien New York: Springer, p. 389.

Hofmann-Wellenhof, B., H. Lichtenegger, and E. Wasle (2008). *GNSS—Global Navigation Satellite Systems.* Wien New York: Springer, p. 516.

Holton, J. R. (1975). *The Dynamic Meteorology of the Stratosphere and Mesosphere.* Vol. 15. Meteorological Monograph 37. American Meteorology Society.

Hsu, H.-H. and B. J. Hoskins (1989). "Tidal fluctuations as seen in ECMWF data." In: *Quarterly Journal of the Royal Meteorological Society* 115.486, pp. 247–264. DOI: 10.1002/qj.49711548603.

Huang, C. M., S. D. Zhang, and F. Yi (2009). "Intensive radiosonde observations of the diurnal tide and planetary waves in the lower atmosphere over Yichang (111°18' E, 30°42' N), China." In: *Annales Geophysicae* 27, pp. 1079–1095.

IGS (2009). *IGS Products.*
URL: http://igscb.jpl.nasa.gov/components/prods.html (visited on Sept. 17, 2009).

Jakob, C. et al. (2000).
"The IFS cycle CY21r4 made operational in October 1999."
In: *ECMWF Newsletter* 87, pp. 2–9.

Jakowski, N., S. Heise, A. Wehrenpfennig, S. Schlüter, and R. Reimer (2002).
"GPS/GLONASS-based TEC measurements as a contributor for space weather forecast." In: *Journal of Atmospheric and Solar-Terrestrial Physics* 64, pp. 729–735.

Jensen, A. S., M. S. Lohmann, H.-H. Benzon, and A. S. Nielsen (2003).
"Full spectrum inversion of radio occultation signals."
In: *Radio Science* 38.3, 1040. DOI: 10.1029/2002RS002763.

– (2004*a*). "Fourier analysis of GNSS-LEO radio occultation signals, resolution and limitations." In: *Occultations for Probing Atmosphere and Climate.*
Ed. by G. Kirchengast, U. Foelsche, and A. K. Steiner.
Berlin, Heidelberg: Springer-Verlag, pp. 53–60.

Jensen, A. S., M. S. Lohmann, A. S. Nielsen, and H.-H. Benzon (2004*b*).
"Geometrical optics phase matching of radio occultation signals."
In: *Radio Science* 39, RS3009. DOI: 10.1029/2003RS002899.

Jensen, A. S., H.-H. Benzon, M. S. Lohmann, and A. S. Nielsen (2006).
"Processing radio occultation data by full spectrum inversion techniques: An overview and recent developments."
In: *Atmosphere and Climate: Studies by Occultation Methods.*
Ed. by U. Foelsche, G. Kirchengast, and A. K. Steiner.
Berlin, Heidelberg: Springer-Verlag, pp. 95–112.

Karl, T. R., J. Hassol, C. D. Miller, and W. L. Murray (2006). *Temperature trends in the lower atmosphere: steps for understanding and reconciling differences.*
Report. Climate Change Science Program and the Subcommittee on Global Change Research, Washington, DC.

Khélifa, N., M. Lecollinet, and M. Himbert (2007).
"Molar mass of dry air in mass metrology." In: *Measurement* 40.7-8, pp. 779–784. DOI: 10.1016/j.measurement.2006.05.009.

Kirchengast, G. (1996).
End-to-end GNSS Occultation Performance Simulator functionality definition.
Technical Report for ESA/ESTEC No. 1/1996.
Institute for Geophysics, Astrophysics, and Meteorology.

– (1998). *End-to-end GNSS Occultation Performance Simulator overview and exemplary applications.* Wissenschaftl. Ber. No. 2/1998.
Institute for Geophysics, Astrophysics, and Meteorology.

Kirchengast, G., S. Schweitzer, J. Ramsauer, and J. Fritzer (2004).
End-to-end Generic Occultation Performance Simulator Version 5 (EGOPS5) Software User Manual (Overview-, Reference-, and File Format Manual).
Technical Report for ESA/ESTEC No. 6/2004.
Institute for Geophysics, Astrophysics, and Meteorology.

Kirk-Davidoff, D., R. M. Goody, and J. G. Anderson (2005).
"Analysis of sampling errors for climate monitoring satellites."
In: *Journal of Climate* 18.6, pp. 810–822. DOI: 10.1175/JCLI-3301.1.

König, R., G. Michalak, K. Neumayer, and S. Zhu (2005).
"Remarks on CHAMP orbit products."
In: *Observation of the Earth System from Space.* Ed. by J. Flury, R. Rummel, C. Reigber, M. Rothacher, G. Boedecker, and U. Schreiber.
Berlin, Heidelberg: Springer-Verlag, pp. 17–26.
DOI: 10.1007/3-540-29522-4_2.

Kuo, Y.-H., S. Sokolovskiy, R. A. Anthes, and F. Vandenberghe (2000).
"Assimilation of GPS radio occultation data for numerical weather prediction."
In: *Terrestrial, Atmospheric and Oceanic Science* 11.1, pp. 157–186.

Kuo, Y.-H., T.-K. Wee, S. Sokolovskiy, C. Rocken, W. Schreiner, D. Hunt, and R. A. Anthes (2004).
"Inversion and error estimation of GPS radio occultation data."
In: *Journal of the Meteorological Society of Japan* 82, 1B, pp. 507–531.

Kursinski, E. R., G. A. Hajj, J. T. Schofield, R. P. Linfield, and K. R. Hardy (1997). "Observing Earth's atmosphere with radio occultation measurements using the Global Positioning System."
In: *Journal of Geophysical Research* 102, D19, pp. 23429–23465.

Lackner, B. C. and B. Pirscher (2005). *Climate diagnostics in radio occultation temperature climatologies of CHAMP and ECMWF.*
Scientific Report No. 7/2005.
University of Graz, Austria: Wegener Center for Climate and Global Change and Institute for Geophysics, Astrophysics, and Meteorology, pp. 1–269.

Lalaurette, F. (1999). "Changes to the operational forecasting system."
In: *ECMWF Newsletter* 83, p. 1.

Larson, W. J. and J. R. Wertz, eds. (1997). *Space Mission Analysis and Design.* Space Technology Library.
USA, The Netherlands: Microcosm, Inc. and Kluwer Academic Publishers, p. 865.

Leroy, S. S. (2001).
"The effects of orbital precession on remote climate monitoring."
In: *Journal of Climate* 14.22, pp. 4330–4337.
DOI: 10.1175/1520-0442(2001)014<4330:TEOOPO>2.0.CO;2.

Leroy, S. S., J. A. Dykema, and J. G. Anderson (2006).
"Climate benchmarking using GNSS occultation."
In: *Atmosphere and Climate: Studies by Occultation Methods.*
Ed. by U. Foelsche, G. Kirchengast, and A. K. Steiner.
Berlin Heidelberg: Springer, pp. 287–302.

Lieberman, R. S. (1991).
"Nonmigrating diurnal tides in the equatorial middle atmosphere."
In: *Journal of the Atmospheric Sciences* 48.8, pp. 1112–1123.

Lindzen, R. S. (1979). "Atmospheric tides."
In: *Annual Review of Earth and Planetary Sciences* 7, pp. 199–225.
DOI: 10.1146/annurev.ea.07.050179.001215.

– (1990). *Dynamics in Atmospheric Physics.*
Cambridge, New York, Melbourne: Cambridge University Press, p. 310.

Lindzen, R. S. (2008). *12.810 Dynamics of the Atmosphere.*
Massachusetts Institute of Technology: MIT OpenCourseWare.
URL: http://ocw.mit.edu/OcwWeb/Earth--Atmospheric--and-Planetary-Sciences/12-810Spring-2008/CourseHome/ (visited on Nov. 20, 2009).

Liu, H., X. Zou, H. Shao, R. A. Anthes, J. C. Chang, J.-H. Tseng, and B. Wang (2001). "Impact of 837 GPS/MET bending angle profiles on assimilation and forecasts for the period June 20–30, 1995."
In: *Journal of Geophysical Research* 106, D23, pp. 31771–31786.
DOI: 10.1029/2001JD000345.

Loiselet, M., N. Stricker, Y. Menard, and J.-P. Luntama (2000).
"GRAS—MetOp's GPS-based atmospheric sounder." In: *ESA Bulletin* 102, pp. 38–44.

Löscher, A., K. B. Lauritsen, and M. Sorensen (2009).
"The GRAS SAF radio occultation processing intercomparison project ROPIC."
In: *New Horizons in Occultation Research: Studies in Atmosphere and Climate.*
Ed. by A. K. Steiner, B. Pirscher, U. Foelsche, and G. Kirchengast.
Berlin, Heidelberg: Springer-Verlag, pp. 49–62.
DOI: 10.1007/978-3-642-00321-9_5.

Luntama, J.-P. (2006). "The operational EPS GRAS measurement system."
In: *Atmosphere and Climate: Studies by Occultation Methods.*
Ed. by U. Foelsche, G. Kirchengast, and A. K. Steiner.
Berlin Heidelberg: Springer, pp. 147–156.

– (2009). "Radio occultation soundings in ionosphere and space weather applications: Achievements and prospects."
In: *New Horizons in Occultation Research: Studies in Atmosphere and Climate.*
Ed. by A. K. Steiner, B. Pirscher, U. Foelsche, and G. Kirchengast.
Berlin, Heidelberg: Springer-Verlag, pp. 63–76.
DOI: 10.1007/978-3-642-00321-9_6.

Marquardt, C. (2009). *GRAS prototype data format description.*
Document number EUM/OPS/TEN/09/2483. EUMETSAT, pp. 1–13.

Marquardt, C., Y. Andres, A. von Engeln, and F. Sancho (2009).
SNR and bending angle noise in CHAMP, GRACE, COSMIC and GRAS data.
Fourth FORMOSAT-3/COSMIC Data Users Workshop, 27–29 October 2009:
Boulder, Colorado U.S.A. URL: http://www.cosmic.ucar.edu/oct2009workshop/prespublic/marquardt-28.pdf
(visited on Feb. 8, 2010).

McLandress, C. (2002*a*).
"The seasonal variation of the propagating diurnal tide in the mesosphere and lower thermosphere. Part I: The role of gravity waves and planetary waves."
In: *Journal of the Atmospheric Sciences* 59.5, pp. 893–906.

– (2002*b*).
"The seasonal variation of the propagating diurnal tide in the mesosphere and lower thermosphere. Part II: The role of tidal heating and zonal mean winds."
In: *Journal of the Atmospheric Sciences* 59.5, pp. 907–922.

Mears, C. A. and F. J. Wentz (2005). "The effect of diurnal correction on satellite-derived lower tropospheric temperature." In: *Science* 309, pp. 1548–1551. DOI: 10.1126/science.1114772.

Meeus, J. and D. Savoie (1992). "The history of the tropical year."
In: *Journal of the British Astronomical Association* 102, pp. 40–42.

Melbourne, W. G., E. S. Davis, C. B. Duncan, G. A. Hajj, K. R. Hardy, E. R. Kursinski, T. K. Meehan, L. E. Young, and T. P. Yunck (1994). "The application of spaceborne GPS to atmospheric limb sounding and global change monitoring." In: *JPL Publication* 94-18, p. 147.

Mohr, P. J., B. N. Taylor, and D. B. Newell (2008). "CODATA recommended values of the fundamental physical constants: 2006." In: *Reviews of Modern Physics* 80, pp. 663–730. DOI: 10.1103/RevModPhys.80.633.

Montenbruck, O., M. Garcia-Fernandez, Y. Yoon, S. Schön, and A. Jäggi (2009). "Antenna phase center calibration for precise positioning of LEO satellites." In: *GPS Solutions* 13.1, pp. 23–34. DOI: 10.1007/s10291-008-0094-z.

Mostert, S. and J.-A. Koekemoer (1997). "The science and engineering payloads and experiments on SUNSAT." In: *Acta Astronautica* 41.4, pp. 401–411. DOI: 10.1016/S0094-5765(98)00095-2.

Mukhtarov, P., D. Pancheva, and B. Andonov (2009). "Global structure and seasonal and interannual variability of the migrating diurnal tide seen in the SABER/TIMED temperatures between 20 and 120 km." In: *Journal of Geophysical Research* 114, A02309. DOI: 10.1029/2008JA013759.

NIMA (2000). *Department of Defense World Geodetic System 1984: Its definitions and relationships with local geodetic systems.* NIMA TR8350.2. National Imagery and Mapping Agency. URL: http://earth-info.nga.mil/GandG/publications/tr8350.2/wgs84fin.pdf (visited on Mar. 20, 2010).

Oberheide, J. (2006). "On large-scale wave coupling across the stratopause." Habilitationsschrift. Bergische Universität Wuppertal.

Pirscher, B., B. C. Lackner, I. Thaler, M. Pock, U. Foelsche, A. K. Steiner, and G. Kirchengast (2007*a*). *Initial validation of GRAS occultation data from MetOp and setup of regional climate monitoring including the IPCC land and ocean regions.* Technical Report for FFG-ALR 5/2007. University of Graz, Austria: Wegener Center for Climate and Global Change, p. 56.

Pirscher, B., U. Foelsche, B. C. Lackner, and G. Kirchengast (2007*b*). "Local time influence in single-satellite radio occultation climatologies from Sun-synchronous and non-Sun-synchronous satellites." In: *Journal of Geophysical Research* 112, D11119. DOI: 10.1029/2006JD007934.

Pirscher, B., U. Foelsche, M. Borsche, and G. Kirchengast (2009).
"Sampling of the diurnal tide of temperature using Formosat-3/COSMIC data."
In: *New Horizons in Occultation Research: Studies in Atmosphere and Climate.*
Ed. by A. K. Steiner, B. Pirscher, U. Foelsche, and G. Kirchengast.
Berlin Heidelberg: Springer, pp. 131–140.
DOI: 10.1007/978-3-642-00321-9_11.

Pirscher, B., U. Foelsche, M. Borsche, G. Kirchengast, and Y.-H. Kuo (2010).
"Analysis of migrating diurnal tides detected in FORMOSAT-3/COSMIC
temperature data." In: *Journal of Geophysical Research.* accepted.
DOI: 10.1029/2009JD013008.

Randel, W., M. L. Chanin, and C. Michaut (2002).
SPARC intercomparison of middle atmosphere climatologies. WCRP 166.
WMO/TD No. 1142; SPARC Report No. 3. SPARC, p. 96.

Randel, W. et al. (2004).
"The SPARC intercomparison of middle-atmosphere climatologies."
In: *Journal of Climate* 17.5, pp. 986–1003.
DOI: 10.1175/1520-0442(2004)017<0986:TSIOMC>2.0.CO;2.

Revathy, K., S. R. Prabhakaran Nayar, and B. V. Krishna Murthy (2001).
"Diurnal variation of tropospheric temperature at a tropical station."
In: *Annales Geophysicae* 19, pp. 1001–1005.

Rieder, M. J. and G. Kirchengast (2001). "Error analysis and characterization of
atmospheric profiles retrieved from GNSS occultation data."
In: *Journal of Geophysical Research* 106, D23, pp. 31755–31770.

Riggin, D. M., E. Kudeki, Z. Feng, M. F. Sarango, and R. S. Lieberman (2002).
"Jicamarca radar observations of the diurnal and semidiurnal tide in the
troposphere and lower stratosphere."
In: *Journal of Geophysical Research* 107, D8. DOI: 10.1029/2001JD001216.

Rocken, C. et al. (1997).
"Analysis and validation of GPS/MET data in the neutral atmosphere."
In: *Journal of Geophysical Research* 102, D25, pp. 29849–29866.

Rocken, C., Y.-H. Kuo, W. S. Schreiner, D. Hunt, S. Sokolovskiy, and
C. McCormick (2000). "COSMIC system description."
In: *Terrestrial, Atmospheric and Oceanic Science* 11.1, pp. 21–52.

Rodgers, C. D. (2000).
Inverse Methods for Atmospheric Sounding: Theory and Practice. Vol. 2.
Series on Atmospheric Oceanic and Planetary Physics.
Singapore: World Scientific Publishing Company.

Rüeger, J. M. (2002). *Refractive index formulae for radio waves.* JS28 Integration of Techniques and Corrections to Achieve Accurate Engineering; FIG XXII International Congress. Washington DC, USA.

Salby, M. L. and P. Callaghan (1997). "Sampling error in climate properties derived from satellite measurements: Consequences of undersampled diurnal variability." In: *Journal of Climate* 10, pp. 18–36. DOI: 10.1175/1520-0442(1997)010<0018:SEICPD>2.0.CO;2.

Schmidt, T., J. Wickert, G. Beyerle, and C. Reigber (2004). "Tropical tropopause parameters derived from GPS radio occultation measurements with CHAMP." In: *Journal of Geophysical Research* 109, D13105. DOI: 10.1029/2004JD004566.

Schmidt, T., S. Heise, J. Wickert, G. Beyerle, and C. Reigber (2005). "GPS radio occultation with CHAMP and SAC-C: global monitoring of thermal tropopause parameters." In: *Atmospheric Chemistry and Physics* 5.6, pp. 1473–1488.

Schreiner, W. S., S. V. Sokolovskiy, C. Rocken, and D. C. Hunt (1999). "Analysis and validation of GPS/MET radio occultation data in the ionosphere." In: *Radio Science* 34.4, pp. 949–966.

Schreiner, W., C. Rocken, S. Sokolovskiy, S. Syndergaard, and D. Hunt (2007). "Estimates of the precision of GPS radio occultations from the COSMIC/FORMOSAT-3 mission." In: *Geophysical Research Letters* 34, L04808. DOI: 10.1029/2006GL027557.

Schreiner, W., C. Rocken, S. Sokolovskiy, and D. Hunt (2009). "Quality assessment of COSMIC/FORMOSAT-3 GPS radio occultation data derived from single- and double-difference atmospheric excess phase processing." In: *GPS Solutions* 14.1, pp. 13–22. DOI: 10.1007/s10291-009-0132-5.

Seeber, G. (2003). *Satellite Geodesy.* Berlin New York: Walter de Gruyter, p. 589.

Seidel, D. J., M. Free, and J. Wang (2005). "Diurnal cycle of upper-air temperature estimated from radiosondes." In: *Journal of Geophysical Research* 110, D09102. DOI: 10.1029/2004JD005526.

Smith, E. and S. Weintraub (1953). "The constants in the equation for atmospheric refractive index at radio frequencies." In: *Proceedings of the IRE* 41, pp. 1035–1037.

Steiner, A. K. (1998). "High resolution sounding of key climate variables using the radio occultation technique." PhD thesis. University of Graz, Austria: Institute for Geophysics, Astrophysics, and Meteorology.

Steiner, A. K., G. Kirchengast, and H. P. Ladreiter (1999). "Inversion, error analysis, and validation of GPS/MET occultation data." In: *Annales Geophysicae* 17.1, pp. 122–138. DOI: 10.1007/s00585-999-0122-5.

Steiner, A. K., G. Kirchengast, U. Foelsche, L. Kornblueh, E. Manzini, and L. Bengtsson (2001). "GNSS occultation sounding for climate monitoring." In: *Physics and Chemistry of the Earth, Part A: Solid Earth and Geodesy* 26.3, D09102, pp. 113–124. DOI: 10.1016/S1464-1895(01)00034-5.

Steiner, A. K., G. Kirchengast, B. C. Lackner, B. Pirscher, M. Borsche, and U. Foelsche (2009). "Atmospheric temperature change detection with GPS radio occultation 1995 to 2008." In: *Geophysical Research Letters* 36, L18702. DOI: 10.1029/2009GL039777.

Suppan, C. (2010). "Untersuchung der Langzeitstabilität des Abtastfehlers von CHAMP Radiookkultationsmessungen 2001–2008." in german. Master's thesis. University of Graz, Austria: Wegener Center for Climate and Global Change and Institute for Physics.

Syndergaard, S. (1998). "Modeling the impact of the Earth's oblateness on the retrieval of temperature and pressure profiles from limb sounding." In: *Journal of Atmospheric and Solar-Terrestrial Physics* 60.2, pp. 171–180. DOI: 10.1016/S1364-6826(97)00056-4.

– (1999). *Retrieval analysis and methodologies in atmospheric limb sounding using the GNSS radio occultation technique.* DMI Sci Rep 99-6. Danish Meteorological Institute, Copenhagen, Denmark, p. 131.

– (2000). "On the ionosphere calibration in GPS radio occultation measurements." In: *Radio Science* 35.3, pp. 865–883.

Thaler, I. (2009). "Climate trends and variability over the IPCC+ regions." Master's thesis. University of Graz, Austria: Wegener Center for Climate and Global Change and Institute for Physics.

Trenberth, K. E. et al. (2007). "Observations: surface and atmospheric climate change." In: *Climate Change 2007: The Physical Science Basis.* Ed. by S. Solomon et al. Cambridge, UK and New York, NY, USA: Cambridge Univ Press, pp. 235–336.

Tsuda, T. and S. Kato (1989). "Diurnal non-migrating tides excited by a differential heating due to land-sea distribution." In: *Journal of the Meteorological Society of Japan* 67, pp. 43–54.

Tsuda, T., T. Nakamura, A. Shimizu, T. Yoshino, S. W. B. Harijono, T. Sribimawati, and H. Wiryosumarto (1997). "Observations of diurnal oscillations with a meteor wind radar and radiosondes in Indonesia." In: *Journal of Geophysical Research* 102, D22, pp. 26217–26224.

The International System of Units (SI) (2001). NIST Special Publication 330. National Institute of Standards and Technology. URL: http://physics.nist.gov/Document/sp330.pdf (visited on Mar. 20, 2010).

Untch, A. et al. (1998).
"Increased stratospheric resolution in the ECMWF forecasting system."
In: *ECMWF Newsletter* 82, pp. 2–8.

Untch, A., M. Miller, M. Hortal, R. Buizza, and P. Janssen (2006).
"Towards a global meso-scale model: The high-resolution system T799L91 and T399L62 EPS." In: *ECMWF Newsletter* 108, pp. 6–13.

Uppala, S. M. et al. (2005). "The ERA-40 re-analysis."
In: *Quarterly Journal of the Royal Meteorological Society* 131.612, pp. 2961–3012. DOI: 10.1256/qj.04.176.

Vinnikov, K. Y., N. C. Grody, A. Robock, R. J. Stouffer, P. D. Jones, and M. D. Goldberg (2006).
"Temperature trends at the surface and in the troposphere."
In: *Journal of Geophysical Research* 111, D03106. DOI: 10.1029/2005JD006392.

Vorob'ev, V. V. and T. G. Krasil'nikova (1994).
"Estimation of the accuracy of the atmospheric refractive index recovery from Doppler shift measurements at frequencies used in the NAVSTAR system."
In: *Izvestiya, Atmospheric and Oceanic Physics* 29, pp. 602–609.

Vose, R. S., D. R. Easterling, and B. Gleason (2005). "Maximum and minimum temperature trends for the globe: An update through 2004."
In: *Journal of Geophysical Research* 32, L23822. DOI: 10.1029/2005GL024379.

WMO (1957). *Meteorology – A three dimensional science.*
World Meteorological Organization Bulletin 6.
Geneva: World Meteorological Organization (WMO).

Wallace, J. M., Y. Zhang, and K.-H. Lau (1993). "Structure and seasonality of interannual and interdecadal variability of the geopotential height and temperature fields in the northern hemisphere troposphere."
In: *Journal of Climate* 6.11, pp. 2063–2082.
DOI: 10.1175/1520-0442(1993)006<2063:SASOIA>2.0.CO;2.

Ware, R. et al. (1996).
"GPS sounding of the atmosphere from low Earth orbit: Preliminary results."
In: *Bulletin of the American Meteorological Society* 77.1, pp. 19–40.
DOI: 10.1175/1520-0477(1996)077<0019:GSOTAF>2.0.CO;2.

Wickert, J. (2002). *Das CHAMP-Radiookkultationsexperiment: Algorithmen, Prozessierungssystem und erste Ergebnisse.* Scientific Tech Rep STR02/07. GeoForschungsZentrum Potsdam, p. 149.

Wickert, J. et al. (2001).
"Atmosphere sounding by GPS radio occultation: First results from CHAMP."
In: *Geophysical Research Letters* 28.17, pp. 3263–3266.

Wickert, J., G. Beyerle, T. Schmidt, C. Marquardt, R. König, L. Grunwaldt, and C. Reigber (2003). "GPS radio occultation with CHAMP." In: *First CHAMP Mission Results for Gravity, Magnetic and Atmospheric Studies.* Ed. by C. Reigber, H. Lühr, and P. Schwintzer. Berlin Heidelberg: Springer, pp. 371–383.

Wickert, J., T. Schmidt, G. Beyerle, R. König, C. Reigber, and N. Jakowski (2004). "The radio occultation experiment aboard CHAMP: Operational data analysis and validation of vertical atmospheric profiles." In: *Journal of the Meteorological Society of Japan* 82, pp. 381–395.

Wickert, J., G. Beyerle, R. König, S. Heise, L. Grunwaldt, G. Michalak, C. Reigber, and T. Schmidt (2005). "GPS radio occultation with CHAMP and GRACE: A first look at a new and promising satellite configuration for global atmospheric sounding." In: *Annales Geophysicae* 23, pp. 653–658.

Wickert, J., T. Schmidt, G. Beyerle, G. Michalak, R. König, S. Heise, and C. Reigber (2006). "GPS radio occultation with CHAMP and GRACE: Recent results." In: *Atmosphere and Climate: Studies by Occultation Methods.* Ed. by U. Foelsche, G. Kirchengast, and A. K. Steiner. Berlin, Heidelberg: Springer-Verlag, pp. 3–16.

Wickert, J., T. Schmidt, G. Michalak, S. Heise, C. Arras, G. Beyerle, C. Falck, R. König, D. Pingel, and M. Rothacher (2009). "GPS radio occultation with CHAMP, GRACE-A, SAC-C, TerraSAR-X, and FORMOSAT-3/COSMIC: Brief review of results from GFZ." In: *New Horizons in Occultation Research: Studies in Atmosphere and Climate.* Ed. by A. K. Steiner, B. Pirscher, U. Foelsche, and G. Kirchengast. Berlin, Heidelberg: Springer-Verlag, pp. 3–16.

Williams, C. R. and S. K. Avery (1996). "Diurnal nonmigrating tidal oscillations forced by deep convective clouds." In: *Journal of Geophysical Research* 101.D2, pp. 4079–4091.

Wu, B.-H., V. Chu, P. Chen, and T. Ting (2005). "FORMOSAT-3/COSMIC science mission update." In: *GPS Solutions* 9.2, pp. 111–121. DOI: 10.1007/s10291-005-0140-z.

Zeng, Z., W. Randel, S. Sokolovskiy, C. Deser, Y.-H. Kuo, M. Hagan, J. Du, and W. Ward (2008). "Detection of migrating diurnal tide in the tropical upper troposphere and lower stratosphere using the Challenging Minisatellite Payload radio occultation data." In: *Journal of Geophysical Research* 113, D03102. DOI: 10.1029/2007JD008725.

Zhang, X., J. M. Forbes, M. E. Hagan, J. M. Russell III, S. E. Palo, C. J. Mertens, and M. G. Mlynczal (2006).
"Monthly tidal temperatures 20–120 km from TIMED/SABER."
In: *Journal of Geophysical Research* 111, A10S08. DOI: 10.1029/2005JA011504.

List of Figures

List of Tables

Abstract:
This report investigates the suitability of RO observations to serve as climate benchmark record by validating the consistency of RO data provided by different satellites. The main focus lies on systematic differences of RO climatologies, originating from different data processing systems, data quality, spatio-temporal sampling, and particular orbit characteristics. Data of six RO satellite missions (including one multi-satellite constellation) are analyzed.
Largest disagreements of RO climatologies are observed when comparing data provided by different processing centers. Mean absolute temperature differences between 8 km and 30 km altitude amount to 0.5 K, while climate time series of temperature changes agree much closer.
Utilizing RO data from the same data center and considering spatio-temporal sampling yield remarkable consistency of temperature climatologies with mean differences being smaller than 0.1 K. Disagreements are found to be largest at 35 km, where they exceed 0.2 K. This results from different data quality and its utilization within the processing scheme. Climatologies, which are derived from data with the same quality agree to within 0.02 K also at high altitudes. The measurement's local time, which depends on the satellite's orbit, has a minor but clearly understandable influence on differences in RO climatologies. The results underline the utility of RO data for long-term monitoring of the global climate.

Zum Inhalt:
In dieser Arbeit wird die Konsistenz von RO Messungen verschiedener Satelliten validiert um festzustellen, ob die Daten tatsächlich als Referenzklimadatensatz geeignet sind. Das Hauptaugenmerk liegt auf der Untersuchung systematischer Unterschiede zwischen Klimatologien, welche durch verschiedene Prozessierungssysteme, unterschiedliche Datenqualität, Orte und Zeiten der Messungen sowie ausgewählte Orbiteigenschaften zustande kommen. Es werden Daten von sechs Satellitenmissionen (darunter eine Multisatellitenmission) analysiert.
Größte Unterschiede zwischen RO Klimatologien entstehen, wenn man Daten verschiedener Prozessierungszentren vergleicht. Mittlere absolute Temperaturdifferenzen zwischen 8 km und 30 km Höhe betragen 0.5 K, während Klimazeitreihen von Temperaturänderungen viel genauer übereinstimmen.
Verwendet man Daten vom selben Datenzentrum und berücksichtigt unterschiedliche Orte und Zeiten der Messungen, so findet man eine bemerkenswerte Übereinstimmung der Klimatologien (im Mittel $\Delta T<0.1$ K). Größte Differenzen ($\Delta T>0.2$ K) lassen sich in großen Höhen (35 km) ausmachen. Die Ursache dafür liegt in der unterschiedlichen Datenqualität, welche in der Prozessierung verwendet wird. Klimatologien, welche von Daten gleicher Qualität berechnet wurden, stimmen auch in großen Höhen bis auf 0.02 K überein. Unterschiedliche Lokalzeiten der Messungen, die von den Satellitenbahnen abhängen, haben nur einen geringen Einfluss auf Unterschiede zwischen Klimatologien verschiedener Satelliten. Die Ergebnisse unterstreichen die Wichtigkeit von RO Daten für die Langzeitklimabeobachtung.

Wegener Center for Climate and Global Change
University of Graz
Leechgasse 25
A-8010 Graz, Austria
www.wegcenter.at
ISBN 978-3-9502940-3-3